The dissertation committee for Christopher Hudson Moore certifies that this is the approved version of the following dissertation:

Monte Carlo Simulation of the Jovian Plasma Torus Interaction with Io's Atmosphere and the Resultant Aurora during Eclipse

Committee:

David B. Goldstein, Co-Supervisor

Philip L. Varghese, Co-Supervisor

Venkatramanan Raman

Laurence M. Trafton

Michael Combi

Monte Carlo Simulation of the Jovian Plasma Torus Interaction with Io's Atmosphere and the Resultant Aurora during Eclipse

by

Christopher Hudson Moore, B.S.

Dissertation

Presented to the Faculty of the Graduate School of
The University of Texas at Austin
in Partial Fulfillment of the
Requirements for the Degree of

Doctor of Philosophy

The University of Texas at Austin
August 2011

To my ever-patient wife Miranda and our son Bryan

Acknowledgements

I would like to thank my advisors, Dr. David Goldstein and Dr. Philip Varghese, and Dr. Laurence Trafton for all of their guidance, support, and many discussions during the course of this research. I also extend thanks to Dr. Michael Combi for his input and insightful comments on this research. Finally, I must also extend my graditude to my advisors again for their eternal patience and understanding for all the delays when I had to take care of my son, Bryan.

I gladly acknowledge my past colleagues, Ju Zhang and Bénédicte Stewart, whose work on the planetary DSMC code allowed for me to do the research presented here. Ju Zhang in particular taught me DSMC when I was but a lowly undergraduate research assistant and continued to mentor me during the first year of graduate school. I am convinced that I would not have finished this dissertation without the support and many, many fruitful discussions with my colleague, and friend, Bénédicte Stewart. Kenji Miki was only a colleague for a short while, but his work on the foundation of the Monte Carlo electron transport code was instrumental and deserves much thanks. Finally I extend my graditude to my friends and colleagues Andrew Walker and James Strand with whom I have had numerous helpful discussions about this work throughout the years. Finally, I wish to express thanks to my other past and present colleagues (and friends): Conrad Lee, Billy McDoniel, Aaron Morris, Kelly Stefani, Parvathy Prem, and Seng Yeoh.

The support, patience, and love of my wife over this long journey cannot be appreciated enough; especially after the birth of our son. I also thank my parents and brother for being there for me throughout my ~26 years of education.

I would like to thank the Texas Advanced Computing Center (TACC) for their computational resources. Funding for this work has been provided by several NASA programs including HST Archive, Planetary Atmospheres, and Outer Planetary Research.

Monte Carlo Simulation of the Jovian Plasma Torus Interaction with Io's Atmosphere and the Resultant Aurora during Eclipse

Christopher Hudson Moore, Ph.D.

The University of Texas at Austin, 2011

Supervisors: David B. Goldstein and Philip L. Varghese

Io, the innermost Galilean satellite of Jupiter, exhibits a wide variety of complex phenomena such as interaction with Jupiter's magnetosphere, volcanic activity, and a rarefied multi-species sublimating and condensing atmosphere with an ionosphere. Io's orbital resonance with Jupiter and the other Galilean satellites produces intense tidal heating. This makes Io the most volcanically active body in the solar system with plumes that rise hundreds of kilometers above the surface. In the present work, the interaction of Io's atmosphere with the Jovian plasma torus is simulated via the Direct Simulation Monte Carlo (DSMC) method and the aurora produced via electron-neutral excitation collisions is examined using electron transport Monte Carlo simulation.

The electron-transport Monte Carlo simulation models the electron collisions with the neutral atmosphere and their transport along field lines as they sweep past Io, using a pre-computed steady atmosphere and magnetic field. As input to the Monte Carlo simulation, the neutral atmosphere was first modeled using prior 2D *sunlit* continuum simulations of Io's atmosphere produced by others. In order to justify the use of a sunlit atmosphere for eclipse, 1D two-species (SO_2 and a non-condensable) DSMC simulations of Io's atmospheric dynamics during and immediately after eclipse were performed. It was found that the inclusion of a non-condensable species (SO or O_2) leads to the formation of a diffusion layer which prevents rapid collapse. The degree to which the diffusion layer slowed the atmospheric collapse was found to be extremely sensitive to both the initial non-condensable mole fraction and the reaction (or sticking) probability on the surface of the "non-

condensable". Furthermore, upon egress, vertical stratification of the atmosphere occurred with the non-condensable species being lifted to higher altitudes by the rapid sublimation of SO_2 as the surface warms.

Simulated aurorae (specifically the [OI] 6300 Å and the S_2, SO, and SO_2 molecular band emission in the middle ultraviolet) show good agreement with observations of Io in eclipse and an attempt was made to use the simulations to constrain the upstream torus electron temperature and Io's atmospheric composition, structure, and volcanic activity. It is found that the position of the bright [OI] 6300 Å wake spot relative to Io's equator depends on the position of Io relative to the plasma torus' equator and the asymmetric electron number flux that results. Using HST/STIS UV-Vis spectra, the upstream electron temperature is weakly constrained to be between 3 eV and 8 eV depending on the flux of a low energy (35 eV), non-thermal component of the plasma (more non-thermal flux requires lower thermal plasma temperatures to fit the spectrum). Furthermore, an upper limit of 5% of the thermal torus density (or 180 cm^{-3} based on the Galileo J0 plasma density at Io) is obtained for the low energy non-thermal component of the plasma. These limits are consistent with Galileo observations of the upstream torus temperature and estimates for the the non-thermal component. Finally, plume activity and S_2 content during eclipse observations with HST/STIS were constrained by examining the emission intensity along the spatial axis of the aperture. During the August 1999 UV-Vis observations, the auroral simulations indicate that the large volcanoes Pele and Surt were inactive whereas Tvashtar was active and that Dazhbog and possibly Loki were also actively venting gas. The S_2 content inferred for the large Pele-type plumes was between 5% (Tvashtar) and 30% (Loki, if active), consistent with prior observations (Spencer *et al.*, 2000; Jessup *et al.*, 2007).

A 3D DSMC simulation of Io's sublimation and sputtered atmosphere including photo- and plasma-chemistry was developed. In future work these atmospheric simulations will replace the continuum target atmosphere in the auroral model and thus enable a better match to the observed high altitude auroral emission. In the present work, the plasma interaction is modeled by a flux of ions and electrons which flow around and through Io's atmosphere along pre-computed fields and interact with the neutral gas. A 3D DSMC simulation of Io's atmosphere assuming a simple thermal model for the surface just prior to

ingress into eclipse and uniform frost coverage has been performed in order to understand how Io's general atmospheric dynamics are affected by the new plasma model with chemistry and sputtering. Sputtering was found to supply most of the nightside atmosphere (producing an SO_2 column of ~5×10^{13} cm^{-2}); however, the dense dayside sublimation atmosphere was found to block sputtering of the surface. The influence of the dynamic plasma pressure on the day-to-night circumplanetary flow was found to be quite substantial causing the day-to-night wind across the dawn terminator to flow slightly towards the equator. This results in a region of high density near the equator that extends far (~2000 km for the condensable species) onto the nightside across the dawn terminator. Thus, even without thermal lag due to rotation or variable surface frost, highly asymmetric equatorial column densities relative to the subsolar point are obtained. The non-condensable O_2, which is a trace species on the dayside, is the dominant species on the nightside despite increased SO_2 sputtering because the loss rate of O_2 is slow. Finally, a very intriguing O_2 flow feature was observed near the dusk terminator where the flow from the leading hemisphere (pushed by the plasma) meets the flow from the dayside trailing hemisphere. Since the O_2 does not condense on the surface, it slowly convects towards the poles and then back onto the nightside, eventually to be dissociated or stripped away by the plasma.

Table of Contents

List of Tables

List of Figures

Chapter 1

Introduction

1.1 MOTIVATION

Io, the innermost Galilean satellite of Jupiter, exhibits a wide variety of complex phenomena such as interaction with Jupiter's magnetosphere, volcanic activity, and a rarefied multi-species sublimating and condensing atmosphere with an ionosphere. Io's orbital resonance with Jupiter and the other Galilean satellites produces intense tidal heating that makes Io the most volcanically active body in the solar system. Several of the plumes produced by the active volcanism have been observed to rise over 300 km above the surface and many leave thick rings, visible from space, as well as a thin patchy frost cover on Io's surface. From this surface frost, a collisional SO_2 sublimation atmosphere is sustained around Io. The extreme temperature sensitivity of SO_2 sublimation at Io's day/night temperatures produces, based on current simulations, an atmosphere that is continuum near the surface in the subsolar region and a thinner, rarefied atmosphere on the nightside. This leads to the development of gas flow from the subsolar region to the nightside, and an apparent standing shock at the terminator (Austin and Goldstein, 2000; Wong and Smyth, 2004; Walker *et al.*, 2010a). Together, the sublimation and volcanism produce Io's atmosphere though the relative importance of each source component is still uncertain. Io's atmosphere has an ionosphere sustained through interaction with the Jovian plasma torus and solar radiation. The plasma torus was itself created by the interaction between the Jovian magnetosphere and Io's atmospheric constituents, though the exact quantitative mix of mechanisms varies over many timescales and is not well known even on average. Io's interaction with the Jovian magnetosphere involves collisions between Io's atmospheric constituents and the plasma confined to Jupiter's field lines; one result of that interaction is Io's aurora. This aurora, unlike Earth's, peaks near Io's geodetic equator and the intensity is asymmetric on the upstream and downstream sides of Io relative to the plasma flow. An objective of this work is to improve our understanding and modeling capability of the interaction between the Jovian plasma torus and Io's atmosphere. The main goal of this work is to constrain various physical

parameters of the Io–plasma torus system through comparisons of our simulations to observations of Io's aurora

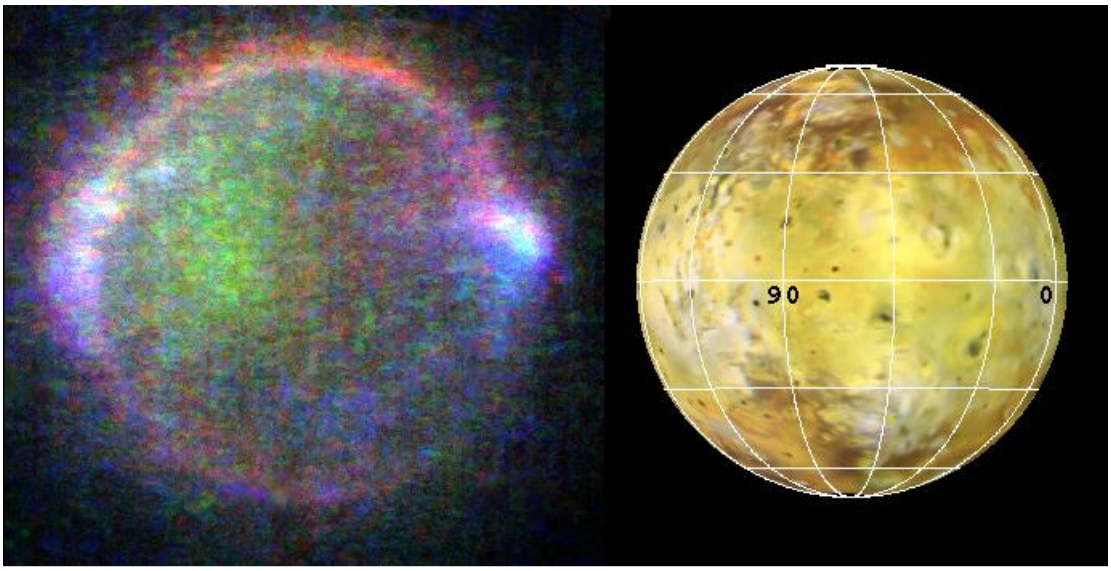

Figure 1-1: Image of Io in eclipse (left) using enhanced visible colors and the sunlit view of Io from the same perspective. There are three distinct components to Io's visible aurora: blue glows near the sub- and anti-Jovian points near the equator, weaker red glows along the polar limbs, and a green glow which extends from the terminator onto Io's nightside. (*From Geissler et al. (1999), courtesy of The American Association for the Advancement of Science*).

Io's atmospheric composition and distribution has only been observed via the radiation transmitted through and, in most cases, produced by thermal or electronic excitation[1] of the gas. Therefore, there is good reason to model both the gas dynamics and the resultant radiation. Prior simulations (Zhang *et al.*, 2003, Gratiy *et al.*, 2010) have focused on thermal emission from, and solar transmission through, the dominant gas species, SO_2. The present work focuses on simulating the electron excited emission of the various atmospheric species that produce Io's aurora. Most remote observations of Io's aurora have been taken with the Hubble Space Telescope (HST) or the Galileo and Cassini spacecraft. Figure 1-1 shows a Galileo image of Io's visible aurora illustrating complex emission morphology with at least three distinct, spatially separated components in the red, green, and blue wavelengths. It is a goal of this work to improve our understanding of the physical mechanisms which

[1] There are observations using transmitted solar light, such as reflected Lyman−α images (Roesler *et al.*, 1999) and those that established the presence of S_2 in Pele (Spencer *et al.*, 2000)

cause the unique morphology of Io's aurora. Clearly, modeling the aurora's morphology will require a detailed model for the structure and composition of Io's atmosphere.

1.2 OBJECTIVES

Comparisons between observations and the present simulations of the many unique auroral features present at different wavelengths at Io should provide insight into the relative importance of the various mechanisms behind Io's auroral features (such as Io's location in the torus, collisional quenching, interaction of the Jovian fields with Io, etc.) and help to constrain the physical parameters (such as upstream electron temperature, atmospheric structure, column abundances and densities, etc.) involved in the interaction. While spatially and temporally resolved simulations of all the physical processes involved in the generation of the aurora (torus plasma dynamics, unsteady gas dynamics, etc.) would be preferred, such simulations are not currently feasible due to the large variation in length and time scales as well as a lack of appropriate data (e.g. temporal plume activity, plasma conditions, etc.).

In the present work we seek to model Io's [OI] 6300 Å emission and Io's ultraviolet–visible (UV-Vis) spectrum which is dominated by band emission from SO_2, SO, and S_2 via Monte Carlo simulation of the electron excitation of a pre-computed atmosphere. The model requires the inclusion of 3D electric and magnetic fields, and electron-neutral reaction cross-sections and resultant band spectra as functions of the collision energy. Accurate total reaction cross-sections are required in order to model the transport of the electrons properly and hence the model will include excitation mechanisms for many other emission lines (such as OI] 1356 Å) for which observations exist and may be investigated in the future.

In addition, a global atmospheric model for Io must be constructed for use in the electron excitation simulation. The initial simulations will examine the resultant aurora using a hybrid atmosphere by superimposing previous rarefied plume simulations (Zhang *et al.* 2004) onto prior continuum simulations of the 2D sublimation atmosphere (Wong and Smyth 2000, Smyth and Wong 2004). Note that above the first atmospheric scale height the gas is actually rarefied. Therefore, eventually it is desired to superimpose the plume simulations onto simulations of the sublimation atmosphere using the Direct Simulation Monte Carlo (DSMC) method which can accurately model both the near surface continuum and the rarefied upper atmosphere. Previously, both 2D (Austin and Goldstein 2000) and 3D (Walker

et al. 2010) DSMC simulations of Io's atmosphere have been performed; however, these have used a crude plasma heating model that lacked chemistry. Since the ultimate source of SO, O_2, O, and S in Io's atmosphere is photo- and plasma-chemistry, it was necessary to add chemistry to our planetary DSMC code. The Total Collision Energy (TCE) model (Bird, 1994) for chemistry is employed for several of the reactions. However, due to the very high collision energies (>100 eV) the TCE model is inadequate (Ozawa *et al.* 2007) and thus the dissociation of SO_2 due to impact with O and S atoms has been simulated using simulated Molecular Dynamics/Quasi-Classical Trajectory (MD/QCT) reaction cross section data (Deng *et al.*, 2011).

1.3 DISSERTATION OVERVIEW

Figure 1-2 shows a schematic overview of the various model pieces used to simulate Io's eclipse aurora. Electron interaction cross sections, emission spectra, magnetic and electric fields, and Io's global atmosphere are used as inputs to the electron transport code. While the various interaction cross sections and the magnetic and electric fields have been previously generated, the global atmosphere developed here is original work. Two sublimation atmosphere models are developed. The first model atmosphere mapped a previously published 2D dayside continuum atmospheric model onto Io's surface and scaled the gas column to account for eclipse. The second, later, model used our group's planetary DSMC code with several new physics implemented for this work in order to generate a 3D sublimation atmosphere (which could then self-consistently simulate the cooling surface after entry into eclipse). A brief description of the content of each chapter is given below.

Chapter 2 gives a broad literature review of the Ionian system, specifically Io's complex atmosphere, the Jovian plasma torus and magnetosphere, and auroral observations. Two different simulation methods (and codes) were developed in the current effort to simulate Io's electron-excited aurora; one which simulates Io's complex atmosphere and another which simulates the electron motion in the perturbed Jovian magnetic field and their interaction with the pre-computed atmosphere. Since the auroral simulations require the pre-computed atmosphere, the atmospheric simulations are presented first. In Chapter 3 an overview of the DSMC method is presented along with a thorough discussion of model improvements implemented for these simulations, such as the invertible adaptive grid, the charged particle motion, and the chemical reaction model.

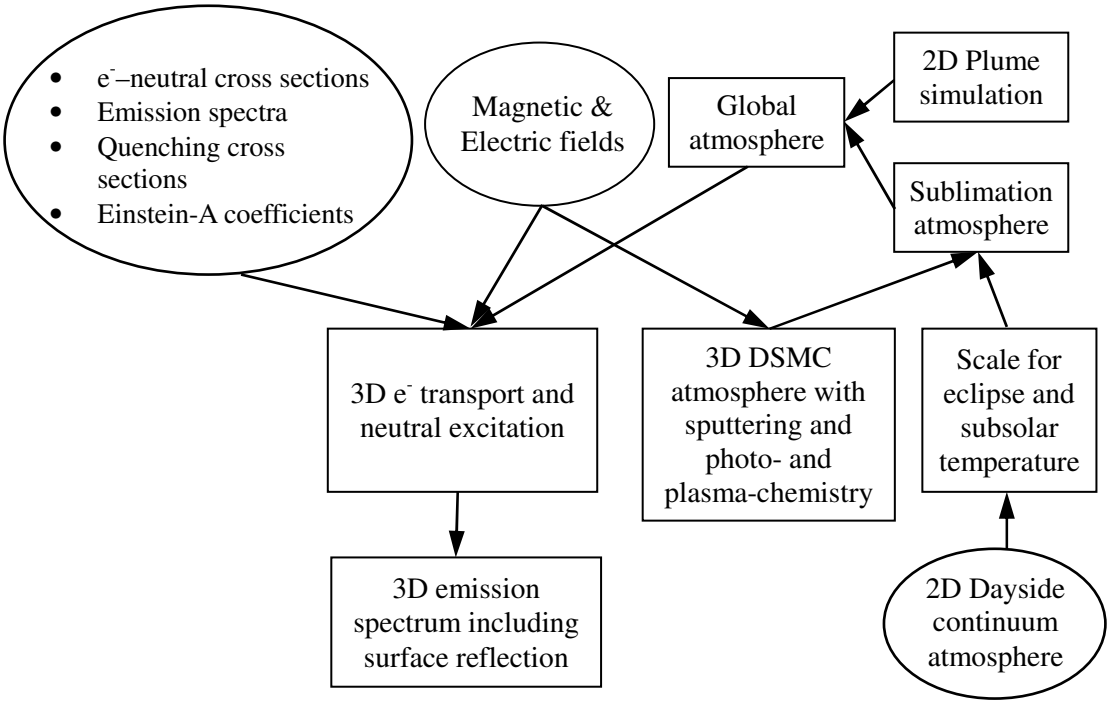

Figure 1-2: Schematic overview of the model used to simulate the aurora. The ovals indicate inputs into the model generated by prior research, the boxes are new work presented here. Arrows from one box to another indicate that the former is used as an input to the latter.

Since the auroral observations examined here were taken during eclipse, Io's sublimation atmospheric dynamics upon ingress into eclipse are examined in detail with and without the presence of a minor non-condensable species in Chapter 4. The fifth chapter provides a detailed description of the Monte Carlo electron transport code developed to simulate Io's auroral emissions due to electron excitation. In Chapter 6 the electron transport code is used to simulate the [OI] 6300 Å emission. Our understanding of the physical mechanisms responsible for the observed auroral features is improved through comparison to observations. Chapter 7 compares the simulated UV-Vis spectrum to an observed spectrum thereby constraining the upstream electron temperature and the giant, Pele-type plume activity. Three dimensional simulations of Io's sublimation and sputtered atmosphere that include photo- and plasma-chemistry are discussed in Chapter 8 and may be later used as an input for the auroral simulation. Concluding remarks are presented in Chapter 9.

Chapter 2

Literature Review

The following literature review will focus on the Jovian system as it relates to our simulations of Io's aurora. Specifically observations and prior simulations of Jupiter's moon Io and the Jovian plasma torus that sweeps past Io will be discussed in detail. Several notable reviews on Io's atmosphere (McGrath *et al.*, 2004; Lellouch *et al.*, 2006) and Io's interaction with the plasma torus (Saur *et al.*, 2004; Schneider and Bagenal, 2006) have been written post-Galileo. Prior work on the simulation methods employed to model Io's aurora will be presented in the chapter in which the simulation method is discussed.

2.1 IO'S ATMOSPHERE

In 1979, the Voyager IRIS experiment revealed that Io's atmosphere was mainly composed of SO_2 (Pearl *et al*., 1979). Voyager also discovered the presence of several volcanic plumes on Io (Smith *et al.* 1979a,b, Strom and Schneider, 1982). Further observations (McEwen *et al.*, 1998, Lopes *et al.*, 2004) of the volcanoes have revealed that some have surprisingly steady activity (e.g. Prometheus), some have a somewhat regular activity cycle (e.g. Loki), and several are highly sporadic (e.g. Tvashtar). Furthermore, ground-based infrared observations suggested that there exist patches of SO_2 frost on the surface (Fanale *et al.*, 1979; Smythe *et al*., 1979) that sustain a sublimation driven SO_2 atmosphere at Io's dayside surface temperatures; however, on the nightside of Io the SO_2 number density drops significantly since SO_2 is condensable at the expected nightside temperatures. Therefore, in addition to the atmospheric variability from volcanic activity, the sublimation SO_2 atmosphere varies strongly depending on the presence of frost and the local surface temperature. While active volcanism is ultimately the source of Io's atmosphere, the relative contribution to Io's *immediate* atmosphere of active volcanoes, sublimation of surface frosts, and surface sputtering by plasma is not yet well known (Ballester *et al*., 1990, 1994; Trafton *et al.*, 1996; Lellouch, 1996; Jessup *et al.*, 2004; Saur and Strobel, 2004; Spencer *et al.*, 2005; Moullet *et al.*, 2008). However, the relative contribution from the various sources is critically important for Io's atmospheric vertical structure, lifetime, composition, and response to insolation variations.

Neutral species other than SO_2 that have been observed in Io's atmosphere include SO (Lellouch *et al.*, 1996; McGrath *et al.*, 2000; dePater *et al.*, 2007; Moullet *et al.*, 2010), S_2 (Spencer *et al.*, 2000; Jessup *et al.*, 2007), NaCl (Lellouch *et al.*, 2003; Moullet *et al.*, 2010), S and O (Ballester *et al.*, 1987; Feaga *et al.*, 2002); Na (Brown, 1973; Brown and Chaffe, 1974; Schneider *et al.*, 1991), K (Trafton, 1975), Cl (Retherford *et al.*, 2000; Feaga *et al.*, 2004), and H (Trafton, 2000; Retherford *et al.*, 2000). While currently undetected, photochemical products of SO_2 such as O_2 are surely present in Io's atmosphere as predicted by multiple simulations (Summers and Strobel, 1996; Wong and Johnson, 2000; Smyth and Wong, 2004). Observations show that the relative abundance of the neutral species varies throughout Io's atmosphere, probably due to the complex sources and sinks for each of the species (McGrath *et al.*, 2000).

Above the exosphere, clouds of neutral gases (Na: Trafton *et al.*, 1974; K: Trafton, 1975) extend far from Io and its gravitational influence. In addition, Io has an ionosphere (Kilore *et al.*, 1974, 1975; Hinson *et al.* 1998) which has been observed to contain molecular SO_2^+ and SO^+ (Russell and Kivelson, 2000) and atomic ions for each of the neutral gas species present in Io's atmosphere (Frank and Paterson, 1999; Russell and Kivelson, 2001). Io also has a corona (Ballester *et al.* 1987; Schneider *et al.* 1991; Wolven *et al.* 2001), that is one of the principal sources of plasma in Jupiter's magnetosphere; the others are Io's ionosphere and its extended neutral clouds.

Observations in the millimeter range and the C^1B_2-X^1A_1 band of sulfur dioxide have found that the SO_2 gas column density is higher on the trailing[2] hemisphere, while the frost is more abundant on the leading hemisphere (Lellouch *et al.*, 1992, Trafton *et al.*, 1996). Over the years, 12 different millimeter SO_2 lines have been detected in emission; they are believed to result from LTE thermal emission of the atmosphere (Lellouch *et al.*, 1992). So far the SO_2 millimeter lines have always been detectable, but temporal variability is observed, most likely due to variations in atmospheric coverage, the surface pressure, and/or the gas temperature (Lellouch, 1996). Since the line widths are dominated by Doppler broadening in Io's rarefied atmosphere they are well suited to determine an "average" atmospheric temperature. Using the IRAM−30 m single-dish antenna Lellouch *et al.* (2000) obtained disk-averaged millimeter

[2] Trailing with respect to Io's orbital motion

observations of the 216.643 GHz line of SO_2 and found that the trailing hemisphere atmosphere was hotter (400 K) and less distributed than the leading hemisphere (200 K).

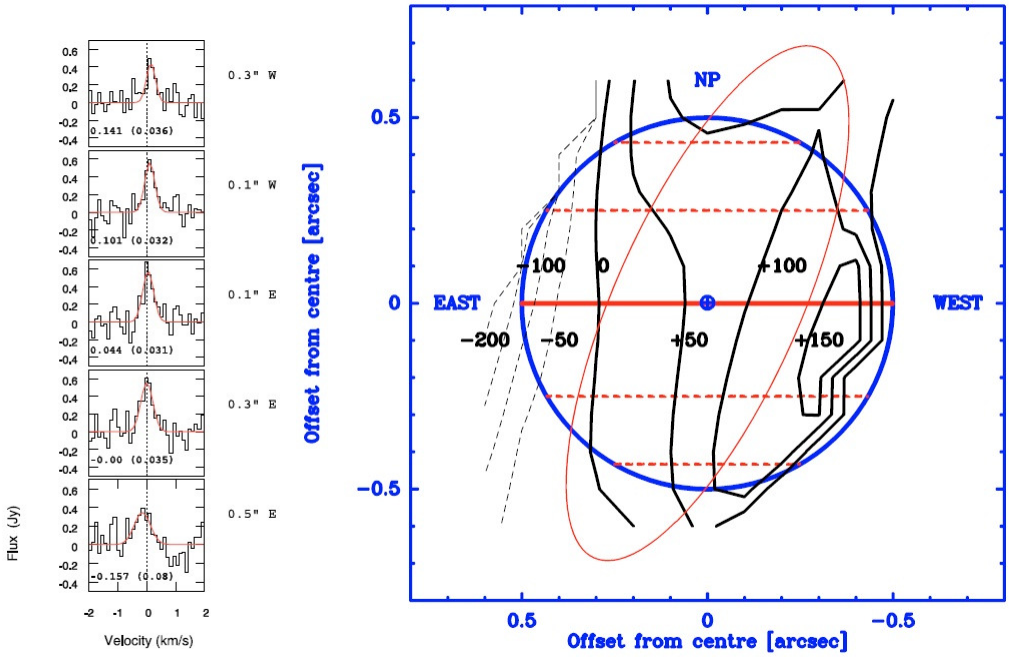

Figure 2-1: Left: SO_2 line spectra observed at five locations along Io's equator with Gaussian fits superimposed used to obtain the Doppler shifts in km s^{-1}. Right: Map of the Doppler shifts across Io's leading hemisphere. Positive velocity contours are shown by solid black lines, negative velocities by the dashed black lines. (*From Moullet et al. (2008), courtesy of ESO*).

More recently, Moullet *et al.* (2008) used the IRAM Plateau de Bure Interferometer to obtain disk-resolved millimeter observations of Io's surface and SO_2 atmosphere at both eastern (leading hemisphere) and western (trailing hemisphere) elongation. The Doppler shifts of the disk-resolved spectra (see Figure 2-1) indicated a limb-to-limb velocity difference of 330 ± 100 m/s; larger than the 75 m/s equatorial solid rotation of Io and hence indicative of atmospheric dynamics. The resolved Doppler shifts were found to be in better agreement if the atmosphere had a 170-300 m/s equatorial wind in the direction of Io's rotation (wind velocities of opposite signs near each limb) as opposed to the sublimation-driven winds away from the sub-solar point as expected due to day/night pressure gradients. It is not understood what physical mechanism would cause an equatorial "super rotational" wind. Moullet *et al.* (2008) tried to use volcanic plumes to explain the limb-to-limb velocity difference; however, they found that the contribution of isolated plumes to the SO_2 emission was small and would therefore require many more plumes than the ~18 that have been

observed in order to reproduce the limb-to-limb velocity difference. Using the Submillimeter Array to observe several lines of SO_2 (346.652, 346.523 GHz), SO (346.528 GHz), and NaCl (338.021 GHz), Moullet *et al.* (2010) reaffirmed their earlier conclusion that the atmosphere is primarily supported by sublimation and that direct volcanic output can contribute only a minor fraction of atmospheric SO_2. Additionally, their thermal emission maps showed that SO and NaCl are concentrated in the anti-jovian hemisphere and that SO is less extended spatially than SO_2. Volcanic output was found to be the most probable source for NaCl; however, it was not sufficient to explain the observed SO column density and distribution even if SO has a long lifetime in the atmosphere. Instead, SO_2 photolysis is the most likely source of SO.

Many observations of Io in the ultraviolet (UV) region of the spectrum have been performed since SO_2, S_2, and SO absorb (and emit) strongly in the UV region. Both disk-averaged (Ballester *et al.*, 1994; Trafton *et al.*, 1996) and disk-resolved (Sartoretti *et al.*, 1994, Hendrix *et al.*, 1999; McGrath *et al.*, 2000; Spencer *et al.*, 2000; Jessup *et al.*, 2004, 2007) spectral observations have been performed. Observations of absorption spectra have been particularly suited to constrain the column density of the absorber. McGrath *et al.* (2000) obtained spatially resolved absorption spectra (1600–2300 Å) at three different locations on Io's surface: Pele (18°S, 257°W), Ra (7°S, 318°W), and "T3" (45°S, 300°W). Ra was chosen since it was a potentially active region with abundant SO_2 surface frost and T3 was chosen as a reference region that was presumably frost poor and had no nearby active volcanic centers. For Pele, Ra, and T3 it was found that the best fit SO_2 column densities (3.25×10^{20}, 1.5×10^{20}, and 7×10^{19} m^{-2}) and temperatures (280, 150, and 200 K) indicated a "collisionally thick" atmosphere at all three locations. They also found that the addition of ~10% SO and ~0.3–0.7% S improved the modeled absorption spectra fits. Spencer *et al.* (2000) performed resolved observations of Pele's plume against Jupiter using HST/STIS from 1680–3060 Å. By using isothermal models of S_2 and SO_2 gas absorption they found evidence of absorption due to S_2 gas with a column density of ~10^{20} m^{-2} and a column density of SO_2 ~7×10^{20} m^{-2} (see Figure 2-2). The observed S_2/SO_2 ratio can be used to constrain the equilibrated oxygen fraction and magma temperature and pressure in Pele (Zolotov and Fegley, 1999). Finally, the presence of S_2 is a reasonable assumption for plumes with red ring deposits which are likely formed by S_2 polymerization into S_3 or S_4 (Spencer *et al.*, 2000).

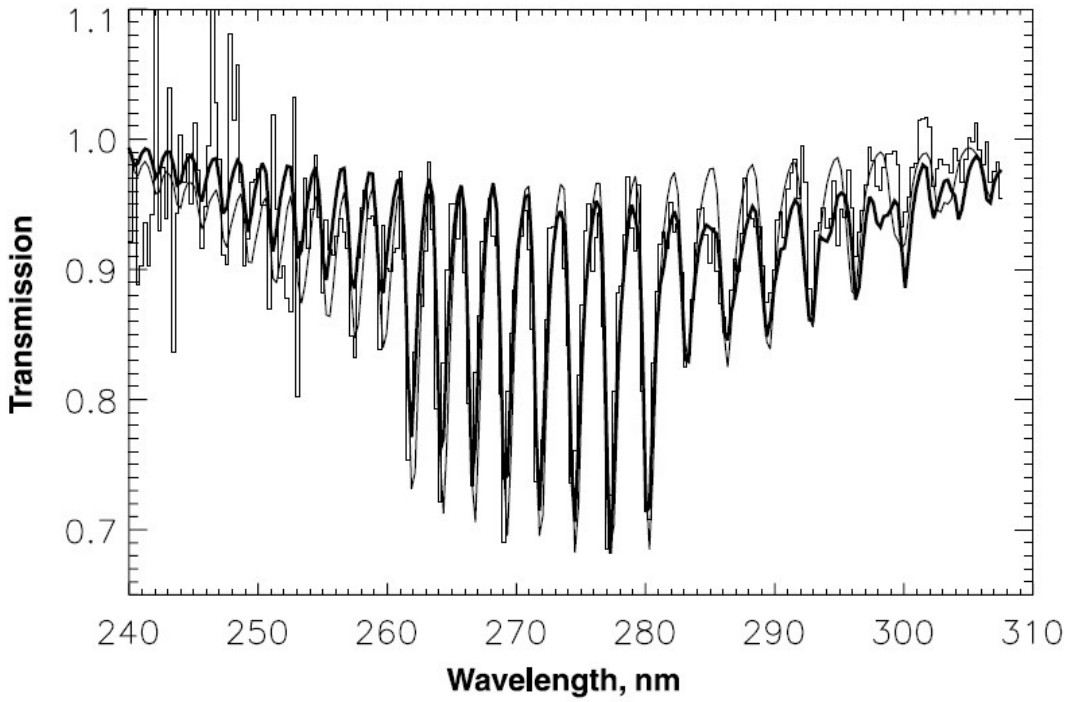

Figure 2-2: STIS spectrum at Pele (stepped line) as compared to the best-fit S_2 (light line) and S_2 + SO_2 (heavy line) model spectra. (*From Spencer et al. (2000), courtesy of The American Association for the Advancement of Science*).

Jessup *et al.* (2004) built upon the work of McGrath *et al.* (2000) and performed a more complete examination of the latitudinal and longitudinal dependence of Io's SO_2 column density. They sampled regions on the anti-Jovian hemisphere with and without volcanic hotspots from ±50° latitude and over ~150° longitude. Local enhancement of the SO_2 column only occurred over the Prometheus plume despite the fact that the entire observational region contained several other volcanic hotspots. While these volcanic hotspots might have been high temperature regions with active volcanism, they were apparently not generating plumes outgassing significant SO_2 gas. They found that the drop-off in the SO_2 column density with latitude near the equator was consistent with control by local vapor pressure equilibrium with local surface frost (see Figure 2-3) supporting the sublimation-dominated view of Io's atmosphere. Finally, they placed an upper limit on the S_2/SO_2 ratio of 0.005 for Prometheus, much less than the 0.08-0.33 observed at Pele (Spencer *et al.*, 2000).

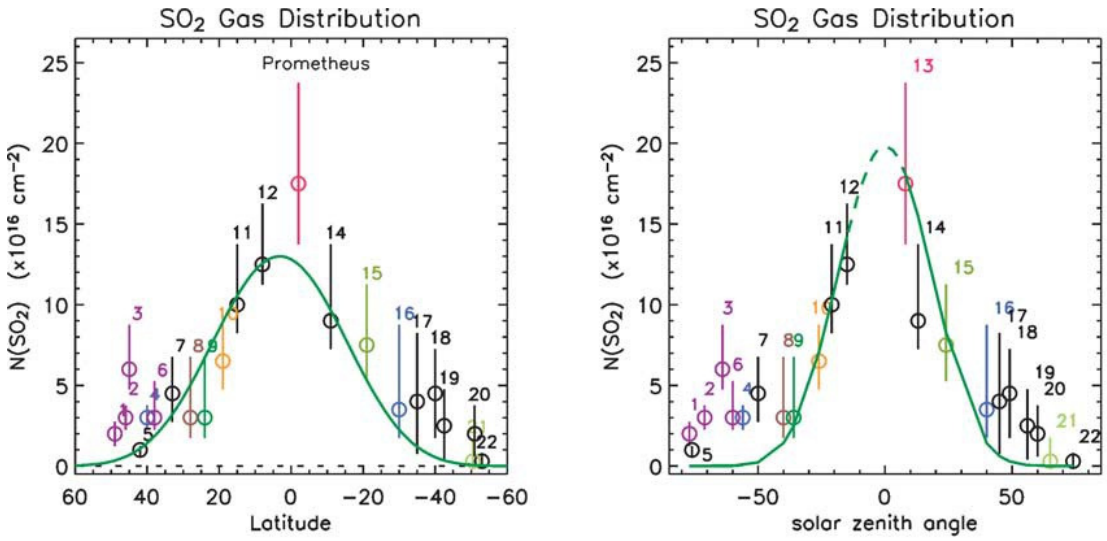

Figure 2-3: SO_2 column density as a function of (a) latitude and (b) solar zenith angle (SZA) as determined by HST/STIS observations. The solid lines are the best-fit SO_2 column density assuming vapor pressure equilibrium with a frost temperature (a) from diurnally-averaged insolation and (b) instantaneous insolation. The peak frost temperatures were (a) 116.7 K and (b) 118.0 K. (*From Jessup et al. (2004), courtesy of Elsevier*).

Space Telescope Imaging Spectrograph (STIS) images of Io's reflected solar HI Lyman-α intensity (Roesler *et al.*, 1999; Feldman *et al.*, 2000; Strobel and Wolven, 2001; Feaga *et al.*, 2009) have shown that Io's atmospheric SO_2 column density is considerably larger near the geodetic equator than near the polar regions. Roesler *et al.* (1999) obtained images of HI Lyman-α that showed a dark equatorial region and bright high latitude regions (>45°). Feldman *et al.* (2000) found that the most likely explanation for this morphology was absorption by SO_2 of solar Lyman-α reflecting off Io's surface. Feaga *et al.* (2009) performed a comprehensive study of the Lyman-α images and obtained spatial and temporal information about Io's SO_2 atmosphere. Their inferred SO_2 distribution maps, one of which is shown in Figure 2-4, shows that the sunlit SO_2 atmosphere is temporally stable with small local changes in time and a persistent anti-jovian/sub-jovian asymmetry in the SO_2 column. The average daytime SO_2 column density was found to be highest on the anti-jovian hemisphere, peaking at 5×10^{20} m^{-2} at 140° longitude.

The precise cause of the column density difference between the equator and the poles is currently not known. The patchy frost from which the sublimation atmosphere originates is not preferentially located near the equator (Douté *et al.*, 2001); hence one might expect that the atmospheric column falloff with latitude is indicative of the surface temperature's

dependence on latitude. However, observations of Io's surface temperature with the Galileo photopolarimeter-radiometer (PPR) (Rathbun *et al.*, 2004) suggest a smaller drop-off in surface temperature with latitude than required to match the observed drop-off in atmospheric column. In addition, the number of active volcanic centers is higher in the equatorial region (Marchis *et al.*, 2005) and presently the relative importance of each effect (frost location versus surface temperature versus volcanic activity) is not well known. Sophisticated surface models coupled with 3D atmospheric simulations are currently being developed to examine the cause of the latitudinal fall-off in Lyman-α (Walker *et al.*, 2010b).

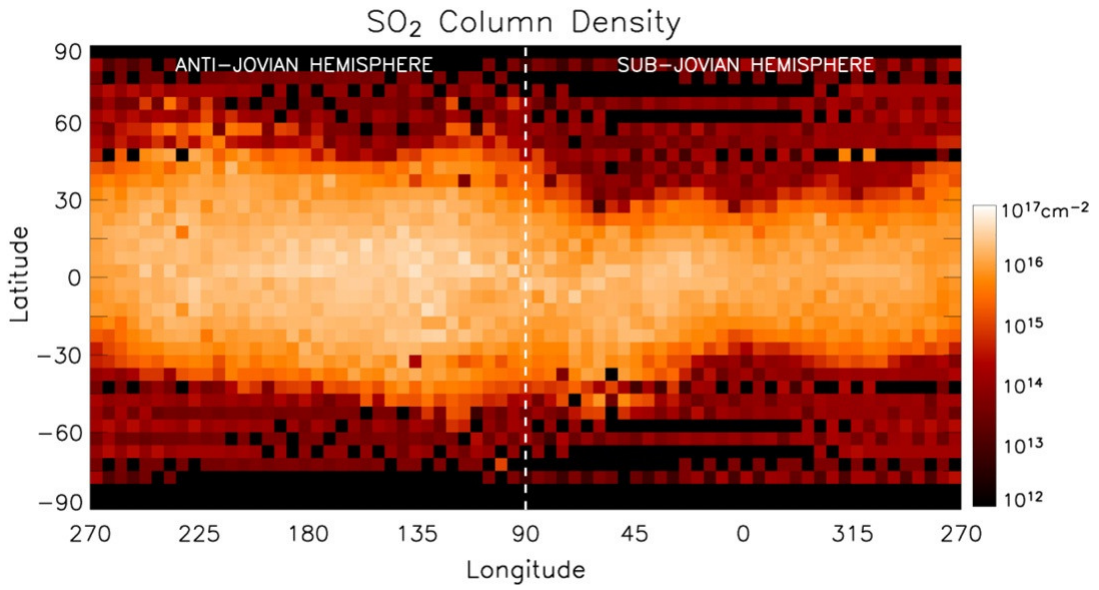

Figure 2-4: Io's average daytime SO_2 column density versus latitude and longitude inferred from Lyman-α images. Notice that the central band of dense SO_2 extends to higher latitudes on the anti-Jovian hemisphere. (*From Feaga et al. (2009), courtesy of Elsevier*).

Disk-averaged observations from 2001–2004 at the NASA Infrared Telescope Facility by Spencer *et al.* (2005) detected ~16 absorption lines of the υ_2 SO_2 vibrational band at ~530 cm^{-1}. Large, temporally stable variations in band strength with longitude are seen; the 530.412 cm^{-1} line varies from 7% absorption at 180° longitude to 1% at 315° longitude. Furthermore, the maximum line depths suggest an average υ_2 vibrational temperature of the SO_2 gas that is below ~150 K. They find that the best fit equatorial column to the data varies from ~1.5×10^{21} m^{-2} at 180° to ~1.5×10^{20} m^{-2} at 300° longitude, in agreement with the values inferred from UV observations. The 2001–2004 data suggest that Io's atmosphere is supported by direct volcanic supply since Io's atmosphere does not appear to decrease as Io

recedes from the sun, as would be expected if the atmosphere were dominated by sublimation of surface frost. However, Tsang *et al.* (2010) continued the 19 μm spectrum observations from 2005–2010 and found that, by considering the entire dataset from 2001 to 2010, the global mean column abundance of SO_2 does in fact vary with heliocentric distance. Furthermore, the variation appears to be consistent with a sublimation dominated atmosphere.

2.1.1 Sublimation and Sputtered Atmospheric Models

In order to describe Io's atmospheric dynamics, several classes of models have been developed. These include early "buffered" models in which the gas remains in vapor pressure equilibrium with the frost-covered surface (Fanale *et al.*, 1982; Matson and Nash, 1983), "dynamic" models that better account for the pressure driven flow from day to night (Ingersoll *et al.*, 1985; Ingersoll 1989; Moreno *et al.*, 1991), "sputtered" models that account for the impact of energetic charged particles on Io's surface (Cheng and Johnson, 1989), "volcanic" models that model the evolution of gas plumes (Moreno *et al.*, 1991; Zhang *et al.*, 2004; McDoniel *et al.*, 2011), and finally "unified" models that fully model the sublimated gas dynamics and its coupling with some of the following: plasma energy deposition/chemistry, photo-chemistry, non-Local Thermodynamic Equilibrium (non-LTE) radiation, and complex surface frost and temperature maps (Wong and Johnson, 1996; Austin and Goldstein, 2000; Smyth and Wong 2004; Walker *et al.*, 2010a). Volcanic models will be discussed in the next section.

As mentioned above, SO_2 surface frosts sustain a sublimation atmosphere. Due to the sensitivity of SO_2 sublimation rate at Io's day/night temperatures, the dayside sublimation atmosphere should partially freeze out during nighttime (and possibly eclipse) as the surface temperature drops to ~90 K and the SO_2 sublimation rate drops by a factor of ~10^5. Thus the local atmospheric density due to sublimation of SO_2 was expected to depend strongly on the local surface temperature and the presence of SO_2 frost (Ingersoll, 1989). While the relative contributions of the sublimation atmosphere and the plumes is not definitively known, Jessup *et al.* (2004) and Moullet *et al.* (2008) recently obtained spatially resolved spectra (UV and mm-wave radio respectively) of Io and concluded that the atmosphere is probably primarily supported by sublimation of surface frost. This finding lends credibility to the various analytic and computational models of Io's atmosphere that only treat the SO_2 sublimated atmosphere.

Early so-called "buffered" models of Io's atmosphere assumed that the SO_2 gas column was in local vapor pressure equilibrium with surface frost. Additionally, these models assumed uniform frost coverage and therefore the atmospheric column density was controlled by the frost temperature. In order to better match observations, Fanale *et al.* (1982) suggested an equilibrium buffered model for the brightest cold regions and regional cold-trapping on the high albedo regions of the surface which limits net SO_2 flux across the disk. Matson and Nash (1983) argued for a sub-surface cold trap model in which the SO_2 was buried several centimeters beneath a porous surface and therefore the SO_2 frost was much colder and the atmospheric pressures much lower. In order to better model the "buffered" atmosphere, Kerton *et al.* (1996) developed a sophisticated model for Io's surface temperature that included the rotation of Io, thermal conduction, internal heat flow, the solid-state greenhouse effect, and latent heat effects of SO_2 sublimation and condensation neglecting mass transport due to pressure gradients. The thermal inertia was found to have a large effect on temperature distribution for thermal conductivities near those of other planetary regoliths, while the combined latent heat and greenhouse effects were roughly half as important as the thermal conductivity.

Various models to describe the vertical atmospheric structure (and its mass supply to the torus) in equilibrium with a surface at a given temperature have accounted for solar heating and photo-chemistry (Kumar, 1985; Summers and Strobel, 1996), plasma ion heating (Johnson, 1989), and joule heating (Stobel, 1994). These physical mechanisms have since been incorporated into the more complete "unified" models discussed below.

Sulfur dioxide's vapor pressure is extremely sensitive at Io's surface temperatures and thus large pressure gradients tangential to the surface could result from even small changes in surface frost temperature. Ingersoll *et al.* (1985) used a dynamic model that approximately accounted for the gas dynamics resulting from these large pressure gradients. They found that the equatorial region should have net sublimation and the mid-latitudes (30°-70°) net condensation as a result of supersonic winds from the hot, high pressure equator to the colder, low pressure mid-latitudes. To account for patchy frost, Ingersoll (1989) developed a characteristic length equal to $\sqrt{2\pi}\, H_s/\alpha$ where H_s is the local atmospheric scale height and α is the local sticking coefficient of SO_2 onto the surface. If frost is present in a given region, then it controls its own pressure over this length scale which is in general of order 100 km. They found therefore that, away from the plumes, the atmosphere should be

nearly in vapor pressure equilibrium since the surface temperature (and pressure) was expected to change little over 100 km. In addition, such a small length scale meant that the atmosphere of Io might be patchy due to the distribution of surface frosts and/or volcanic plumes. Moreno *et al.* (1991) improved the previous dynamic models by numerically simulating the 3D continuum gas dynamic equations including an approximate radiative transfer model that accounted for radiation to space and heating from the surface. Like previous dynamic models they found that, for a sublimation atmosphere, there is a net sublimation from ±27° latitude, a net condensation poleward of ±27° latitude, and that the atmosphere develops supersonic winds from the subsolar point due to horizontal pressure gradients determined by the surface temperature variation.

More recent computational modeling of Io's sublimation atmosphere has focused on the *steady-state* atmosphere dynamics assuming a surface temperature as a function of the solar zenith angle (SZA). The "unified" computational models fall within two groups: Continuum simulations that, generally, solve the Navier Stokes equations (Wong and Johnson, 1995, 1996; Wong and Smyth 2000; Smyth and Wong 2004) and rarefied simulations which solve the Boltzmann equation (Pospieszalska and Johnson 1996, Austin and Goldstein 2000, Walker *et al.* 2010a, Walker *et al.* 2011).

Strobel *et al.* (1994) developed a radiative-thermal conduction model for the vertical thermal structure of Io's SO_2 atmosphere that included solar heating (absorption in the UV and near-IR bands), non-LTE cooling via rotation and vibration, and Joule heating by the plasma torus. They found that a mesopause exists when the surface pressure exceeds ~10 nbar and that the thermospheric temperature asymptotes to as high as 1800 K with Joule heating whereas without it the atmosphere only reaches ~270 K (depending on solar heating efficiency).

Wong and Johnson (1995) examined the effect of plasma heating on the sublimation driven flow and found that along with raising the altitude of the exobase, the collisional heating enhanced the supersonic flow from the dayside to the nightside. Wong and Johnson (1996) developed a multiple species, continuum, two dimensional, sublimation-driven model atmosphere for Io, considering plasma and Joule heating (but not plasma-induced chemistry), non-local thermodynamic equilibrium cooling, and photochemical reactions. Their result, which was qualitatively consistent with results of other models, showed that SO_2 was the dominant atmospheric species (compared to SO, O, O_2, and ions) and that the SO_2 column

density dropped significantly on the night-side. Plasma heating was found to cause the average column density in the trailing hemisphere to exceed that of the leading hemisphere, consistent with the observations by Lellouch *et al.* (1992) and Trafton *et al.* (1996). Furthermore it was found that the ratio of nightside to dayside SO_2 column density decreases by a factor of ~10^3 if SO is condensable at Io's nightside temperatures. On the other hand, if SO is non-condensable, they found that its presence and build-up on the nightside did not overwhelm the dayside atmospheric flow, though the wind speed from the subsolar point to the nightside was reduced.

Wong and Smyth (2000) improved upon the earlier model by including Na chemistry and crudely considering re-acceleration of the plasma ions above the ion gyropause (the altitude at which the ion-neutral collision frequency equals the ion gyration frequency). Their ratio for the SO_2 column density at the sub-solar point to that of the night-side minimum was ~10^3 (assuming SO and O_2 were non-condensable/reactive) and they suggested that other condensable/reactive species (S and O) follow this trend as well. Wong and Smyth found a dayside SO/SO_2 ratio of 3.2 – 7.1% that is consistent with Jessup *et al.'s* (2004) constraint of 1–10% SO/SO_2 based on their observed spectra. Recently Smyth and Wong (2004) argued that the O density is enhanced at high altitudes through dissociation of SO_2, O_2, and SO by thermal electrons from the plasma torus. These high-altitude, diffuse concentrations of O should result in diffuse, extended regions of [OI] 6300 Å radiative emission.

Pospieszalska and Johnson (1996) examined Io's atmospheric column and mass loss rate due to ion-induced sputtering using 1D Monte Carlo simulations. They found that the exobase temperature was sensitive to the ion-neutral interaction cross section, but that the density of the atmospheric column was largely unaffected over the range of cross sections used. Also, a non-negligible fraction of the ions was found to reach the surface indicating that surface sputtering should occur. However, for the interaction cross section used, the net mass flux from Io's atmosphere was found to be roughly one tenth of the rate inferred as necessary to supply the plasma torus.

Austin and Goldstein (2000) simulated Io's rarefied, sublimation driven circumplanetary flow with a 2D DSMC method and parametrically varied the subsolar surface temperature, the amount of background non-condensable gas, and plasma energy flux. It was found that for high subsolar temperatures the atmospheric flow may become supersonic and have an oblique shock near the terminator. In the region beneath the shock

appreciable condensation onto the surface occurs which they suggest should have implications for Io's frost coverage. Furthermore, it was found that the circumplanetary flow convects any non-condensable species present to the nightside behind the terminator shock; however, the buildup of the (trace) non-condensable gas on the nightside was found to have little effect on the bulk SO_2 gas dynamics.

Walker *et al.* (2010a) improved upon the previous DSMC work by extending the simulation domain to three dimensions, including inhomogeneous surface frost, a molecular residence time of SO_2 on the non-volatile rocky surface, and a two temperature model (frost, non-frost) for the surface including the effect of Io's rotation. The terminator shock was found to move slightly upstream of the previous simulation (Austin and Goldstein, 2000) results. Io's rotation was found to result in an asymmetric frost surface temperature due to the frost's assumed high thermal inertia. This asymmetric temperature leads to column densities and circumplanetary flow that are not symmetric about the subsolar point. Figure 2-5 shows the asymmetric column density distribution. The asymmetric surface temperature results in a peak column away from the subsolar point (towards dusk) because at the subsolar point the surface is still warming from nighttime and a gradual reduction of column upon entry into night as the surface itself gradually cools. Non-uniform frost coverage on the other hand, results in irregular "protrusions" in the column densities that distort the otherwise circular (on a sphere) column density contours. Finally, they found that a longer residence time for SO_2 on Io's non-volatile surface (as compared to SO_2 on SO_2 ice) gave a better fit to mid-infrared observations. Gratiy *et al.* (2010) simulated various emission features (mid-infrared SO_2 υ_2, Lyman-α, and millimeter emission profiles) that would be observed given the simulated atmosphere of Walker *et al.* (2010a). They found that the atmospheric model reproduces the orbital longitudinal variation (though offset by ~30°) in band depth (Spencer *et al.*, 2005) and that the simulated millimeter emission line profiles accounting for the atmospheric winds are not entirely consistent with observations of prograde planetary winds (Moullet *et al*, 2008, 2010). However, the model did not reproduce the morphology of the Lyman-α images (Feaga *et al.*, 2009), which were bright at high latitudes, suggesting that the modeled atmospheric column was too large near the poles.

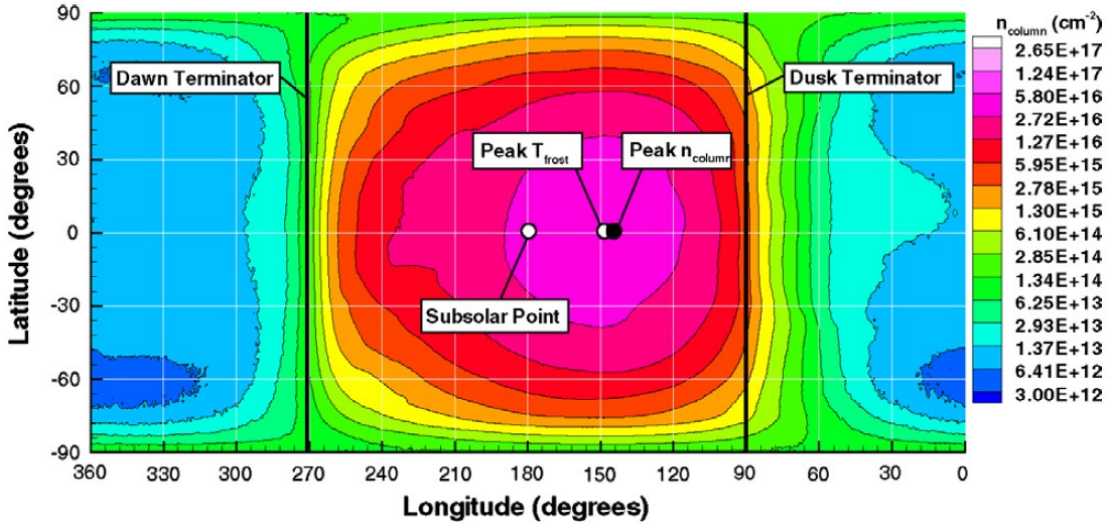

Figure 2-5: Simulated column density map for the "long" residence time and peak frost temperature of 115 K case. Note that the subsolar point is not the same as the peak frost temperature and the peak column density does not occur exactly at the peak frost temperature. (*From Walker et al. (2010a), courtesy of Elsevier*).

In addition to an atmosphere supported by sublimation of SO_2 surface frosts, it is possible that the atmosphere of Io is supported through sputtering of material off the surface due to the impact of energetic magnetospheric particles. Cheng and Johnson (1989) give a good review of the sputtering models which have demonstrated that sputtering alone can generate a large rarefied atmosphere; however, such an atmosphere is limited to $<10^{15}$–10^{16} cm^{-2} since larger gas columns prevent further penetration of energetic particles to the surface (Haff *et al.*, 1981, Lanzerotti *et al.*, 1982). While large portions of Io's dayside atmosphere exceed this limit (see Figure 2-4) and are therefore not dominated by sputtering, higher latitudes and the nightside atmospheres may be dominated by sputtering. Additionally, the energetic magnetospheric particles present about Io can sputter gas from above the exobase of a pre-existing atmosphere in order to generate a large corona and inject new ions and neutrals into the plasma torus (Sieveka and Johnson, 1984, 1985). Regardless of the atmosphere and whether the exobase is close to or far from the surface, collisional ejection from the sputter-produced corona has been shown to be very important to the mass loading rate of the plasma torus as opposed to other sources such as direct volcanic injection, surface sputtering, or Jean's escape (McGrath and Johnson, 1987).

2.1.2 Volcanic Atmosphere

Volcanic plumes of various sizes and activity levels have been observed on many of the flybys of Io. Strom and Schneider (1982) gave observational descriptions of the plumes imaged by Voyagers 1 and 2 and suggested that the bright envelope observed in UV images of Pele might be a concentration of particulates due to a canopy shock. McEwen and Soderblom (1983) categorized two distinct classes of gas plumes based on the Voyager spacecraft images: a Pele-type and a Prometheus-type. The Pele-type plumes are giant, short episodic eruptions (~days) with large, reddish rings which generally occur at higher latitudes, though Pele itself is near the equator and seems to be long-lived (though still variable over on 7–14 day timescales, Jessup *et al.*, 2007). The Prometheus-type plumes are generally longer-lived (~years), near the equator, and result in smaller, white rings.

Geissler *et al.* (2004a) also distinguished two distinct types of plumes based on the size and color of the ring deposits, in agreement with the plume types inferred from Voyager-era data (McEwen and Soderblom, 1983). The detection of S_2 in Pele by Spencer *et al.* (2000) and in another, unknown plume (Jessup *et al.*, 2007) is consistent with the hypothesis that the red ring deposits common to Pele-type plumes are due to polymerization of S_2 into S_3 and S_4 on the surface. The observed S_2/SO_2 ratio for Pele of 8–33% in 1999 (Spencer *et al.*, 2000) and 20–31% in 2003 and 2004 (Jessup *et al.*, 2007) seems to be relatively stable and can be used to infer the volcanic source temperature and oxygen fugacity (Zolotov and Fegley, 1998; 1999). Specifically for Pele, the ratio suggests an oxygen fugacity near either the quartz-fayalite-magnetite or the wüstite-magnetite buffer depending on whether equilibration occurs at ~1 or ~100 bar with mafic magmas (~1400 K) or ultramafic magmas (~1800 K) respectively. In addition, the oxidation level of the gas supports Zolotov and Fegley's (1999) conclusion that there is little metallic iron near Io's surface.

Determining the location of the volcanic sources and their activity was one of the primary goals of the Galileo spacecraft. The spatial distribution and activity level of the volcanic sources (McEwen *et al.*, 1998; Lopes *et al.*, 2004; Marchis *et al.*, 2005) is important for the global atmospheric structure. Geissler *et al.* (2004a) used Galileo SSI surface images of Io to estimate plume activity during the Galileo mission from 1996 to 2001 by comparing surface changes (new rings, coloration, etc.) from image to image. Their reconstructed timeline is shown in Figure 2-6 and will be used to determine plume activity during the various observations we will be simulating. They found that only a few of Io's active

volcanic centers produced large scale gas eruptions and that ~80% of Io's surface remained unaltered throughout the Galileo mission. In fact, there were no visible signs of large-scale surface changes (>10 km) at many volcanic centers known to be actively erupting during the Galileo mission. The most prominent of these eruptive volcanic source (and not listed in Figure 2-6) is Loki which experienced several periods of greatly increased brightness at infrared wavelengths. This was likely caused by lava erupting onto frost-poor or lava surfaces (Geissler *et al.*, 2004a) as can be expected at Loki which is presumed to be an overturning Lava lake (Rathbun *et al.*, 2002; Howell and Lopes, 2007). Episodic activity has even been observed at Prometheus, one of the smaller, more steady gas plumes (Davies *et al.*, 2006).

In addition to the volcanic sources there are currently over 157 hot spots/active regions that have been detected on Io's surface. Walker *et al.* (2011) simulated the interaction between Loki, Io's largest hotspot, and Io's circumplanetary winds that develop as a result of the day/night vapor pressure gradients. The smaller hotspots were found to have little effect on the atmospheric column and winds. Loki, however, was found to reduce the column immediately above the hotspot. In the absence of plasma heating (or for very low plasma energy fluxes), Loki obstructed the supersonic day-to-night winds; however, with plasma heating Loki's effect on the atmospheric day-to-night winds was greatly reduced.

Cook *et al.* (1979) showed that the ballistic model of the plumes, which assumed that the gas decoupled from the particulates and then followed a ballistic trajectory upon leaving the vent, was insufficient to explain Voyager 1 plume observations. They then proposed an aerodynamic model that assumed the particulates were entrained in the gas flow until they began to descend, at which point the particles follow ballistic trajectories. With their model they were able to predict the formation of a curved canopy shock front. Moreno *et al.* (1991) developed an explicit, finite-volume, inviscid, compressible gas solver for the volcanic atmosphere. While their model assumed the gas was continuum, they found that the volcanic atmosphere had a shock generated as the gas falls supersonically to the surface and that the simulated deposition rings qualitatively matched Voyager observations. In addition, their simulations found that an extended nightside atmosphere could be formed by horizontal flow from multiple volcanoes and that the plumes produced horizontal supersonic winds away from the vent region.

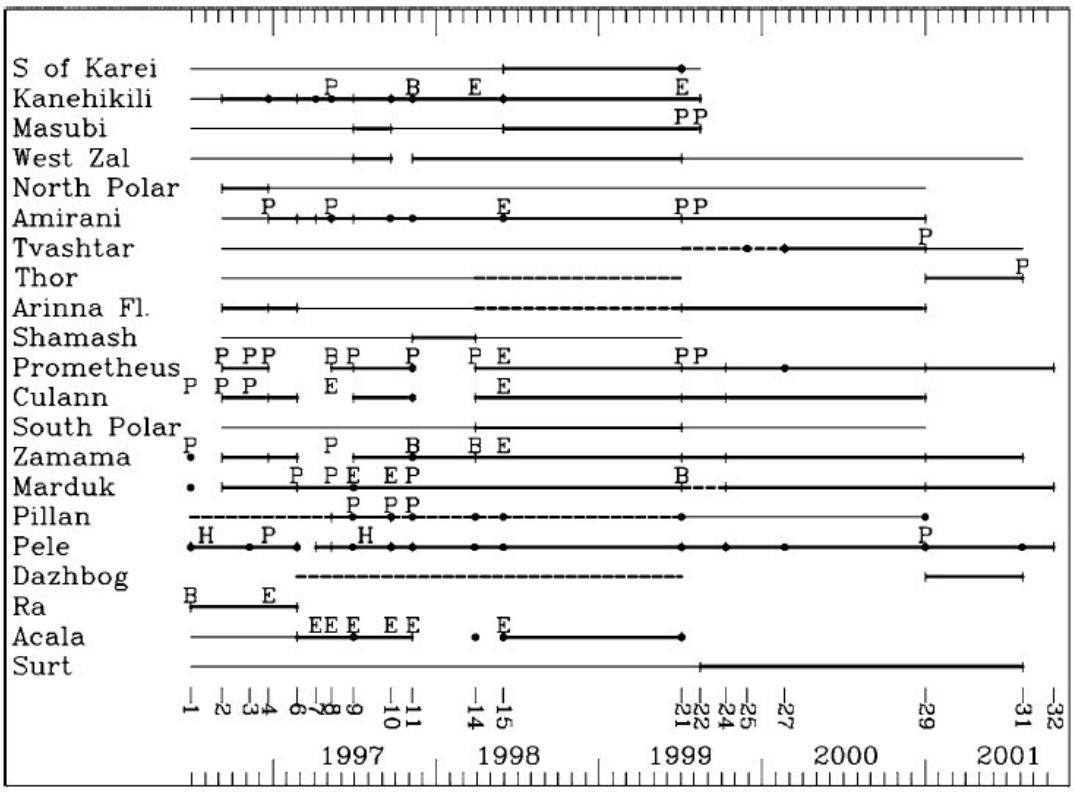

Figure 2-6: Timeline of the major eruptions on Io during the Galileo mission. Observations were only acquired during the orbits shown at bottom (integers from 1 to 32). A thick line bounded by vertical bars indicates substantial surface changes during the time interval, dashed lines indicate lesser changes, a thin line indicates no detectable changes, and no line is shown during periods with no/poor image coverage. A "P" indicates sunlit plume detections, "E" indicates detected auroral emission in eclipse, and "B" indicates plumes seen in both sunlight and eclipse. (*From Geissler et al. (2004a), courtesy of Elsevier*).

The most complete simulation of the volcanic plumes' gas dynamics was done by Zhang *et al.* (2003, 2004) and included most of the relevant physical processes assuming an axisymmetric plume (and vent). For the simulations they used the DSMC method which correctly models the rarefied gas flow present in the plumes. Their model included non-LTE radiation from rotational and vibrational modes, plasma heating, sublimation and condensation from the surface, and large particle (micron size) coupling with the gas flow. Their simulations were able to produce plumes with canopy shock heights and ring radii in agreement with observations for both Prometheus and Pele plumes. A re-entry shock was found to form when a sufficiently dense dayside sublimation atmosphere was present; for Prometheus-type plumes this resulted in multiple "bounces" of the volcanic gas and could

explain the multiple ring structure seen for many Prometheus-type plumes. Additionally, it was found that the majority of plume emission occurs near the vent, that the surface is negligibly heated by the plume emission, and that non-LTE rotational cooling dominates cooling in the υ_2 band of SO_2 at high altitudes, even in the canopy shock. They found that entrained particulates in the plumes build up at the canopy shock as suggested by Strom and Schneider (1982) in order to explain the bright envelope appearing in UV images of Pele. Finally, particulates smaller than ~10 nm were found to track the gas flow; this particulate size is consistent with those inferred by photometric studies of Loki's canopy (0.1–1.0 nm; Collins, 1981) and by optical depth observations of Pele (<80 nm; Spencer *et al.*, 1997).

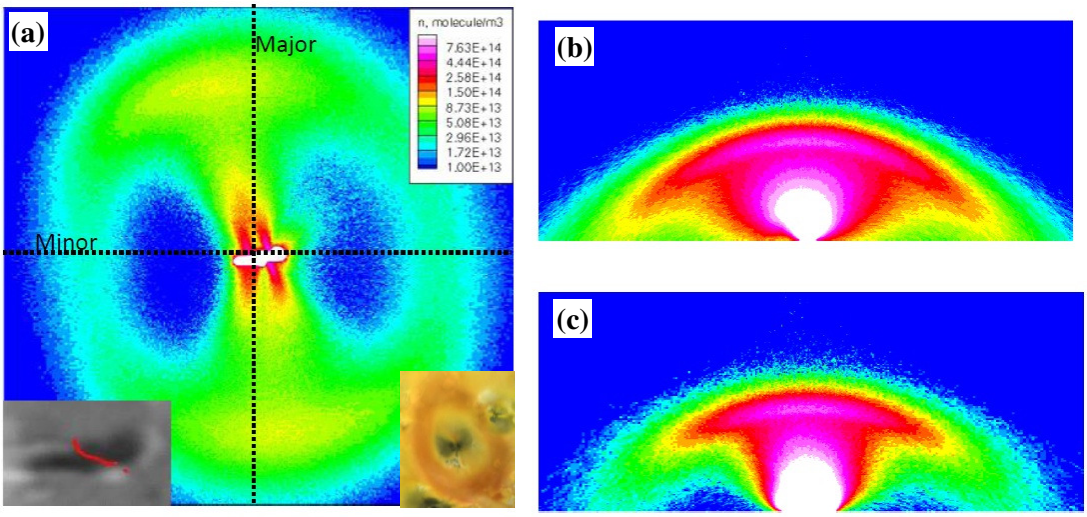

Figure 2-7: Simulated gas number density contours for a "cold" Pele with a "Peanut"-shaped vent (dark region in the lower left inset). (a) The ground level number density showing "butterfly wings" (dark inner area see in lower right inset) as regions of low gas density. (b) The number density in the vertical slice through the ring's minor axis. (c) Similar slice through the major axis. (*From McDoniel et al. (2011), courtesy of the American Institute of Physics*).

More recently, McDoniel *et al.* (2011) have built upon the work of Zhang *et al.* (2004) by simulating a fully three dimensional Pele plume emanating from an irregular vent. It was found that Pele's far-field deposition structure, both of the dark inner region and the orange ring, were dependent on the source geometry. Specifically, vent curvature focuses the streamlines where the vent is concave leading to high density regions and potentially even standing shocks. Figure 2-7 shows simulated density contours for a Pele plume with a "peanut"-shaped vent at a vent density of 2×10^{16} m^{-3}, temperature of 180 K, and velocity of

200 m/s. The simulation showed good agreement between the near surface gas density and the observed butterfly-wing and ring deposition patterns.

2.1.3 Atmospheric Response During and After Eclipse

The atmospheric dynamics upon ingress into eclipse affects the resultant auroral emission morphology and intensity during eclipse. For example, Io's disk averaged auroral emission has been observed to decrease during eclipse. However, certain emission features (linked to active volcanoes) actually brighten during eclipse (Geissler *et al.* 1999, 2001). The sublimation component of Io's SO_2 atmosphere might be expected to "freeze-out" or "collapse" upon entering eclipse because the day/night vapor pressure of SO_2 varies by four orders of magnitude. Accurate simulation of Io's electrodynamic interaction with the Jupiter plasma torus during eclipse (and the resulting auroral emissions) therefore requires a time-varying atmospheric model.

Clarke *et al.* (1994) observed the behavior of UV emissions during eclipse and found that the emission decreases by roughly a factor of 3 within 20 minutes of ingress. They found that the decrease in FUV emission intensity might be due to either the cutoff of exciting solar EUV radiation or due to a substantial decrease in the atmospheric column if plasma excitation is the primary source of emission and the atmosphere is partially transparent to the plasma. Geissler *et al.* (2004b) suggested that the timescale asymmetry between post-ingress dimming and egress brightening of Io's disk averaged brightness are consistent with a partial collapse of Io's atmosphere. Based on the observed asymmetry they infer a collapse timescale of ~20 minutes, after which the emission intensity and, presumably, the atmospheric gas density remained relatively constant until egress. Furthermore, if the sublimation atmosphere remains in equilibrium with the local surface temperature, then Geissler *et al.* (2004b) found that the atmosphere must be supported by a substantial volcanic component in order to retain auroral emissions throughout eclipse as has been observed. Similarly, Retherford *et al.* (2007b) examined Io's far ultraviolet aurora during eclipse using New Horizons Alice and HST and found disk averaged intensities which decreased by a factor of 2 during the initial 40-60 minutes after ingress and then changed little over the rest of the eclipse.

Additionally, observations of the forbidden ro-vibronic $a^1\Delta \rightarrow X^3\Sigma^-$ transition of SO at 1.707 μm by Laver *et al.* (2007) on several different days and times during Io's eclipse found that the emission varied by a factor of 3 throughout eclipse. Possible volcanic origin of the

SO is suggested by the inferred rotational temperature of 550-1000 K and by simultaneous variations in Loki's infrared brightness. However, as mentioned previously, Moullet *et al.* (2010) concluded that SO was primarily generated by photo-dissociation of SO_2 and not by plume out-gassing. Therefore the observed reduction of SO emission most likely indicates a drop in the SO column density through eclipse due to condensation onto the surface and/or a reduced SO_2 column.

The volcanic contribution to the atmospheric column was investigated by Saur and Strobel (2004) through examination of Io's delayed electrodynamic response and far-ultraviolet (FUV) brightness (specifically the OI] 1356 Å emission line) during eclipse. By assuming the sublimation atmosphere remains in hydrostatic equilibrium with the surface as it cools during eclipse and considering an improved equatorial atmospheric model, they were able to constrain the *volcanic* contribution to the atmospheric column density to ~3–5×10^{18} m^{-2}. Modeling of the New Horizon's Alice UV spectroscopic observations of Io during eclipse by Retherford *et al.* (2007b) agreed with the previous work by Saur and Strobel (2004). In order to explain the ~1.8 drop in FUV emission during the first ~30 minutes and the relatively constant emission thereafter, Retherford *et al.* (2007b) found that a volcanic atmosphere representing 1-3% of the dayside atmospheric column (2–4×10^{18} m^{-2}) is needed.

For certain *volcanic* column densities, Saur and Strobel (2004) found that the FUV emission from Io would decrease during eclipse (as observed) and then increase upon egress due to the atmosphere's electrodynamic interaction with the plasma torus. Furthermore, Bellucci *et al.* (2004) found that post-eclipse brightening events are not the result of SO_2 condensation on the surface during eclipse because the amount of observed brightening was different between infrared and visible wavelengths. Since SO_2 frost has a uniform reflectance over these wavelengths, no difference in brightening should be observed if increased frost coverage were the cause of the brightening. If one assumes that either there is a low concentration of condensed surface contaminants or that they negligibly alter the wavelength dependence of the reflectance, then the atmospheric behavior upon egress (and the resultant plasma interaction) seems to be crucial for understanding post-eclipse brightening.

2.2 THE PLASMA TORUS

Jupiter's magnetosphere is larger and stronger than any planet in the solar system and is tilted by ~10° relative to Jupiter's rotation axis. In the vicinity of Io, the Jovian magnetic

field is perturbed by Io (Frank, *et al.*, 1996); furthermore, Kivelson *et al.* (2001) found that Io does not have an intrinsic magnetic field. An excellent review of the Jovian magnetosphere and the torus, shown in Figure 2-8, is given in Kivelson *et al.* (2004) and Saur *et al.* (2004). Material from Io's atmosphere continually supplies an ionized ring of plasma called the Io plasma torus which corotates with Jupiter. The Io plasma consists predominantly of O^+, S^+ and electrons and sweeps past Io at ~57 km/s since Io's orbital period is slower than Jupiter's rotational period. The plasma, confined to move along the rotating Jovian magnetic field lines, interacts with Io's atmosphere as it sweeps past the satellite, ionizing neutrals in Io's atmosphere via collisions. These new ions (and electrons) are then accelerated by the rotating field lines to resupply the torus. In eclipse, the only significant source of the observed [OI] emission is the interaction of electrons (and ions) from the plasma torus with Io's atmosphere. Additionally, Voyager 1 detected a ~6 MA current of high energy electrons along the Io flux tube (green arc in Figure 2-8) which extends between Io and the Jovian North and South Poles. These field-aligned electrons create a UV auroral footprint in Jupiter's ionosphere (Clarke *et al.*, 2002) and triggers Jovian decametric radio emission (Bigg, 1964).

The Io plasma torus has a cold inner torus from 4.9-5.3 R_J (R_J is Jupiter's radius), a "ribbon" of warmer plasma from 5.5-5.9 R_J, and a warm region out to 7.5 R_J (Schneider and Trauger, 1995; Delamere *et al.*, 2005). At Io's orbit (5.9 R_J), the thermal electrons in the plasma have a temperature of ~5eV and hence a mean energy, $\overline{E}$, of 7.5eV (Sittler and Strobel, 1987), and a number density of ~3600 m^{-3} (Frank *et al.*, 1996); though both these quantities vary with Io's System III longitude as Io passes through the plasma "ribbon" (Smyth and Marconi, 1998). Charged particles in the torus are confined on the Jovian magnetic field lines; however, due to the centrifugal "force" of rotation about Jupiter, the torus equator is inclined by only 7° relative to Io's orbital plane as compared to 10° for the Jovian magnetic equator (Spencer and Schneider, 1996).

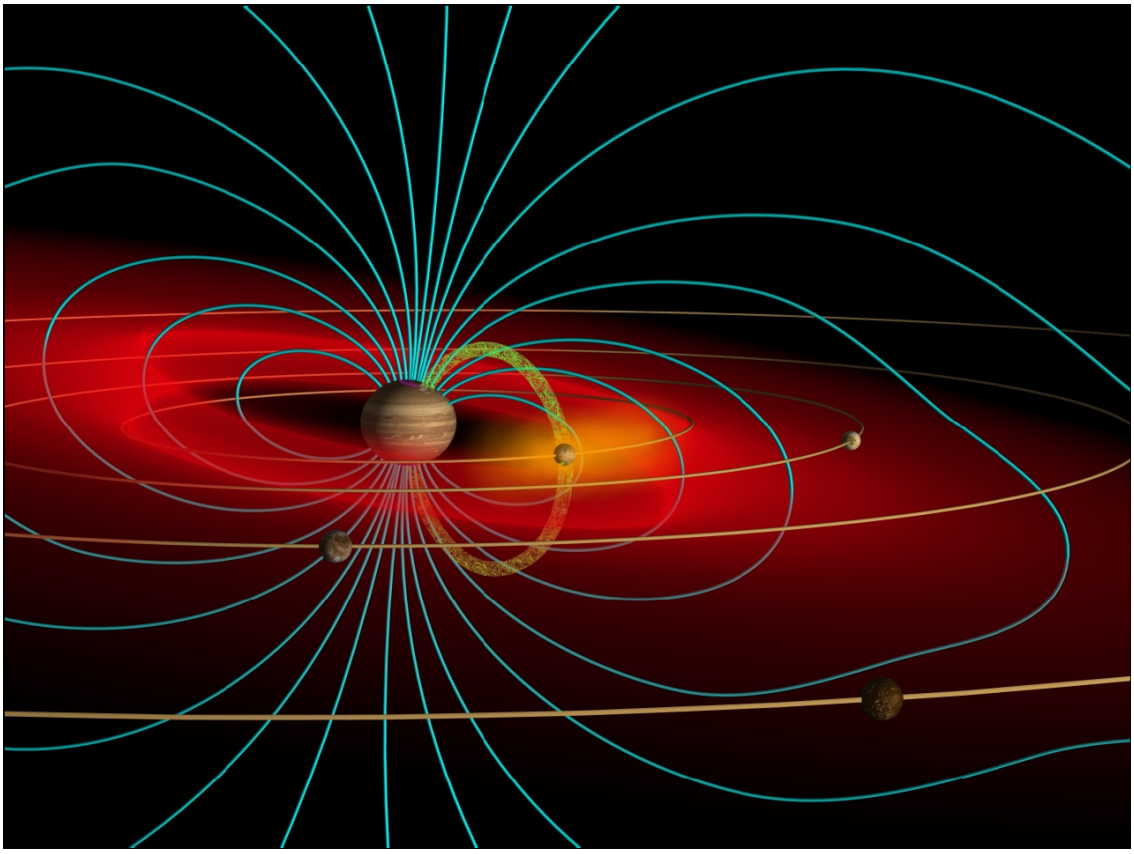

Figure 2-8: Schematic of the Jovian magnetosphere. The Jovian polar aurora, Jovian magnetic field lines (blue), the Io plasma torus (red), the Galilean Satellites and their orbits (orange), the Io flux tube (green), and Io's neutral cloud (yellow) are shown. Illustration by Dr. John Spencer, taken from http://www.boulder.swri.edu/~spencer/digipics.html.

The plasma density varies latitudinally in the torus along field lines due to the competition between centrifugal forces and an ambipolar electric field. The ambipolar field is generated to keep the plasma quasi-neutral given the separation that would otherwise result from the high mobility of electrons along field lines and the confinement of the more massive ions to the centrifugal equator. The plasma density along a field line is approximately given by an exponential:

$$n(Z) = n(Z = 0)\exp\left(-\left(\mathrm{Z}/\mathrm{H}_{\mathrm{plasma}}\right)^2\right) \qquad 2\text{-}1$$

where Z is the (small) distance along a field line from the centrifugal equator, and with a scale height, H_{plasma}, given by:

$$H_{plasma} = \sqrt{\frac{2k(T_i + Z_i T_e)}{3m_i \Omega_J^2}} \qquad 2\text{-}2$$

where k is the Boltzmann constant, T_i is the ion temperature, Z_i is the ion charge, m_i is the mass of the ion, T_e is the electron temperature, and Ω_J is Jupiter's rotation rate (Bagenal, 1985). For typical conditions of the plasma at Io, the scale height is $\approx\sqrt{2}R_J$, though Eqn. 2-2 shows that the different ion species (and electrons) will have different scale heights.

Io's interaction with the plasma torus has been simulated numerous times using the magnetohydrodynamic (MHD) equations (Linker *et al.*, 1991; Linker *et al.*, 1998; Combi *et al.*, 1998). The corotational electric field is altered by collisions in Io's ionosphere, causing most of the plasma flux tubes to divert around Io and inducing a twist of the electric field across Io (Saur *et al.*, 1999). Additionally, the corotational electric field generates the observed ~10 MA current which is thought to be carried to Jupiter's poles along field-aligned Alfvén wings (Neubauer, 1980; Saur *et al.*, 1999).

Combi *et al.* (1998) developed a 3D global, multi-scale magnetohydrodynamic (MHD) simulation for a one fluid plasma that accounted for mass-loaded flow. The model assumed that Io did not have an intrinsic magnetic field, which has since been confirmed (Kivelson *et al.*, 2001). They qualitatively reproduced the Galileo fly-by plasma and field observations in Io's wake (Frank *et al.*, 1996) such as the plasma density peak and the plasma pressure; however, they did not quantitatively match detailed features such as the magnitude of the double-peaked magnetic field disturbance in the wake. The simulated magnetic field and plasma density is shown in Figure 2-9. It is seen that the magnetic field is compressed and the field strength increases upstream of Io and that the plasma density in Io's wake is enhanced by a factor of ~5 relative to the upstream density as Io's atmosphere supplies the torus plasma.

Saur (Saur *et al.*, 1999; 2000; 2002; 2004) used an electrodynamic model and calculated the density, velocity and temperature of thermal electrons and one representative ion species, and the electric field near Io in a self-consistent manner. They assumed a spherically symmetric atmosphere and a spatially uniform unperturbed Jovian magnetic field, requiring the actual perturbation in the magnetic field magnitude about Io to be relatively small. The 3D model of Io's aurora used by Saur *et al.* (2000) investigated the formation of OI] 1356 Å equatorial spots at western elongation and indicated that the Hall effect produces a brighter spot on the anti-Jovian side than the sub-Jovian side. Their model was able to describe certain aspects of Io's far-ultraviolet aurora, such as the relative brightness and position of the sub-Jovian and anti-Jovian spots. Saur *et al.* (2002) were able to reproduce the

magnitude and structure of the double peak magnetic field fly-by data in Io's wake and attributed the origin of the structure to diamagnetic and inertia currents. Finally, they found that, due to the drag force of the plasma, Io's atmosphere should be longitudinally asymmetric with the upstream scale height being significantly smaller than the downstream scale height. The model did not require an intrinsic magnetic field to match the data and so they predicted results for a generic polar pass to distinguish between magnetic field perturbations due to an internal field of Io and those due to ionospheric currents and the rotated Alfvén wings generated by the Hall effect.

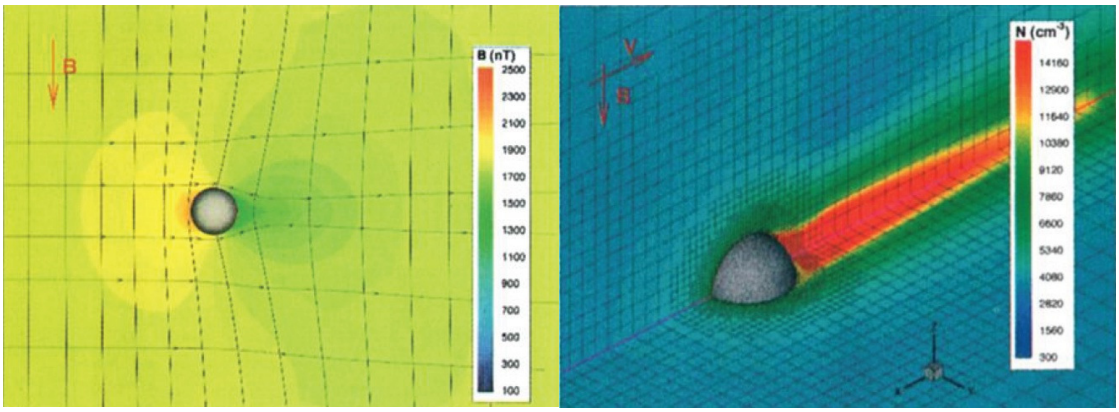

Figure 2-9: Simulated (left) streamlines, magnetic field, and (right) plasma density for Combi *et al.*'s (1998) fixed boundary, mass loading case when Io is at the torus equator. In (a) the view is of the plane aligned along the upstream magnetic field direction. The streamlines all have arrows and go primarily left to right and the magnetic field lines are vertical upstream and then perturbed across Io. The colorbar shows the magnitude of the magnetic field. (*From Combi et al. (1998), courtesy of the American Geophysical Union*).

More recently, Lipatov and Combi (2006) performed a 3D hybrid simulation of the magnetic and electric environment about Io using a kinetic description for the ion motion and MHD equations to solve for the electron motion. Their model was able to account for a more realistic anisotropic ion velocity distribution, charge-exchange, photo-ionization processes, and solve for the magnetic and electric fields self-consistently. They obtained good agreement to the Galileo I0 flyby data and found that the plasma flow around Io was strongly affected by the whistler and quasi-stationary Alfvén waves. A major finding was that the finite ion gyroradius results in an asymmetrical boundary layer near the ionosphere of Io and that the observed inverse structure of the magnetic field is due to the kinetic behavior of the ions. Also, the finite gyration of non-isotropic pickup ions was found to broaden the B-field

perturbation and increase the temperature at the edge of the wake as observed. Their model produces a cold, dense wake; however, the pickup distribution in the wake could be heavily influenced by the electron temperature, requiring a full hybrid simulation that accounts for the effect of electron-neutral collisions on the electron temperature. Finally, they found that the induced magnetic field in Io might be reduced by 20-40% due to the ionosphere's conductivity.

2.3 BRIEF SUMMARY OF AURORA OBSERVATIONS

Oliverson, *et al* (2001) showed that Io's disc-averaged [OI] 6300 Å intensity varies with Io's latitude in the plasma torus and Retherford (2002, 2003) noted that the brightness ratio between the north and south limb-glows agreed with the ratio of the thermal electron column densities above the respective poles. Furthermore, the latitudes (on Io) of the sub- and anti-jovian equatorial bright spots were argued to be correlated with Io's system III longitude based on individual images of the aurora at many different system III longitudes (Roesler 1999, Retherford 2000, Geissler 2001). Recent observations by NASA's Cassini spacecraft of Io's auroral features during eclipse definitively show (by a series of observations as Io crosses the torus) that the equatorial auroral spots gradually shift in latitude (relative to Io) as Io's system III longitude changes (Porco *et. al.*, 2003, Geissler *et al.*, 2004b).

Several bright regions of [OI] 6300 Å emission, shown in Figure 2-10, were seen in observations of Io ~10 minutes after entering Jupiter's shadow by Trauger *et al.* (1997) with WFPC2 in May 1997. Several general features characterize this aurora: a bright spot in the wake centered at ~250 km above Io's southern hemisphere, an equatorial band located along the extended Jovian magnetic equatorial plane, a limb glow near each pole (in Figure 2-10b it is stronger in the North), and extended diffuse emission particularly on the downstream (left) side. If present at all, the upstream bright spot is much less intense and smaller than the wake spot. The absolute peak intensity of the wake spot is ~15 kR in each case and the background diffuse emission is ~5 kR. The data used to generate these images were processed further and used for comparison to our simulations in Chapter 6.

Retherford *et al.* (2000) obtained multiple HST/STIS observations of Io's UV emissions in 1997 and 1998. They found that the brightest UV emissions came from localized regions near Io's equator. The equatorial spots were found to be linked to the interaction between the Jovian magnetosphere and Io's atmosphere. Specifically, the location of the

equatorial spot is correlated with the Jovian magnetic field orientation at Io, the brightness of the UV emission is correlated with Io's distance from the plasma torus centrifugal equator, and the anti-Jovian equatorial spots are ~20% brighter than the sub-Jovian spots. Retherford *et al.* (2003) used HST/STIS data from 1997 to 2000 to examine Io's FUV auroral emission, and in particular, the OI] 1356 Å auroral limb glow at Io's poles. They found that the limb glow on the hemisphere facing the torus centrifugal equator was up to a factor of ~2 brighter (when Io was furthest from the equator) than the opposite hemisphere's limb glow. Since the electrons in a plasma flux tube can travel along the field lines and collide with Io's atmosphere before the flux tube convects downstream past Io's poles, the difference in limb glow brightness was attributed to the greater electron energy in the plasma flux tube on the side facing the centrifugal equator. This effect illustrates the importance of field-aligned electron energy transport on production of Io's aurora. Finally, they found that a Kappa distribution of plasma torus electron column density above each hemisphere predicts the ratio of north/south limb glow brightness versus Io's distance from the torus centrifugal equator.

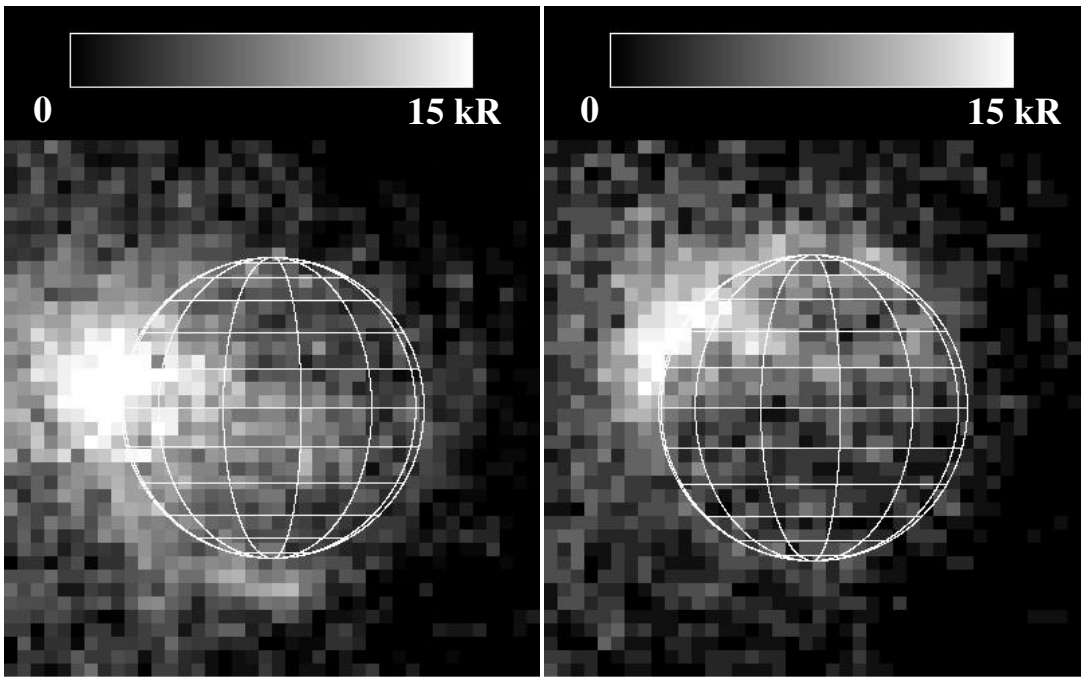

Figure 2-10: Observations of [OI] 6300 Å emission from Io in eclipse on (left) May 17, 1997 when Io is near the torus equator and (right) May 22, 1997 when Io is near the maximum southern latitude of the torus. Images taken by Traguer *et al.* (1997) with HST's WFPC2 and the contours run from 0 to 15 kR.

More recently, Retherford *et al.* (2007a,b) observed Io in eclipse with the Long Range Reconnaissance Imager on the New Horizons spacecraft. They observed atmospheric emission features and volcanic hotspots on Io's surface that were consistent with previous observations, in addition to observing emission (presumably) from East Girru's plume. The observed brightness at different viewing geometries can be explained by a large difference between the dayside and nightside column densities. Comparison of the observed auroral brightness variations upon ingress and egress to simulations of Io's aurora indicate that the volcanoes supply 1 to 3% of the dayside atmosphere. This is consistent with Saur and Strobel's (2004) findings, though they again assume the SO_2 gas column is in equilibrium with the frost-covered surface.

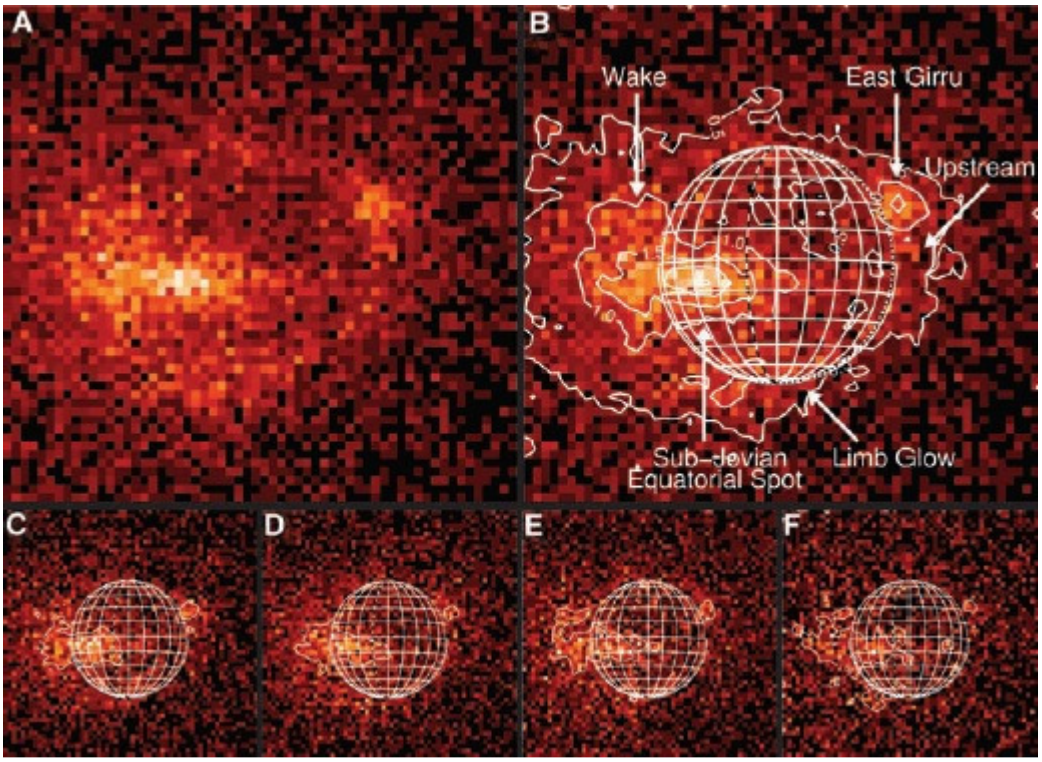

Figure 2-11: HST/SBC FUV (1250–2000 Å) images of Io on February 27, 2007. Eight 5-minute exposures were taken upon ingress. (a) Average of all 8 exposures. (b) Same as (a), but with auroral features labeled. Contours are in 0.5 kR increments. Note that the wake, sub-jovian spot, and the region upstream near the East Girru plume are bright and that the southern polar limb glow is relatively dim. (c)-(f) Time series of 10-min exposures. The contours are re-scaled in each image for better comparison of the equatorial spot and latitudinal extent. (*From Retherford et al., 2007b, courtesy of The American Association for the Advancement of Science*).

Trafton *et al.* (2011a, 2011b) observed spectra from 1800–5700Å of Io in eclipse using HST/STIS in August of 1999. The August 18, 1999 observations were made with the MAMA detector and the G230L grating (1800–3100 Å) and the August 7, 1999 observations were made with the CCD detector and the G430L grating (2900–5700 Å). Figure 2-12 shows the smoothed, merged spectrum (both the MAMA and the CCD) after subtraction of the sky background. While the sky background intensity is large compared to Io's aurora above ~4000 Å, it has been approximately subtracted from the spectrum and the emission features above ~4000 Å are probably not due to refracted and scattered sunlight through Jupiter's atmosphere. Instead these emissions are thought to be molecular band emission from an unidentified species (Trafton *et al.*, 2011a).

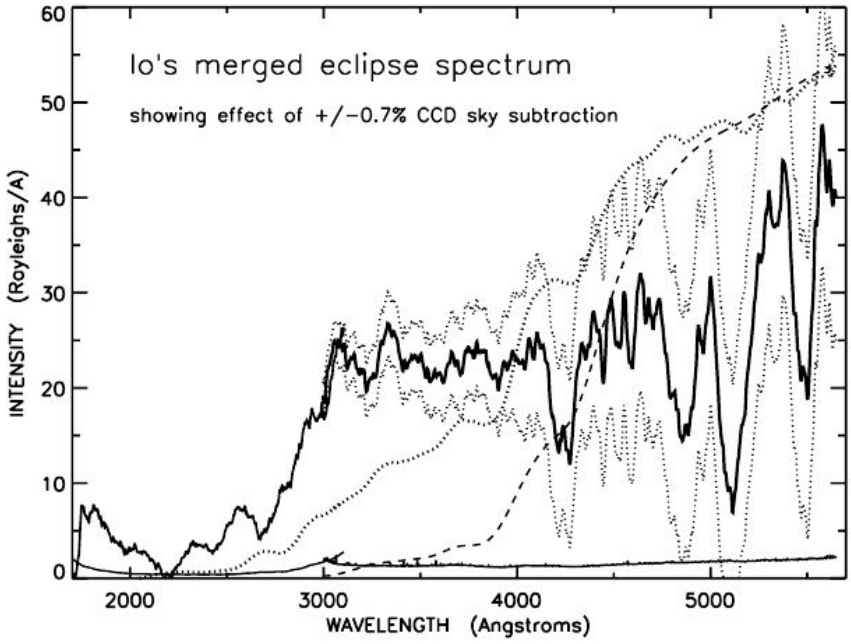

Figure 2-12: Disk averaged UV-Vis spectrum of Io observed with HST/STIS and a ~110 Å resolution element. The thick sold line shows the nominal emission intensity bracketed by the emission if the subtracted sky background was varied (dotted lines). The 1–σ error is plotted by thin solid lines. The subtracted sky spectrum (thick dotted line) and Io's daytime continuum spectrum (dashed line) are shown. (*From Trafton et al. (2011b), courtesy of Laurence Trafton*).

Below this threshold though, several emission features are evident. The double peaks at ~1800 Å and ~1900 Å have been shown to be due to S I emission while the peak at ~2400 Å is due to SO emission from the $\tilde{A}^3\Pi$ and $B^3\Sigma$ excited states. Furthermore, SO_2 and S_2 both exhibit molecular band emission from ~2800–6000 Å. The HST/STIS data used in Figure

2-12 were processed further and used for comparison to our simulations in order to infer properties of the upstream plasma and plume activity in Chapter 7.

Chapter 3

Direct Simulation Monte Carlo Method

The Direct Simulation Monte Carlo (DSMC) method stochastically models gas dynamics using simulation pseudo-particles, each of which represents some large (typically $>10^{20}$) number of real particles in the gas (Bird, 1994). Theoretically DSMC is capable of modeling unsteady, chemically reacting gas flows accurately, from the rarefied, free molecular limit to the continuum regime. Basic DSMC collision routines have been shown to satisfy the collision integral of the Boltzmann equation (Nanbu, 1986) and basic DSMC itself solves the basic Boltzmann equation for sufficiently large numbers of monatomic simulation pseudo-particles (Wagner, 1992). In DSMC the simulation proceeds with a discrete timestep and the domain is divided into cells. Over a given timestep the simulation particles are first moved (simply using $F=ma$ for body forces) and then collided with other simulation particles that reside within the same cell. Macroscopic flow properties may be obtained by sampling the simulation molecules in each cell (though the sample cells and collision cells need not be the same) and, in the case of steady flows, the samples may be averaged over many independent timesteps.

While DSMC is not subject to standard stability constraints of traditional CFD approaches, both the timestep and cell size must be properly chosen to obtain accurate results. A fundamental assumption of traditional DSMC is that the simulated gas is dilute (for an extension of DSMC to dense gases see Alexander *et al.*, 1997). In other words, the vast majority of collisions are binary and the timescale for intermolecular collision dynamics is much smaller than the time between collisions allowing the collisions to be uncoupled from the particle motion. Furthermore, DSMC typically requires that the simulation timestep be smaller than the mean time between collisions. Note that in most implementations of DMSC only binary collisions are modeled, and that the use of collision cells to choose collision partners can cause gradients to smear across the cell because collision partners are randomly picked from the particles within the cell. This means that it is preferable for the cell size to be small compared to the length scale of the macroscopic flow gradients. Typically the cell size is taken to be a fraction of the mean free path since, in a collisional flow with no external

forces, gradient length scales smaller than the mean free path cannot be sustained. Finally, note that the statistical fluctuations in the sampled macroscopic quantities scale inversely with the square root of the number of independent simulation particles in the sample.

Many DSMC solvers have been implemented by independent groups; our 3D parallel DSMC code, developed to simulate atmospheric flows, has many unique features. These include spontaneous radiation from rotational and vibrational modes (Zhang *et al.*, 2003), variable gravity (Zhang *et al.*, 2004), a three dimensional spherical geometry (Stewart *et al.*, 2009), an option for one-way unsteady coupling to continuum data along arbitrary boundaries in the flow (Stewart *et al.*, 2009, 2011; McDoniel *et al.*, 2011, Morris *et al.*, 2011), a collision limiting scheme to allow more efficient simulation near the continuum regime (Stewart *et al.*, 2009; Stewart, 2010), and time variable surface temperature based on radiative equilibrium and coupled with latent heat gain/loss from condensation and sublimation (Moore *et al.*, 2009, Walker *et al.*, 2010a, 2010b).

3.1 GENERAL IMPROVEMENTS

Below some of the more general (and minor) improvements that I have made to our planetary DSMC code are described. More extensive improvements developed specifically for the current atmospheric simulations are discussed in their own sections. Our implementation utilizes the no time counter (NTC) scheme to determine the number of collision pairs to select and therefore it is important to allow $(\sigma_{Tot}V_{rel})_{max}$ to relax for each timestep. This is so that the selection routine remains efficient even for unsteady flows despite rare collision events with very large $(\sigma_{Tot}V_{rel})$. Previously, during every timestep the largest (σV_{rel}) of all selected pairs in a given cell, $(\sigma V_{rel})_{largest}$, was stored and $(\sigma_{Tot}V_{rel})_{max}$ of the cell updated (Zhang, 2004b; Stewart, 2010):

$$(\sigma_{Tot}V_{rel})_{max} = (1 - f_{relax})(\sigma_{Tot}V_{rel})_{max} + f_{relax}(\sigma V_{rel})_{largest} \qquad 3\text{-}1$$

where f_{relax} is the relaxation fraction set to 0.05 in current simulations.

For nearly collisionless regions of the flow, however, Eqn. 3-1 could lead to over relaxation in $(\sigma_{Tot}V_{rel})_{max}$ (Stewart, 2010). While this has not been an issue in the past, the current simulations require timestep splitting to simulate the charged particle motion accurately, and the time between collision-pair selections might be hundreds of timesteps. In this case, the fact that no selections occur in a given timestep results in positive feedback in Eqn. 3-1 and leads to there being less of a chance of a selection on the following timestep.

The solution was simply to make $(\sigma V_{rel})_{largest}$ a function of ratio of the number of selections to the total possible pair selections, N_{pairs}. If $N_{sel}/N_{pairs} > 1$ then Eqn. 3-1 is used, otherwise $(\sigma_{Tot}V_{rel})_{max}$ is relaxed by:

$$(\sigma_{Tot}V_{rel})_{max} = \left(1 - f_{relax}\frac{N_{sel}}{N_{pairs}}\right)(\sigma_{Tot}V_{rel})_{max} + f_{relax}\frac{N_{sel}}{N_{pairs}}(\sigma V_{rel})_{largest} \quad 3\text{-}2$$

Using Eqn. 3-2, $(\sigma_{Tot}V_{rel})_{max}$ does not relax if there were no selections during a timestep, and in fact only relaxes by the full amount, f_{relax}, if there are more selections than possible pairs. Note however, that this does not prevent the case where an unsteady flow which previously had virtually no pair selections (i.e. it was nearly collisionless) suddenly becomes collisional due to variation in (σV_{rel}). In this case, the collision rate would be artificially low and the probability of a selection each timestep would remain too small until selections were made and $(\sigma_{Tot}V_{rel})_{max}$ was updated. To fix this we simply require at least one selection each timestep in every cell. If a selection must be forced (in other words the computed N_{sel} equaled zero), then only the quantity (σV_{rel}) is computed for the pair and no collision is computed. Obviously this can still underestimate $(\sigma_{Tot}V_{rel})_{max}$; however, sampling every possible collision pair in every cell each timestep and using the resulting values of $(\sigma_{Tot}V_{rel})_{max}$ is computationally inefficient. While a rigorous study was not performed, a single forced selection was deemed to be a reasonable tradeoff for computational time and accuracy. Furthermore, this procedure corrected the artificially low collision rates originally obtained during reformation of the atmosphere upon egress from eclipse (Chapter 4.2.4)

Another minor improvement was the addition of a large radial "free molecular buffer" cell at the top of the domain. The purpose of the buffer cell was to simulate the upper boundary of the domain more accurately with minimal additional computational cost. For our atmospheric simulations, the initial domain boundary was placed above the exobase; however, most of the molecules which reached this altitude still did not have escape velocity and therefore a simple vacuum boundary was not appropriate. In order to count the escaping particles more accurately, a "free molecular buffer" cell was added to the top of the domain in which the flow was treated as free molecular. In other words, molecules were moved, underwent photo-chemistry, and radiated as usual; however, no collisions were allowed to take place. Since the "buffer" cell begins above the exobase, the lack of collisions should only impact the accuracy slightly while saving the computational cost of computing the

number of selections (usually zero) and of forcing a selection every timestep for computing $(\sigma_{Tot}V_{rel})_{max}$. In addition, the "buffer" cell was excluded from the adaptive grid discussed below and always began at the same altitude (the initial upper radial domain boundary). The height of the "buffer" cell was set to 1320 km so that the total radial simulation domain was one Io radius. The top of the buffer cell was treated as a vacuum and any simulation particle that reached the top of the "buffer" cell was deleted.

For many of our simulations involving polyatomic molecules (SO_2 or H_2O), the single largest computational cost was incurred in the collide routine when computing the vibrational collision number[3], $Z_{V,im}(T_{col})$, for each of the modes, *im*, at a collision "temperature", T_{col}. Obviously, in these simulations significant regions of the flow were continuum (or nearly so) and therefore many collisions were being computed. Furthermore, our code uses curve fits to experimental relaxation data for species specific $Z_{V,im}(T_{col})$ (requiring *if* statements) that involve several exponentials and powers which were then solved in every accepted collision. Therefore the simple solution was to create a precomputed look up table for the vibrational collision numbers (using a constant spacing in T_{col}) and during collide merely look-up the nearest tabulated value given the collision "temperature". The loss of accuracy in $Z_{V,im}$ was generally less than the uncertainty in this parameter. With moderate memory usage this simple change was sufficient to reduce the computational cost of picking the vibrational collision number to ~1% (and speed up the code by ~14%).

The last minor improvement (of note) of the basic DSMC algorithm was to implement timestep splitting (or substeps) for the vibrational radiative relaxation. Frequently our timestep is larger than the mean lifetime (the inverse of the Einstein *A* coefficient) in a given state. This was especially true if it is a high lying vibrational state since, assuming a harmonic oscillator, the Einstein *A* coefficient for transition from $v' \rightarrow v''$ is given by $A_{v' \rightarrow v''} = v' A_{1 \rightarrow 0}$. Before the substeps were implemented, a molecule could only decay one vibrational level per timestep even if the gas timestep was large enough that it should decay multiple levels. This resulted in higher vibrational temperatures and increasing over-population as the vibrational level increased. In order to simulate the radiative decay more accurately, the timestep over which the radiation probability was computed was reduced. The

---

[3] Our profiling tool, `gprof`, frequently found that ~75% of the simulation time was spent in collide and that ~15% of the simulation was spent picking $Z_{V,im}$.

substep time interval was set such that an integer number of substeps equaled the full gas timestep and was approximately equal to one tenth of the mean lifetime (equal to $A_{v'\rightarrow v''}^{-1}$) for the initial vibrational state. Use of the substeps gives the correct distribution of vibrational states among the simulation particles at each global gas timestep. However, the substeps do not resolve the location of the emission (it is still all located at the particle position corresponding to the gas timestep). Because the particles rarely move across multiple cells during a timestep any radiative emission should arise within the cell or it's nearest neighbors.

3.2 INVERTIBLE ADAPTIVE GRID

As discussed above, it is important that the collision cells (or grid) be resolved with respect to the macroscopic gradient length scales. However, there are two complications when making a grid for a computational domain. First, in DSMC it is highly desirable for the grid to be invertible[4] for computational speed since at every timestep each simulation molecule must be indexed into the appropriate cell after being moved. Otherwise, collision partners for a simulation particle might not be chosen from within the same cell. If the grid is not invertible, then the search routine to index the molecule into the correct cell can consume significant computation time – especially when the flow is nearly collisionless and each dimension has $O(10^2–10^3)$ cells. Alternatively, to obviate a search through the cells, ray tracing methods have been developed to determine which cell a molecule ends up in after the move step if it crossed a cell boundary. Typically this also comes with a notable performance penalty (Bird, 1994). The planetary code does not currently have this capability. Although adding it would allow the use of fully unstructured grids, it was outside the scope of this dissertation which is more concerned with the implementation and simulation of the plasma interaction with Io's atmosphere.

The second complication to making a grid is that, in practice, one does not know *a priori* the grid structure required to properly resolve the gradients for a given flow. This is especially true if the flow is unsteady. One can always over–resolve the flow by brute force; however, increasing the number of cells increases the total number of particles required and the computational cost and memory usage increases with the number of particles simulated. In general, it is necessary to have at least ~30 simulation particles per cell per species in order

[4] So one is able to analytically determine the cell number given the position of the molecule.

to correctly model the physics of the flow (Stephani *et al.*, 2011). Furthermore, the noise scales with the inverse of the square root of the number of particles per cell and therefore increasing the number of cells increases the total number of particles needed for a desired (instantaneous) noise level. Note that the prior limitations only apply to the collision cells and that the sample cells may not need to be constrained in this way.

Unfortunately the required grid structure with the fewest total cells is generally unstructured and not invertible. Therefore, as a compromise between invertability and having few cells to resolve a given flowfield, the domain is broken into N_{seg} "linear" segments in a given dimension. The cell sizes at both ends of each segment are based on a local length scale determined by the local gas properties and the cell sizes vary linearly between the two end cell sizes. In this way, the gradients of the flow may be approximately captured by proper placement of segments. Indexing proceeds by first searching for the particular segment where the molecule is located, and then analytically inverting the segment's grid to obtain the exact cell number. Typically N_{seg} need not be larger than ~10; in the current simulations 5 segments are used (see Chapter 8), and thus the search to place the simulation molecule in a segment is much faster than having to search over all of the simulation cells in that dimension.

An alternate way to grid the domain is to use many segments which are invertible and contain an associated array of all the unstructured collision cells with any portion of their volume inside the invertible segment. Index then proceeds by determining which segment a particle is in by inversion and then searching over all the collision cells within that segment until the appropriate collision cell is found. The advantage of this method would be that third-party grid generation software could be used to make a body-fitted unstructured grid and still have a reasonably fast index routine due to the invertible segments. We did not pursue this method because we desired adaptability to unsteady flows and that would have required us to either write our own unstructured grid code (beyond the scope of this work) and a third-party grid generation code was not available.

The remainder of this discussion will focus on applying the multiple linear segments scheme to the radial dimension. Furthermore, for a 3D simulation each column of radial cells in the θ and φ directions has its own set of radial segment parameters. The method discussed below to obtain the parameters is repeated for every column of radial cells and in this way the grid is radially adapted independently in the θ and φ directions. While it should be easy to apply the method to either the θ or φ dimensions in the future, it will be difficult to extend the

method to work in all dimensions at the same time. Furthermore, extension of the segments across processors (currently arrayed in θ and φ) would be difficult. Prior simulations of Io's atmosphere (Austin and Goldstein, 2000; Walker *et al.*, 2010a) used a uniform grid in the θ and φ dimensions and a radial grid spacing that increased exponentially for part of the atmosphere and then was constant once the cell size exceeded a user-defined value. This grid required a search over the radial cells since the bottom of a given cell was given by the sum of the exponentially sized cells below it. For some of the simulations currently run with our planetary DSMC code (including those to be presented here, see Chapter 8), mean free path grid resolution is only feasible in the radial dimension (Walker *et al.*, 2010a, 2011; Moore *et al.*, 2010c). However, the flows parallel to the surface are weak enough that the atmospheric column remains everywhere nearly in hydrostatic equilibrium (Walker *et al.*, 2010a) and that equilibrium is controlled by the local surface temperature and gravity. On the other hand, the strongest gradients are often radial: canopy shocks in volcanic plumes (McDoniel *et al.*, 2011), impingement shocks from nozzle exhaust (Morris *et al.*, 2011), and density and temperature gradients due to atmospheric collapse, plasma heating, and non-LTE cooling (Moore *et al.*, 2009; Walker *et al.*, 2010a, 2011). Therefore, we chose to first perform radial adaptation and better resolve the radial flowfield as described below.

3.2.1 Grid Adaptation

In order to adapt the grid using our linearly stretched segments scheme, the spatial distribution of segments and the local length scales to resolve at the start and end of each segment must be determined. To compute these, the flowfield is sampled every timestep[5] between adaptations of the grid, which occur every N_{adapt} timesteps. During the grid adaptation routine these sampled macroscopic parameters are then boxcar smoothed and used to determine the needed grid parameters. In general, one would place the segment ends ($H_{cum,j}$ in Figure 3-1) at locations of maximum curvature in the desired macroscopic parameter. Then the grid would resolve the length scales as best as possible since the cells at the end of each segment are sized to the local length scale. In the current implementation the segments' radial spatial distribution is determined by balancing the number of particles in each segment. Therefore, if there are N_{seg} segments, the segments are spaced such that the fraction of the

[5] One only needs to sample independent timesteps which is not, in general, every timestep.

total radial column's mass that each segment contains is roughly $1/N_{seg}$. This was found to provide a reasonably good segment distribution because we are attempting to resolve a gravitationally bound atmospheric density distribution. Hence, a more general method of distributing the segments was not required.

Once the spatial positions of the segment ends are determined, the local length scales, L_j, at each segment end are computed (j=0 corresponds to the surface and j=N_{seg} to the upper domain boundary). In the current implementation two length scales are computed and the L_j is taken to be the smaller of the two. The first length scale is the mean free path for a multi-species gas

$$\lambda = \frac{1}{\sqrt{2}\sum_k^{N_s} \sigma_{tot,k} n_k}, \tag{3-3}$$

where N_s is the total number of species, $\sigma_{tot,k}$ is the total collision cross section, and n_k is the number density for the k^{th} species. While this is the typical length scale that is desirable to resolve for DSMC, it is insufficient to resolve nearly collisionless flows with applied external forces which themselves cause gradients. For the simulations presented here, the gravitational force on the nightside (which is nearly collisionless) causes gas density gradients that are much smaller than the mean free path. Therefore, the second length scale computed is the total number density, $n_{tot} = \sum n_k$, gradient length scale in the radial direction:

$$L_{GLS} = n_{tot}\left(\frac{dn_{tot}}{dr}\right)^{-1} \tag{3-4}$$

Once the segment locations and the local length scales, $L_j = \min(\lambda, L_{GLS})$, have been computed, the grid can be constructed. The basic structure of the segmented grid is shown schematically in Figure 3-1 for a grid with 3 segments. As can be seen, each segment has its own unique height, H_j, and the grid size, Δ, stretches linearly between the desired length scales, L_j, times a constant, α_{ls}, at each end of a segment. Also, note that the cell size is held constant (within round–off caused by the integer number of cells) across each segment boundary in order to prevent large, discontinuous changes in the cell size due to noise in the sampled data across the adjoining cells.

From Figure 3-1 it can be seen that the cell top, $z_{i_s}^j$, of cell i_s in a given segment, j, has the following constraints (for $j < N_{seg} + 1$):

$$z^{j}_{i_s=0} = \Delta_j = \alpha_{ls} L_j \quad (a)$$
$$z^{j}_{i_s=N_j} = H_j \quad (b)$$
$$z^{j}_{i_s=N_j} - z^{j}_{i_s=N_j-1} = \Delta_{j+1} = \alpha_{ls} L_{j+1} \quad (c)$$
$$N_{cell} = \sum_{j=0}^{N_{seg}} (N_j + 1) \quad (d)$$

3-5

where, as indicated in Figure 3-1, α_{ls} is a constant which scales the cell size with L_j, the local length scale, H_j is the height of the j^{th} segment, and N_{cell} is the total number of cells in the radial direction (set in the input file). Note that $\alpha \ll 1$ is required to resolve a given length scale.

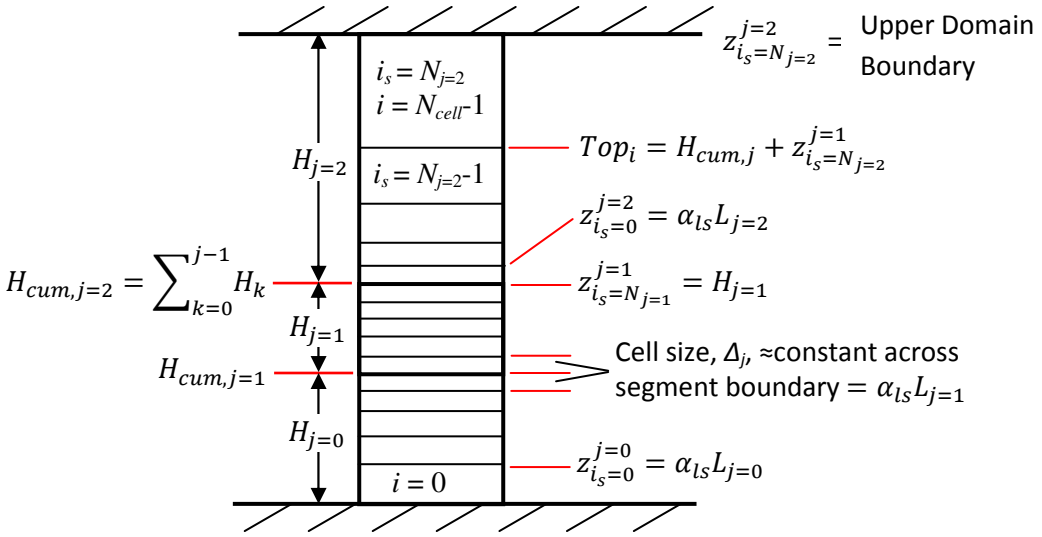

Figure 3-1: Schematic of the segmented grid structure for N_{seg} = 3. The index j denotes the segment number, i_s denotes the segment cell number, and i denotes the absolute radial cell number. Note that the indices start at 0 and that each segment has N_j+1 cells.

In a given segment we desire the grid spacing to scale linearly, $z^{j}_{i_s} - z^{j}_{i_s-1} = a + b i_s$, and therefore the location of the cell tops (within a segment) are given by

$$z^{j}_{i_s} = [A_j + B_j i_s](i_s + 1), \quad 3\text{-}6$$

where A_j and B_j are segment-specific constants. From Eqn. 3-5a we see that

$$z^{j}_{i_s=0} = \alpha_{ls} L_j = A_j, \quad 3\text{-}7$$

and using Eqn. 3-7 in Eqn. 3-5c we find that

$$B_j N_j = \alpha_{ls} \frac{L_{j+1} - L_j}{2}. \quad 3\text{-}8$$

To get the number of cells in a segment we combine Eqn. 3-5c, Eqn. 3-7, and Eqn. 3-8 to get $z^{j}_{i_s=N_j} = H_j = \left[A_j + B_j N_j\right]\left(N_j + 1\right) = \frac{\alpha_{ls}}{2}\left[L_j + L_{j+1}\right]\left(N_j + 1\right)$. This can then be solved for N_j+1:

$$\left(N_j + 1\right) = \frac{2H_j}{\alpha_{ls}\left(L_j + L_{j+1}\right)}. \qquad 3\text{-}9$$

With Eqns. 3-7, 3-8, and 3-9 the grid is now known given the local length scales at the ends of each segment, L_j, the segment heights, H_j, and a constant scaling factor, α_{ls}.

The length scales and the segment heights are computed based on the sampled flow properties as discussed above; α however is computed such that the total number of (radial) cells remains constant during the entire simulation.[6] Note this means that there is no guarantee that $\alpha < 1$ for a given flowfield and total number of cells. While one could allow the user to chose α, this would require the total number of cells in a column to vary during each adaptation. While it would generally be desirable to have fewer cells in columns that do not require the resolution and more in the ones that do, it causes additional difficulties. First, since the domain is typically 3D, the number of radial cells would vary for each latitudinal and longitudinal cell and extension of the segmented grid to all three dimensions would then be cumbersome if the number of cells in all three dimensions were allowed to vary. Also, this would cause problems when displaying data in standard plotting packages like Tecplot though this could be avoided by having a separate output grid. Second, varying the number of cells in a column would require reallocation of the cell structure every time the grid is adapted and then this would slow the code down slightly since the cell structure is actually quite large. Also, if there is not enough memory to increase the number of cells given a fixed α, then either the adaptation would fail or α would still have to be allowed to vary so that the grid could adapt without increasing the memory required (number of cells). Therefore, to keep it relatively simple, it was decided to allow α_{ls} to vary and to hold the number of cells constant.

To solve for α_{ls}, substitute Eqn. 3-9 into Eqn. 3-5d and simplify to:

$$\alpha_{ls} = \frac{2}{N_{cell}} \sum_{j=0}^{N_{seg}-1} \frac{H_j}{\left(L_j + L_{j+1}\right)} \qquad 3\text{-}10$$

Equation 3-10 gives a single value of α_{ls} for the entire radial column; unfortunately, in general one cannot satisfy Eqn. 3-5d with the value for α_{ls} obtained in Eqn. 3-10

[6] Technically this means that the grid is being realigned, not adapted.

because the number of cells in each segment (Eqn. 3-9) must be an integer. Therefore the actual number of cells in a segment, for a specified α_{ls} computed with Eqn. 3-10, is given by

$$\left(N_j + 1\right) = Floor\left(\frac{2H_j}{\alpha_{ls}(L_j + L_{j+1})}\right) \qquad 3\text{-}11$$

where the *Floor*() of Eqn. 3-9 must be taken so that the number of cells in a given segment is an integer value. This is important since N_j and α_{ls} are used in Eqns. 3-7 and 3-8 to obtain A_j and B_j; these are used to invert the grid once the segment a molecule lies in has been determined (see Chapter 3.2.2). Therefore, for each segment N_j is computed by Eqn. 3-11 with α_{ls} and then Eqn. 3-9 is inverted to solve for a corrected $\alpha_{ls,j}$ which is slightly different for each segment, j, given N_j , H_j, L_j, and L_{j+1}. While this leads to slight differences in the cell sizes across a segment, it is a simple means to accurately determine the segment parameters given that the number of cells in a segment must be an integer value. However, having to *Floor*() Eqn. 3-9 to obtain N_j and then adjust α_{ls} to $\alpha_{ls,j}$ has the consequence that Eqn. 3-5d is not necessarily satisfied due to round–off. To correct for this simply the number of cells in the final segment is changed such that Eqn. 3-5d is satisfied. In practice this is not a large change from the expected value. In the simulations presented here the gas in the last radial segment is nearly free molecular and the grid is merely resolving gradients produced by gravity.

The preceding discussion would be sufficient to generate a grid, provided that the length scales computed in both Eqns. 3-3 and 3-4 do not go to infinity (or zero). In general it is desirable to limit the cell size to some maximum value, Δ_{max},

$$\alpha_{ls}L_j = \Delta_j < \Delta_{max}. \qquad 3\text{-}12$$

This ensures that the flow is at least nominally resolved if it changes between grid adaptations. Specifically, in the atmospheric simulations presented here, the hydrostatic length scales in the upper atmosphere can become quite large (~100 km) and yet, when the atmosphere collapses upon ingress into eclipse and then reforms upon egress it is desirable to have smaller cells in the upper atmosphere. Similarly, a simulation of a pulsing volcano would benefit from having an upper limit to the cell size. Furthermore, there must be at least two cells in a given segment which gives the following cell size constraint:

$$\Delta_j + \Delta_{j+1} \leq H_j \qquad 3\text{-}13$$

Forcing a cell size limit upon the scheme developed above requires iteration when computing α_{ls}. If the cell size at a segment edge, Δ_j, violates either Eqn. 3-12 or 3-13 for a

given α_{ls}, then the cell size constraints can be satisfied at the current α_{ls} if the length scale for those cells are adjusted appropriately. However, changing the length scales might change the value of α_{ls} as computed in Eqn. 3-10 and therefore the process is iterated until the length scales, and thus α_{ls}, do not change. In practice this convergence seems to be very robust and occurs after less than 3 iterations. The algorithm leaves the adaptation routine (leaving the grid unchanged) if the iteration count exceeds ten, though this never happened in my simulations.

The iteration scheme is performed as follows. An initial value for α_{ls} is computed using the original length scales for the segment edges, L_j. The original length scales are then stored and used in subsequent iterations in conjunction with the cell size constraints (Eqns. 3-12 and 3-13) to compute adjusted length scales, L_j', and a new value of α_{ls} is computed if the values of L_j' (initially set to L_j) change. The iterations continue until the values of L_j' converge and they are then used in place of the original length scales, L_j, to compute the segment parameters (Eqns. 3-7, 3-8, and 3-11). If the constraint given by Eqn. 3-12 is violated (using the original length scale L_j and the current iterations α_{ls}), then L_j' is given by

$$L_j' = \frac{\Delta_{max}}{\alpha_{ls}}, \tag{3-14}$$

and then, if the constraint given by Eqn. 3-13 is violated using the new length scale L_j' and α_{ls}, then L_j' is given by:

$$\begin{aligned} L_j' &= \frac{L_j'}{L_j' + L_{j+1}'}\left(\frac{H_j}{\alpha_{ls}}\right), \\ L_{j+1}' &= \frac{L_{j+1}'}{L_j' + L_{j+1}'}\left(\frac{H_j}{\alpha_{ls}}\right). \end{aligned} \tag{3-15}$$

Since L_j' is dependent on L_{j+1}', if the length scale of segment j ($j > 0$) is changed then the condition must be tested again on the previous segment. Finally, after the new length scales have been adjusted so that they all pass the constraint given by Eqn. 3-13, it is possible that the max cell size constraint (Eqn. 3-12) is violated. To avoid even more complication this case is ignored since the max cell size is merely a user desired constraint, whereas Eqn. 3-13 is required.

3.2.2 Inverting the Grid

In order to find the global radial cell number, i_R, of a simulation particle during the index routine, first the segment that the particle is in is determined by a simple linear search. A binary search could be used; however, since N_{seg} is small it is possible that the simple linear search actually has better performance due to better memory caching. Once the segment that the particle is in has been determined, the radial cell number is then found by summing the number of cells in all the prior segments, N_{cum}, and the segment cell number, i_s. The total number of radial cells up to the current segment, j, is obtained (during the adaptation of the grid) by summing Eqn. 3-11:

$$N_{cum,j} = \sum_{k=0}^{j}(N_k + 1). \tag{3-16}$$

The segment cell number, i_s, is obtained from Eqn. 3-6 using the segment parameters A_j and B_j determined during adaptation. The particle location in the segment, Z, is given by the difference between the particle's absolute radial location above the surface and the cumulative height of the segments, $H_{cum,j}$ (determined during adaptation, see Figure 3-1). If $B_j \neq 0$:

$$i_R = N_{cum,j} + Floor\left(\frac{-(A_j+B_j)+\sqrt{(A_j+B_j)^2-4B_j(A_j-Z)}}{2B_j}\right) + 1, \tag{3-17}$$

and if $B_j = 0$ then the cells in the segment where the particle is located are not linearly stretched, and the radial cell number is then given by

$$i_R = N_{cum,j} + Floor(Z/A_j). \tag{3-18}$$

3.2.3 Performance and Verification of the Invertible Adaptive Grid Routine

As discussed initially, the invertible adaptive grid is desirable for two important reasons: (1) it ensures better simulation accuracy over the entire domain, and (2) it speeds up simulations that require non-linear grids. The grid generation method described above, which uses several linearly stretched grid segments to adaptively fit the grid as best as possible to the local length scale, fulfills the first criterion by design. The speedup obtained is more problem dependent. The method reduces the time required to index the molecules by solving Eqn. 3-17 or Eqn. 3-18 instead of searching through the cells. The speedup, if any, is obviously dependent on the number of cells (and the number of separate linear segments). Additionally, the simulation time is generally dominated by computing the collisions in

collisional flows, so any speedup of the index routine could be masked by increases in the collision rate due to the different grids. Therefore, the speedup is reported here both as the speedup of the individual index routine and of the whole simulation run. For the atmospheric simulations of interest in this dissertation, the most obvious representative speedup test problem is a 1D atmosphere simulation with radial plasma heating (5 ergs cm^{-2} s^{-1}) from above, run at a surface temperature of 90 K (essentially collisionless). The specifics of the radial plasma heating and the sublimation model are found in Austin and Goldstein (2000) and the non-LTE radiative cooling model used is described in Zhang *et al.*, (2003, 2004). These physical models have been used in numerous other atmospheric simulations of Io by our group (Moore *et al.*, 2009, 2010, 2011; Walker *et al.*, 2010a,b, 2011).

The speedup test simulated the formation of a steady state 1D sublimating atmosphere starting from a vacuum and then running for 20,000 seconds until steady state is established. For this speedup test, the domain extended to an altitude of 500 km and 200 radial cells were used. The exponential grid (which indexes by searching through the cells) had a cell size to mean free path ratio of 0.005. For this test case the segmented grid length scales were determined only from the local mean free path which resulted in $\alpha_{ls} = 0.004$ for the segmented grid and therefore the two grids (exponential and invertible segments) were essentially the same. The segmented grid had 5 segments and was not adapted for the speedup test so that the grids remained nearly identical throughout the simulation. A maximum cell size of 10 km was used for both simulations. Even though the profile tool, `gprof`, found that index took a negligible amount of the total run time with the segmented grid compared to ~10% with the exponential grid, very little wall-clock speedup (~1%) of the entire run was observed. However, the main reason for using a segmented grid is not increased computational speed but improved resolution of the high density/large gradient regions of the flow.

The analytical procedure for indexing the molecules into the appropriate cells (Eqn. 3-17) was checked for various numbers of segments by randomly generating several grids (the A_j's and B_j's). A simulation molecule was placed at the top, bottom, and randomly inside each cell and then the index was computed and compared to actual value. The grid adaptation routine (which supplies the A_j's and B_j's) was then verified on various simple static analytic densities: a constant, linear, a step discontinuous, and an exponential density. After the adaptation routine was verified on the analytic densities, a transient collapsing atmosphere

simulation was performed with a constant, uniform, 100 m grid (that resolved the gradients) and the adapting linear segmented grid (Figure 3-2).

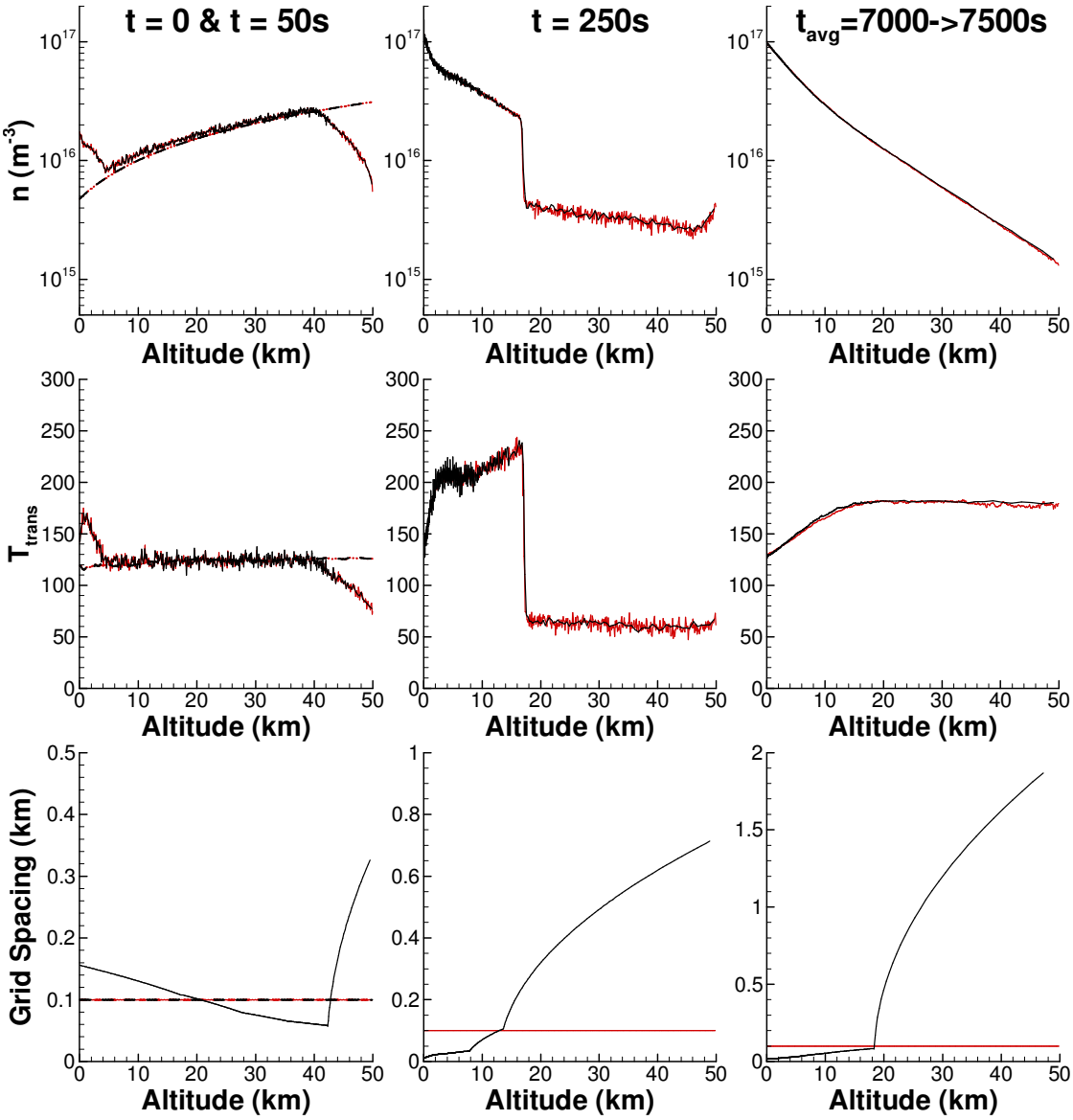

Figure 3-2: 1-D simulation of gas column collapsing under gravity; red lines are for a constant grid size and the black for an adapting, linearly stretched, segmented grid. The adaptive grid was adapted every 50 seconds, except during time averaging. The number density (top), translational temperature (middle), grid spacing (bottom) are shown at 4 different times (note the grid spacing increases linearly from one grid point to the next; this appears as a curved line when plotted versus altitude which is itself a function of the sum of the prior grid spacing). The rightmost flowfield, though it is still not quite in steady state, is time averaged over 500 seconds.

The agreement between the uniform and adaptive segmented grid is seen to be within the noise. In these simulations, the initial temperature was 125 K and the initial density profile increased linearly with altitude

$$n_{init}(z) = n_0\left(1 + \frac{z}{H_s}\right), \tag{3-19}$$

where z is the altitude above the surface, n_0 is the density at the surface, and $H_s=kT_s/mg$ is the scale height of the gas based on the surface temperature, T_s, and mass, m, of the SO_2 gas molecule. The surface temperature was held fixed at 125 K giving a scale height of ~9 km for the gas diffusely reflected off the surface (there was no sublimation), and the simulation domain was set to 50 km altitude. Given that there was no radial plasma flux and no rotational or vibrational radiative cooling, the analytic steady state atmospheric density is that of an isothermal hydrostatic atmosphere with a surface density of 10^{17} m^{-3}.

As seen in Figure 3-2, over time the initial atmosphere collapses due to gravity and a shock forms as material scatters diffusely off the surface. If the surface interaction were specular, then the difference between gravitational potential in the initial and steady state atmospheric columns would lead to a net increase in the gas temperature; however, with the diffuse surface, as time progresses the gas is cooled to the surface temperature. This thermal diffusion takes a long time and is clearly seen in the right-most panel in Figure 3-2. Additionally, the increased temperature above ~10 km results in a larger scale height and slower (nearly) exponential falloff in the density as seen. Ultimately the atmosphere reaches an isothermal steady state with the expected surface density and exponential falloff. Furthermore, while the initial segmented adaptive grid is the same as the uniform grid, it changes a lot during the simulation. Finally, note that the current method to place the segments does not, in general, capture a shock or other sharp (rapidly moving) gradients in the flow even when adapting to the local gradient length scale.[7] However, it does a satisfactory job increasing the resolution in the higher density regions where the mean free path is smallest and we find that this is sufficient for the current work.

[7] This is because the cells resolve the desired length scale at the *top and bottom* of the segments. Therefore, to resolve a shock one should place the segments such that their ends are located where the curvature of the gradient length scale was at a local maximum.

3.3 PHOTO-CHEMISTRY MODEL

Summers and Strobel (1996) showed that photo-chemistry was an important mechanism for production of the minor dayside species (SO, O_2, S, and O) from the sublimated SO_2 gas. While our auroral simulations are modeling observations in eclipse, it will be shown (Chapter 4) that the initial dayside atmosphere will persist into eclipse and therefore it is necessary to properly account for the photo-chemistry of the initial quasi-steady dayside atmosphere before simulating the atmosphere into eclipse. The prior photo-destruction model (Stewart *et al.*, 2011) employed in the planetary DSMC code simply destroyed the simulation particle (H_2O) when it was ionized or dissociated since the focus was on the water retention rate at the lunar poles and did not consider the OH or O dissociation products. Additionally, the previous model assumed the gas was optically thin and thus the photo-reactions occurred at a specified solar flux and hence constant photo-reaction rate. In this case, the probability of a photo-reaction in a timestep, Δt, for each particle of species type i in sunlight is given by

$$P_{react,i} = 1 - exp\left(-\sum_j^{N_i} k_{react,i,j}\,\Delta t\right), \tag{3-20}$$

where $k_{react,j}$ is the reaction rate coefficient (s^{-1}) of the j^{th} reaction, and N_i is the number of different photo-reactions. A photo-reaction is determined to occur if a random number is less than $P_{react,i}$. If a photo-reaction occurs, then another random number is drawn and the reaction type is determined by sequential comparison of the random number to

$$P_{react,i,j} = \sum_k^j k_{react,i,k} \Big/ \sum_k^{N_i} k_{react,i,k}, \tag{3-21}$$

where the reaction type, j, is the first reaction for which the random number is less than $P_{react,i,j}$.

For the current work, the photo-chemistry model still assumes the gas to be optically thin, but now when a photo-dissociation or photo-ionization event occurs, the simulation particle is broken into the appropriate products for the specific photo-reaction and the total number of simulation particles is increased. Furthermore, reflected light from the surface is not included in the model; generally the photo-reaction cross sections are small at the longer wavelengths (>4000 Å) where the surface reflectance of Io is significant (see Figure 5-13). If the initial simulation particle is a molecule, then any internal energy of that molecule is assumed to go into the relative translational motion of the products and any molecular products are assumed to have no internal energy upon creation. Furthermore, the current

model assumes that the products can simply be given an additional mean excess energy upon dissociation or ionization as given by Huebner (1992) instead of determining the excess energy by drawing from the rate coefficient distribution relative to photon wavelength (energy). Furthermore, all of the excess energy is put into the relative translational motion of the products, and the resultant relative velocity is oriented isotropically. Below the exobase, this excess energy is collisionally equilibrated and therefore using the mean excess energy should be acceptable. The mean excess energy is ~1 eV for each photo-dissociation event (and ~10× higher for photo-ionization) and is sufficient to heat the atmospheric column appreciably above the temperature of the surface and cause atmospheric escape. However, above the exobase the use of a mean excess energy could result in an incorrect escape rate if the rate coefficient does not peak near the excess energy. While the SO_2 rate coefficient does peak near the mean excess energy, it also has several small peaks at lower wavelengths. Also, the ionization rate coefficient distribution is nearly uniform with photon wavelength up to the ionization energy and so using a mean excess energy is questionable. Future models should consider drawing the excess energy for each photo-chemistry event from the rate distribution with energy.

Table 3-1: Summary of included photo-reactions assuming a Sun-Jupiter distance of 5.2 AU.

Reaction	Rate Coefficient† (s^{-1})	Rate Coefficient‡ (s^{-1})	Excess Energy (eV)
$SO_2 + h\nu \rightarrow SO + O$	1.0×10^{-5}	5.9×10^{-6}	0.44
$SO_2 + h\nu \rightarrow O_2 + S$	6.3×10^{-7}	1.9×10^{-6}	0.75
$SO_2 + h\nu \rightarrow SO_2^+ + e^-$	4.2×10^{-8}	3.9×10^{-8}	12.0
$SO + h\nu \rightarrow S + O$	1.8×10^{-5}	2.3×10^{-5}	0.62
$SO + h\nu \rightarrow SO^+ + e^-$	1.8×10^{-8}	3.2×10^{-8}	8.62
$O_2 + h\nu \rightarrow 2O$	9.4×10^{-8}	1.6×10^{-8}	1.48
$O_2 + h\nu \rightarrow O_2^+ + e^-$	1.8×10^{-8}	1.7×10^{-8}	19.30
$S + h\nu \rightarrow S^+ + e^-$	7.6×10^{-9}	4.0×10^{-8}	6.30
$O + h\nu \rightarrow O^+ + e^-$	7.6×10^{-9}	7.8×10^{-9}	21.60

†Rate coefficients from Strobel and Strobel (1996). ‡Rate coefficients from Huebner (1992).

Table 3-1 shows the included photo-reactions and the associated rates and excess energies. Two different rates are given for comparison, those compiled and used in Summers and Strobel (1996) and subsequent works on Io's atmosphere (Smyth and Wong, 2000; Moses *et al.*, 2002) and those reported in Huebner *et al.* (1992) assuming a quite Sun and a

Sun-Jupiter distance of 5.2 AU (note that the 1 AU rates are input and scaled by the square of the inverse Sun-Jupiter distance in AU). In the current implementation the electronic state of the DSMC simulation particle is not tracked; therefore, the photo-reaction rates given are from the ground state to all (given) excited states of the products. The rates given by each reference are within a factor of 2 of each other; the largest (and most important) difference is in the SO_2 photo-dissociation rates. These differences mean that a steady hydrostatic sublimation atmosphere with Huebner *et al.*'s (1992) rate data will have more SO_2 and O_2 and less SO than the same atmosphere modeled using Summers and Strobel's (1996) reaction dataset. While having more O_2 might significantly alter the atmospheric dynamics shortly after eclipse (Chapter 4), it is beyond the scope of this work to determine the better dataset. Therefore, to remain self-consistent with the tabulated excess energies, the rate data from Huebner (1992) is used in the final atmospheric simulations assuming Jupiter is 5.2 AU from the Sun (Chapter 8).

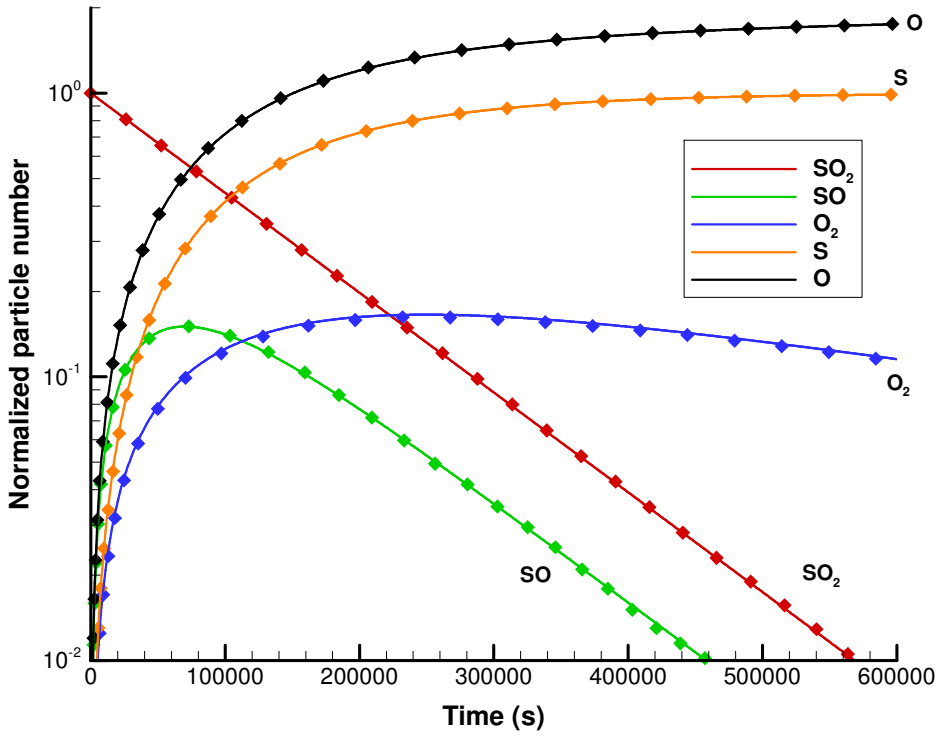

Figure 3-3: Photo-dissociation "0-D box" test case. Initially there is only SO_2 gas present which is then allowed to photo-dissociate into products. Lines are the analytic solution and the diamonds are from the DSMC simulation which used a 1 second timestep.

In order to verify that the photo-chemistry model implemented in the DSMC code, a simple 0-D test case was run in which the simulation particles were fixed in space (though they were allowed to collide with each other). Initially, all of the ~10^5 simulation particles were SO_2. The photo-dissociation reactions given in Table 3-1 then proceeded to break apart the SO_2 into SO, O_2, O, and S. Furthermore, for this test case the O_2 photo-dissociation rate was increased by a factor of 10 (to 1.6×10^{-6}) so that the decrease in the O_2 density due to photo-dissociation would be visible on the same timescale as the decrease in SO_2 and SO densities. Additionally, during this test case it was verified that the two newly created simulation particles conserved mass, momentum, and energy (accounting for the added excess energy) within machine precision over millions of photo-reactions. Figure 3-3 shows the normalized particle count (by the initial particle count) from the DSMC simulation compared with the analytic solution obtained by solving the simple system of rate equations. Note that the total particle count will increase with time since one SO_2 will ultimately become 3 atomic simulation particles. Excellent agreement is obtained with the analytic solution; slight deviations from it are presumably due to noise.

3.4 PLASMA MODEL

As previously discussed (Chapter 2.2), Jupiter's magnetic field sweeps a thermal plasma torus of predominantly O^+ and S^+ ions past Io at ~57 km/s. The plasma, confined to move along the rotating Jovian magnetic field lines, interacts with Io's atmosphere as it sweeps past the satellite, ionizing, dissociating and heating the neutrals in Io's atmosphere via collisions. Above the exobase, fast neutrals and ions created by the plasma interaction can escape Io and resupply the torus. Furthermore, after collisions with Io's atmosphere, the plasma particles are re-accelerated by the field lines so that further energetic interactions may occur. It is this interaction, along with photo-chemistry that produces the majority of SO_2 daughter products (SO, O_2, S, and O) in Io's atmosphere.[8]

[8] S_2 is believed to be produced mainly in Pele-type plumes, Na and Cl are produced by surface sputtering.

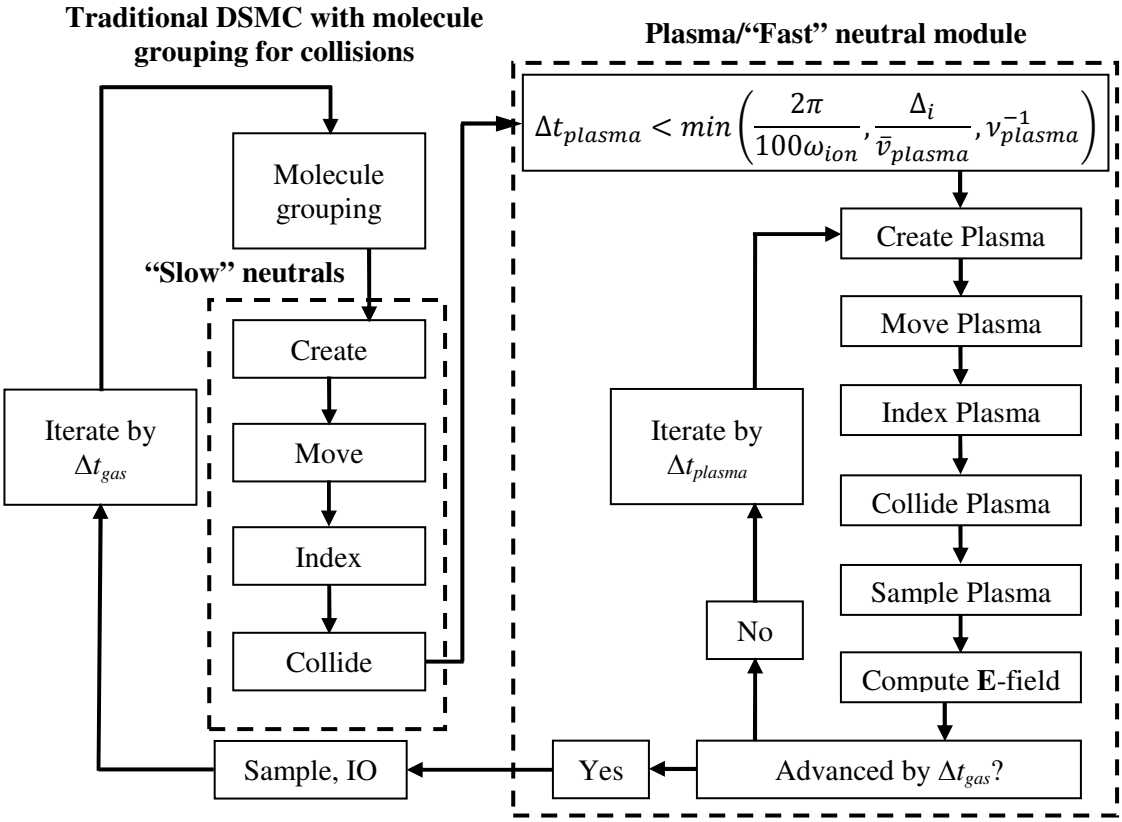

Figure 3-4: Flowchart of the DSMC method with a plasma/"fast" neutral sub-timestep routine. Note that for clarity only the plasma timescales are shown in sub-timestep routine.

In order to have a more accurate model of Io's atmosphere for simulation of the aurora, the interaction of thermal torus ions and electrons with Io's neutral atmosphere is simulated in the planetary DSMC code. However, due to the large differences in timescales (see 3.4.1) it was necessary to substep the plasma interaction within the overall DSMC code. This allowed for the gas to be simulated at the larger gas timestep and then, holding the gas fixed, simulate the plasma interaction with the standard DSMC routine at a much smaller timestep. Figure 3-4 shows a flowchart of the current implementation with the plasma substep routine performed after the neutral gas has moved and collided during the current timestep. After the (slow) neutral gas collisions have been performed, the DSMC code calls the substep routine which performs the standard DSMC routine (create, move, index, collide) and also computes the **E**-field on a timestep that is smaller than the neutral gas timestep. In order for the neutrals and plasma to end the global timestep at the same time, the plasma timestep is chosen such that performing an integer number of the plasma substeps results in Δt_{gas} time

elapsing. The criterion used for determining the plasma timestep is shown in Figure 3-4. Ideally, the timestep should be less than three conditions for the current model which are based on the ion gyrofrequency (the factor of 100 is due to the time integration method, see Chapter 3.4.1), the distance traveled by a typical ion should be less than the cell size (currently this is violated near the surface due to fast ions and very small cells), and finally the collision rate of the plasma with the neutral gas (ν_{plasma}^{-1}).

Note that even though the plasma timestep is much smaller than the neutral timestep the neutral gas and plasma routines take roughly the same amount of computational time since the plasma density is several orders of magnitude less than the neutral gas density (except above the exobase). In addition to the plasma substepping, fast neutrals produced by collisions with the charged particles (typically due to charge exchange) are grouped into the "plasma" molecule structure and are simulated on the "plasma" timestep. This allows for better computational efficiency since it prevents very large $(\sigma_{Tot}V_{rel})_{max}$ from occurring during the neutral-neutral collide step, and allows for the use of our collision limiter scheme (Stewart, 2010) for the slow neutral–neutral collisions which do not chemically react.

3.4.1 Charged Particle Motion

During the plasma substep routine, the heavy charged particles are moved each plasma timestep accounting for gravity and the Lorentz force

$$\vec{a} = \frac{d^2\vec{x}}{dt^2} = -g\left(\frac{R_{Io}}{r}\right)^2 \hat{e_r} + \frac{eZ}{m}\left(\vec{E} + \vec{v} \times \vec{B}\right), \qquad 3\text{-}22$$

where g is the gravitational acceleration at the surface, R_{Io} is Io's radius, r is the radial position of the particle, $\hat{e_r}$ is the radial unit vector, eZ is the charge of the particle, m is the mass of the particle, $\vec{v}$ is the particle velocity and $\vec{E}$ and $\vec{B}$ are the local electric and magnetic fields respectively. Note that both the gravitational force and the electric field will cause the charged particles to drift in the $\vec{g} \times \vec{B}$ and $\vec{E} \times \vec{B}$ directions. While the ion velocities are accelerated by the Lorentz force (Eqn. 3-22), the electron velocity components (used for collisions) in the DSMC simulation are currently not accelerated during the move step. With the current time integration scheme and timestep size, if the electrons are allowed to accelerate over the plasma (ion) timestep, they achieve unrealistically large velocities. This can be fixed in future simulations by implementing a substep electron timestep to compute the new electron velocity during the move routine or by using a better time integration

scheme for charged particle motion in magnetic and electric fields (e.g. Birdsall and Langdon, 2005).

Solution of Eqn. 3-22 for a charged particle in a uniform, constant magnetic field results in gyration around the magnetic field with a gyration frequency, ω, of

$$\omega = \frac{|eZ||\vec{B}|}{m}, \tag{3-23}$$

where $|\vec{B}|$ is the strength of the local magnetic field. If one desires to resolve the motion of the charged particles, then the period of gyration must be temporally resolved. Near Io, the strongest magnetic field is <2500 nT and therefore, for a singly ionized oxygen atom the gyration period to resolve is ~0.4 seconds; for an electron the gyration period is ~10^{-5} seconds. The Larmor radius, or gyroradius, r_L, of the charged particles is given by

$$r_L = \frac{mv_\perp}{|eZ||\vec{B}|}, \tag{3-24}$$

where $v_\perp$ is the speed of the particle perpendicular to the magnetic field. Resolution of the particle gyro-motion may not be important if the Larmor radius is much smaller than the atmospheric length scales of interest. This is the case for the electron Larmor radius which is ~7 m for a typical 5 eV electron and the minimum magnetic field expected (~1200 nT). This is roughly equal to the mean free path near the surface at the subsolar point (115 K; ~5 m), but much smaller than the atmospheric scale height (>10 km). Everywhere else the Larmor radius will be smaller, and the mean free path bigger, therefore, resolution of the electron gyro-motion should not be critical. This is fortuitous since timestep resolution of the electron gyration period is currently not feasible for typical atmospheric simulations which require several hours to fully develop neutral gas flows and to reach steady state.

Currently the predictor-corrector method is utilized to move all particles. For simple orbital motion due to gravity this has previously been shown to yield stable orbits for "large" timesteps (~1/75th of the orbital period; Stewart, 2010). For gyro-motion about the magnetic field, the predictor corrector method was found to yield unstable orbits, likely because the Lorentz force depends on the velocity, not position, of the particle which is O(dt) accurate. However, for a reasonable timestep size (1/100th of the gyro-period) the orbit was found to increase by ~1.75% over 100 orbits. Since a typical ion will either collide with a neutral or travel across much of the domain in this time (57 km/s × ~41 s = 2400 km), the small increase in the Larmor radius was deemed acceptable. Future simulations should investigate different numerical integration schemes if a stable Larmor radius is deemed necessary.

While resolution of the exact electron trajectory is not necessary, the electrons must obviously still be moved in space. Therefore, in the current DSMC implementation, the electrons are assumed to move with a given ion (Bird, 1985) for computational ease. A plasma is quasi-neutral over length scales larger than several Debye lengths, λ_D, given by

$$\lambda_D = \left(\frac{\epsilon_0 k T_e}{n_e e^2}\right)^{0.5}. \quad 3\text{-}25$$

Here ϵ_0 is the permittivity of free space, T_e is the electron temperature, n_e is the electron number density, and e is the elementary charge. For the plasma conditions at Io, with number densities from 10^9 m^{-3} (free stream) to 10^{11} m^{-3} (near surface) and electron temperatures less than 5 eV, the Debye length varies from ~0.02 m (near surface) to 0.5 m (free stream). Therefore, the Debye length is everywhere much smaller than the DSMC simulation cell size linked to the mean free path and neutral gas gradients. While this justifies forcing the electrons to move with the ions in order to preserve quasi-neutrality, it also means our simulation cannot resolve plasma gradients on the Debye length scale in which quasi-neutrality does not hold. This occurs, for example, in surface sheaths.

When forcing the electrons to move with the ions, the production of an ambipolar electric field due to the electron's higher mobility must be approximated in some way or the effect that the electrons would have on the ion motion through the Coulomb force would not be included. In the current implementation the ambipolar electric field is computed using the Boltzmann relation for electrons, derived from the continuum ion and electron momentum equations, and noting that the mobility of electrons results in near infinite heat conductivity (Chen, 1984)

$$n_e = n_{e,0} exp(e\phi/kT_e). \quad 3\text{-}26$$

Here $n_{e,0}$ is an initial electron density and ϕ is the electric potential ($\vec{E} = -\nabla\phi$). Tonks and Langmuir (1929) use Eqn. 3-26 in their analysis of arc plasmas. Bird (1986) applied what he termed the "Langmuir–Tonks equation" to compute the ambipolar electric field in a ionized shock

$$\vec{E}_{ambi} = -\frac{kT_e}{e}\nabla ln(n_e), \quad 3\text{-}27$$

where $\vec{E}_{ambi}$ is the ambipolar field. Equation 3-27 follows from Eqn. 3-26 assuming that the gradient of the electron temperature is negligible which is consistent with very high electron thermal conductivity. This was necessary from a simulation standpoint since gradients of the temperature would be even noisier than the gradient of the electron density and therefore

more likely to lead to spurious electric fields. In general it was necessary to first smooth the electron density using nearest neighbor cells, then, average the $\vec{E}_{ambi}$ from Eqn. 3-27 with the previous value of $\vec{E}_{ambi}$, and finally repeat the smoothing procedure on the new averaged value for $\vec{E}_{ambi}$. The ambipolar electric field is superimposed onto the precomputed (externally applied) electric field obtained by MHD simulations.

An alternate method which lets the electrons move independently of the ions but forces quasi-neutrality with an imposed electric field computed from the difference in the ion and electron flux (Carlson and Hassan, 1992) might be tried in the future. However, since the ion density is much smaller than the neutral gas density, noise in the ion fluxes, which would translate into noise in the electric field, is expected to be too high to give a meaningful electric field using this method. Therefore, the current implementation moves the electrons with the ions and uses the Langmuir-Tonks equation with the assumption that the electron temperature is nearly constant across adjacent DSMC cells and that the plasma can be adequately described by the continuum and momentum equations.

A 1D hydrostatic plasma atmosphere is a simple, relevant verification test for the ambipolar field that demonstrates the importance of its inclusion for an atmospheric simulation with gravity. The equations of drift motion for the charged particles in a steady isothermal plasma atmosphere can be shown (Chapter 1.4 in Booker, 1984) to simplify to

$$\begin{aligned} n_e q_e E_z - n_e m_e g - kT_e \, {dn_e}/{dz} = 0; \\ n_e q_i E_z - n_e m_i g - kT_i \, {dn_e}/{dz} = 0. \end{aligned} \qquad 3\text{-}28$$

Here z is the altitude, and the ion and electron densities have been set equal to one another (quasi-neutral) but their temperatures are allowed to differ. Adding the two equations and assuming singly ionized ions ($q_e = -q_i$), one obtains the standard hydrostatic atmosphere relation for the electron density as a function of altitude

$$n_e = n_e(z=0) exp\left(-\frac{z}{H_{ie}}\right); \quad H_{ie} = \frac{k(T_e+T_i)}{(m_e+m_i)g}, \qquad 3\text{-}29$$

where H_{ie} is the scale height of the plasma. While the density of the electrons (and ions) decreases with altitude, they do so at a slower rate than an atmosphere of neutral gas with the same mass as the ion. For the test simulation the ion and electron temperatures are equal and $m_i \gg m_e$; therefore the plasma scale height simplifies to $H_{ie} \cong 2kT/m_i g$, double the scale height of a similar neutral gas. This occurs because the light electrons would have a large

scale height in the absence of the ions. However, because there are ions present, the electrons are pulled down by the heavy ions and the ions are themselves levitated through the Coulomb force; this maintains quasi-neutrality. The electric field can be determined by inserting Eqn. 3-29 into Eqn. 3-28 and noting that substituting Eqn. 3-29 into the Langmuir-Tonks equation (Eqn. 3-27) results in $E_{ambi} = E_z$:

$$E_z \cong \frac{m_i g}{e} \frac{T_e}{(T_i + T_e)}. \qquad 3\text{-}30$$

For $T_e = T_i$, the positive polarization electric field exerts a force equal to half the gravitational force resulting in a plasma scale height that is twice as large as the scale height for a similar neutral gas.

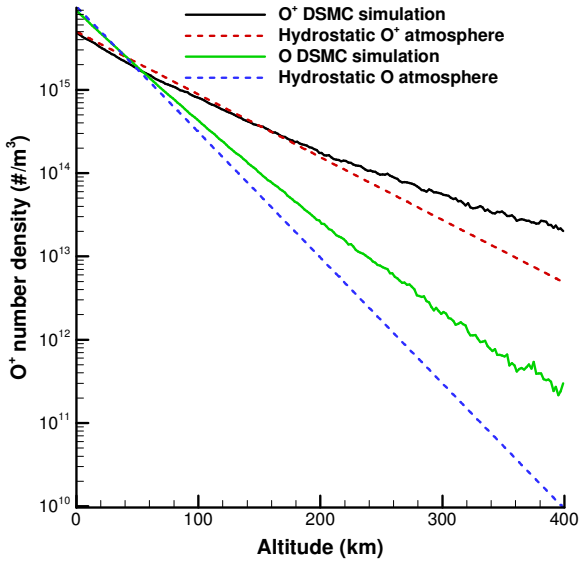

Figure 3-5: Density and ambipolar electric field for a 1D hydrostatic plasma atmosphere. Also shown are the analytic density profiles with (red) and without (blue) accounting for the ambipolar field but neglecting the variation of the gravitational acceleration with altitude that is included in the DSMC simulation.

Figure 3-5 shows the DSMC simulation results for 1D hydrostatic O and O^+ ion atmospheres. For each simulation, the simulation particles (O or O^+ ions and electrons) were initially distributed with a hydrostatic neutral gas density profile (scale height equal to kT/mg) and a gas temperature of 100 K. The atmosphere was then allowed to relax to steady state as the electric field was computed from Eqn. 3-27 every 10,000 timesteps. In this instance, the plasma timestep is equal to the "slow" gas timestep since the plasma is at 100 K.

As seen in Figure 3-5, the steady state simulation density profile agrees very well with the analytic density profile up to about 200 km altitude. The two results diverge at high altitude because the analytic result is based on constant g and does not account for its decrease as the altitude increases. Similiarly, the neutral oxygen simulation curve diverges around ~100 km altitude with the density profile decreasing less with altitude than the analytic due to the increasing scale height. If gravity is held constant, then the DSMC results agree very well with the analytic curves. Without the ambipolar field, the O^+ density profile's scale height remains equal to kT/mg and follows the neutral oxygen density profile in Figure 3-5.

3.4.2 Electric and Magnetic Fields

The current implementation uses a 3D magnetic field, $\vec{B}$, and bulk plasma velocity, $\vec{v}_{plasma}$, precomputed using a steady state multiscale MHD simulation (Combi, 1998). The (co-rotational) electric field is computed (at the start of the simulation) by taking the cross product of the plasma bulk velocity and the magnetic field and the fields are interpolated onto the DSMC grid. As mentioned previously, the electrons are moved with the ions and therefore the total electric field, $\vec{E}$, that effects the charged particles in Eqn. 3-22 is

$$\vec{E} = \vec{E}_{ambi} - \vec{v}_{plasma} \times \vec{B}. \qquad 3\text{-}31$$

A slice of the 3D interpolated background magnetic and electric field used in the atmospheric simulations (Chapter 8) is shown in Figure 3-6 on the actual simulation grid (Chapter 8) with the processor edges shown to clarify the spatial extent of the slices. While the free-molecular buffer cell extends out to one Io radius, the actual grid over which the particles can collide only extends to an altitude of 800 km. Unfortunately, this is not far enough for the magnetic field to reach it's unperturbed value on the upstream side of Io, and the field is still varying at the top of the simulation domain upstream. Future work should investigate the effect this has on the overall atmospheric dynamics. Additionally, one can see in Figure 3-6 that the plasma corotational speed slows down across Io's poles and speeds up slightly along the equator. The plasma flux at the top (radial) boundary is determined by computing the $\vec{E} \times \vec{B}$ velocity normal to the surface and accounting for the ion temperature in order to generate a Maxwellian inflow with an acceptance-rejection procedure (Garcia and Wagner, 2006).

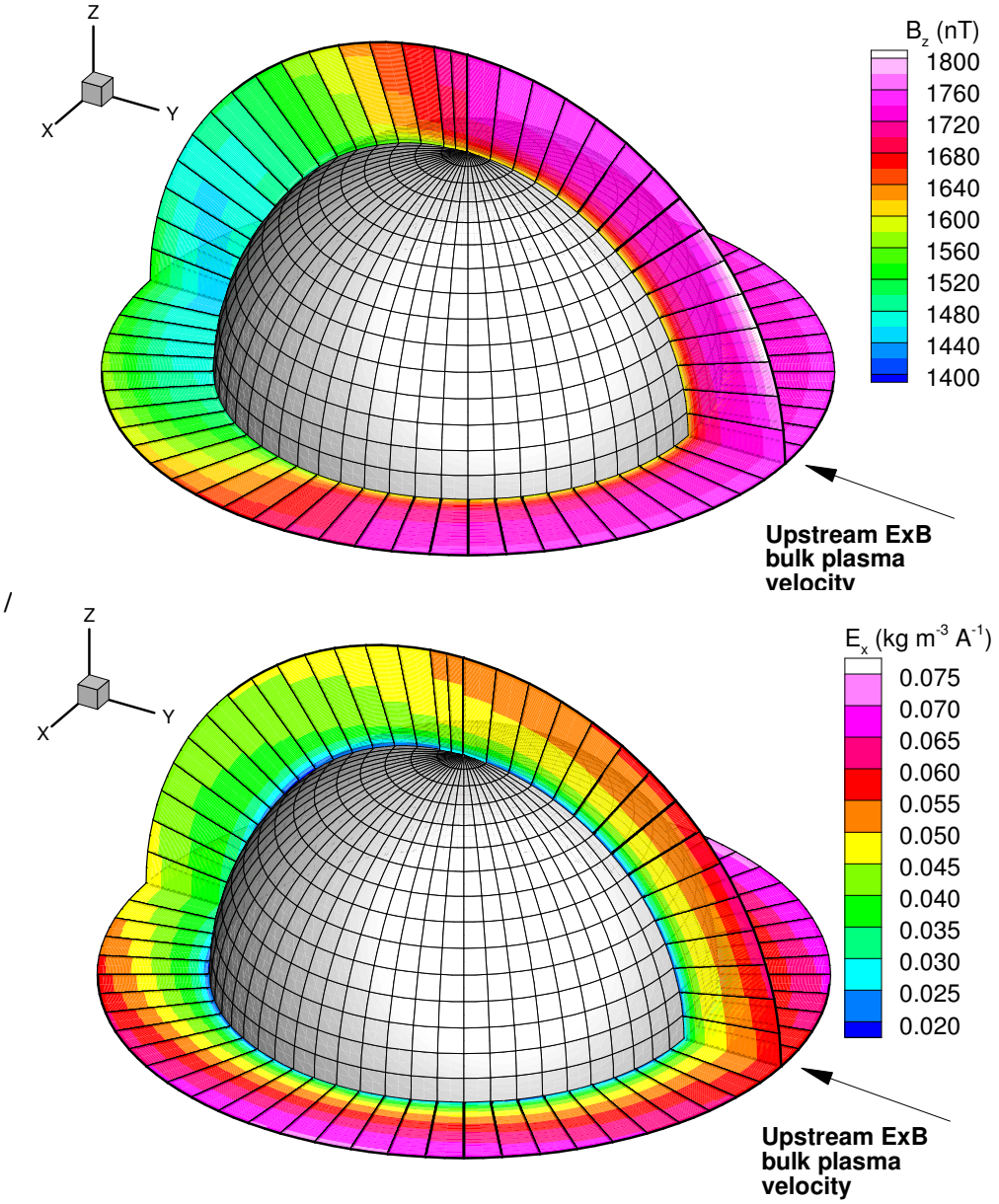

Figure 3-6: Interpolated magnetic (top) and electric ($-\vec{v}_{plasma} \times \vec{B}$; bottom) fields across the north pole and Io's equator from the sub-plasma to anti-plasma point (nearly perpendicular to the sub-solar-anti-solar points).

While the use of precomputed fields means that the fields are not self-consistent with the gas dynamics, it gives Io's perturbation of the Jovian field to first order and dramatically reduces the computational cost of the simulation. Because of the field's sensitivity to charged particle noise (e.g. a particle crossing into a cell is a current which creates a magnetic field)

when solving Maxwell's equations, a self-consistent simulation would most likely require a particle weighting scheme or implementation of a Particle-In-Cell (PIC) code (Birdsall and Langdon, 2005) to determine the fields.

3.5 ELECTRON-HEAVY INTERACTION MODEL

As mentioned earlier, the electrons move with the ions but collide independently with the heavy neutral particles in the flow. Electron-ion collisions are currently neglected, mainly due to lack of meaningful statistics in a given collision cell. However, neglecting charged particle collisions with other charged particles is a reasonable simplification since the neutral gas density >> plasma density and the gas is in the weakly ionized limit in much of the simulation domain (below the exobase). Elastic, ionization, attachment and excitation electron-neutral (atomic or molecular) interactions were considered through the use of collision energy dependent cross sections for each species. For the cross sections, when a reference did not specify an equation to use, piecewise polynomial curve fits were used to fit the cross section data. While the polynomial curve fits themselves have no physical basis, they generally provide excellent numerical approximations to the data; this is all a DSMC implementation requires. To avoid the expense of computing the energy-dependent interaction cross sections and total interaction cross sections for each electron every timestep, we pre-compute the cross sections for a set of several thousand electron impact energies with a fine energy step (ΔE = 0.02eV) and tabulate the values.

The major collision processes for electron–SO_2 collisions are included in the model and are given in Table 3-2. Note that vibrational and rotational electron excitation of SO_2 (or SO and O_2) is not included in the model due to lack of data. The cross sections for rotational excitation are small and, except near resonance energies, so are the vibrational excitation cross sections. Therefore, the electron energy loss due to rotational and vibrational excitation should be small and have little effect on the electron temperature (and electron induced chemistry and excitation). In the future these should be included since the O^+–SO_2 dissociation cross section (computed by MD/QCT) has been found to depend fairly strongly on the initial internal energy of the SO_2 (see Figure 3-10, Chapter 3.6). Furthermore, while the strong multiplets in EUV and FUV are included, most of the EUV and FUV SO_2-electron impact dissociative-excitation cross sections (e.g. OI (1040 Å, 1027 Å, etc.) or SII (998 Å, etc.)) are not included because their cross sections were small (~10^{-19} cm^2) and the threshold

energies were large (>30 eV). In addition, the model does not include SO_2 dissociation into un-ionized ground state products because detailed cross section data were unavailable. However, note that SO_2 dissociation into $SO(\tilde{A}^3\Pi)$ and $O(^3P)$ (resulting in the MUV1 spectral feature) as well as into excited OI, OII, SI, and SII is included (see Table 3). Bhardwaj and Michael (1999b) found that if SO_2 has a similar ratio of dissociation to excitation cross section as O_2, N_2, or H_2O, then the SO_2 dissociation cross section was only ~3% of the total cross section. Hence the effect of dissociation of SO_2 into ground-state products should be relatively minor and can be neglected.

Table 3-2: Electron-SO_2 collision processes for neutrals initially in the ground state. Emission wavelength(s) (in Å) are indicated in parenthesis.

Collision Process	**Reaction Products, excluding e^-**	**Reference**
SO_2 elastic	SO_2	1
MUV1	$SO(\tilde{A}^3\Pi)$ + $O(^3P)$ (2385-2670)	2
MUV2	$SO_2(\tilde{A}^1A_2)$; $SO_2(\tilde{B}^1B_1)$ (2670-6000)	2
SO_2 electronic excitation	$\tilde{C}$+$\tilde{D}$; $\tilde{E}$+$\tilde{F}$; $\tilde{G}$+$\tilde{I}$; $\tilde{H}$	1
SO_2 ionization	SO_2^+	1
SO_2 dissociative ionization	SO^+; O^+; O_2^+; S^+	1
SO_2 dissociative attachment	SO^-; O^-; S^-	1
SO_2 dissociative excitation	OI (1304); OI (989); SI (1479); SI (1900); OII (834); SII (911); SII (1204)	1

[1]Bhardwaj and Michael (1999b); [2]Ajello *et al.* (2002)

While SO_2 is the dominant dayside species, electron interactions with the other minor dayside species (S_2, O_2, SO, O, and S) must also be accounted for in the model. Table 3-3 shows the electron–neutral collision processes for the minor species that are included in the model. Since S_2, O_2, and SO are relatively minor constituents, we neglect the electron energy degradation due to inelastic collisions with these minor molecular species except for S_2 excitation to the B $^3\Sigma_u^-$ state which, upon transition to the X $^3\Sigma_u^-$ ground state, results in

intense band emission in the SO_2 MUV 2 wavelength range from 2800–6400 Å (Peterson *et al*., 1980). Unfortunately there is little experimental data on electron-S_2 excitation; to my knowledge, there are no measured excitation cross sections to date. However, there has been theoretical work on electron-S_2 interaction cross sections by Garrett *et al.* (1985) and Tashiro (2008). Garrett *et al.* used the impact parameter method to calculate integral electron impact cross sections for electronic excitation and dissociation of S_2. It is hoped that the intense emission due to S_2, which has been observed in Pele's plume (Spencer *et al.*, 2000) and several other locations on Io (Jessup *et al.*, 2007), might allow for Io's plume activity to be constrained with UV-Vis spectra (Chapter 7) since the theoretical S_2 excitation cross section is ~20 times larger than the SO_2 MUV 2 cross section at typical torus electron energies.

Table 3-3: Electron collision processes with the minor species initially in the ground state. Emission wavelength(s) (in Å) are indicated in parenthesis.

Collision Process	**Reaction Products, excluding e^-**	**Reference**
$O_2^{\dagger}$	O_2	3
$SO^{\dagger}$	SO	4
S_2	S_2	6
S_2	S_2 B $^3\Sigma_u^-$	6,7
O elastic	O	5
O electronic	$2p^4$ ^{1}D (6300, 6364, 6392)	5
	$2p^4$ ^{1}S (2958, 2972, 5577)	5
	3s $^3S_0$ (1304)	5
	3p ^{3}P (1128)	5
	3d $^3D_0$ (1027)	5
	4p ^{3}P (1003)	5
	3s' $^3D_0$ (989)	5
	3s'' $^3P_0$ (878)	5
O ionization	O^+	5

[3]Szmytkowski *et al.*(1996); [4]Joshipura and Gangopadhyay (2008); [5]Itikawa and Ichimura (1990); [6]Tashiro (2008); [7]Garrett *et al.* (1985); [†]Treated total scattering cross section as elastic

The elastic electron-neutral interactions for the trace species are still important (especially for the Monte Carlo electron transport simulations) since they randomize the electron trajectories (up or down along the field lines) and can trap electrons in the wake region or allow them to penetrate deeper into the higher magnetic field upstream of Io. Due to

the importance of scattering, electron-O_2 and electron-SO elastic collisions are included via their reported total scattering cross sections. Many atomic oxygen electronic excitation cross sections are included in order to model various observed emission lines, but many others are neglected because their cross sections were small (~10^{-18} cm^2) and their threshold energies relatively high (~20 eV). Due to the lack of available SO_2 and SO cross sections for direct creation of [OI] 6300 Å emission by electron impact dissociation, we consider only electron impact excitation of atomic oxygen as the source for 6300 Å emission. Thus, our resulting emission (see Chapter 5) should be considered a lower bound since Oliversen *et al*. (2001) reported that the [OI] emission line width implied that a non-trivial amount of the emission was produced via electron impact dissociation. Furthermore, Retherford (2002) argued that emission from O, SO_2, and SO may be comparable; therefore, it is not unreasonable to expect that our total simulated emission might be as low as 1/3 of the observed value.

Many of the included electron impact cross sections for SO_2 and the minor gas species are shown in Figure 3-7 as functions of energy. It can be seen that degradation of high-energy electrons occurs mainly via ionization of SO_2 which has the largest inelastic cross section above ~30 eV. Ionization events produce lower energy secondary electrons that are tracked by the model leading to an energy cascade from the high-energy electrons to low-energy secondary electrons which then tend to scatter off the atmosphere through elastic collisions and/or undergo attachment or excitation reactions.

The number of electron-neutral collisions is computed using the standard NTC method (Bird, 1994). As discussed previously, the NTC method utilizes a $(\sigma_{Tot}V_{rel})_{max}$ to compute the number of collision pair selections. The electron–neutral collision pair is then accepted if the random number, $R_{\#}$, satisfies

$$R_{\#} < \left(\sigma_{Tot}^{j}V_{rel}\right)/(\sigma_{Tot}V_{rel})_{max}. \quad 3\text{-}32$$

The total cross section used to accept collision pairs is simply the sum of all the electron reactions with species *j* included in the model:

$$\sigma_{Tot}^{j}(E_{rel}) = \sum_{i}^{N_j}\sigma_{i}^{j}(E_{rel}), \quad 3\text{-}33$$

where N_j is the number of included electron reactions with species *j*. The reaction type is then selected by looping until another random number is less than the i^{th} cumulative reaction cross section normalized by the total cross section:

$$R_{\#} < P_{i}^{j}(E_{rel}) = \frac{\sum_{k}^{i}\sigma_{k}^{j}}{\sigma_{Tot}^{j}}. \quad 3\text{-}34$$

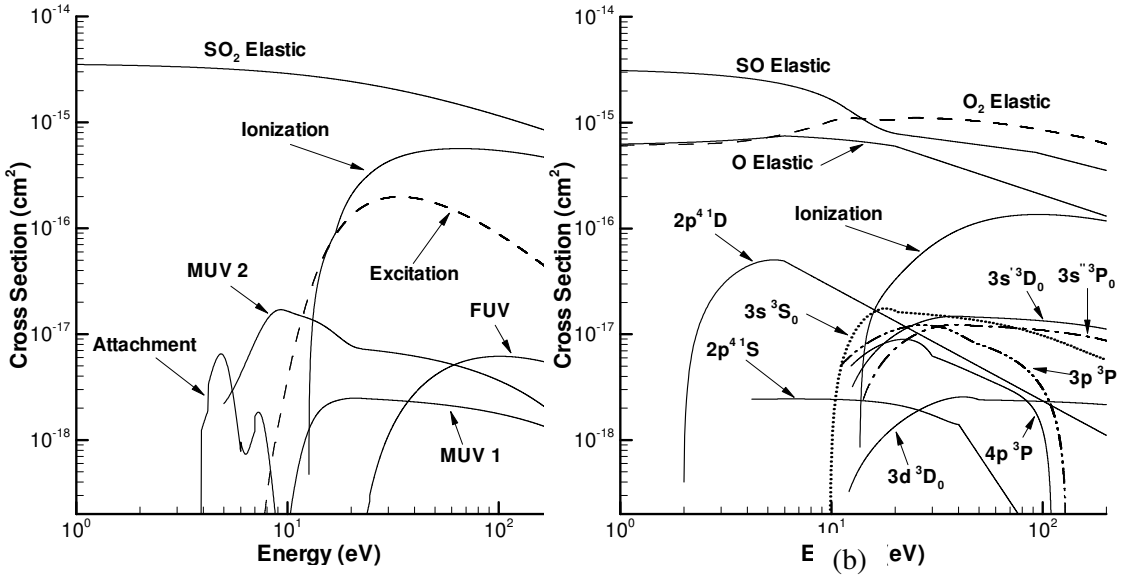

Figure 3-7: The cross sections of all inelastic and elastic processes considered for (a) the dominant species, SO_2 (Table 3-2) and (b) the minor species O, SO, and O_2 (Table 3-3). In (a) the ionization cross section is obtained by summing the cross section for production of SO_2^+, SO^+, S^+, O^+, O_2^+ and the excitation cross section is obtained by summing dissociative excitation to OI(1304 Å, 989 Å), SI(1479 Å, 1900 Å), OII(834 Å), and SII(911 Å, 1204 Å). In (b) the excitation cross sections ($2p^4\ ^1D$, etc.) are for O and the ionization cross section is for the production of O^+ from O atoms.

Since there are ~30 electron reaction cross sections for a given neutral species and polynomial curve fits are used to compute the reaction cross sections, the total cross section for a neutral species, *j*, (Eqn. 3-33) and reaction probability for reaction *i*, (Eqn. 3-34) are precomputed versus relative kinetic energy, E_{rel}. This saves computational cost while still computing the cross sections to within the accuracy of the curve fits (and the data itself).

After the collision the electron energy is changed appropriately and the velocity vector direction (pitch angle) is randomized, resulting in a new helical angle and magnetic moment. The electron is left on the same field line because the gyration radius is small compared to the spatial gradients in the magnetic field. In general, it is necessary to have the differential scattering cross section, $\frac{d\sigma}{d\Omega}$, for each collision process in order to pick the electron post-collision velocity properly; however, at low energies (less than 1 eV) the scattering is approximately isotropic. Since the penetration depth of the electrons into the atmosphere is sensitive to the differential cross section, it was important to correctly model the scattering angle distribution of the dominant collision process: elastic electron-SO_2 collisions. In the

current model Gulley and Buckman's (1994) measured differential scattering cross section data at various electron energies for elastic electron-SO_2 collisions is used. Figure 3-8 shows the differential scattering cross section data from Gulley and Buckman (1994) for 5 eV incident electrons on SO_2. Even at the relatively low energy of 5 eV there is a strong bias towards forward scattering and a minimum for 90° scattering. If an elastic electron-SO_2 collision occurs, the resultant scattering angle is sampled from the differential scattering curve at the nearest energy. All other electron-neutral collisions, including inelastic electron-SO_2 collisions, are assumed to scatter isotropically.

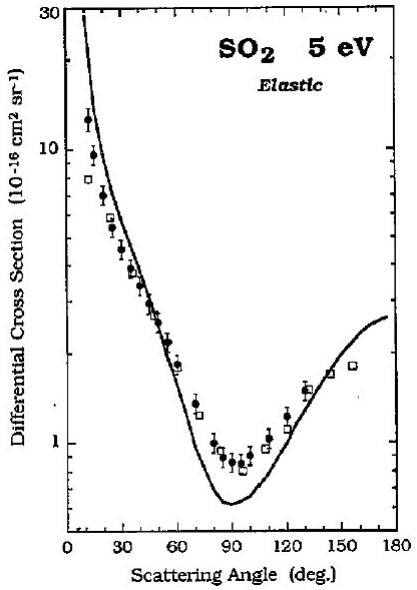

Figure 3-8: Differential cross section for elastic scattering for 5 eV electron–SO_2 collisions. The symbols are data from various experiments and the solid line is a theoretical approximation. The interaction is strongly biased to forward scattering and has a minimum for 90° scattering. (*From Gulley and Buckman (1994), courtesy of IOP Publishing Ltd*).

Secondary electrons generated by ionization are given a kinetic energy determined by the method of Bhardwaj and Michael (1999b) and a random pitch angle. Once the energy of the secondary electron has been determined, the primary electron energy is set by subtracting the energy of the secondary electron and the ionization potential from the initial energy of the primary electron (the internal energy of the target does not contribute). In the current DSMC implementation, the electronic states of the particles are not tracked and all electron-neutral interactions that result in excited products merely act to reduce the electron's energy while the simulation neutral atoms and molecules remain in the electronic ground state. This

assumes that the excited neutrals radiatively decay to the ground state (and that the gas is transparent) before a collision with another neutral occurs in which the excited state is quenched and the energy heats the gas instead of radiating away. Since the mean time between collisions even in the dense regions of the atmosphere is still ~0.05 s, this assumption is valid for allowed transitions with large Einstein *A* coefficients, but is probably not good enough for forbidden transitions (like 6300 Å emission from ^{1}D oxygen) with small Einstein *A* coefficients and in the future these states (at least) should be tracked in the DSMC simulation to more properly account for the energy flow from the plasma to the gas. Also, since there were no data about the post dissociation internal energies, all molecular products are assumed to be in the ground rotational and vibrational states. Therefore, the electron-neutral interactions in the current model dissociate and ionize the neutral gas and, additionally, the electrons lose energy via excitation collisions.

3.6 HEAVY-HEAVY CHEMISTRY MODEL

DSMC is ideally suited to modeling chemically reacting gas flows due to the molecular nature of the reactions. In theory, DSMC can account for reaction probabilities that vary based on the relative collision velocity and the internal electronic, vibrational, and rotational states of the colliding DSMC pseudo-particles. In practice, direct microscopic data for the reaction cross section as a function of the internal state is sparse and one must frequently use kinetic theory to infer cross sections from the continuum rate constants (Bird, 1994). However, the molecular dynamics/quasiclassical trajectory (MD/QCT) method can yield accurate cross section data provided the potential energy surfaces of the interacting particles are adequate and quantum effects such as tunneling are not important (Bose and Candler, 1996; Ozawa *et al.*, 2007). In our model we will utilize MD/QCT or experimental cross section data when available and linearly interpolate between the data points. If no cross section data are available (MD/QCT or experimental) the total collision energy (TCE) model (Bird, 1994) is used to obtain cross sections that result in continuum rate constants in the modified Arrhenius form. Only reactions for which cross sections or Arrhenius rate coefficients are available are currently modeled.

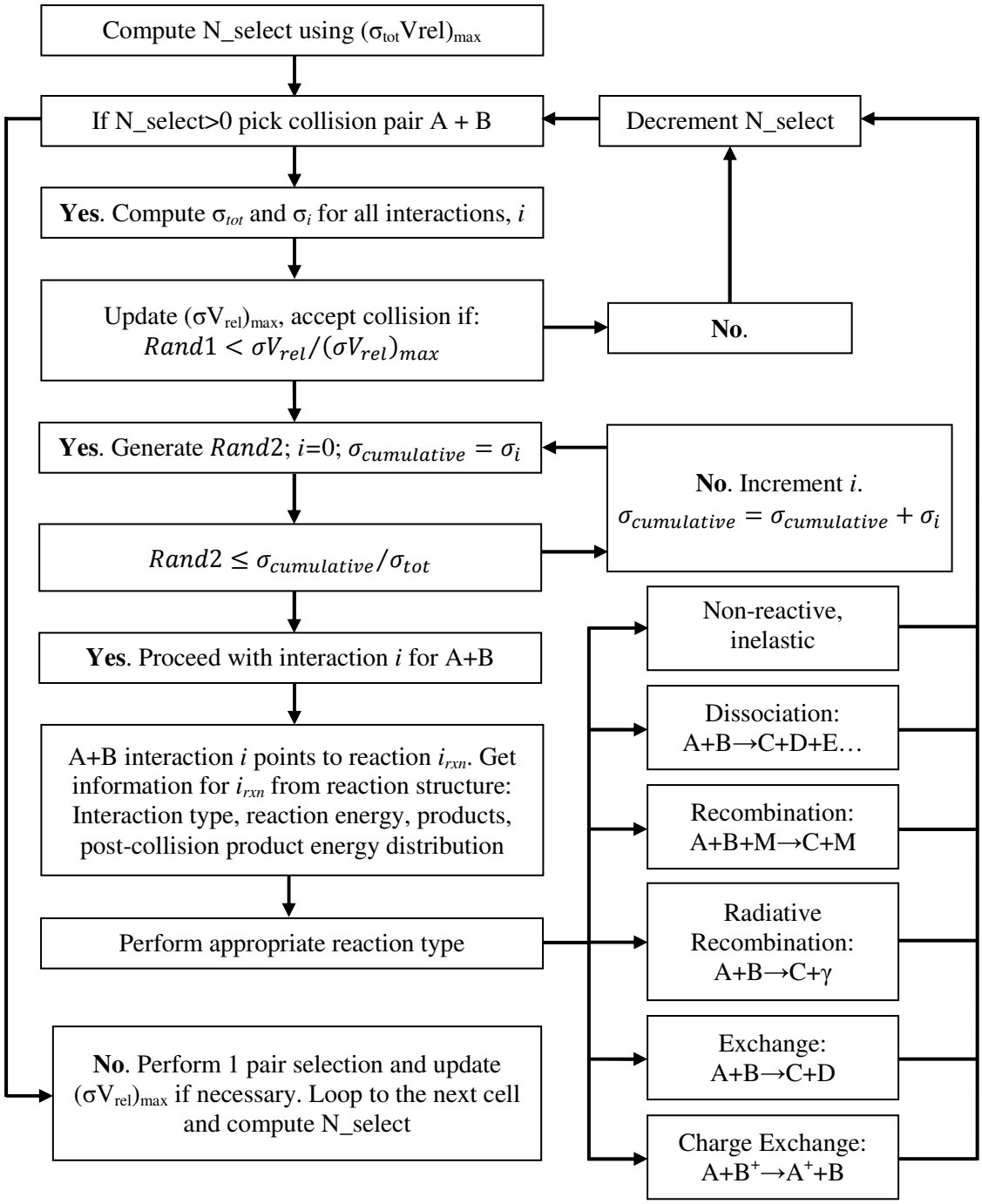

Figure 3-9: Collide Flow chart used to determine which, if any interaction to perform.

Figure 3-9 shows the collision routine which now allows for an arbitrary set of interactions between a collision pair to be modeled. The code still computes the number of

pair selections using the no time counter (NTC) method; however, now the total collision cross section is explicitly used when determining the collision rate. Previously the collision rate was calculated using the VHS cross section which is essentially equal to the total cross section at low collision energies but is much less than the total cross section at the very large collision energies expected for plasma bombardment of Io's upper atmosphere (see Figure 3-10). After selecting a collision pair, all of the interaction cross sections for that combination of species at their specific relative velocity and internal energy state must be computed and then summed to obtain the total collision cross section. The use of the MD/QCT data or the Arrhenius rate coefficients to obtain the cross sections will be elaborated below. The standard acceptance criterion is used (Eqn. 3-32) and, if the collision pair is accepted, then the nature of the interaction must be determined. This is accomplished by drawing a second random number and then sequentially comparing it to the ratio of the cumulative cross section up to the i^{th} reaction to the total cross section. This is similar to the procedure used to determine the reaction type for the electron-neutral interactions (Eqn. 3-34).

In order to save memory, the reaction data are stored in a separate structure and the i^{th} reaction for the species pair points to the i_{rxn} location in the heavy-heavy reaction structure which stores the various properties of the reaction. Modeled interaction types are non-reactive inelastic collisions, charge exchange, dissociation, recombination, and radiative recombination. Exchange reactions are neglected (and not implemented) for the current model; in the future they should be included for completeness (e.g. $SO + SO \rightarrow S_2 + O_2$). Note that the nature of the reaction data (TCE or MD/QCT) only affects how the reaction cross section is computed; the actual physics of the given reaction is identical whether the TCE or MD/QCT method is used to compute the reaction cross section.

As explained above, the cross sections for the electron-heavy interactions are precomputed at the start of a simulation using a user-defined energy spacing. In general, segmented polynomial curve-fits to the data for each interaction are hard coded into subroutines in the code. The probability of each electron-heavy reaction for a given energy "bin" is precomputed and thus, during a collision, only the energy bin index need be computed and a comparison made to a random number to determine the interaction.

A similar procedure could have been used for the heavy-heavy interactions; however, this use of "hard coded" cross section subroutines to precompute the reaction probabilities was not as desirable for several reasons. First, in the case of the electron-heavy interactions,

the data is fairly complete for each of the major species and their specific interaction (unless new, conflicting experimental data are obtained). However, for the heavy-heavy interaction data obtained through MD/QCT simulations at a small number of points in relative velocity and internal energy space, one might expect frequent changes to the data (either through new data points or more accurate physics in the MD/QCT simulation). Furthermore, multiple MD/QCT heavy-heavy simulations of new collisional pairs are expected in the near future and the ability to incorporate those quickly and easily into the code was desirable. Also, in these simulations at least, there are ~30 electron-heavy interactions[9] possible per heavy species (see Figure 3-7) as opposed to the ~5 heavy-heavy interactions possible per combination of heavy species (see Figure 3-10). Therefore the speed-up obtained by not having to compute all the possible interaction cross sections for every collision pair is much greater for the electron-heavy interactions. Moreover, electron-heavy collisions also occur much more frequently than the heavy-heavy interactions at the same density and temperature due to the much higher relative velocity between electrons and heavies. Finally, since the electron-heavy interaction data do not vary the cross section based on the internal energy of the heavy particle, the pre-computed electron-heavy reaction probability array in relative velocity can be much more resolved and not take up a prohibitive amount of memory. Conversely, a decently resolved precomputed heavy-heavy interaction array (with only 10 species) would consume a large amount of memory and reduce the number molecules that could be of simulated by ~5%.

Therefore, in order to keep the routine as general and flexible as possible, the heavy-heavy interactions are input in a file and the information on each reaction read into the code. For each reaction the type, parents and products, and activation and reaction energy are read in. If the reaction type is "Arrhenius", then the Arrhenius coefficients are also read in; if the reaction is "MD/QCT" then the number of data points in both relative velocity and internal energy space are read. The MD/QCT data are then given point by point below the input line for the specific reaction to which they apply.

The heavy-heavy reactions included in the model are shown in Table 3-4 along with the corresponding reference. Note that several of the sulfur reaction cross sections (e.g. $SO_2 + S \rightarrow SO + S + O$) are obtained by using the corresponding oxygen reaction cross section (e.g.

[9] Such as elastic, dissociation, ionization, and excitation to each excited state.

$SO_2 + O \rightarrow SO + 2O$) as a function of the total collision energy. In other words, the sulfur reaction cross section as a function of the relative collision velocity for a given reaction, i_{rxn}, is given by

$$\sigma_{S,i_{rxn}}(V_{rel}) = \sigma_{O,i_{rxn}}\left(\sqrt{\frac{m_{r,O}}{m_{r,S}}}V_{rel}\right). \quad 3\text{-}35$$

Here $m_{r,i}$ is the reduced mass of the particle type i each with the same collision partner (SO_2 in the example reaction above). This was done because MD/QCT data were available for the oxygen reactions but not the sulfur reactions and at the expected high energies which are much greater than the reaction energy, the cross sections should be almost independent of the details of the interaction potential surface.

Table 3-4: Included Heavy-Heavy Interactions.

Collision type	Reaction	Reference
Elastic	$SO_2 + O \rightarrow SO_2 + O$	1
Dissociation	$SO_2 + O \rightarrow SO + 2O$	1
Dissociation	$SO_2 + O \rightarrow O_2 + O + S$	1
Dissociation	$SO_2 + O \rightarrow 3O + S$	1
Dissociation	$SO_2 + S \rightarrow SO + O + S$	1†
Dissociation	$SO_2 + S \rightarrow O_2 + 2S$	1†
Dissociation	$SO_2 + S \rightarrow 2O + 2S$	1†
Dissociation	$O_2 + O \rightarrow 3O$	2
Dissociation	$O_2 + S \rightarrow 2O + S$	2†
Charge Exchange	$O^+ + O \rightarrow O + O^+$	3
Charge Exchange	$S^+ + S \rightarrow S + S^+$	3
Radiative Recombination	$SO + O \rightarrow SO_2 + \gamma$	4
Recombination	$O + SO + M \rightarrow SO_2 + M$	5
Recombination	$2O + M \rightarrow O_2 + M$	5
Recombination	$O + S + M \rightarrow SO + M$	5

[1]Deng *et al.*, 2011; [2]Johnson, *et al.*, 2002; [3]Smirnov, 2000; [4]Singleton and Cvetanović, 1988; [5]Moses *et al.*, 2002; †Cross section obtained by scaling corresponding $SO_2 + O$ reaction.

3.6.1 TCE Model

The TCE model is used if Arrhenius rate coefficients are available and no MD/QCT cross section data are available in a similar energy range for a given reaction between particles of type A and B. A brief review of the TCE model follows; a more detailed

discussion can be found in Chapter 6 of Bird (1994). Rate coefficients are empirically observed to be functions of the gas temperature and can be well fit by the modified Arrhenius equation

$$k(T) = A_{Arr}\left(\frac{T}{T_{ref}}\right)^{\eta} exp\left({}^{-E_a}/_{kT}\right), \tag{3-36}$$

where A_{Arr} and η are constants and E_a is the activation energy of the reaction. Generally all three of these values are determined by the best fit to the experimental data over some temperature range. Note that Bird (1994) uses the notation

$$k(T) = \Lambda(T)^{\eta} exp\left({}^{-E_a}/_{kT}\right),\ \Lambda = AT_{ref}^{-\eta}. \tag{3-37}$$

It has been shown in Bird (1979, 1981) that the functional form of Eqn. 3-37 for the reaction rate coefficient can be obtained for a bi-molecular reaction by using a reaction cross section, σ_R, of the form

$$\begin{aligned} \sigma_R &= 0 && E_{col} \le E_a; \\ \sigma_R &= \sigma_{Tot} * C_1(E_{col} - E_a)^{C_2}(1 - E_a/E_{col})^{C_3} && E_{col} > E_a. \end{aligned} \tag{3-38}$$

Here σ_{Tot} is the total cross section and is assumed to be equal to the VHS cross section (Bird, 1994) at the reference temperature, T_{ref}, and E_{col} is the total collision energy. It is possible in this expression for the steric factor, σ_R/σ_{VHS}, to exceed unity at high collision energies and therefore violate the assumption that the total cross section equals the VHS cross section. However, test cases found that this does not cause large errors (<10%) in the simulated Arrhenius rates as long as the total collision cross section ($\sigma_{VHS} + \sigma_R$) is still used to compute the number of collision pair selections as mentioned earlier. The constants in Eqn. 3-38 are derived by Bird (1994):

$$\begin{gathered} C_1 = \frac{\pi^{0.5}\varepsilon\Lambda}{2\sigma_{ref}} \frac{\Gamma(\bar{\zeta}+5/2-\omega_{AB})}{\Gamma(\bar{\zeta}+\eta-3/2)} \left(\frac{m_r}{2kT_{ref}}\right)^{0.5} \frac{T_{ref}^{1-\omega_{AB}}}{k^{\eta-1+\omega_{AB}}}, \\ C_2 = \eta - 1 + \omega_{AB}, \\ C_3 = \bar{\zeta} + 1.5 - \omega_{AB}, \end{gathered} \tag{3-39}$$

where ε is the symmetry factor equal to unity if the two colliding particles are dissimilar and two if they are identical, Γ is the gamma function, $\bar{\zeta}$ is the average number of internal degrees of freedom that contribute to the collision energy, m_r is the reduced mass, and ω_{AB} is the VHS viscosity-temperature exponent for collisions between particles of type A and B. The average number of internal degrees of freedom for the collision pair is an arbitrary parameter in that generally a range of $\bar{\zeta}$ can match the Arrenhius rates (Bird, 1994). In the current implementation, $\bar{\zeta}$ is based on the effective internal degrees of freedom of the collision cell,

assuming that the rotational modes, ζ_{rot}, are fully excited and the vibrational modes are partially excited (Bird, 1994)

$$\bar{\zeta} = \zeta_{rot} + \sum_{m=1}^{N_{vib}} 2 i_{v,m} \ln\left(1 + i_{v,m}^{-1}\right), \tag{3-40}$$

where $i_{v,m}$ is the average quantized vibrational level of the molecules in the cell in the m^{th} vibrational mode. Cell-based values are used because, even if the gas is very hot, the most probable vibrational state is the ground state. If only the collision pair were used to compute $\bar{\zeta}$, then if $i_{v,m}$ is zero (both collision molecules in the ground state), then the contribution of the vibrational degrees of freedom in that mode is zero. Similarly, as the average vibrational level goes to infinity (though $i_{v,m}$ cannot exceed the limit set by dissociation), the contribution of the vibrational degrees of freedom from each mode goes to two, as one would expect for a vibrational mode. However, this means that even for a very hot gas, the average value of $\bar{\zeta}$ would be too low if it were based on the collision pair.

For reactions involving three particles (e.g. recombination), the cross section can be obtained in a similar manner above, except that the coefficient C_1 now has a dependence on the density of the third body, n_M:

$$C_1 = \frac{\pi^{0.5}\varepsilon\Lambda}{2\sigma_{ref}} \frac{\Gamma\left(\bar{\zeta}+5/2-\omega_{AB}\right)}{\Gamma\left(\bar{\zeta}+\eta-3/2\right)} \left(\frac{m_r}{2kT_{ref}}\right)^{0.5} \frac{T_{ref}^{1-\omega_{AB}}}{k^{\eta-1+\omega_{AB}}} n_M. \tag{3-41}$$

Furthermore, if the activation energy of the reaction is zero, then per Bird (1994), the contribution from the internal degrees of freedom, $\bar{\zeta}$, is also zero and C_1 now equals:

$$C_1 = \frac{\pi^{0.5}\varepsilon\Lambda}{2\sigma_{ref}} \frac{\Gamma\left(5/2-\omega_{AB}\right)}{\Gamma\left(\eta-3/2\right)} \left(\frac{m_r}{2kT_{ref}}\right)^{0.5} \frac{T_{ref}^{1-\omega_{AB}}}{k^{\eta-1+\omega_{AB}}} n_M. \tag{3-42}$$

3.6.2 MD/QCT Data

While the TCE model utilizing the Arrhenius rate coefficients works well at lower collision energies, at high collision energies the TCE model becomes invalid for several reasons. The TCE model discussed above assumes that the total cross section is equal to the non-reactive inelastic VHS cross section; however, at high collision energies, the non-reactive inelastic cross section falls off faster than the VHS model (Dimpfl *et al.*, 2008). This is because higher relative collision velocities probe further into the steep, near field repulsive molecular potential which rises exponentially (e.g. Born-Mayer) whereas the VHS model assumes the near field repulsive potential rises as an inverse power law (e.g. Lennard-Jones). Furthermore, at very high energies, the reaction cross sections can exceed the non-reactive

inelastic cross section and therefore the TCE steric factor will, unphysically, exceed unity (see Figure 3-10). Finally, the Arrhenius coefficients are obtained by fitting reaction rates at low temperatures and extrapolation to higher temperatures (collision energies) can result in incorrect reaction rates.

Thus a parallel MD/QCT code was developed by Ozawa *et al.* (2007) to calculate reaction and viscosity cross sections more accurately at various relative collision velocities and internal energy states for O+HCl collisions. Deng *et al.* (2011) modified this code to compute reaction and viscosity cross sections for O+SO_2 collisions at typical collision energies present at Io. The MD/QCT method simulates an ensemble of individual trajectories through the potential field generated by the molecules; each trajectory is initialized with a random impact parameter less than b_{max}. After a set amount of time the post-interaction products, scattering angles, velocities, and internal energy states are examined. Therefore one can obtain the reaction cross section for a given relative velocity and internal energy from the fraction of trajectories that lead to a specific reaction:

$$\sigma_{rxn} = \pi b_{max}^2 \frac{N_{rxn}}{N_{traj}} . \qquad 3\text{-}43$$

Similarly, one can obtain distributions for the post-interaction velocities, internal energies, and scattering angles. While the total collision (scattering) cross section is infinite due to the inverse power dependence of the long-range interaction potential, the momentum cross section is finite. Hence, a viscosity based cross section can be computed from the non-reactive trajectory data (Ozawa *et al.*, 2007, Deng *et al.*, 2011). In general, at low collision velocities (<10 km/s), the VHS model fits the MD/QCT viscosity based cross section data reasonably well. Therefore, for O+SO_2 collisions slower than 2 km/s (a variable set in the input file for each non-reactive interaction), the non-reactive cross section in our code is computed using the standard VHS model (Bird, 1994) but with parameters set by the curve fit to the MD/QCT viscosity cross section data. For relative collision velocities greater than 2 km/s, the non-reactive cross section is determined directly by linear interpolation between the available MD/QCT viscosity cross section data points. This is necessary because the VHS curve fit greatly over-estimates the non-reactive cross section above ~20 km/s for O+SO_2 collisions (see Figure 3-10).

Previously, Boyd *et al.* (1997) used MD/QCT generated cross sections for the formation of NO by the first Zeldovich reaction in DSMC simulations of hypersonic reentry bow shocks. They proposed a generalized collision energy (GCE) model based upon the TCE

model which used the MD/QCT cross section data to calibrate the GCE parameters. The GCE model was found to agree much better than the TCE model with bow-shock ultra-violet (BSUV) flight experiments (Levin *et al.*, 1993). However, the use of the GCE model requires computation of the Arrhenius rate coefficients based on the MD/QCT data and then selecting the three GCE parameters that best-fit the cross section data over the energy range of interest. We decided that the MD/QCT cross section data would be used directly in our implementation thereby allowing us to match the MD/QCT cross sections exactly[10] at the relative translational and internal energies for which there are data and allowing for easier inclusion of additional MD/QCT data for new reactions.

The current implementation obtains the reaction cross section for a given collision at a relative velocity of v_{rel} and internal energy of E_{int} by linearly interpolating between the MD/QCT data points. First, we linearly interpolate between MD/QCT relative velocity data points for both internal energy MD/QCT data points bracketing the total internal energy of the collision pair. Then we linearly interpolate in internal energy using the previous interpolated cross sections in relative velocity. For collisions that have relative velocities beyond the lowest or highest MD/QCT data point, the cross section is extrapolated assuming the slope from the nearest two data points. If the internal energy of the collision is lower or higher than the available MD/QCT data, the cross section is assumed to equal the nearest data point.

Figure 3-10 shows some of the MD/QCT data (symbols) for $O+SO_2$ and $O+O_2$ collisions that are used in the current simulations. Above ~20 km/s the $O+SO_2 \rightarrow SO+2O$ and $O+ SO_2 \rightarrow S+3O$ reactions both exceed the non-reactive MD/QCT cross section. Therefore it is very important to use the total cross section to get the correct collision rate. Note that the $O+ SO_2 \rightarrow O_2+S+O$ reaction cross sections were found to be negligible ($<10^{-17}$ cm^2) by the MD/QCT simulations. While the $O_2+O \rightarrow 3O$ cross section is relatively small, it is an important loss mechanism for O_2 since we currently assume that O_2 is a non-condensable at Io's surface temperatures. Also, the MD/QCT data has large differences in the reaction cross section due to internal energy, especially near threshold total collision energies, that cannot be simply scaled away by renormalizing the cross sections as functions of the total collision energy. Therefore, it is important to simulate the SO_2 internal energy as accurately as possible

[10] By this I mean match the reaction probability for an individual interaction.

to get an accurate dissociation rate. Future work should include the MD/QCT post-interaction vibrational and rotational energy state distributions and attempt to include the electron vibrational/rotational excitation.

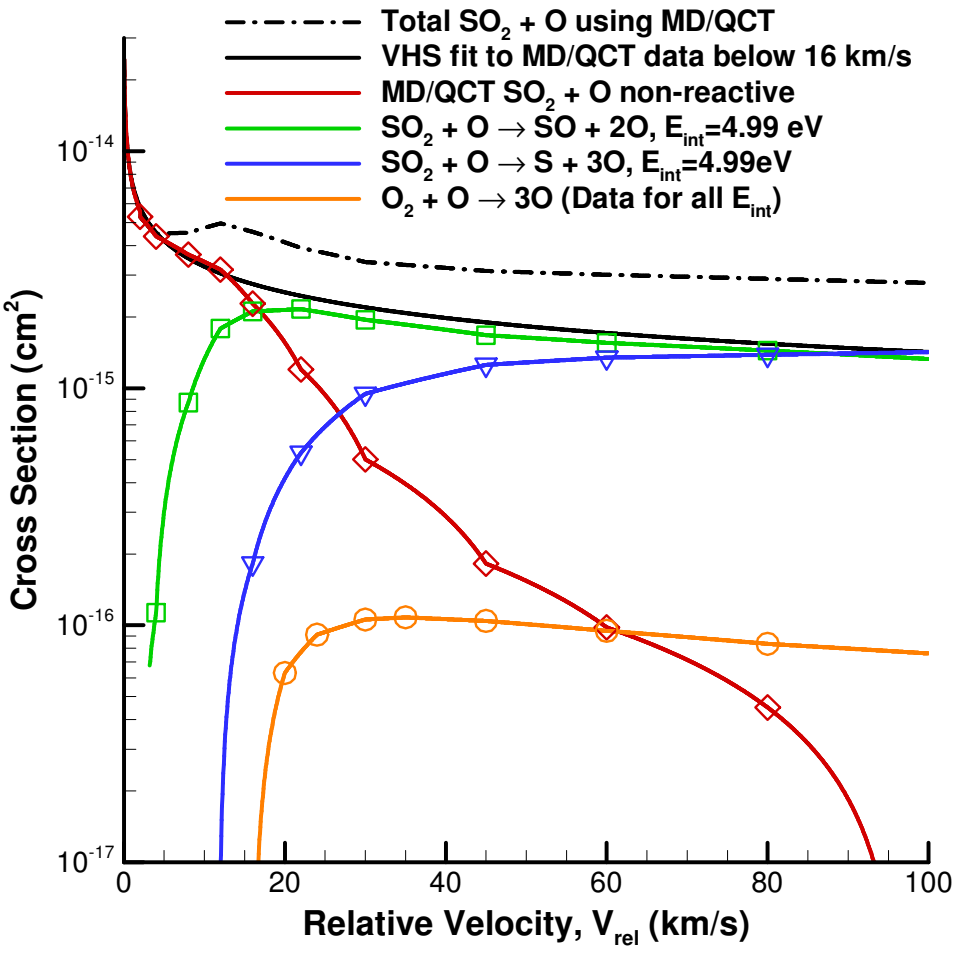

Figure 3-10: Cross section versus relative velocity for several included reactions. Between the MD/QCT data points (symbols) the cross section is obtained via linear interpolation (curved lines on the log plot) in both relative velocity and internal energy (see dashed black line).

3.6.3 Dissociative Reactions

If a dissociative reaction is determined to occur, the dissociation energy is subtracted from each mode of energy (translation, rotation, vibrational states) in proportion to the amount that each contributed to the total collision energy. These reduced energies are then used in an inelastic collision between the initial collision pair (before dissociation) in which rotational and vibrational energy is transfer is forced (Z_R and $Z_{v,i}$ equal to unity). Generally, in

a dissociation reaction due to heavy particle impact (as opposed to electron dissociation), the dissociation occurs due to the transfer of internal energy to the molecule greater than the dissociation energy for that electronic state. Therefore, there will be a transfer of rotational and vibrational energy in most heavy-heavy dissociation events. However, if the standard equations for Z_R and $Z_{v,i}$ as functions of the collision temperature are used, then rotational and vibrational energy transfer will not occur in most collisions. This causes an additional problem because the internal energy of the dissociating molecule is used to obtain the relative velocity of the daughter products in the current model. Therefore, it is assumed that rotational and vibrational energy transfer occurs at the start of every dissociation event; however, for the reactions with MD/QCT data, this assumption is in theory unnecessary since the distribution of final energy states of the products could be tracked and used in the DSMC model. Currently this data is unavailable, but future work will examine the final energy states obtained via MD/QCT simulations.

At this point in the dissociation collision, the internal energy and velocity of the particle which does not dissociate (if there is one) has been determined and all that remains is to determine the internal energies and velocities of the dissociation products. Without MD/QCT (or other) data for the post dissociation energy distributions, the product energies are generally approximated by performing a inelastic pseudo-collision between the products which re-partitions the energy in the internal modes of the post dissociation products. In this "collision" between the two new product particles, the center of mass velocity is equal to the parent velocity and the total relative energy is set equal to the internal energy of the parent molecule. The internal energies are then partitioned into the products using standard Larsen-Borgnakke.

3.6.4 Charge Exchange Reactions

Currently only resonant charge exchange reactions are modeled in which a charged atom or molecule exchanges an electron with a neutral atom or molecule of the same species. Non-resonant charge exchange was neglected in the current work since the resonant charge exchange cross section is typically 10–100 times greater than the non-resonant cross section. However, near the surface of Io, it is possible that non-resonant charge exchange is non-negligible since the SO_2 density greatly exceeds the primary charged particle (O and S) densities.

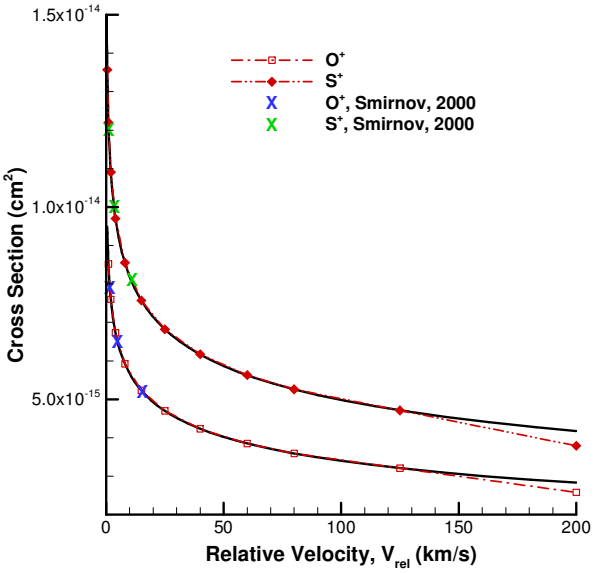

Figure 3-11: Resonant charge exchange cross sections versus relative velocity.

In a resonant charge exchange interaction, only the electron is transferred and since its mass is negligible compared to the atom or molecule, the momentum and energy of the two interacting particles is unchanged by the interaction. Resonant charge exchange cross sections at relative energies of 0.1, 1, and 10 eV were obtained from Smirnov (2000). In order to extend the cross section data to the higher energies of interest for Io, the data were used to fit the parameters in the theoretical equation for resonant charge exchange (Smirnov, 2000):

$$\sigma(V_{rel}) = \frac{\pi}{2\gamma^2} ln^2\left(\frac{v_o}{V_{rel}}\right) \qquad 3\text{-}44$$

where V_{rel} is the relative velocity between the ion and the neutral atoms and γ and v_0 are constants for a given atom. Equation 3-44 was then used to generate 10 cross sections at relative energies that were used as input for the DSMC simulations. Figure 3-11 shows the analytic (solid black lines, Eqn. 3-44) and DSMC resonant charge exchange cross sections (red curves) versus relative velocity for the O^+ and S^+ ions as well as the original charge exchange cross section data ("X" symbols). Note that the DSMC cross sections are linearly interpolated between the set of "data points" obtained from Eqn. 3-44, and that above 125 km/s (the last data point), the slope between the two previous cross sections is used to extend the cross section. However, very few ions will have velocities greater than 100 km/s and therefore the small error due to linear extrapolation is acceptable.

3.6.5 Radiative and Third-body Recombination Reactions

If a radiative or third-body recombination reaction occurs, then the molecular velocity after recombination is determined by conservation of momentum. Note that the cross reference array used to pick collision pairs from the cell must be adjusted otherwise invalid collision pairs might be selected since one of the simulation particles is deleted upon recombination. If the reaction is a radiative recombination, then the excess energy of the initial collision pair is assumed to be radiated away instantaneously and the reaction is complete. If the recombination involves a third body, then the third body is selected at random from the simulation particles in the cell. Currently, there is no bias on the selection based on relative velocity or species type. The new recombined molecule, with the excess energy distributed among its internal modes, then undergoes an inelastic collision with the third body in which rotational and vibrational energy transfer are forced.

3.7 SURFACE SPUTTERING MODEL

As discussed in Chapter 2.1.1, sputtering of surface frost via energetic ion impact is important when the atmospheric column density falls below ~10^{16} cm^{-2} (Haff *et al.*, 1981; Lanzerotti *et al.*, 1982). Assuming non-negligible local frost coverage, this occurs locally when the surface frost temperature falls below ~90 K. Since the surface frost temperature drops below 90 K near the poles and, depending on the thermal inertia, on the nightside as well, direct surface sputtering will occur over regions of Io's surface. Consequently an atmospheric column forms that is greater than that due to sublimation alone. Furthermore, the reduction in the subsolar–polar and subsolar–nightside pressure gradient should effect the strength of the circumplanetary winds. Since auroral limb glow emission is observed at the poles, inclusion of surface sputtering should be important.

To my knowledge, laboratory data are lacking for surface sputtering of SO_2 ice via oxygen and sulfur ions at energies typical for the jovian thermal plasma torus (<0.6 keV). A non-thermal energetic component of ions is present at Io and, while the sputtering yield per incident ion is much higher at larger energies, the flux incident to the surface is much smaller than the co-rotating thermal ions. Accounting for both effects, the overall sputtering yield of the energetic ions is an order of magnitude less than for the co-rotating ions (Cheng, 1984) and sputtering due to energetic ions is ignored in the present work. Unfortunately, the laboratory data are only available at incident ion energies greater than 10 keV and are from

the 1980s,[11] presumably motivated by Voyager 1 observations. For example, Lanzerotti *et al.* (1982) studied SO_2 erosion by 10–2000 keV He^+, H^+, and H_2^+ ions, Melcher *et al.* (1982) bombarded SO_2 frost with 0.08–1.3 MeV/amu He^+ and F^+ ions, and Boring *et al.* (1983, 1984) examined SO_2 sputtering by 15–1500 keV He^+ and Ar^+ ions. There are many additional papers on SO_2 sputtering; however, the references cited represent most of the relevant data on SO_2 sputtering.

Boring *et al.* (1983) found that bombardment of cold (10–30 K) condensed molecular gas solids (H_2O, D_2O, CO_2, and SO_2) by energetic (>keV) ions results in significant chemical activity and sputtering of the chemical products (e.g. SO, SO_3, and O_2 for an SO_2 solid). While the sputtering yield of the parent molecule from the solid was independent of the surface temperature below a critical temperature, they found that the yield of molecular products (SO, SO_3, and O_2) increased with surface temperature. This makes sense if a thermal diffusion process is required to produce the molecular products from the fragments of the parent molecule produced by the initial ion impact. For D_2O sputtering by 1.5 MeV He^+ ions Boring *et al.* (1983) also found that the relative sputtering yields of the D_2, D_2O, and O_2 varied considerably with temperature. The product sputtering yield (D_2 and O_2) relative to the parent sputtering yield was found to increase with surface temperature up to ~130 K; it decreases rapidly as the surface temperature is further increased because the deposition of ion energy locally enhances sublimation of the parent species. Johnson *et al.* (1984) found that, for 45 keV Ar^+ impacting SO_2 frost, the SO sputtering yield was ~10% of total yield and that the SO_3 and S_2O yield was at most several percent. Also, they determined that particles with an atomic mass of 32 (presumably S and O_2) are ejected upon ion bombardment; however, they did not obtain relative yields for this mass group. Furthermore, the energy distributions of the various sputtered species were found to be very similar.

The sputtering model implemented in the planetary DSMC code is outlined next. During the move step, if an ion hits the frost covered surface the total sputtering yield is determined based on the ion and frost species and the incident ion energy. Next, the number sputtered and the incident ion energy are stored along with the location for each ion that impacts the surface. Then, at the start of the next time step, the sputtered particles for each ion impact are created and given a translational energy based on the Thompson collisional

---

[11] This has been confirmed through discussions with Robert Johnson (Johnson, 2011).

cascade energy distribution. The velocity vector is picked assuming an isotropic angular distribution away from the surface. I know of no data for the internal energy distribution of the sputtered molecule. Therefore, since the model already assumes that sputtering proceeds via a collisional cascade, the molecules are given an internal energy based on equilibrium with the local surface temperature. This is almost certainly too "cold" of a distribution, but any error in the species' densities (the primary quantity of interest) caused by this approximation is negligible compared with the errors in determining the total and fractional yields.

Another issue is that DSMC has difficulty handling the fact that a sputtering event is (nearly) a point source of molecules expanding away from each other. The problem is that, for small enough time steps, the sputtered molecules remain in the same cell (which is much larger than the sputtered area) and are then likely to be selected for collision with each other, because they have large relative velocities with each other (see Figure 3-12). The center of mass velocity of the sputtered particles is normal to the point of impact on the surface (excluding noise); however, collisions between particles streaming away from each other will tend to reduce the expansion velocity parallel to the surface. Consequently, the unphysical collisions between the sputtered particles lead to the formation of a vertical jet of particles instead of an expanding cloud.

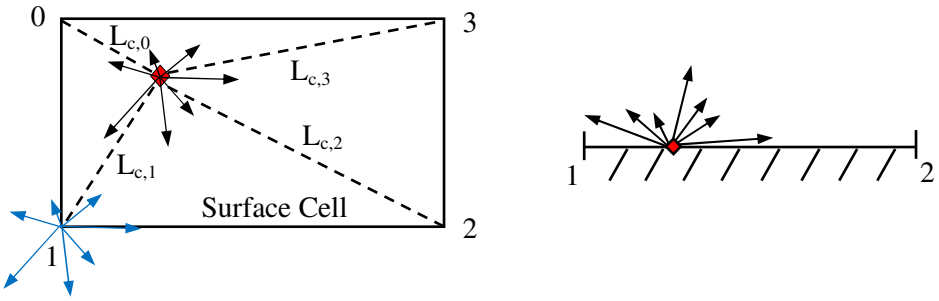

Figure 3-12: Schematic of sputtered particle placement to the surface cell corners from an ion surface impact located at the red diamond. Left: Top view of the surface cell. Right: Side view of the cell. The velocity vectors for seven sputtered particles are shown at the impact point (black) and at the (randomly determined) particle's creation corner (blue). The distance from the cell corners are given by dashed black lines.

A "sputtered" identifier flag on the molecule structure to prevent collisions would both add memory overhead and add computational cost during the `collide` routine. For the timesteps we are able to simulate currently, collisions between sputtered particles are rare because the sputtered particles move before colliding and generally they distribute themselves

across several altitudinal cells in a single timestep. However, to further reduce the error and address this problem for future simulations, the sputtered particles are all placed at a surface cell corner with the probability that the i^{th} corner is picked inversely proportional to the distance of the sputter event from that cell corner:

$$P_{sput,i} = \frac{1/L_{c,i}}{\sum_{j=0}^{3} 1/L_{c,j}}, \quad 3\text{-}45$$

where $L_{c,i}$ is the distance from the sputter location to the i^{th} corner (see Figure 3-12). If an ion impacts exactly on a corner, then all of the sputtered particles are placed at the corner. As seen in Figure 3-12, putting the sputtered particles at a cell corner instead of the ion impact point reduces the likelihood that two particles which are moving away from each other remain in the same cell, and hence reduces the probability of collisions between them. This does introduce errors linked to the cell size and, over many impacts, smears the sputtered particles over the cell area. This smearing, which is at the spatial resolution limit of the computation, was deemed preferable to forming unphysical jets of particles streaming radially away from the surface.

3.7.1 Sputtering Yield

Once an ion hits the frost, the first step is to determine the number of sputtered particles. Since SO_2 sputtering data are available only for much higher incident ion energies (>10 keV) than the energy of the corotating torus oxygen and sulfur ions, the high energy measured yields (Lanzerotti *et al.*, 1982; Boring *et al.*, 1984) must be extrapolated to the relatively low torus energies. The physical mechanism for low energy sputtering is summarized below and given in detail in Johnson (1990).

Assuming that each recoil atom interacts independently with the other surface atoms, a collisional cascade of momentum and energy transfer between the recoil atoms and the surface atoms occurs. Any of the independent collision cascades near the surface can result in surface particles being sputtered. Therefore, the number of recoil particles set into motion by an incident ion is directly proportional to the nuclear elastic energy deposited. The sputtering yield for incident ions of species A and a surface of species B, $Y_{A,B}$, has the form

$$Y_{A,B}(E_i, cos\theta_i) \approx F_{D,AB}(E_i, cos\theta_i, 0)\Lambda/N_B, \quad 3\text{-}46$$

where $F_{D,AB}(E_i, cos\theta_i, 0)$ is the net elastic collision energy deposited per unit path length at the surface by an incident ion with energy E_i and angle θ_i to the surface normal, Λ is the

sputtering efficiency, and N_B is the number of atoms per condensed gas molecule (N_B = 3 for SO_2). Johnson (1990) derived an estimate of Λ using the average diffusion cross section and an effective binding energy, U_b; however, for the current model Λ is determined by fitting to the data. Currently, we assume that for rough surfaces (as one expects for Io's surface), the angular dependence drops out (Sigmund, 1969) and all that is needed is the dependence of the sputtering yield on the incident ion energy. However, more recent Monte Carlo modeling of sputtering within a regolith by Cassidy and Johnson (2005) has found that the sputtering yield has a $cos^{1.6}(\theta_i)$ dependence and future simulations should include this effect. For collisional cascades dominated by nuclear momentum transfer, Sigmund (1969) finds that

$$F_{D,AB} \approx \alpha_{A,B}\left(\frac{dE_i}{dx}\right)_n = \alpha_{A,B} n_B S_n \qquad 3\text{-}47$$

where $\alpha_{A,B}$ is a parameter accounting for the fraction of energy deposited near the surface that does not contribute to sputtering, $(dE_i/dx)_n$ is the average energy loss per unit path length, n_B is the density of particles in the surface, and S_n is the nuclear elastic stopping cross section. The fraction, $\alpha_{A,B}$, of the energy deposited which does not contribute to sputtering has been experimentally measured for various ions and surfaces. Within the accuracy of the model $\alpha_{A,B}$ is found to be a function of m_A/m_B only (see Figure 3.17 in Johnson, 1990). For the planetary DSMC code, data on $\alpha_{A,B}$ were taken from Johnson (1990) and a curve fit versus m_B/m_A was obtained; for oxygen ions sputtering condensed SO_2 $\alpha_{A,B}$ = 0.4, and for sulfur ions $\alpha_{A,B}$ = 0.25. The nuclear elastic stopping cross section is proportional to the incident ion energy and the diffusion cross section, σ_d, (Johnson, 1990):

$$S_n = \frac{\sigma_d}{2}\gamma E_i,\ \gamma = \frac{4m_A m_B}{(m_A+m_B)^2} \qquad 3\text{-}48$$

where γ is the mass factor dependent on the mass of the incident ion particles, m_A, and the mass of the surface particles, m_B. If we assume that the diffusion cross section is independent of the incident ion species then substituting Eqns. 3-48 and 3-47 into Eqn. 3-46 gives the sputtering yield due to the collision cascade at low incident ion energies:

$$Y_{A,B} \approx Const. \times \alpha_{A,B}\gamma E_i. \qquad 3\text{-}49$$

The collision cascade sputtering yield is seen to be linear in the ion impact energy and the constant is determined by linearly fitting to the available sputtering yield data. Unfortunately, the measured sputtering yields are not fully in the collision cascade regime even at the lowest incident ion energies and the electronic sputtering component (sputtering due to electronic excitation) is non-negligible. Johnson *et al.* (1984) and Chrisey *et al.* (1987)

estimate the electronic sputtering component, subtract it from the total yield, and then give the collision cascade sputtering yield for O^+ and S^+ at their respective corotational energies. Due to collisions with Io's atmosphere, the ions impacting the surface will, in general, have a distribution of energies. Therefore, the sputtering yield (Eqn. 3-49) is determined using a linear fit to the O^+ and S^+ yields (Johnson *et al.*, 1984; Chrisey *et al.*, 1987) normalized by $\alpha_{A,B}\gamma$, as shown by the solid black line in Figure 3-13. The sputtering yields for a given incident ion are then computed by multiplying the normalized sputtering yield, $Y_{A,B}/(\alpha_{A,B}\gamma)$, by the appropriate value of $\alpha_{A,B}\gamma$, as shown for O^+ ions (red dashed line) and S^+ ions (blue dot-dashed line) in Figure 3-13.

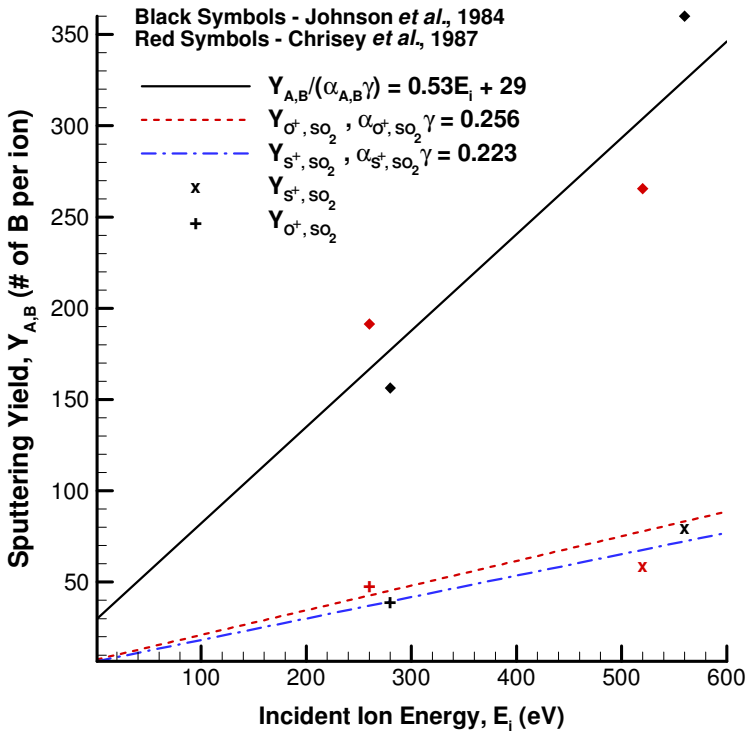

Figure 3-13: Curve fit sputtering yield versus incident ion energy. The black solid line and diamond symbols are actually the sputtering yield normalized by $\alpha_{A,B}\gamma$, the dashed and dot-dashed lines and the '+' and 'x' symbols give the sputtering yields for O^+ and S^+ ions incident onto SO_2 frost.

Note that the linear curve fit for the sputtered yield in Figure 3-13 is not equal to zero when an ion is incident on the surface with zero energy. Obviously, this is not physical since the model assumes $E_i \gg U_b$ and at very low incident ion energies this condition does not hold

and the model breaks down. A threshold for sputtering occurs when the maximum energy transfer is of order the surface binding energy and the collisional cascade model fails. The threshold energy, E_t, has been experimentally investigated and E_t/U_b is primarily a function of m_B/m_A. For sputtering of SO_2 frost by the ions of interest here, $E_t/U_b \leq 10$ (see Figure 3.19 in Johnson, 1990) and the binding energy, U_b, is roughly equivalent to the sublimation energy which, for SO_2, is 0.357 eV (Boring *et al.*, 1984). However, due to energy distribution constraints below (Eqn. 3-54), it is found to be computationally desirable in the current model to set the sputtering yield to zero below $20U_b = 7.14$ eV.

All the above data on sputtering yields were obtained for ion bombardment of SO_2 frost at 15 K. As the SO_2 frost temperature, T_s, increases, one might expect the sputtering yield for a given incident ion energy to increase. Brown *et al*. (1982) first examined the sputtering yield as a function of surface temperature for condensed gas solids including SO_2 and found that sputtering yield does indeed increase with increasing surface temperature above a threshold temperature. Figure 3-14 shows the sputtering yield from SO_2 frost by 1.5 MeV He^+ ions. While the sputtering yield due to the He^+ ions is dominated by electronic deposition, in the current model it is assumed, for lack of any other data, that the increase in sputtering yield with surface temperature is similar at the vastly lower incident ion energies of present interest (Johnson, 2011). However, the extreme sensitivity of the sputtering yield to surface temperature, independent of the incident ion temperature, might lead to problems wherever there are sharp surface temperature gradients. This dependence should be examined more thoroughly in future work. It is seen in Figure 3-14 that the sputtering yield is constant until a frost temperature of ~60 K, above which the yield increases exponentially. Boring *et al.* (1983) attribute the increase in SO_2 sputtering to two mechanisms. The initial (small) increase in sputtering yield is due to increased production of SO_2 products: SO, O_2, and SO_3. Above a threshold temperature the yield increases because energy that does not go into sputtering a particle locally heats the solid and increases the local sublimation rate. (This threshold temperature is not precisely known because there are no data available on product-production as a function of surface temperature for SO_2.)

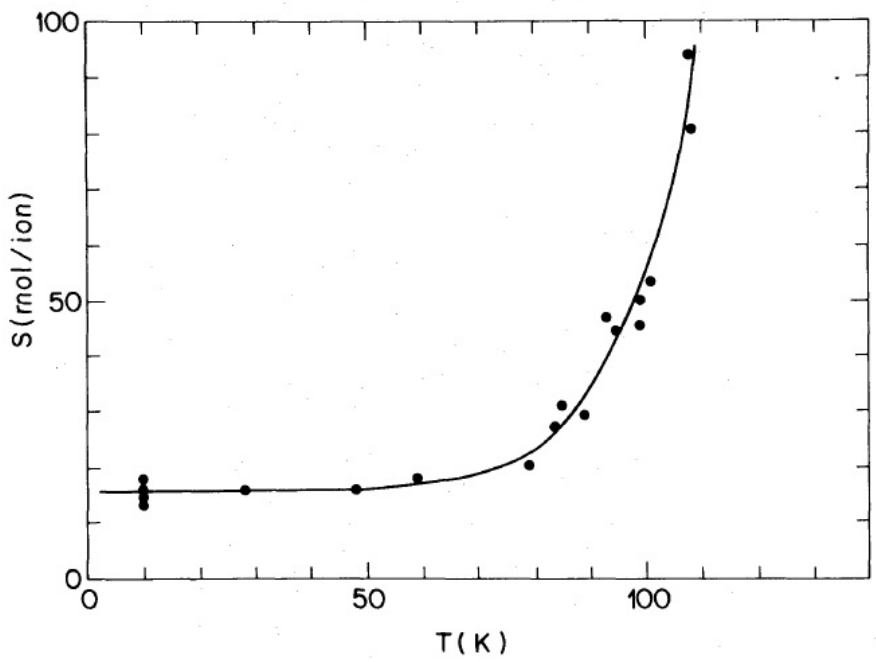

Figure 3-14: Sputtering yield (S) versus the SO_2 frost temperature, T_s, for 1.5 MeV He^+ incident on SO_2. Note that the sputtering yield shown is the number of molecules ejected per incident ion and does *not* include the increase in sublimated molecules as the surface temperature increases. The solid line is a constant equal to 16 below 60 K and above is given by $Y = Y_0 + Y_1 exp(-\Delta E/kT_s)$, where Y_0 = 16, $Y_1 = 2.8\times10^4$, and ΔE = 0.056 eV. (*From Lanzerotti et al. (1982), courtesy of the American Astronomical Society*).

To account for the both the sputter yield dependence on incident ion energy and the surface temperature, the total number of sputtered particles in the current model is given by

$$Y_{A,B} = floor\left(\frac{Y_{A,B}}{(\alpha_{A,B\gamma})} \times \alpha_{A,B\gamma} \times \left[1 + \frac{Y_1}{Y_0} exp(-\Delta E/kT_S)\right] + R\right), \qquad 3\text{-}50$$

where the *floor*() is taken and a random number, R, added since $Y_{A,B}$ must be an integer. $Y_{A,B}/(\alpha_{A,B}\gamma)$ is given by curve fit (Figure 3-13) to be $Y_{A,B}/(\alpha_{A,B}\gamma) = 0.53E_i + 29$, $\alpha_{A,B}\gamma$ is determined based on the ion species and Figure 3.17 in Johnson (1990), and Y_0, Y_1, and ΔE (16, 2.8×10^4, and 0.056 eV respectively) are given by the curve fit shown in Figure 3-14. The yield as a function of surface temperature given by Eqn. 3-50 is shown in Figure 3-15 for O^+ ions hitting SO_2 frost at several incident ion energies above the threshold energy (7.14 eV). The peak surface frost temperature in the current model (Chapter 8) is 115 K and an energetic O^+ ion incident onto the surface would yield ~500 SO_2 molecule, but the sublimation atmosphere present above 115 K SO_2 frost should be sufficient to prevent such high energy

ions from reaching the surface. However, the sensitivity of both sublimation and sputtering yield to the surface temperature could conceivably result in sharp density gradients as the surface temperature drops towards the poles (and terminators), as inferred from Lyman-α observations (Strobel and Wolven, 2001; Feaga *et al.*, 2009). This will be discussed further in Chapter 8.

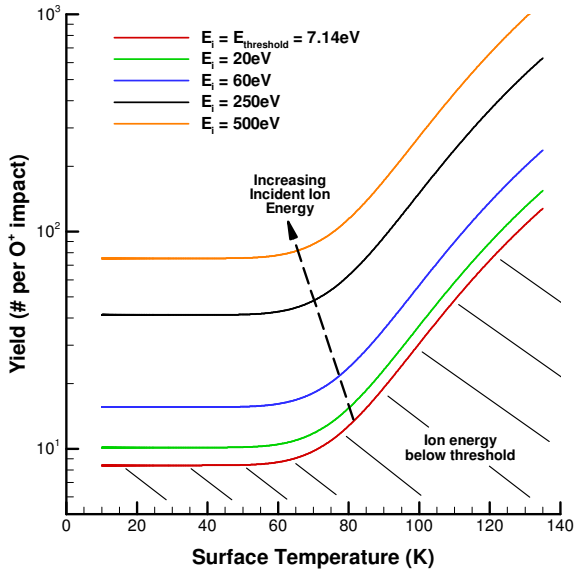

Figure 3-15: Simulation sputtering yield versus surface temperature at several O^+ ion energies. Note that S^+ ion yield curves would be similar in shape, displaced slightly due to the $\alpha_{A,B}\gamma$ factor. Note that at very high temperatures the yield asymptotes to $1 + Y_1/Y_2$ times the low temperature yield (see Eqn. 3-50).

Incident corotational ions have energies of several hundred eV and can, in theory, readily dissociate the condensed SO_2 frost. However, lower energy ions incident on the surface might be much less effective at sputtering SO_2 daughter species since dissociating the SO_2 would take up a significant fraction of the ion energy. Johnson *et al.* (1984) found that, for 45 keV incident Ar^+ ions, ~10% of the sputter particles were SO and at most several percent were SO_3 or S_2O. However, as noted earlier, Boring *et al.* (1983) attributed the increased sputtering with increasing surface temperature to first increased chemical activity and then to increased local sublimation. It is therefore unclear what fraction of the sputtered particles should be daughter products of SO_2 at a given surface temperature and incident ion energy. The current model neglects sputtering of species other than the parent frost species since the fraction of sputter daughter products is relatively low for 45 keV Ar^+ ions incident

on 15 K SO_2 frost and would arguably be even lower for <0.5 keV O^+ and S^+ ions incident on >90 K SO_2 frost. However, this is an approximation that might be poor over the colder surfaces if the sputtered products are non-condensable and could therefore build up a more significant atmosphere.

3.7.1 Sputtered Particle Energy Distribution

For a given ion incident onto the surface knowing the number of sputtered particles is, by itself, insufficient to model the sputtered atmosphere. At the least, a kinetic energy distribution for the sputtered particles must be prescribed and, if the particles are molecules, internal energy distributions must be given. Again, the corotating ions are in the low energy regime and therefore impacts should result in limited electronic excitation of the surface particles. Therefore, the kinetic energy distribution, f_E, is reasonably described by the Thompson distribution (Sigmund, 1969) derived using the collisional cascade model:

$$f_E(E_s) = \frac{C_E(E_s,\theta_i)E_s}{(E_s+E_b)^3}, \qquad 3\text{-}51$$

where E_s is the sputtered particle energy, E_b is the effective binding energy of the surface (different from U_b), and $C_E(E_s,\theta_i)$ is a proportionality constant estimated from experimental data. In the current model, the proportionality constant is set to $C_E(E_s,\theta_i) = 2E_b$ based on the experimental yield (Sieveka and Johnson, 1985; McGrath and Johnson, 1987). As shown in Figure 3-16, Boring *et al.* (1984) found excellent agreement between the experimental sputtered particle energy distribution and the collisional cascade energy distribution. For 45 keV Ar^+ ions incident onto 15 K SO_2 frost, the experimental data was best fit by an effective binding energy, E_b, of 0.054 eV. While the measured distribution falls off faster than E_s^{-2} at high energies (as predicted by the Thompson distribution), the errors bars are large enough that no definitive conclusion about the departure from E_s^{-2} can be reached. Note that the Thompson distribution is independent of the incident ion energy since in the collision cascade model the particles which sputter off the surface are, in general, given the energy to leave the surface not by the initial ion momentum transfer, but by successive collisions with the other particles in the solid.

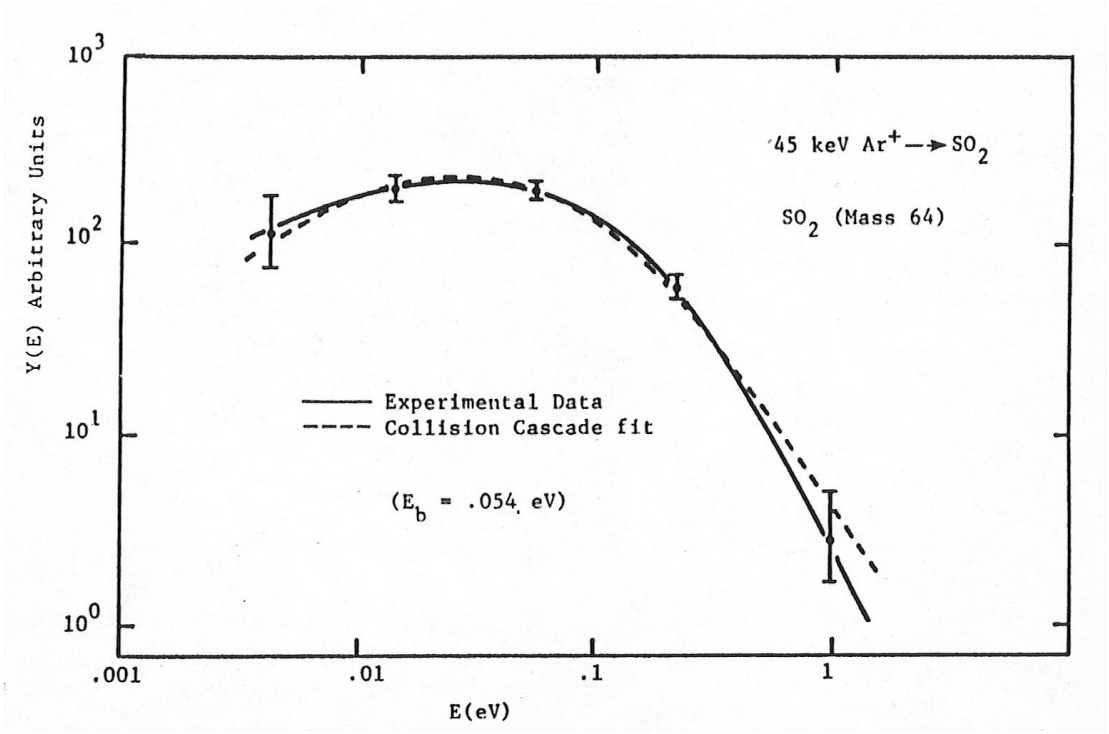

Figure 3-16: Measured sputtered particle energy distribution (arbitrary units) for 45 keV Ar^+ ions incident onto 15 K SO_2 (solid line) compared to the collision cascade energy distribution (Eqn. 3-51) best fit (dashed line). (*From Boring et al. (1984), courtesy of Elsevier*).

To my knowledge, there are no other data on the sputtered energy distribution for either lower energy incident ions or for higher surface temperatures. Additionally, I know of no data on the internal energy distribution of the sputtered SO_2 molecules. Therefore, the current model draws each sputtered particle's kinetic energy from Eqn. 3-51 and draws its internal energies from equilibrium distributions at the local surface temperature. To draw the kinetic energy from the Thompson energy distribution the distribution is integrated to give the cumulative distribution function, $F_E(E_s)$, from [0,1]:

$$F_E(E_s) = 1 - \frac{E_b(E_b+2E_s)}{(E_b+E_s)^2}. \qquad 3\text{-}52$$

The cumulative distribution is then inverted giving $E_s(F_E)$ and, replacing F_E with a random number draw, R = (0,1], the sputtered particle energy is given by:

$$E_s = \frac{\sqrt{R}}{1-\sqrt{R}} E_b \qquad 3\text{-}53$$

It is noted that drawing the sputtered particle energies from Eqn. 3-53 could result in the sum of the sputtered particle energies exceeding the incident ion energy because there is no

dependence in Eqn. 3-53 on the incident ion energy. While the probability that this occurs is very small for most incident ion energies and surface temperatures, it does occur more frequently for near-threshold ion energies when the surface temperature is high (~115 K). One can attempt to force energy conservation for a given sputtering event with $Y_{A,B}$ sputtered particles by enforcing a maximum energy for the J^{th} particle's energy given by

$$E_{max} = E_i - Y_{A,B}U_b - \sum_{k=1}^{J-1} E_k - E_{left}\left(Y_{A,B} - J\right), \quad 3\text{-}54$$

where E_i is the incident ion's energy, the second term accounts for the total energy required for $Y_{A,B}$ sputtered particles to escape the surface, the third term is the sum of the kinetic energies of all prior sputtered particles, and the last term is arbitrary and ensures that the remaining particles have some kinetic energy left available to them. However, the arbitrary nature of last term (how much energy to leave for the remaining particles) distorts the distribution and artificially increases the number of particles given very low energies due to the rare high energy sputtering event (that uses most of the incident ion energy) occurring for one of the first particles generated. It is more reasonable to expect that the sputtered energy distribution for $E_i \sim E_t$ at high E_s falls off faster than E_s^{-2} and that the distribution asymptotes to a maximum energy based on the incident ion energy. Since this is a relatively minor issue except for high surface temperatures in which local ion heating of the solid increases the sublimation rate, the current model ignores the lack of energy conservation and instead assumes that any excess energy required is provided by the surface. The surface cooling due to this effect should be minor though future models should include it (or at least examine it in more detail) as well as general cooling of the surface due to sublimation.

The sputtering model used in the current simulations (Chapter 8), while accurate to first order and vastly superior to no sputtering model, has several limitations. First, no daughter products of the surface species are sputtered (SO, O_2, O, and S). However, if sputtering is like D_2O around ~90 K then ~50% of the sputtering yield is daughter species (Boring *et al.*, 1983), and the polar and nightside atmosphere might be primarily SO and O_2. Such an atmosphere would be transparent to Lyman-α and still able to quench [OI] 6300 Å emission. Second, the sputtering yield as a function of the surface temperature is based on the assumption that the very high energy results can be extended to lower energies. However, this might not be valid especially for incident ion energies near threshold, and this would have a significant impact on the overall effect of sputtering on Io's atmospheric dynamics. Finally, the sputtering yield is assumed to be linear with incident ion energy (Eqn. 3-50) and the

Thompson distribution is used for the sputtered particle energies (Eqn. 3-53), but these assumptions break down for ion energies near the threshold energy. This assumption likely does not affect the overall atmospheric dynamics much because ions generally impact the surface with energies near the threshold energy only when there is already a significant atmospheric column present.

Chapter 4

Atmospheric Response during and after Eclipse

During Io's orbit around Jupiter Io experiences a ~120 minute eclipse during which its surface will cool. The sublimation component of Io's SO_2 atmosphere might be expected to "freeze-out" or "collapse" to some extent upon entering eclipse because the vapor pressure of SO_2 varies by 4 orders of magnitude over the expected surface temperature range for Io's day (~120 K) to nighttime (~90 K). Therefore, the extent and rate at which the atmospheric column collapses upon ingress into eclipse (particularly the response of the upper atmosphere) is critically important for certain physical processes (emission during eclipse, torus supply rates, etc.). As mentioned earlier (Chapter 2.1.3), Io's disk averaged total auroral emission has been observed to decrease during eclipse while certain other emission features brighten during eclipse (Geissler *et al*. 1999, 2001). A time-varying atmospheric model is clearly required to understand Io's electrodynamic interaction with the Jupiter plasma torus during eclipse and the resulting auroral emissions. In order to simulate Io's far-ultraviolet (FUV) brightness during eclipse and upon egress Saur and Strobel (2004) modeled Io's atmosphere as a single species (SO_2) that remained in hydrostatic equilibrium with the surface as it cooled throughout eclipse. However, the assumption that the gas column remains in hydrostatic equilibrium with the surface ignores several physical processes that will influence the atmospheric column and its collapse dynamics. Specifically, the equilibrium assumption neglects atmospheric winds due to pressure gradients (including radial 'winds' due to escape), that the gas has a finite ballistic collapse time, a finite speed of sound, and that non-condensable gas species, specifically SO and O_2, are present.[12]

Based on prior work, one may expect that even a small amount of non-condensable gas would have a significant effect on the atmospheric collapse dynamics. Sone *et al.* (1992) modeled a semi-infinite two species gas mixture flowing towards an infinite surface upon which one of the species condensed, while Taguchi *et al.* (2003) extended the analysis to a

[12] SO is now expected to be at least partially condensable on Io's surface at nighttime temperatures (Laver *et al.*, 2007; Baklouti *et al.*, 2008); however, the identity of the non-condensable gas does not significantly affect the results, as will be shown.

gas mixture flowing at incidence to the surface; similar to what one might expect to find near Io's terminator. They found that the presence of the non-condensable species affected the gas flow. Furthermore, in the continuum limit Aoki *et al.* (2003) found that even a trace amount of non-condensable gas dramatically altered the gas flow's dynamics. The non-condensable gas was found to accumulate in a Knudsen layer along the boundary, retarding condensation and altering the flow field. Hence even a small amount of non-condensable might be expected to significantly alter Io's atmospheric collapse dynamics. However, major differences between the previously modeled flows and Io's atmosphere (Io's finite gas column accelerated by gravity versus an infinite gas column with a constant bulk inflow velocity and the fact that much of Io's atmosphere above ~10 km is rarefied) might diminish the effect of a non-condensable gas.

Therefore, before simulating the aurora several minutes into eclipse (Chapters 7 and 8) the dayside atmospheric dynamics throughout eclipse were simulated. The effect of a small concentration of a non-condensable species on the atmospheric changes during eclipse and egress is of particular interest here. The resultant degree of non-equilibrium and the rate of atmospheric collapse have been investigated for several initial surface temperatures, plasma energy fluxes, and non-condensable species fractions. Note that the following discussion is based on 1-D simulations from an earlier version of the planetary DSMC code which did not have the more sophisticated photo- or plasma-chemistry models. Most of the results presented here were discussed in Moore *et al.* (2009).

4.1 OVERALL MODEL

Our computations simulate the atmospheric dynamics above a specific location (a fixed longitude and latitude) on Io's surface from the time of ingress into eclipse until after egress. The assumption of a 1-D atmosphere limits the validity of the model to regions of Io's surface with relatively small lateral property gradients along the surface. This condition is most likely satisfied everywhere on the surface except near the terminator where there may be a standing shock (Austin and Goldstein, 2000; Walker *et al.*, 2010a). Furthermore, lateral gas flow near the surface would tend to sweep away the non-condensable species over time if lateral gradients in species exist; hence, negligible near-surface winds are needed if significant lateral species gradients exist. Near (±40°) the subsolar point, the near surface wind speed is less than ~10 m/s (and decreases towards the subsolar point); therefore, for a

subsolar zenith angle (SZA) of less than 40° our simulation should be reasonable even near the frost margins where large gradients might exist. Further from the subsolar point, the simulations should remain valid except near frost margins and at large solar zenith angles near the terminator shock (Austin and Goldstein, 2000; Walker *et al.*, 2010a).

4.1.1 Simulation Method

The sublimation atmosphere was simulated by a one-dimensional two species (SO_2 and a non-condensable) model using the direct simulation Monte Carlo (DSMC) method (Bird, 1994). As discussed earlier, DSMC is capable of accurately simulating the near-continuum lower atmosphere as well as the rarefied regime present at higher altitudes. The model used for thses simulations is adopted from our groups Planetary DSMC code that included SO_2 sublimation based on the surface temperature, internal energy modes (rotation and quantized vibration), a radial plasma heating model, and rotational and vibrational cooling. A more detailed description of the planetary DSMC code used here may be found in Austin and Goldstein (2000), Moore *et al.* (2006, 2008), Stewart *et al.* (2009), and Zhang *et al.* (2003, 2004). The bulk of the improvements to the DSMC code discussed in Chapter 3 were not implemented for these simulations. Note that we do not model ion-induced SO_2 sputtering from the surface which may become significant for the simulations of a pure SO_2 atmosphere through eclipse as the column density drops and allows significant ion flux to the surface. However, it should not be a significant factor for the simulations with a non-condensable gas present since the gas column is found to decrease far less.

In the model SO_2 molecules are assumed to have a unit sticking probability on the surface; when an SO_2 molecule hits the surface it is deleted, having condensed onto the surface. This is because the sublimation rate of SO_2 molecules is computed from the SO_2 equilibrium vapor pressure at the current surface temperature and hence if the gas is in equilibrium with the surface then every SO_2 molecule that hits (and condenses onto) the surface will have a corresponding SO_2 molecule sublime from the surface. The non-condensable component is assumed to have a constant probability of sticking to the surface. This probability ranges from 0 for a perfectly non-condensable gas, to 1 for a perfectly condensable gas. If a molecule does not stick to the surface, it is assumed to scatter diffusely off the surface with the local surface temperature. However it should be noted that specularly reflecting the non-condensable molecules off the surface had little effect on the results. The

only significant effect was to increase the near-surface gas temperature upon egress, but this did not change the overall atmospheric dynamics. The model also includes plasma heating (Austin and Goldstein, 2000), though the plasma only transfers translational and rotational energy to the target molecules. By assumption, the plasma neither dissociates nor directly excites the vibrational modes of the target molecules. Chapter 8 discusses results for a 3D atmosphere which includes a more complete model of the plasma's interaction with the atmosphere (i.e. impact dissociation and vibrational excitation), surface sputtering of the SO_2 frost, and photo-chemistry.

The Einstein *A* coefficients for SO radiative de-excitation from excited vibrational states were unavailable. However, it was found that the atmospheric dynamics and the resultant profiles (even vibrational temperature profiles) were insensitive to order of magnitude changes in the Einstein *A* value used for SO. For the following simulations an Einstein coefficient A_{10}=10 s^{-1} was used, similar to that of CO.

4.1.2 Surface Temperature Model

The steady-state dayside surface temperature before eclipse was assumed to follow (Austin and Goldstein, 2000):

$$T_{SS}\big(\theta(t)\big) = \begin{cases} 30cos^{0.25}\big(\theta(t)\big) + T_{s,min} & \theta(t) < 90° \\ T_{s,min} & \theta(t) \geq 90° \end{cases} \quad 4\text{-}1$$

where $T_{s,min}$ is the nightside temperature which was set to 90 K, and $\theta(t)$ is the subsolar zenith angle which varies in time because we are simulating the atmosphere above a given longitude which rotates relative to the subsolar point. Figure 4-1(a) shows a schematic relating the SZA and the local longitude. Note that for a given SZA, there are two corresponding longitudes along the equator. As seen in Figure 4-1(b), the subsolar point just before ingress (point (a)) rotates into the nightside by the time Io has reached eastern elongation. Also note that part of the anti-Jovian hemisphere never enters eclipse since throughout the eclipse it remains on the nightside of Io.

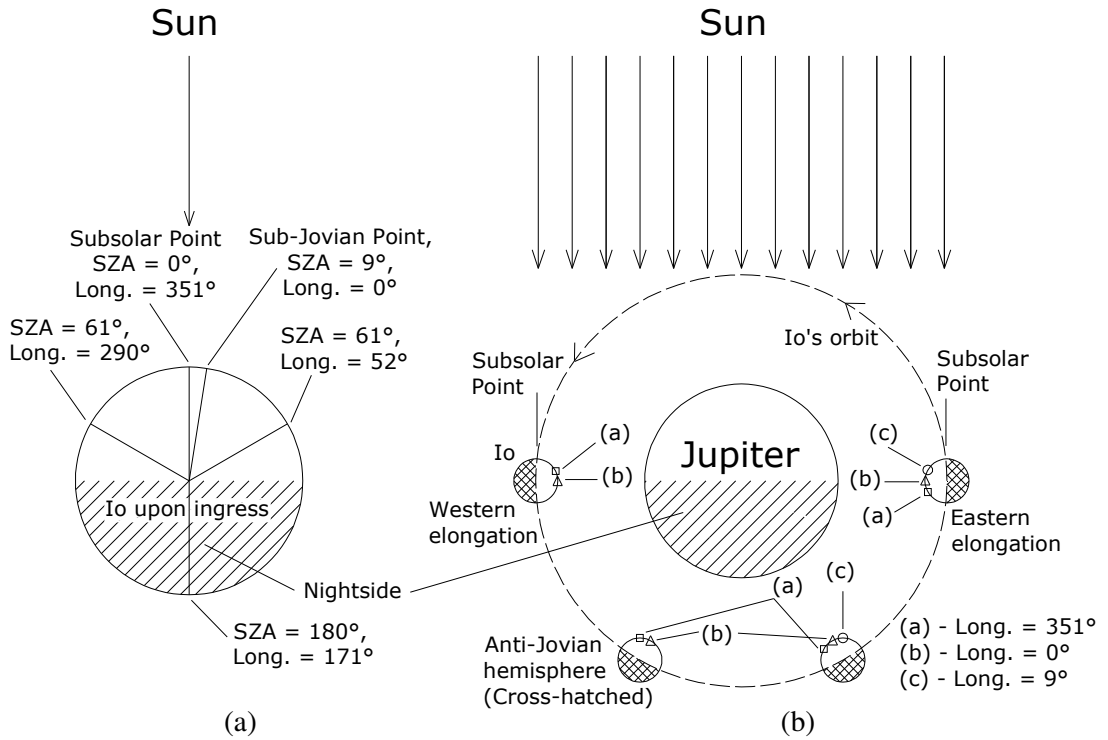

Figure 4-1: Schematic of (a) Io and the relation between sub-solar zenith angle (SZA) and a location's longitude and (b) the Jovian system at various times during Io's orbit. In (b) the SZA of the simulated longitudinal location is seen to change in time as Io orbits Jupiter.

A time-variable surface temperature, $T_s(t)$ was used to model the surface cooling for all times following ingress. The surface temperature was obtained by solving the energy balance equation numerically with a simple forward Euler scheme:

$$\frac{d}{dt}T_s(t) = \begin{cases} \frac{\varepsilon\sigma}{Mc}\left(T_{s,min}^4 - T_S^4\right), & t \le \tau_{Eclipse} \\ \frac{\varepsilon\sigma}{Mc}\left(T_{SS}^4(\theta(t)) - T_S^4\right), & t > \tau_{Eclipse} \end{cases} \quad 4\text{-}2$$

where ε is the bolometric emissivity, σ is the Stefan-Boltzmann constant, M is the local mass per unit area of the surface material, c is the surface's specific heat, and $\tau_{Eclipse}$ is the time spent in eclipse, equal to 120 minutes. Saur *et al.* (2004) computed a value for $(\varepsilon/Mc)^{-1}$ of 350 J-m^{-2}-K^{-1} from observations by Sinton and Kaminski (1988). The value of ε/Mc used in the present simulations was increased and decreased by a factor of two in order to examine the sensitivity of the simulation dynamics to uncertainty in this parameter. Note that thermal conduction of tidal heat from beneath the surface and plasma heating of the surface have been accounted for, to first order, by equating the energy transfer from these sources to the energy lost at the steady-state nightside temperature, $T_{s,min}$. From the desired initial surface

temperature, the corresponding initial SZA can be computed by assuming the temperature is in steady-state before eclipse based on Eqn. 4-1. This in turn sets the specific longitude of the surface point that we are simulating with our initial surface temperature since we are only considering cases along Io's equator. Note that we have neglected the effect on the transient surface temperature of both the latent heat exchange due to the condensing/sublimating SO_2 and the change in the plasma energy flux to the surface as the atmosphere column decreases. Both of these energy sources were verified to be relatively minor *a posteriori*, especially when a non-condensable species was present.

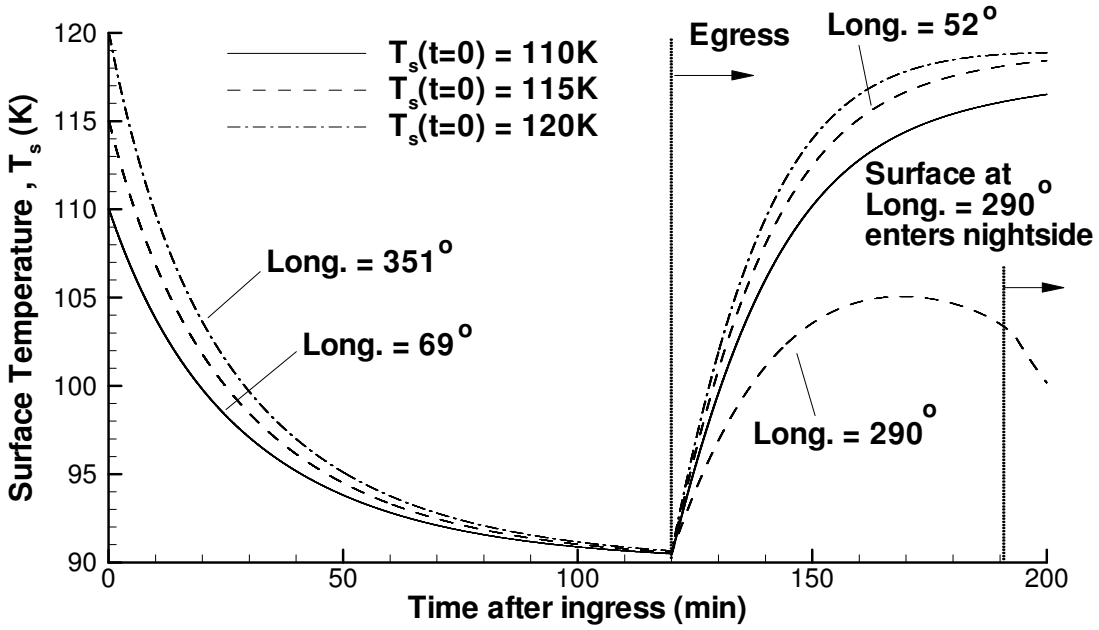

Figure 4-2: Surface temperature versus time for various representative initial surface temperatures and longitudes assuming $(\varepsilon/Mc)^{-1}$ = 350 J-m^{-2}-K^{-1}. The surface temperature for all cases nearly reaches $T_{s,min}$ by the end of eclipse; however, if ε/Mc is cut in half, the temperature falls more slowly and only reaches ~95 K by the end of eclipse.

The resulting surface temperature as a function of time during eclipse is shown in Figure 4-2 and is similar to that obtained by Saur and Strobel (2004). Upon ingress into eclipse the surface temperature asymptotes to the nightside temperature, $T_{s,min}$, with the temperature difference between different initial longitudes (and temperatures) decreasing as eclipse progresses. However, upon egress our modeled surface temperature diverges from Saur and Strobel's because we are simulating a given location on Io's surface as it traverses through eclipse. Hence, as the tidally locked satellite orbits Jupiter during eclipse, the SZA

(equivalently the local time of day) of the simulated location changes as does the local steady-state surface temperature, T_{ss}. Figure 4-2 shows the surface temperature as a function of time computed for several of the cases. Since a given SZA (and hence initial steady state surface temperature) at the equator describes two different longitudes – one on either side of the subsolar point (see Figure 4-1(a)) – the surface point can either proceed into night or approach the subsolar point upon eclipse egress, depending on the longitude. This leads to very different surface temperatures and atmospheric behavior several minutes after egress as shown by the 52° and 290° longitude curves in Figure 4-2.

4.1.3 Steady State Atmosphere Initialization

It was assumed that the atmosphere just prior to eclipse was (nearly) in hydrostatic equilibrium with the surface. Therefore, before simulating ingress into eclipse and the consequent cooling of the surface, it was first necessary to run the simulation atmosphere until it reached steady-state for each initial temperature, such that the SO_2 sublimated from the surface was balanced by condensation onto the surface and loss out of the top of the domain (escape). At Io's surface temperatures it is unclear whether or not SO is non-condensable/non-reactive with the surface (Wong and Johnson, 1996). For the majority of the simulations, we treat SO as a non-condensable species that does not stick to the surface. SO was used for the non-condensable species instead of O_2 (which does not condense/react at Io's surface temperatures) since Smyth and Wong (2004) find that $N_{SO}/N_{O_2} \sim 10$. Thus if SO does not condense then it is the major non-condensable species. However, some simulations were run with O_2 as the non-condensable (assuming SO condenses) and will be briefly discussed.

Since, at the time of these simulations, the model did not account for production of SO (or O_2) from SO_2, or any plasma-induced chemistry, it was necessary to artificially add the second species, SO (or O_2). Once the SO_2 sublimation atmosphere reached steady-state, the second species was added with a uniform mole fraction across the domain and then the atmosphere was run until a quasi-steady-state was re-established. The fraction of SO added is given in Table 4-1 and in most cases is equal to the ratio of the SO column density to the SO_2 column density at the corresponding SZA in Smyth and Wong (2004). We use this value since we are simulating a specific, fixed location on the surface as Io passes through eclipse. Furthermore, note that Jessup *et al.* (2004) constrained the overall anti-Jovian hemisphere

SO/SO_2 ratio to less than 10%. However, for their observations at sub-solar zenith angles near those of our simulations (0°, 61°, and 78°), the observations do not limit the SO/SO_2 ratio to be less than 10% (Table 2 in Jessup *et al.*, 2004). Hence, we choose to use Smyth and Wong's (2004) column densities for SO despite the fact that these simulated column densities may be too high in some regions.

The model does not allow for destruction of SO via ion or electron impact dissociation and hence, as the eclipse progresses and the SO_2 density falls, the simulated SO density is expected to be a little higher than the true SO density. However, the lifetime (the inverse of the reaction frequency) of an SO molecule near the surface (altitudes less than 10 km) is ~4 hours based on a dissociation cross section of 5.3×10^{-20} m^2, an electron temperature of 5 eV, and a conservative effective electron density near Io's surface of ~2000 cm^{-3} (Fig. 2, Smyth and Wong, 2004). Moreover, the SO lifetime based on ion-dissociation is almost 2 orders of magnitude larger than the electron-dissociation lifetime, mainly because of the large thermal velocity difference between ions and electrons. Furthermore, this SO lifetime estimate does not account for the production of SO from the dissociation of SO_2. Neglecting winds, the production of SO should cancel SO dissociation in the steady-state before ingress and during the initial eclipse period, but should be negligible by egress as the SO_2 density decreases. The ~4 hour SO lifetime is therefore a conservative estimate and the reduction in SO density due to plasma dissociation during the 2 hour eclipse should be minor and should not change the overall results dramatically.

4.2 1-D RESULTS

Several cases were simulated in order to examine how the atmospheric behavior upon ingress and egress varied with initial surface temperature (and hence longitude), the properties of the non-condensable species (type, concentration, and sticking probability), the plasma energy flux, and the thermal inertia of the surface. Table 4-1 shows the parameters for the simulated cases. For a given initial surface temperature the initial SZA of the 1-D simulation column can be computed from Eqn. 4-1 and a longitude can be obtained by reference to the subsolar point at the time of ingress which is at 9° longitude. Due to variability of the conditions in the upstream plasma torus of more than a factor of two in time, several plasma energy fluxes were examined to determine the sensitivity of the atmospheric dynamics to the incident plasma energy flux. Previous simulations used a plasma energy flux

from the plasma torus of 1.3 erg cm^{-2} s^{-1} to heat Io's atmosphere (Pospieszalska and Johnson, 1996, Austin and Goldstein, 2000). This value was obtained by accounting for the fact that only a fraction (~20%; Johnson, 1989) of the upstream plasma flux reaches the exobase of Io's atmosphere and the rest is deflected around Io (Wolf-Gladrow *et al.*, 1987; Linker *et al.*, 1988). In otder to obtain a plasma energy flux of 1.3 erg cm^{-2} s^{-1}, it was assumed that only 20% of the upstream torus plasma reaches the exobase, that the average ion energy (due to co-rotation kinetic energy) is nearly 400 eV (Pospieszalska and Johnson, 1996), and that the upstream torus density was ~1750 cm^{-3} (Sittler and Strobel, 1987). In fact, the fraction of plasma reaching the exobase will almost certainly change as eclipse proceeds due to variations in the atmospheric column (Saur and Strobel, 2004). In addition, the upstream torus density at the time of Galileo was closer to ~3600 cm^{-3} (Frank *et al.*, 1996), a factor of ~2 higher than during Voyager 1. As indicated in Table 4-1, a nominal plasma energy flux of 5 erg cm^{-2} s^{-1}, as well as cases with high (10 erg cm^{-2} s^{-1}) and low (1 erg cm^{-2} s^{-1}) plasma energy fluxes were used.

Table 4-1: Simulation parameters for each case. [1]Smyth and Wong (2004)

Case #	$T_s(t=0)$ (K), SZA (°)	Longitude (°)	N_{nc} / (N_{total})	Non-condensable species	Plasma Flux (erg s^{-1} cm^{-2})	$(\varepsilon/Mc)^{-1}$ (J-m^{-2}-K^{-1})	Timestep (s)
1	110, 78	69	0	-	5	350	0.1
2	110, 78	69	0.07 [1]	O_2	5	350	0.1
3	110, 78	69	0.35	O_2	5	350	0.1
4	110, 78	69	0.35 [1]	SO	1	350	0.1
5	110, 78	69	0.35 [1]	SO	5	350	0.1
6	110, 78	69	0.35 [1]	SO	10	350	0.1
7	110, 78	69	0.35 [1]	SO	5	700	0.1
8	110, 78	69	0.35 [1]	SO	5	175	0.1
9	115, 61	52	0	-	5	350	0.03
10	115, 61	52	0.22 [1]	SO	5	350	0.03
11	120, 0	351	0	-	5	350	0.006
12	120, 0	351	0.03 [1]	SO	5	350	0.006

The timestep size (given in Table 4-1) was chosen such that it was less than the mean time between collisions everywhere in the domain and at all times during the simulation and therefore it varied depending on the simulation parameters. Since the lifetime for de-excitation through spontaneous emission from certain excited vibrational states is smaller than our simulation timestep, it was necessary to use a finer timestep, or sub-step, to correctly model the de-excitation as discussed in Chapter 3.1.

4.2.1 Simulation Grids

The grid spacing increased linearly up to a given altitude, then increased linearly with a different stretching constant up to a second altitude, and finally increased linearly to the edge of the domain with yet another stretching constant if needed. In order to determine the linear stretching and the altitude ranges needed to have adequate grid resolution for each case, the simulation was first run with an exponential-constant grid. For this grid an exponential grid was used below 50 km, and a constant grid size of 15 km was used above this altitude. The number density profiles obtained from these coarse, under-resolved cases allowed us to estimate the necessary grid distribution with altitude at steady-state by computing the mean free path. Linear segments were then fit to the desired grid distribution and used to generate the grid for the eclipse simulations. Linear segments were used because the density profiles were not exponential even in steady state due to the plasma heating. Furthermore, linear segments are easily invertible and hence computing a molecule's grid location during the index subroutine is simple. However, note that the grid used here was not adapted during the simulation; in fact these simulations served as the impetus for developing the adaptable invertible grid discussed in Section 3.2. The 3D atmosphere results in Chapter 8 utilize the adaptable grid.

In all cases the computational domain extended to an effective altitude of ~1000 km and had between ~1000 cells (110 K initial surface temperature cases) and ~10000 cells (120K initial surface temperature cases). The last cell of the domain was extended from ~1000 km to 2000 km in order to model the upper escape boundary condition more correctly by reducing the number of molecules actually reaching the top boundary to a trivial number. Of the small number of molecules which cross the top boundary (at 2000 km), only those with a velocity exceeding the escape velocity are deleted, the rest are instantly reflected. The last cell is extended to such high altitudes to prevent the reflected molecules (which should have come back into the domain after a time delay) from affecting the lower atmosphere during the unsteady collapse and reformation.

Grid convergence was assured in two ways: (1) the grid size was everywhere less than the local mean free path at all times during the simulation, and (2) reducing the cell size by a factor of two did not change the solution (outside of the noise). Sensitivity to the number of molecules per cell was also checked by doubling the number of simulation molecules. For the simulations with a non-condensable species, on the order of 10^6 computational molecules

(at the initial surface temperature) were used. This resulted in >4 molecules (and at least 2 molecules of each species) per cell below altitudes of ~500 km at all times during the simulations even as the surface cools and the column density drops. For the pure SO_2 atmosphere simulations ~2×10^7 computational molecules were used; however, by the end of the eclipse computational cells above ~200 km had zero simulation molecules because of the extremely low density due to the more pronounced collapse of the atmosphere in the absence of a non-condensable. We utilized ensemble averaging over many (~50) different runs with different random number seeds in order to reduce the simulation noise at high altitudes and after long times into eclipse.

4.2.2 Overview of Eclipse Atmospheric Dynamics

Before discussing the specifics of each simulated case, we present an overview of the atmospheric collapse and reformation dynamics illustrated in Figure 4-3. Note that the initial steady state atmosphere is collisional enough at low altitudes such that the two species mix and there is a single scale height based on the reduced mass of the species. At higher altitudes above the homopause, where the atmosphere is no longer collisional, the SO and SO_2 have different scale heights based on their respective masses and hence eventually the SO number density exceeds the SO_2 number density. At early times during eclipse, the surface temperature (and hence the equilibrium SO_2 vapor pressure) drops and both the SO_2 and SO gas develop bulk velocities toward the surface. The duration of this early eclipse period depends mainly on the initial absolute amount of non-condensable near the surface. Once the non-condensable has built up a diffusion layer several mean-free paths thick (~20 minutes into eclipse), the atmospheric collapse slows dramatically and both species essentially stop falling toward the surface. The SO gas (which does not react with the surface) actually develops a small upward bulk velocity as the atmosphere establishes a new, larger, scale height (seen in the center panel of Figure 4-3) since it no longer is collisionally mixed at low altitudes with the heavier SO_2. Eventually the SO density greatly exceeds the SO_2 number density far above the surface due to this upward migration of SO gas. Near the surface SO_2 condensation lowers the SO_2 density below the non-condensable's density.

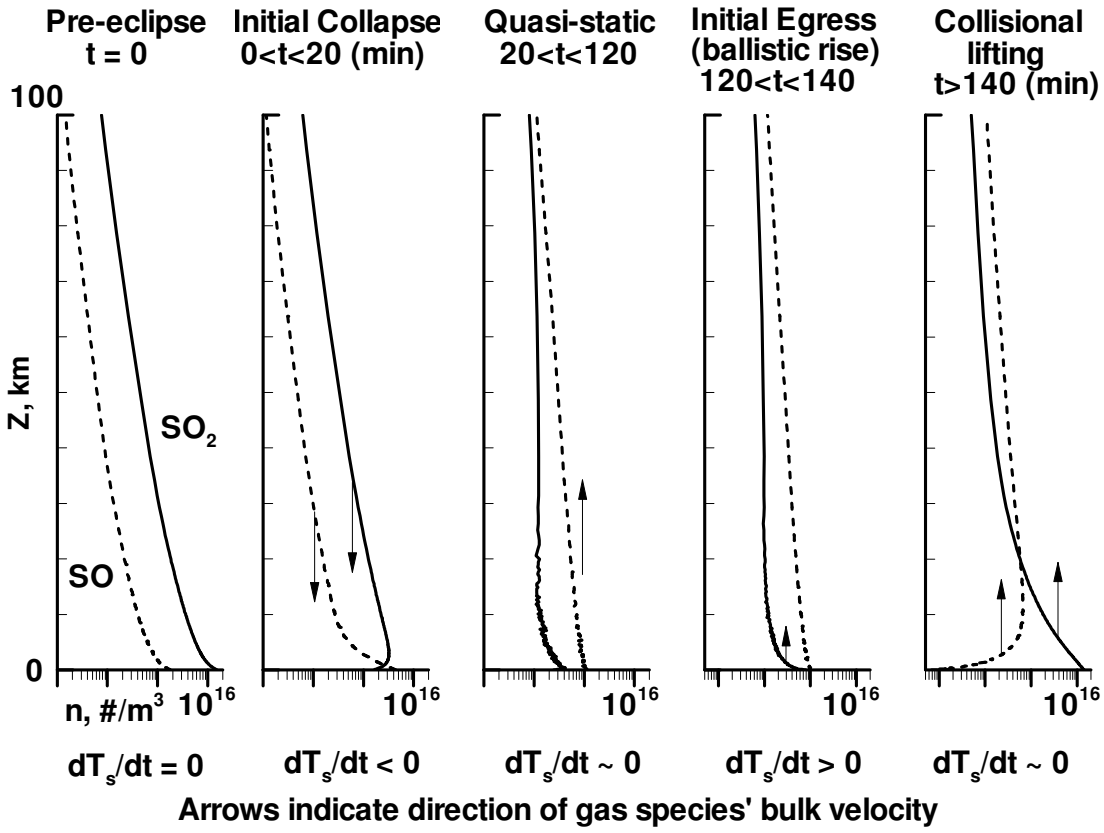

Figure 4-3: Overall schematic of the atmospheric dynamics throughout eclipse and egress. The altitude is shown on a linear scale on the vertical axis up to 100 km and the number density is shown on a log scale from 10^{13} to 2×10^{16} m^{-3}. The solid lines represent SO_2 and the dashed lines the SO number density. Several distinct periods (labeled at the top) occur during eclipse and early egress and are shown from left to right. For reference the initial quasi steady-state atmosphere just before eclipse is shown in the left-most plot.

Once egress starts, for surface longitudes that are not entering dusk upon egress, a new period begins with increased SO_2 gas sublimation from the surface; however, the gas densities are initially low enough that the atmosphere is collisionless. Therefore the SO_2 gas sublimes ballistically away from the surface and little to no momentum is transferred to the SO. Roughly 20 minutes into egress the gas is sufficiently collisional that a transition occurs as non-negligible momentum transfer from the sublimating SO_2 to the SO gas occurs and the SO is lifted to higher altitudes. Since there is no source of SO, this in turn leads to a several orders of magnitude drop in the SO density near the surface and thus the atmosphere becomes stratified as compared to the species distribution in the pre-ingress atmosphere. After stratification has occurred there is primarily SO_2 at low altitudes and a roughly 70/30 mixture

of SO and SO_2 at higher altitudes. The simulation was not run all the way to ingress again since it would be relatively meaningless without plasma chemistry and photo-dissociation. Hence whether or not the post-eclipse atmosphere recovers to the initial condition atmosphere is unknown. However, the simulation was run long enough past egress to observe the species stratification lessening due to diffusion, suggesting that the initial atmospheric profiles might be recovered over the course of ~40 hours past egress.

4.2.3 Ingress

Having given a brief overview of the atmospheric dynamics during eclipse, the following section will discuss the dynamics during ingress into eclipse in detail. Figure 4-4 shows the total number density, temperature, and SO mole fraction plotted as a function of altitude at three different times near the start of eclipse for an initial surface temperature of 110 K. Figure 4-4(a) (Case 1) shows the atmospheric response without the presence of a non-condensable. Note that due to the low total column density at a surface temperature of 110 K, the plasma penetrates to the surface and the gas temperature is seen to increase monotonically with altitude and time near the surface even as the surface temperature drops and the gas condenses. In Figure 4-4(a), the SO_2 number density near the surface drops by ~1 order of magnitude after 10 minutes because the radiative cooling of the surface during eclipse reduces the SO_2 vapor pressure by several orders of magnitude. However, the atmosphere above ~100 km remains relatively unaffected shortly after eclipse because the finite ballistic times and speed of sound (~230 m/s) limit the response of the upper atmosphere to temperature changes at the surface. If the model were to include warming due to SO_2 condensation onto the surface, then the cooling rate of the surface would be reduced slightly though it would still cool faster than Case 7 with an $(\varepsilon/Mc)^{-1}$ equal to 700 J-m^{-2}-K^{-1}.

Figure 4-4(b) (Case 5) shows that the atmospheric response with a non-condensable (SO) present is substantially different. In Figure 4-4(b), after 10 minutes the SO_2 number density near the surface is seen to drop by a factor of only ~5. The gas temperature remains essentially the same (because the total gas column density as seen by the impinging plasma from above remains nearly constant) and the mole fraction of SO near the surface increases from ~30% initially to ~84%. Above ~20 km there is little change in the SO_2 density indicating that something other than the finite ballistic times limits the collapse, in contrast to the pure SO_2 case. After 10 minutes the mean free path of SO_2 near the surface is ~60 m;

therefore, an SO diffusion layer (an SO mole fraction greater than 50%) ~30 mean free paths high has formed severely restricting net convection towards the surface. Thirty minutes past ingress (not shown) the SO_2 density near the surface drops by another factor of 5, but remains relatively unchanged above ~30 km. By comparison, without the non-condensable present (Case 1 Figure 4-4), the density drops significantly up to altitudes of ~300 km thirty minutes past ingress. The formation of this static collisional diffusion layer (in Case 5) clearly retards the rapid freeze-out of the lower SO_2 atmosphere as compared to the case without the non-condensable species present.

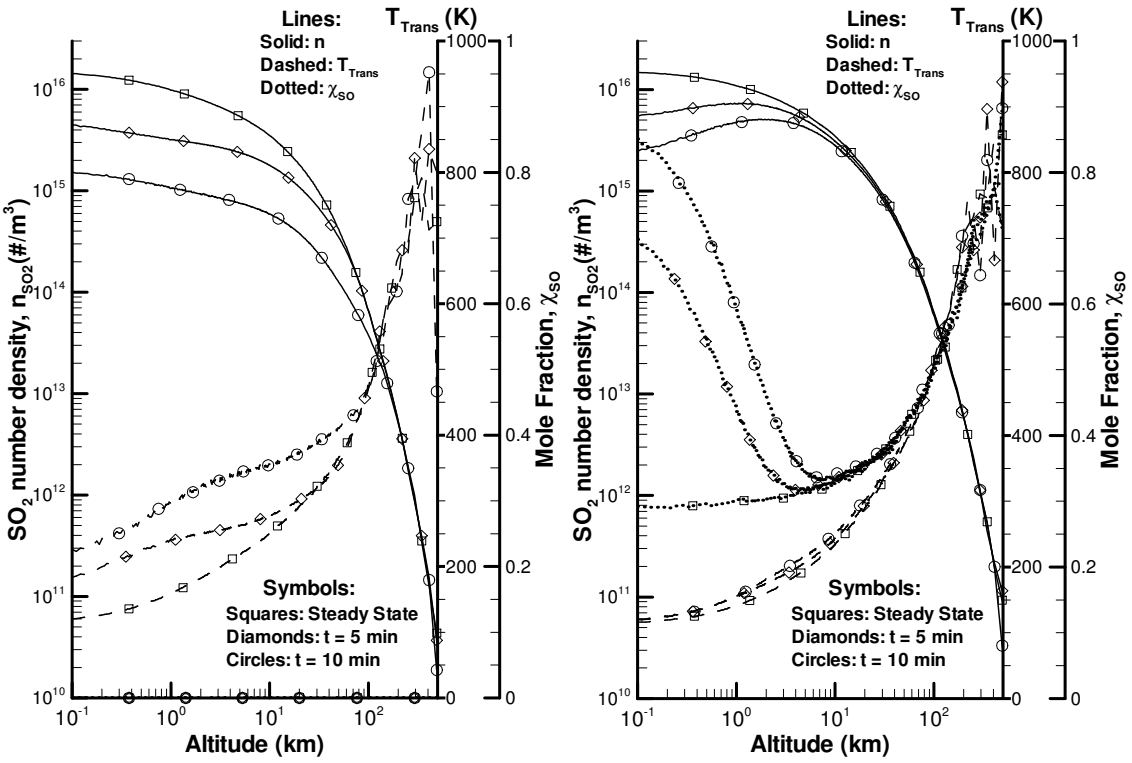

Figure 4-4: Atmosphere profiles (number density, temperature, and non-condensable mole fraction) upon ingress and 5 and 10 minutes post ingress for an initial surface temperature of 110 K and (a) no non-condensable species (χ_{SO} =0 everywhere, Case 1), (b) non-condensable mole fraction (χ_{SO}) of 0.35 for the total gas column (Case 5).

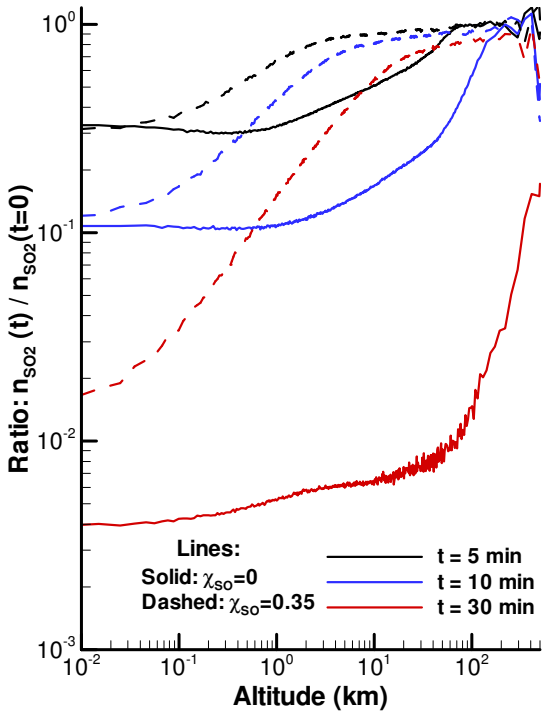

Figure 4-5: Ratio of SO_2 atmospheric density profiles at 5, 10, and 30 minutes after ingress into eclipse to the initial steady state SO_2 density. The solid lines are the profiles if there is no non-condensable (χ_{SO} =0 everywhere, Case 1) and the dashed lines are profiles if there is a non-condensable mole fraction (χ_{SO}) of 0.35 for the total gas column (Case 5).

The ratio of the SO_2 density to the initial, steady state SO_2 density versus altitude is shown in Figure 4-5 at several times after ingress. The solid lines are the ratio profiles if there is no non-condensable (SO or O_2) present (Case 1) while the dashed lines are the profiles with 35% SO present (Case 5). It is clear that the presence of the non-condensable dramatically reduces the collapse of the SO_2 atmosphere. Note that the assumption of instantaneous hydrostatic equilibrium with the surface would result in horizontal lines corresponding to the surface temperature at that instant. Clearly, that assumption is poor at 'high' altitudes and when there is a non-condensable present. In the absence of a non-condensable, it turns out that the instantaneous SO_2 density approaches the density predicted by hydrostatic equilibrium with decreasing altitude. Very near the surface the simulated ratios are only slightly higher than the instantaneous equilibrium value due to the slight increase in number flux from the higher altitudes. As can be seen there is a relatively well defined altitude below which significant deviations from the steady state density occur. This altitude

is especially sharp in the absence of a non-condensable since the non-condensable acts to diffuse this boundary. Furthermore, without the presence of a non-condensable the altitude at which significant deviations from the steady state density occur is given by the speed of sound multiplied by the time since eclipse. Note that with the non-condensable diffusion layer obstructing the flow of SO_2 towards the surface, the altitude of significant deviation from steady state is considerably lower. Curves such as these are used to scale the sublimation atmosphere (to account for eclipse) in the aurora simulations that use Wong and Smyth's (2000) dayside sublimation atmosphere model (see Section 6.2.2).

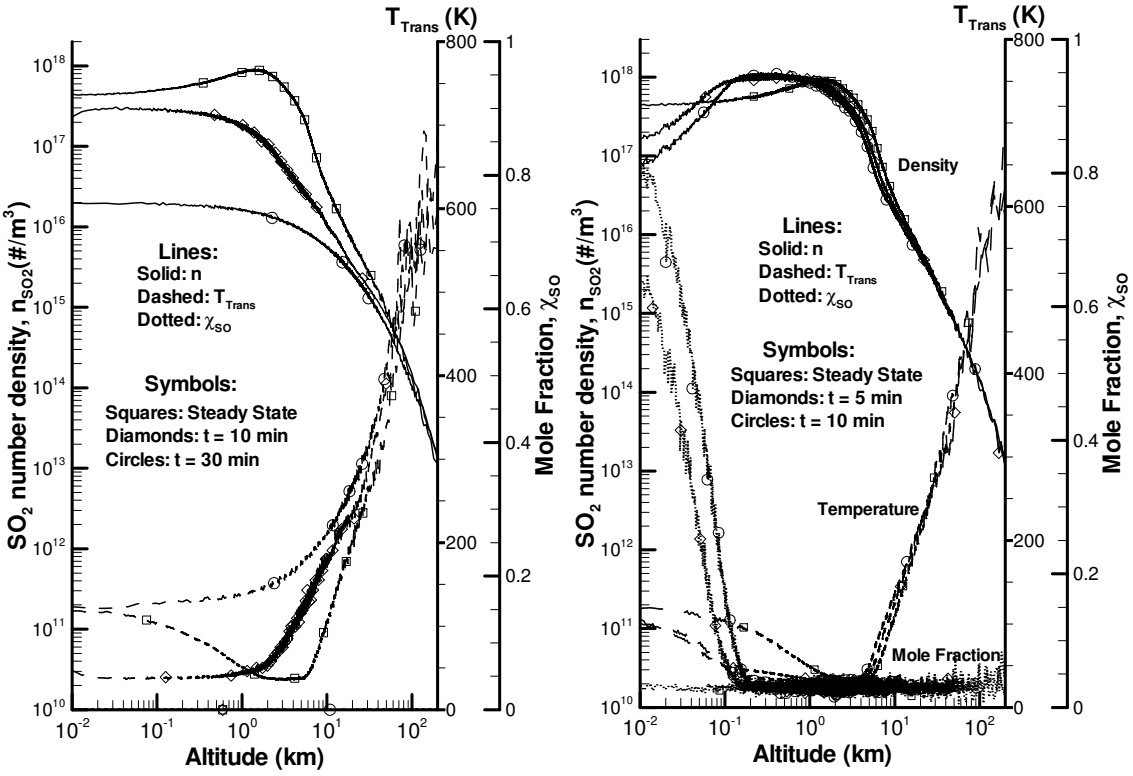

Figure 4-6: Atmosphere profiles during eclipse for an initial T_s of 120 K and (a) no non-condensable (Case 11) and (b) 3% SO mole fraction (Case 12). Note that slight smoothing has been used for some curves to improve clarity.

In Figure 4-6 (Cases 11 and 12) the total number density, temperature, and SO mole fraction are again plotted as functions of altitude at several times near the start of eclipse but this time for an initial surface temperature of 120 K. In this case the initial SO mole fraction is only 3%; however, the SO column density is nearly equal to the SO column density for

Case 5 (35% SO mole fraction, 110 K initial surface temperature). Note that the plasma (for the plasma heating model used in these runs) does not penetrate all the way to the surface initially. Since the plasma only heats the atmosphere down to ~5 km, the temperature drops with altitude near the surface (with a minimum at ~5 km), due to rotational and vibrational radiative cooling of SO_2 and SO in the transparent, collisional atmosphere. The temperature then rises at higher altitudes where the plasma warms the gas. This drop in temperature with altitude near the surface leads to an increase in the number density with altitude near the surface; however, the pressure (not shown) still decreases monotonically with altitude as one would expect for hydrostatic equilibrium.

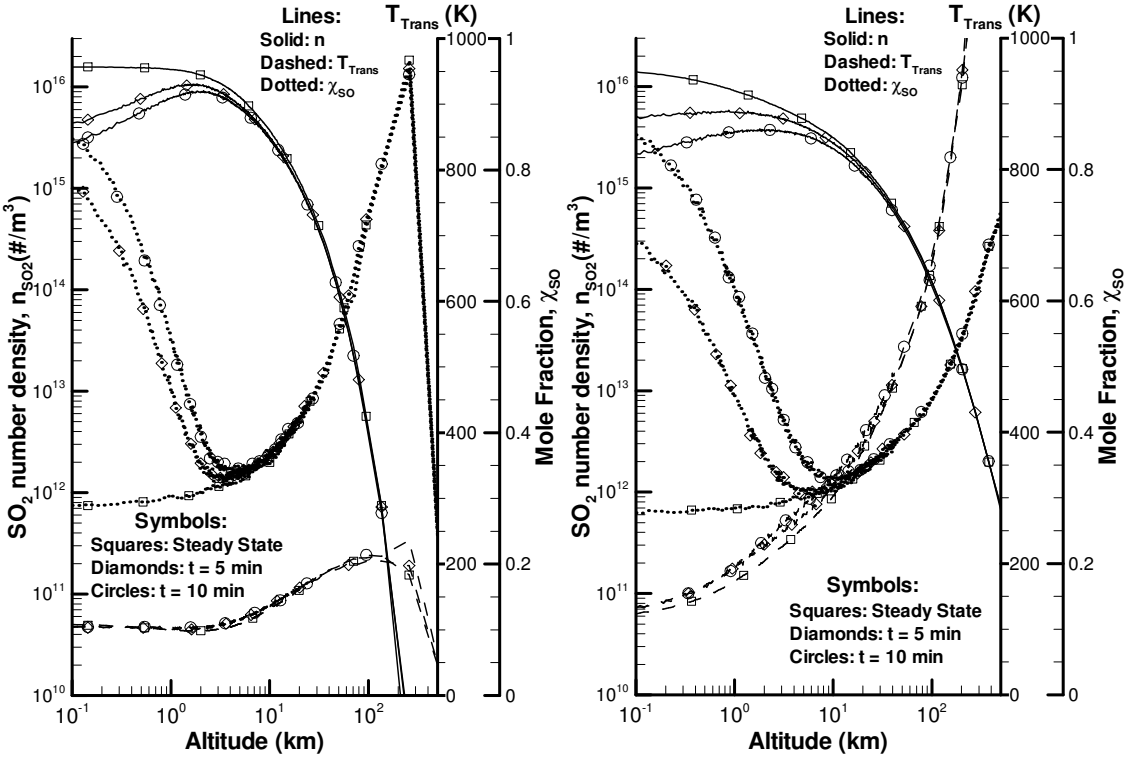

Figure 4-7: Atmosphere profiles for an initial surface temperature of 110 K and (a) a plasma energy flux of 1.0 erg cm^{-2} s^{-1} (Case 4) and (b) a plasma energy flux of 10.0 erg cm^{-2} s^{-1} (Case 6).

As with the 110 K pure SO_2 case (Case 1, shown in Figure 4-4(a)), the number density and other properties for the 120 K pure SO_2 case (Case 11, Figure 4-6(a)) are essentially unchanged above ~100 km 10 minutes into the eclipse. Near the surface, the number density drops by a factor of ~20 after 10 minutes and the density inversion seen in

steady state is no longer present because the plasma now penetrates to the surface. When the nominal amount (3%) of non-condensable SO is present (Case 12, Figure 4-6(b)), after 10 minutes the atmospheric properties above ~20 km do not change, just like the 110 K case. The effect of the diffusion layer to prevent SO_2 at higher altitudes from reaching the surface is clearly seen in Figure 4-6(b). The SO_2 density drops sharply below 100 m as the SO mole fraction increases dramatically from 3% at 100 m to 80% 10 m above the surface. After 10 minutes the diffusion layer is ~50 m thick which corresponds to ~20 mean free paths.

The atmospheric profiles early in eclipse for a smaller, 1.0 erg cm^{-2} $s^{\neg 1}$ (Case 4), and larger, 10 erg cm^{-2} s^{-1} (Case 6), plasma flux are shown in Figure 4-7. Other parameters are the same as Case 5. Note that the density drops off with altitude much faster for the lower plasma flux since the atmosphere is much colder and the scale height therefore much smaller. Also, the lower plasma energy flux does not fully penetrate the atmosphere and the gas temperature drops slightly near the surface due to expansion and rotational radiative cooling. Though the initial steady state density and temperature profiles shown in Figure 4-7(a) and (b) are different, the collapse proceeds at similar rates, with the lower plasma energy flux case forming the thick diffusion layer slightly faster than the high plasma energy flux case. The similarity is primarily due to the fact that the amount and vertical distribution of non-condensable is essentially the same for each case because in this model the plasma does not control the formation of the non-condensable. The collapse is more pronounced after 5 minutes for the lower plasma flux; however, after 10 minutes the SO_2 density near the surface is essentially the same for each case. This is because once the diffusion layer reaches a certain thickness relative to the mean free path the loss of SO_2 to the surface slows substantially. Furthermore, though not shown, the profiles remain very similar for the remainder of the eclipse.

If SO were, in fact, condensable (and hence its effects on the collapse dynamics could be ignored since it is a minor species), then O_2 would take the role of the major non-condensable species. Case 3 examined the collapse dynamics when O_2 was used as the non-condensable and every other parameter was the same as the base SO Case (5). Very little difference in the collapse dynamics was found; once again a diffusion layer many mean free paths formed early on in the eclipse which slowed the collapse considerably. The similarity exists because the SO and O_2 collision cross sections differ by less than 10% and therefore a similar amount of non-condensable is needed near the surface to form the diffusion layer

whose effect overwhelms the effect of the mass difference between the two species. Furthermore, our plasma energy deposition cross section was a constant and therefore did not depend in any way on the concentration or type of species present.

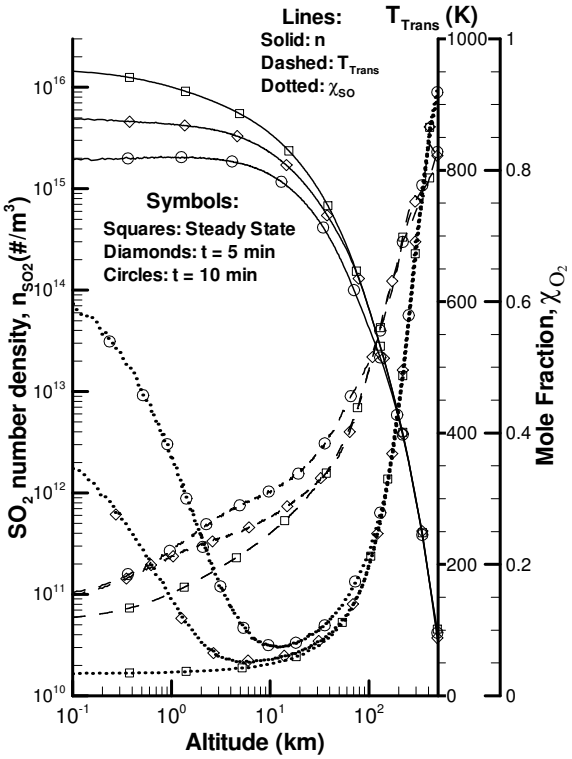

Figure 4-8: Atmosphere profiles during eclipse for an initial surface temperature of 110 K and a non-condensable mole fraction (χ_{O_2}) of 0.07 for the total gas column (Case 2).

On Io, however, the column density (and correspondingly the mole fraction) of O_2 is roughly 5 to 10 times less than the SO column (mole fraction) depending on the SZA. For the 110 K case (2) at a SZA of 78°, the O_2 column density is just ~7% of the SO_2 column density (Smyth and Wong, 2004). As shown in Figure 4-8, despite the much smaller amount of non-condensable, a collisionally thick O_2 diffusion layer still forms during eclipse and the atmospheric collapse is slowed dramatically as compared to the pure SO_2 case (1) shown in Figure 4-4(a). In Figure 4-8 the total number density is seen to decrease only slightly more than in the SO case (5) (Figure 4-4(b)), and the mole fraction of O_2 near the surface rises to 50% ten minutes after ingress. Similar insensitivity to whether SO or O_2 is the non-condensable species was found for the other initial surface temperature cases and suggests

that only a small amount (<7%) of a non-condensable is necessary in order to substantially alter the collapse dynamics.

Figure 4-9 summarizes the previous simulations by comparing the total SO_2 column density during eclipse and shortly after egress to see the effect of the diffusion layer on the various cases. Nine curves are shown corresponding to different cases; in each case the initial surface temperature is 110 K. The equilibrium column density curve (assuming the entire atmospheric column is in equilibrium with the surface) is plotted from the analytic solution obtained by assuming constant gravity, a hydrostatic, isothermal atmosphere, and using the saturation vapor pressure of SO_2 (Wagman, 1979):

$$N_{SO_2} = 1.516 \times 10^{13} \exp\left[-\frac{4510}{T_s(t)}\right] / m_{SO_2} g_{Io} \qquad 4\text{-}3$$

where m_{SO_2} is the mass of SO_2 (kg), and g_{Io} = 1.81 m/s^2. The assumption of constant gravity is valid since Io's atmospheric scale height (~10 km) is very small compared to the radius of Io (1820 km) and hence g_{Io} will not vary much across the bulk of the atmospheric column. Furthermore, the initial analytic column density was very close to the initial simulated column densities even though the simulated atmospheres were not isothermal (due to the plasma flux).

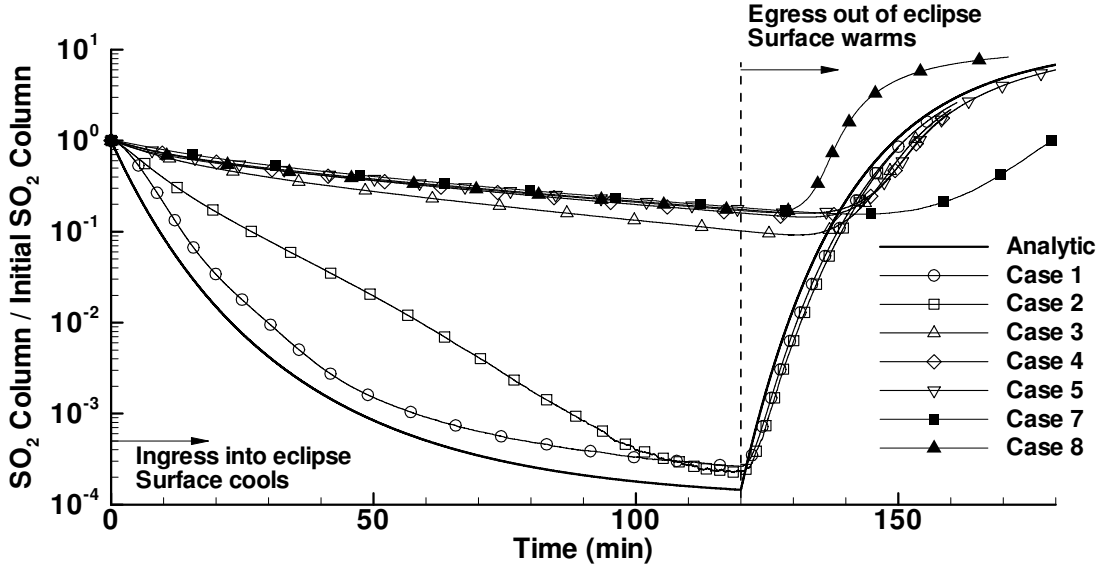

Figure 4-9: Normalized SO_2 column density during eclipse and egress for various cases with initial surface temperatures of 110 K; other initial surface temperature values showed similar results. Note that the Analytic case assumes the nominal value for ε/Mc.

It is seen in Figure 4-9 that the equilibrium (analytic) SO_2 column density drops ~4 orders of magnitude during eclipse; however, the SO_2 column for the simulated result with pure SO_2 (case 1) is seen to lag slightly behind the equilibrium solution due to the finite ballistic fall times which limits the altitude at which the surface temperature drop is felt. However, with a non-condensable present (cases 2–8) the simulated DSMC result lags substantially behind the equilibrium result since a relatively large amount of SO_2 is prevented from condensing by the diffusion layer. Specifically for the cases 3–8, the column density only drops ~75% by the end of eclipse. Note that it is the relative amount of non-condensable (cases 2 and 5) which controls the rate at which the SO_2 column decreases. The smaller the non-condensable mole fraction, the smaller the diffusion layer that is formed and the more readily the SO_2 gas can diffuse through the non-condensable layer. There is virtually no difference in the SO_2 column when the plasma energy flux is decreased/increased (cases 4–6) and only slight differences (due to slightly different cross sections) when the non-condensable species is changed (cases 3 and 5). Furthermore, during eclipse, changing ε/Mc (cases 5, 7, and 8) had virtually no effect on the collapse dynamics if a non-condensable gas was present. The finding that a substantial column of SO_2 can remain throughout eclipse is at odds with the suggestion that the aurora emission observed during eclipse requires that the atmosphere have a substantial volcanic component (Geissler et al., 2004b, Saur and Strobel, 2004). All that seems to be needed is a modest amount of some non-condensable to prevent collapse.

In order to better quantify the atmosphere's initial collapse, we define the collapse time, τ_c, to be the time at which the simulated SO_2 column density is e^{-1} of the initial SO_2 column density,

$$\frac{N_{SO_2}(t=\tau_c)}{N_{SO_2}(t=0)} = e^{-1}. \qquad 4\text{-}4$$

Only the SO_2 column was used to determine this collapse time because no substantial loss mechanism for the SO is included in the model.[13] For reference, the analytic collapse times (obtained using Eqn. 4-3 in Eqn. 4-4) for initial surface temperatures of 110, 115, and 120 K are 3.9, 2.9, and 2.4 minutes respectively except for cases 7 and 8 (increasing and decreasing ε/Mc by factors of two, respectively) which have analytic collapse times of 7.3

[13] Jeans escape occurs but is negligible

and 1.8 minutes. The collapse time for each simulation case is shown in Table 4-2. Note that even without a non-condensable species (case 1) the time to collapse is ~83% longer than predicted by assuming the gas column is in equilibrium with the surface; the upper atmospheric response lags the surface changes due to the finite speed of sound, i.e. the propagation speed of pressure disturbances. Even small concentrations of a non-condensable species dramatically increase the collapse time. Also, we find that the amount of plasma energy flux has little effect on the overall collapse time. This might be expected because our plasma model mainly controls the overall thermal structure of the atmosphere. This in turn affects the ballistic collapse time by increasing the scale height, but should do little to alter the dynamics of the diffusion layer. Even changes in ε/Mc have little effect on the collapse time indicating that, when a non-condensable is present, the gas column dynamics are largely de-coupled from the rate of surface cooling because of the formation of the diffusion layer. Also note that, for a pure SO_2 atmosphere, the collapse time decreases as the initial surface temperature rises. This is because of the difference in the atmospheric density profiles with altitude (compare Figure 4-4(a) and Figure 4-6(a)) which then translates into differences in time for the bulk of the atmosphere to reach the surface ballistically.

Table 4-2: Simulated Atmospheric Collapse Times into Eclipse.

Case	τ_c (min)	$\tau_c / \tau_{c,analytic}$
1	7.1	1.83
2	10.7	2.74
3	33.8	8.66
4	49.2	12.61
5	51.8	13.28
6	51.1	13.11
7	57.4	14.73
8	50.2	12.87
9	4.5	1.56
10	$>\tau_{Eclipse}$	-
11	3.6	1.5
12	75.9	31.63

The simulated collapse time versus the non-condensable mole fraction is shown in Figure 4-10(a). Not surprisingly, the collapse time increases with increasing non-condensable mole fraction. Therefore, the disk averaged total (SO, O_2, etc.) non-condensable mole fraction might be further constrained by auroral intensity observations during eclipse. Previous auroral intensity observations have suggested that the atmospheric collapse occurs in the first

~20 minutes after ingress and that the emission intensity changes little over the rest of the eclipse (Retherford *et al.*, 2007b; Geissler *et al.*, 2004b; Clarke *et al.*, 1994). If the observed emission decrease is due to a corresponding decrease in the SO_2 column density, then Clarke *et al.*'s (1994) finding of a ~33% decrease in FUV emission intensity within 20 minutes constrains the disk averaged total (SO, O_2, etc.) non-condensable mole fraction to less than ~15% since the majority of the dayside is hotter than 110 K.

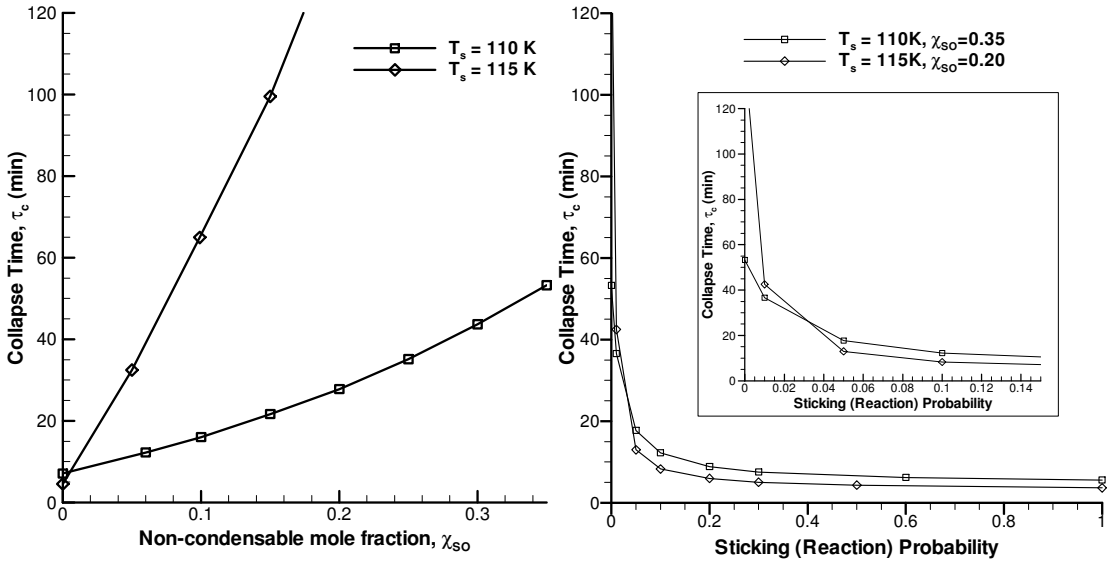

(a) (b)

Figure 4-10: The simulated collapse time versus (a) The non-condensable mole fraction present in the total atmospheric column upon ingress and (b) The sticking (or surface reaction) probability. The non-condensable present was SO and a plasma energy flux of 5 erg cm^{-2} s^{-1} was used.

It is seen in Figure 4-10(a) that for the same mole fraction, the hotter the initial surface temperature, the longer the collapse time except if non-condensables are only present in trace amounts. The reason that the 115 K pure SO_2 atmosphere collapses faster than the 110 K pure SO_2 atmosphere is because the vertical structure of the gas columns are different. For the 115 K steady state case, there exists (as seen in Figure 4-6(a) for the 120 K case) a density peak just above the surface because the plasma does not penetrate to the surface and the gas radiatively cools. As the surface cools and the sublimation vapor pressure at the surface drops, this density peak falls towards the surface and a rapid loss of column density results as it condenses onto the surface. For higher concentrations of non-condensable, the hotter initial surface temperature leads to longer collapse times because the SO_2 column

density increases with increasing surface temperature. Hence, for a given initial non-condensable mole fraction, increasing the surface temperature increases the absolute amount of non-condensable. The increased amount of non-condensable leads to a denser diffusion layer near the surface and therefore a thicker diffusion layer relative to the mean free path and an even slower collapse. However, if it is only present in trace amounts then there is not enough non-condensable to form a collisional diffusion layer.

In all the simulations discussed so far the non-condensable was assumed to be perfectly non-condensable upon the surface. However, one might expect fractional sticking or reactivity with the surface (likely for SO) to alter our simulated collapse dynamics. In order to see the effects of partial reactivity on the collapse dynamics, the SO was allowed to stick to (or react with) the surface and be permanently lost with a probability (or coefficient), $P_{stick} \leq 1$; the results are shown in Figure 4-10(b). It was found that for a given initial non-condensable mole fraction, χ_{nc}, the collapse dynamics were very different depending on the fractional condensability, P_{stick}. As seen in Figure 4-10(b), the atmospheric collapse time was found to be extremely sensitive to P_{stick}; for sticking probabilities greater than ~0.25 the collapse time was virtually identical to the collapse time for a pure SO_2 atmosphere despite large initial SO mole-fractions. Furthermore, even very small sticking coefficients (~0.02) reduce the collapse time by a factor of ~2 over the perfect non-condensable case. There are two main causes of the extreme sensitivity to the sticking coefficient. First, if the SO molecule does not stick upon hitting the surface, then the ballistic bounce time leaving the surface is $13.56\sqrt{T_s}$, or ~140 seconds for a surface temperature of 110K; however, collisions will tend to reduce this time. Furthermore, the fraction of non-condensable molecules lost to the ground after N_B bounces is

$$F_{lost} = (1 - P_{Stick})^{N_B} \qquad 4\text{-}5$$

and hence, as the eclipse progresses, the number of "non-condensable" molecules available to sustain the diffusion layer decreases.

From Eqn. 4-5, for a 10% sticking probability, roughly half of the molecules have been lost after 15 minutes (T_s = 110K) and thus the size of the diffusion layer relative to the mean free path is greatly reduced. In addition to the reduction in the diffusion layer's size, a non-zero sticking probability actually prevents an effective diffusion layer from forming. For a true non-condensable (P_{stick} = 0), the formation of the diffusion layer brings the column of gas above it essentially to rest, and the SO_2 gas above the SO layer must diffuse through the

layer in order to reach the surface and condense as discussed earlier. However, for a non-zero sticking probability, the SO layer retains a slight vertical velocity into the surface and hence does not bring the gas column above to rest. Thus the SO_2 gas above can convect to the surface (with the convection velocity set by P_{stick}) instead of having to diffuse slowly to the surface.

4.2.4 Egress

The total SO_2 column density upon egress for several cases is also shown in Figure 4-9. It is seen that the SO_2 column density does not increase immediately upon egress for the simulated cases and that the larger the non-condensable mole fraction is, the larger the time until the column increase begins. The time lag between egress and post-eclipse brightening should be indicative of the non-condensable mole fraction present – if post-eclipse brightening is due to atmospheric emission. The simulated column densities continue to *decrease* upon egress because the non-condensable diffusion layer (and to a much lesser extent the ballistic collapse time) prevents the SO_2 number density near the surface from being in equilibrium with the surface. Specifically, the equilibrium SO_2 number density upon egress is ~2×10^{12} m^{-3} whereas the simulated number density is ~50 times larger (see Figure 4-9) because the diffusion layer prevented the atmosphere above ~10 km from collapsing. It is the elevated flux of SO_2 from the upper atmosphere to the near surface region that keeps the SO_2 number density elevated above the equilibrium value. Hence the SO_2 condensation onto the surface exceeds the SO_2 sublimation rate until the surface warms sufficiently. The more the SO_2 column exceeds the equilibrium value upon egress, the more the temperature must rise before the column can increase. This explains why changing the value of ε/Mc affects how quickly the SO_2 column begins to recover.

The atmospheric profiles upon egress are shown in Figure 4-11 for case 5. The number density of SO_2 near the surface at the end of the eclipse is seen to be two orders of magnitude smaller than before ingress; on the other hand, the SO_2 density above ~50 km remains virtually un-changed. Moreover, because the surface temperature increases quickly, the near-surface density increases by two orders of magnitude over the first 30 minutes after egress. Interestingly, with this much non-condensable present, the temperature of the atmosphere is largely unaffected by the eclipse (as compared to Figure 4-4b). As the surface warms and SO_2 sublimates during the first 30 minutes of egress, the gas temperature near the

surface drops slightly since the increased gas density near the surface allows the near-surface gas to better equilibrate with the surface and the sublimated gas is relatively cold compared to the plasma heated atmosphere. Figure 4-11 also shows that the atmosphere at the end of eclipse consists largely of SO, with mole fraction being greater than 50% over the whole domain and ~96% near the surface. However, 30 minutes past egress, the atmospheric species have stratified, with the atmosphere at high altitudes ~70% SO while near the surface the atmosphere is composed almost entirely SO_2. Electron and ion impact dissociation of SO_2 (which is not modeled) near the surface will of course tend to reduce the severity of the stratification. However, the electron and ion densities and energies will have been depleted somewhat near the surface (Smyth and Wong, 2004) and the SO_2 dissociation lifetime can be expected to be greater than the time to form the stratified atmosphere (~30 minutes).

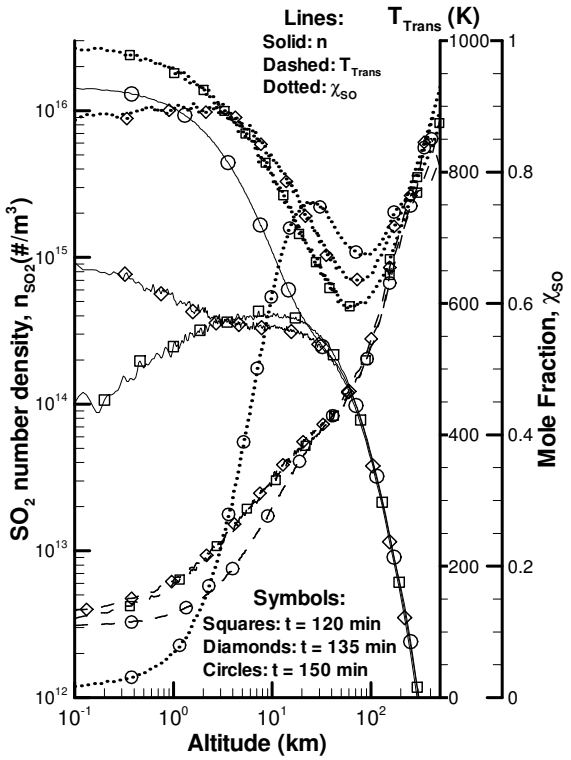

Figure 4-11: Atmosphere profiles (slightly smoothed for clarity) during egress for an initial surface temperature of 110 K and an SO mole fraction of 0.35 (case 5).

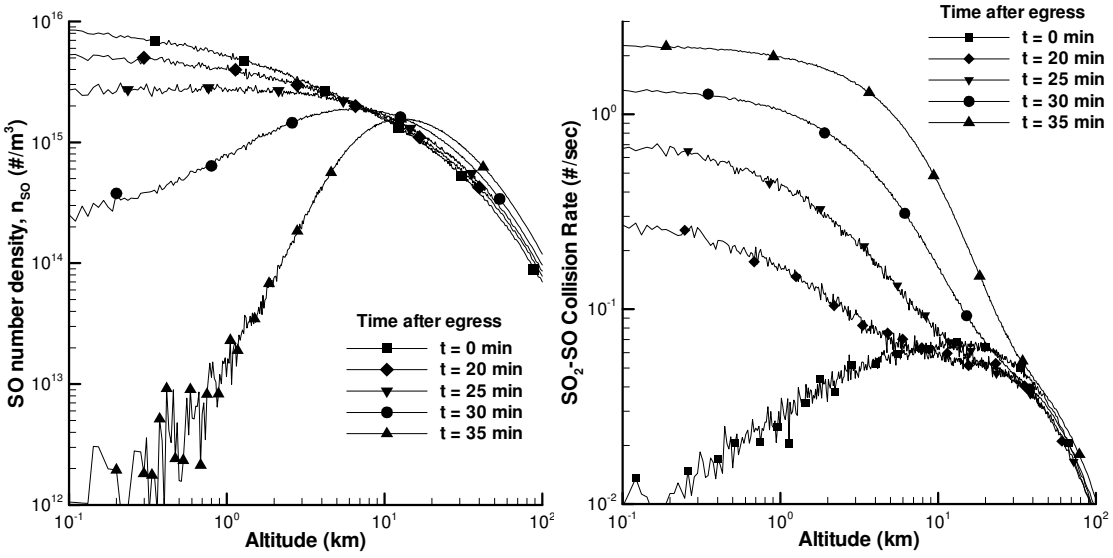

(a) (b)

Figure 4-12: Atmosphere profiles at several times after egress for an initial eclipse surface temperature of 110K (case 5). (a) The SO number density changes very little until ~20 minutes after egress, when it then drops by a factor of ~25 in 10 minutes near the surface. (b) The collision rate also increases dramatically near the surface after ~15 minutes; at egress the atmosphere is nearly collisionless but becomes collisional after ~20 minutes.

Atmospheric SO density profiles at several times after egress for case 5 are shown in Figure 4-12(a) and (b). As shown in Figure 4-12(a), the SO number density changes very little until ~20 minutes after egress, after which it drops by ~3 orders of magnitude over the next 15 minutes near the surface. The result is that 30 minutes after egress, the atmospheric species (SO and SO_2) are segregated with nearly pure SO_2 at lower altitudes and an SO/SO_2 mixture above ~10 km. The reason why the number density drops sharply after ~20 minutes is seen in Figure 4-12(b). At egress the atmosphere is nearly collisionless with a mean time between collisions of ~100 seconds, but after ~15 minutes the SO_2-SO molecular collision rate near the surface increases dramatically. At early times little momentum is transferred by the expanding SO_2 gas to the SO layer due to the low collision rate; the SO_2 just streams ballistically through the SO. As the collision rate increases, the rising SO_2 gas can no longer pass through the SO layer and an upward velocity away from the surface develops and reaches ~20 m/s after 30 minutes. The result is that the SO layer is "lifted" to higher altitudes by the SO_2 gas and the SO number density falls rapidly. This SO deficit persists for longer than an hour after egress since the SO cannot diffuse down to lower altitudes due to the non-

negligible vertical velocity. Furthermore, note that the stratification is not limited to the non-condensable species. The presence of the diffusion layer will segregate other condensable species (O, S, etc.) during eclipse to higher altitudes (as the atmospheric scale height changes) and upon egress this stratification should increase via momentum transfer with the subliming SO_2.

Also, as seen in Figure 4-9, larger non-condensable mole fractions lead to a larger difference between the equilibrium column density and the simulated column density after egress. This is because, for the high mole fraction cases, the SO_2 subliming away from the surface encounters a collisionally thick diffusion layer and transfers radial momentum away from the surface to the diffusion layer, keeping the number density of SO_2 near the surface artificially high. Hence, an increased number of SO_2 molecules hit the surface and stick relative to case 1 where there was no momentum transfer and the SO_2 molecules were free to stream away from the surface ballistically.

Stratification of the atmospheric species could have a significant effect on the morphology and intensity of auroral emissions. This should be especially true for emission from forbidden lines because stratification might lead to a given species (e.g. O produced by dissociation of SO and O_2 that are lifted to the upper atmosphere) being predominantly located at higher (or lower) altitudes. This affects the emission intensity because the lower density at higher altitudes results in a slower collisional quenching rate than at lower altitudes. Hence, the emission intensity for a given amount of emitter species would be higher if most of the emitter species was located at higher altitudes and lower if they were mostly located at lower altitudes. The relative intensity of non-forbidden lines would not be expected to change since collisional quenching will not be a factor at these pressures; however, the morphology of the emission should be affected, especially the altitude at which the limb glow intensity peaks. Furthermore, since the diffusion timescale (from an altitude of 10 km down to the surface) is ~1 hour and the plasma chemistry (dissociation) timescale is ~4 hours, the species segregation might persist until eastern elongation (10 hours after egress) because the initial "blow-off" of SO_2 overwhelms diffusion to the surface; however, the segregation certainly should not persist until western elongation (31 hours after egress). This suggests that, everything else remaining constant, forbidden line emission on the sub-Jovian hemisphere would be more intense at eastern elongation than at western elongation since the atmosphere would still be partially stratified at eastern elongation, but fully mixed by western

elongation. Of course, other variables affect the emission intensity, e.g. changes in the plasma torus density at eastern and western elongation, the resultant changes in the plasma interaction with Io, and the overall species abundance in the atmosphere. Oliverson *et al.*'s (2001) analysis of many observations concluded that the west/east [OI] 6300 Å emission ratio was 1.07 versus their model prediction of a ratio of 1.56. The discrepancy between their model and the observations could be due to species segregation and its tendency to brighten the aurora preferentially at eastern elongation.

Much of the anti-Jovian hemisphere never enters into eclipse since Io is tidally locked; that is, the anti-Jovian side of Io experiences gradual day/night changes, never the abrupt ingress/egress of eclipse. Because the timescale for circum-Io winds is ~10 hours, the anti-Jovian atmosphere may be less segregated than the Jovian side near eastern elongation and so one might expect brighter forbidden line emission on the Jovian side relative to the anti-Jovian side near eastern elongation. Note that the increased brightness due to the segregation of species to higher altitudes would act independent of the Hall effect which similarly brightens the Jovian hemisphere relative to the anti-Jovian side as discussed by Saur *et al.* (2000).

4.3 CONCLUSIONS

Io's SO_2 atmospheric collapse upon entry into eclipse and the sublimation atmosphere formation upon egress are modeled. It is found that, 10 minutes after ingress, essentially no collapse has occurred at altitudes above ~100 km for a pure SO_2 atmosphere. The dynamics of the collapse is greatly altered by the presence of a small concentration of a non-condensable species which forms a diffusion layer near the surface preventing rapid collapse of the SO_2 atmosphere upon ingress into eclipse. The dynamics were found to be sensitive to the non-condensable mole fraction and the condensability, as measured by the sticking probablility P_{stick}, of the 'non-condensable'. Furthermore, the collapse dynamics are largely insensitive to parameters such as the plasma energy flux, non-condensable species type, and reasonable changes in the thermal parameters of the surface. If the second gas species is weakly condensable (non-zero sticking/reaction coefficient) then the diffusion layer's effect on the dynamics is dramatically reduced. In fact, if the non-condensable sticking coefficient exceeds ~0.25, then the atmospheric dynamics are the same as if there was no non-condensable present. This sensitivity is due to the reduction of the effective

diffusion layer size as the weakly condensable species is lost to the surface. Also, if the surface is even a partial sink (i.e. a weakly condensable species) then the "diffusion" layer has a bulk velocity towards the surface and hence the SO_2 merely convects to the surface and does not need to diffuse through the weakly condensable layer.

The effect of the diffusion layer may be less severe than our 1D model predicts because horizontal winds along the surface could carry away the non-condensable species. Upon egress, it is found that the temperature of the lower atmosphere decreases due to the increased atmospheric density at higher altitudes which absorbs the plasma energy and shields the lower atmosphere. Stratification of the SO_2 and non-condensable species was observed shortly after egress. The atmospheric species stratification should alter the morphology and possibly intensity of auroral emissions. Forbidden line emission should be especially sensitive to species stratification to higher (or lower) altitudes since the emission brightness scales inversely with the quenching (de-excitation) collision frequency (and hence the number density). The stratification should be present near eastern but not western elongation since both the diffusion timescale and the plasma dissociation timescale are appreciably shorter than half of Io's orbital period. Furthermore, we do not expect to see the same stratification at sunrise because the nighttime is sufficiently long for surface winds and plasma-neutral chemistry to eliminate the non-condensable diffusion layer. More generally, circumplanetary flows near the terminator will prevent a direct analogy of these eclipse results to the atmospheric structure at dawn or dusk.

Chapter 5

Monte Carlo Electron Transport

The multiple interaction mechanisms between the Jovian magnetosphere and Io's atmosphere make it difficult to simulate all the physical processes around Io in detail and obtain the various observed auroral features. In general, one would need to consider plasma dynamics in the entire torus, chemical reactions, photo-reactions, and unsteady gas dynamics to describe the atmospheric flow driven by the sublimation/condensation of SO_2 frost and the episodic volcanoes. Therefore, in this analysis, certain physical mechanisms and their coupling to the auroral generation have been simplified, as is discussed below.

5.1 OVERVIEW

The numerical approach used in the aurora simulations focuses on the two most important physical mechanisms for auroral emissions around Io: 1) electron dynamics and 2) neutral dynamics. The electron dynamics are simulated using the "Excitation" routine, which follows electron motion along field lines and computes electron-neutral collisions. The neutral dynamics are modeled using the "Emission" routine to simulate the transport of excited neutrals as they de-excite via collisions with other neutrals or through spontaneous decay based on the Einstein *A* coefficients for each emission process that produces emission. The transport (and collisional quenching) of excited neutrals is most important (if at all) for forbidden or semi-forbidden emission such as [OI] 6300 Å, OI] 1356 Å, or [SII] 6716 Å which have very long lifetimes.

The simulation can be split into the two sequential routines (Excitation and Emission) because the mean collisional de-excitation time due to electron collisions is long ($> \sim 10^3$ sec) compared to the longest emitter lifetime of interest ($\tau_{[OI]}$ = 134 sec). Hence, *electron de-excitation* will be negligible relative to spontaneous emission even for forbidden states such as [OI]. Similarly, the fraction of neutrals excited at any given instant is relatively small and so it is not expected that neutral excitation will be reduced due to saturation effects. Therefore, excitation (through electron collisions) and de-excitation (through spontaneous emission or collision with the surface or other neutrals) are uncoupled in the present simulations allowing the use of two significantly different timesteps for the two models. Both

routines model the dynamics using a Monte Carlo method in which representative electrons or neutrals move and probabilistically collide in space during a finite timestep. In each routine a pre-computed steady-state neutral SO_2/O/SO/S/O_2 atmosphere is employed. Gas dynamics, chemistry, and plasma heating are included only in the sense that the prescribed, pre-computed atmospheric model used includes these effects. In addition, it is assumed that residual auroral excitations due to sunlight (dayglow) are negligible for the eclipse observations being modeled. This is reasonable since the observations start 5 or more minutes into eclipse while the halflife of [OI] 6300 Å spontaneous emission is ~2.2 minutes and the mean time between quenching collisions is, below the exobase, typically even shorter than the emission halflife. Finally, the Emission model explicitly assumes the atmosphere is optically thin and that Io's surface is a uniform mix of SO_2 frost and non-frost when computing the reflected emission off Io.

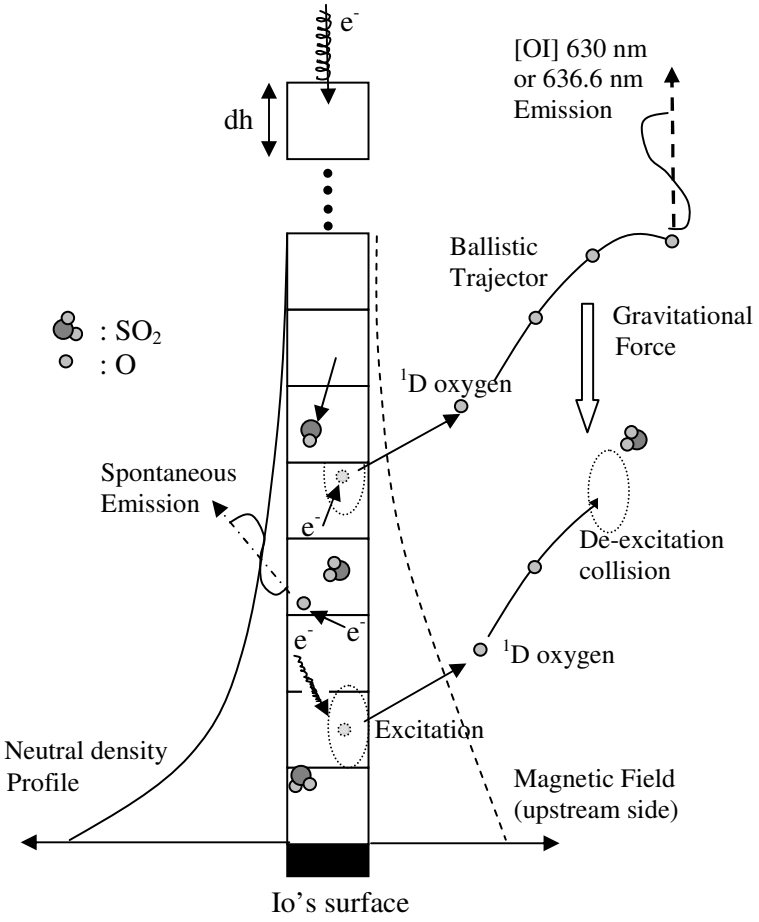

Figure 5-1: Schematic of the computational features for the 1-D Excitation and Emission Model.

The problem was first analyzed with a 1-D code that was subsequently developed into a 3D code. The essential elements of the simulation are shown schematically in 1-D in Figure 5-1. Electrons enter the domain and follow along the magnetic field lines, occasionally interacting with the neutral atmospheric species. The excited neutrals that result are then allowed to move ballistically until they spontaneously emit, collisionally quench, or impact the surface. The grid is only used to interpolate the precomputed fields and to sum up spatial emission statistics.

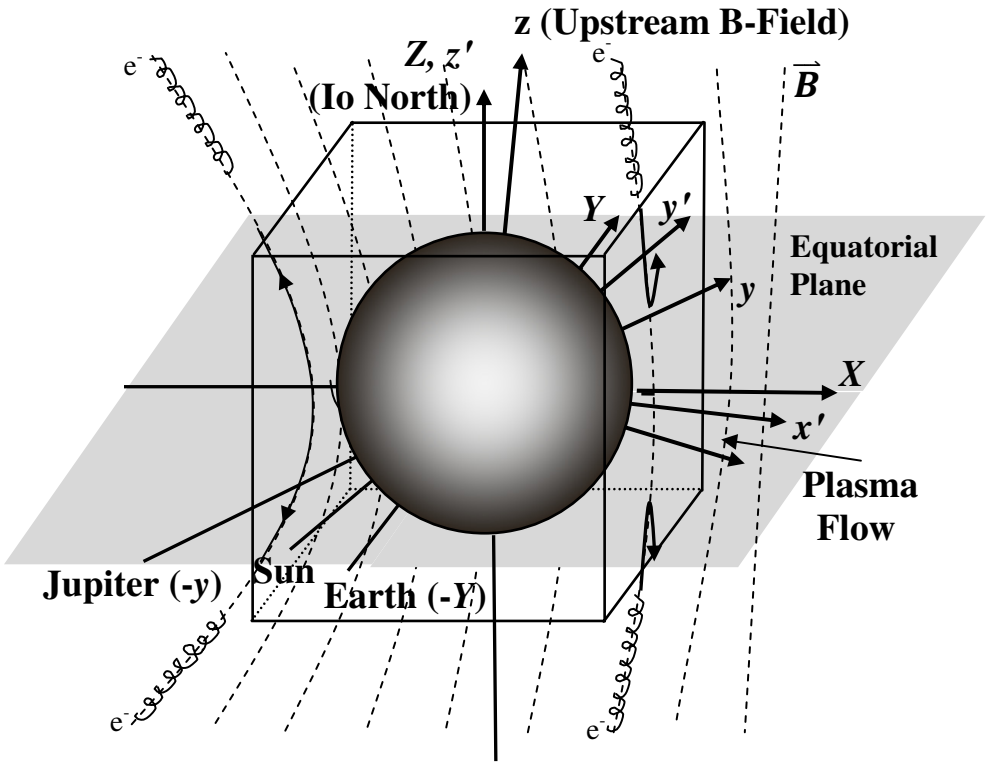

Figure 5-2: Schematic of interaction model and illustration of geometry when Io is in eclipse. Three coordinate systems are shown: the electron transport is computed in the xyz system and the excited oxygen transport in the x′y′z′ system and the subsequent emission is computed in the *XYZ* system. The *xyz* axes are aligned with the upstream magnetic field and the anti-jovian spot, the *x′y′z′* axes are aligned with Io north and away from the sub-solar point, and the *XYZ* axes are aligned with Io north and the anti-Earth spot. Io's equatorial plane (*XY* plane) is shown in the figure. The plasma flow is coming from the right side. Io is at the center of our simulation domain [in a box (9000km×6000km×6000km)]. The Jovian background magnetic field (dashed lines) bends around Io.

Figure 5-2 is a schematic depiction of the 3D domain and Io's orientation. Io is placed at the center of the computational domain which is a 9000 km×6000 km×6000 km

box. The atomic oxygen number density outside the domain is assumed to be small enough that any emission produced is both small and relatively uniform across the domain. The problem naturally contains two coordinate systems: one in the torus frame of reference and the other in the atmospheric frame of reference. Since the pre-computed magnetic fields are in the torus coordinate system, the electrons are moved in the torus frame of reference where the z-axis points up along the undisturbed magnetic field direction at Io, the y-axis points away from Jupiter, and the x-axis points against the plasma flow. Then, in order to compute the neutral density and determine if an electron-neutral collision should occur, the electron's position vector is transformed into the atmospheric coordinate system where the z'-axis is aligned with Io north and the y'-axis points away from the Sun. Excited neutrals are also moved in the atmospheric coordinate system in order to facilitate faster computation of the collision rate from the local density and bulk velocity. Finally, the emission is line-of-sight integrated in the Earth-Io coordinate system where the Z-axis is aligned with Io north and the Y-axis points away from the Earth.

Figure 5-3 shows a general overview of the electron transport model in the near vicinity of Io. The model can be summarized as follows: electrons are input at the domain boundaries and move along pre-computed magnetic field lines and can collide with a pre-computed steady state atmosphere which consists of a sublimation component and superimposed volcanic plumes. The excited molecules and atoms created through electron impact of the neutral gas are then given a bulk and thermal velocity and moved until they either emit or collide (and quench) with the surface or molecules in the pre-computed atmosphere. If the MUV 1 or MUV 2 molecular band for SO_2 or the B $^3\Sigma$ S_2 band is excited then the emitted photon wavelength is picked from the spectra based on the incident electron's energy. A Cartesian grid is used to bin the emission events for output visualization. The details of the pre-computed atmospheric models used in the present simulations are presented below before describing the models for the Excitation and Emission routines.

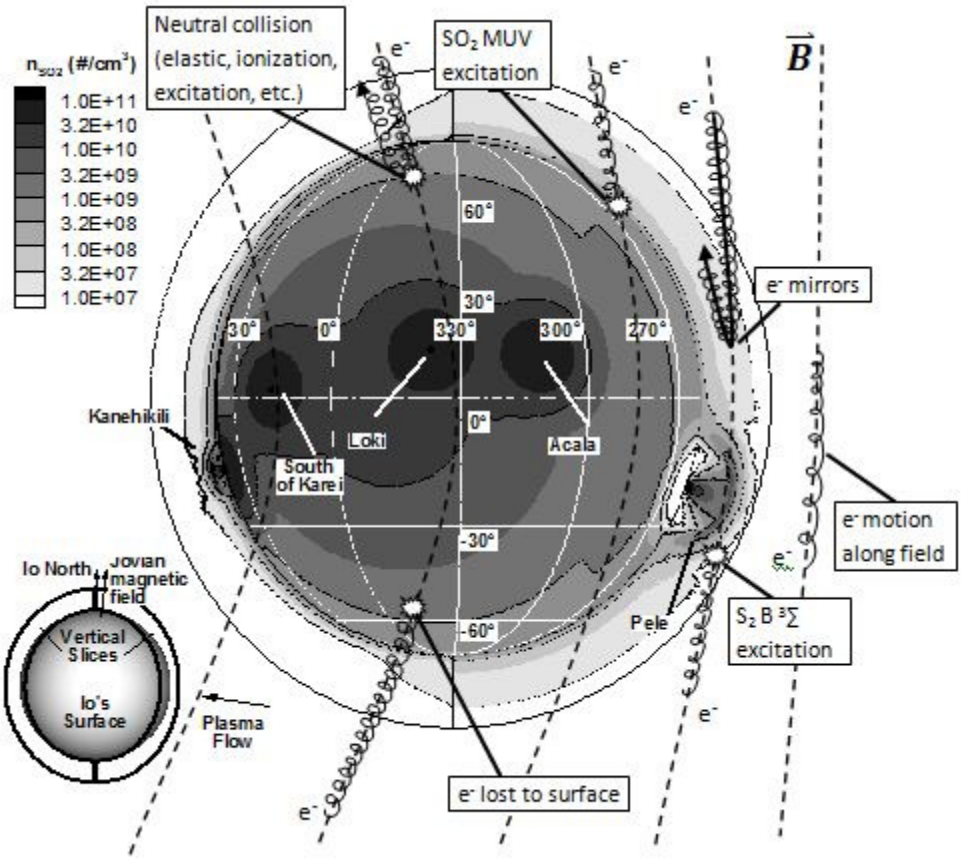

Figure 5-3: Schematic 3D overview of the electron transport model. The plasma flows from right to left and electrons travel along the dashed magnetic field lines, occasionally interacting with the local neutral atmosphere (contours show the SO_2 density at the surface and in radial slices near the limb).

5.2 ATMOSPHERIC MODEL

Io's SO_2 atmosphere is thought to be produced by two separate physical processes: volcanic eruptions and sublimation from SO_2 frost patches at the surface (see Chapter 2.1). Since the morphology and intensity of the auroral emission is expected to depend on the local atmospheric density and composition, it is important that the atmospheric model used in the auroral simulations adequately represents the local variability of the neutral atmospheric species (including the minor daughter species of SO_2). In addition to obvious atmospheric variability from volcanic activity, the sublimation component of the atmosphere varies strongly depending on the local surface temperature, the presence of surface frost, and on the resultant dynamic winds from high to low pressure regions. Furthermore, on the dayside, Io's

atmosphere is expected to be collisional near the surface; however, at higher altitudes and on the nightside the atmosphere will be rarefied. Before the atmospheric simulation presented in Chapter 8, the best available sublimation atmospheric model which included photo- and plasma-chemistry was a 2D continuum simulation of Io's atmosphere (Wong and Smyth, 2000; Smyth and Wong, 2004) at western elongation (not in eclipse).

In order to simulate Io's 3D auroral morphology it was therefore necessary to construct a 3D model atmosphere that included chemistry, volcanic activity, and the effect of eclipse. To this end, the 2D atmospheric simulation (Wong and Smyth, 2000) as a function of subsolar zenith angle was mapped to the corresponding latitude and longitude on Io assuming a subsolar point at 0° latitude and 351.1° longitude (ie ingress into eclipse). At this point the atmospheric profiles were the same at the pole and the terminator since both points are at a subsolar zenith angle of 90°. To approximately account for the effect of eclipse across Io, the 1D collapse results from Chapter 4 are utilized to scale the sublimation atmosphere. Finally, several volcanic plume types were simulated and then superimposed onto the sublimation atmosphere wherever there was an active plume of that type. Future auroral simulations (not performed here) will use a model sublimation atmosphere in eclipse generated by 3D DSMC simulations (see Chapter 8) superimposed with the precomputed plumes. The sublimation atmospheric component would then be truly 3D, accurately simulate the rarefied nature of the atmosphere, include surface sputtering, photo- and plasma-chemsitry, and would self consistently account for collapse of the atmosphere upon entry into eclipse. The current implementation of the model atmosphere is described below (first the volcanic and then the sublimation component) and the resultant aurorae are compared in the following chapters (6 and 7).

5.2.1 Volcanic Atmosphere Component

Large active volcanoes like Pele and Tvashtar cause large local density variations in the atmosphere. Because Ionian plumes can cover a region the size of an entire auroral bright spot they could be important for modeling the emission features. Our atmospheric model contains many volcanoes that are suspected or known to have been active during the relevant observation period; see the discussion in Chapters 7 and 8 for specific plumes active during the respective observations. Geissler *et al.*'s (2004a) timeline of major eruptions (see Figure 2-6) that is based on observed surface changes in the vicinity of the volcanoes is used to

determine which plumes were active during a given observation. Since some of the volcanic areas (e.g. Culann, Ra) had no image coverage or poor image quality during the 1997 HST eclipse observations, we have run cases with those plumes both active and inactive. Similarly, while Loki's volcanic activity was known during the observations, its activity as a plume source was unknown and therefore its activity (as a plume source) was also varied.

The simulation uses two general volcanic types, each of which can be either dayside (when the sublimation atmosphere beneath the plume is substantial, e.g. surface temperatures greater than ~110K) or nightside (when the sublimation atmosphere is minor). Large volcanoes with a ring radius exceeding ~400 km and shock heights of several hundred kilometers are classified as Pele type, and there were 6 such plumes (Dazhbog, "North Polar Ring", Pele, Grian (South of Karei), Surt, and Tvashtar) on Io during our observation timeframe. The smaller volcanoes are simulated as Prometheus type plumes with a ring radius of ~180 km and a shock height of ~120 km. Parameters for each volcano type are found in Table 5-1. The Pele type plumes have a virtual vent temperature of 650 K, a gas velocity of 900 m/s, and a mass flow rate of 1.1×10^4 kg/s. The Prometheus type plumes have a virtual vent temperature of 300 K, a gas velocity of 500 m/s, and a mass flow rate of 5.9×10^3 kg/s. While the plume parameters given here are adequate for the current work, future simulations would benefit from using the improved, fully 3D plume models of McDoniel *et al.* (2011). Furthermore, it will be shown in Chapter 7 that unique plume models for the Pele-type giant plumes might be necessary to accurately model some features of the auroral emission across Io.

Table 5-1: Volcano parameters; the centerline column density, N_{col}, is taken along the axis of symmetry over the vent (Zhang *et al.*, 2003, 2004).

Type	T_{surf} (K)	V_{vent} (m/s)	T_{vent} (K)	n_{vent} (#/cm^3)	N_{col} (#/cm^2)	R_{ring} (km)	H_{shock} (km)
Day Prometheus	112	500	300	$5*10^{13}$	1.1×10^{18}	175	110
Night Prometheus	90	500	300	$5*10^{13}$	2.2×10^{18}	175	100
Day Pele	111	900	650	$5*10^{13}$	1.4×10^{18}	580	315
Night Pele	90	900	650	$5*10^{13}$	1.4×10^{18}	580	315

The volcanic plumes were pre-computed using our existing volcanic model (Zhang *et al.* 2003, 2004) using the vent parameters in Table 5-1 and assumed a pure SO_2 plume. The volcanic flowfields obtained by running the existing volcanic code were then superimposed onto the sublimation atmosphere component (Chapter 5.2.2) in order to obtain the final target

atmosphere for the 3D electron transport code. Both plume types were simulated using our prior crude plasma heat flux model (Austin and Goldstein, 2000) assuming a radial energy flux into the top of the domain of 5 erg s^{-1} cm^{-2}. Figure 5-4 shows a comparison of the pre-computed day and night-side Pele-type plumes; Figure 5-5 shows the same comparison for the model's Prometheus-type plumes. The largest morphological difference between a dayside and nightside plume is seen to be the extent of the dayside plume beyond the canopy ring radius. The multiple "bounces" of downfalling plume material reported in Zhang *et al.* (2003) are no longer seen because plasma heating of the gas above the canopy shock diffuses the downfalling gas (Figure 5-4(a) and Figure 5-5(a)).

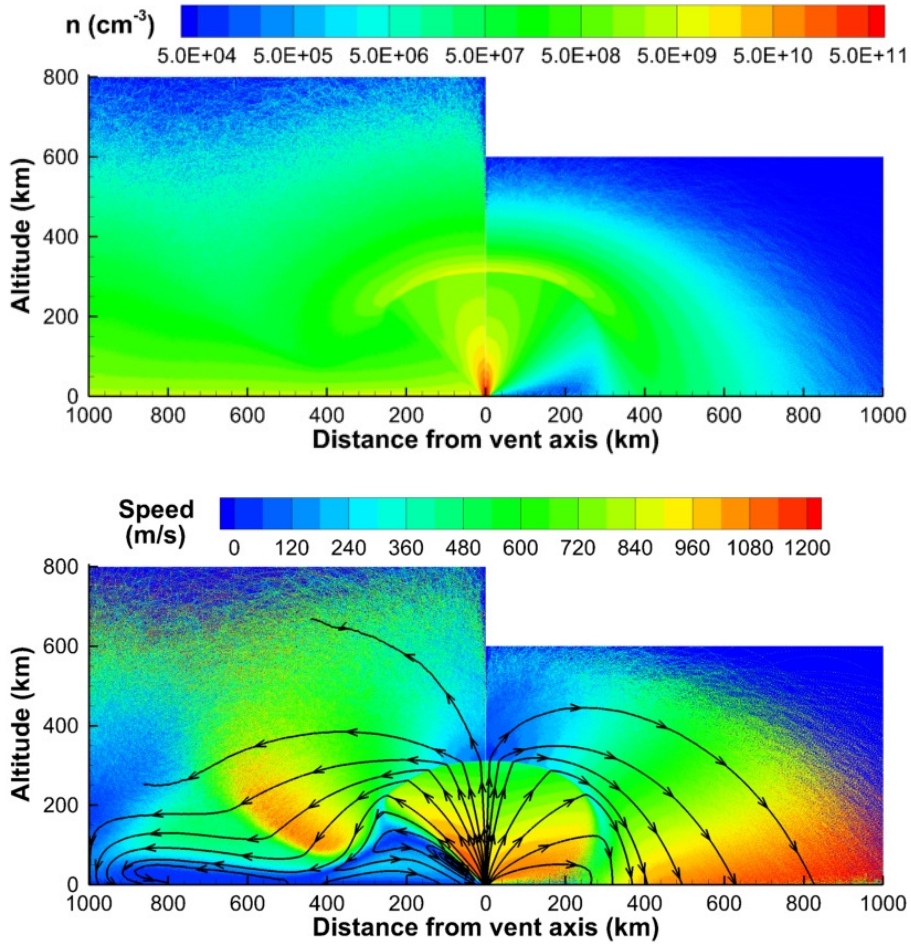

Figure 5-4: Comparison of (a) number density and (b) speed contours between the model dayside (left) and nightside (right) Pele-type plume.

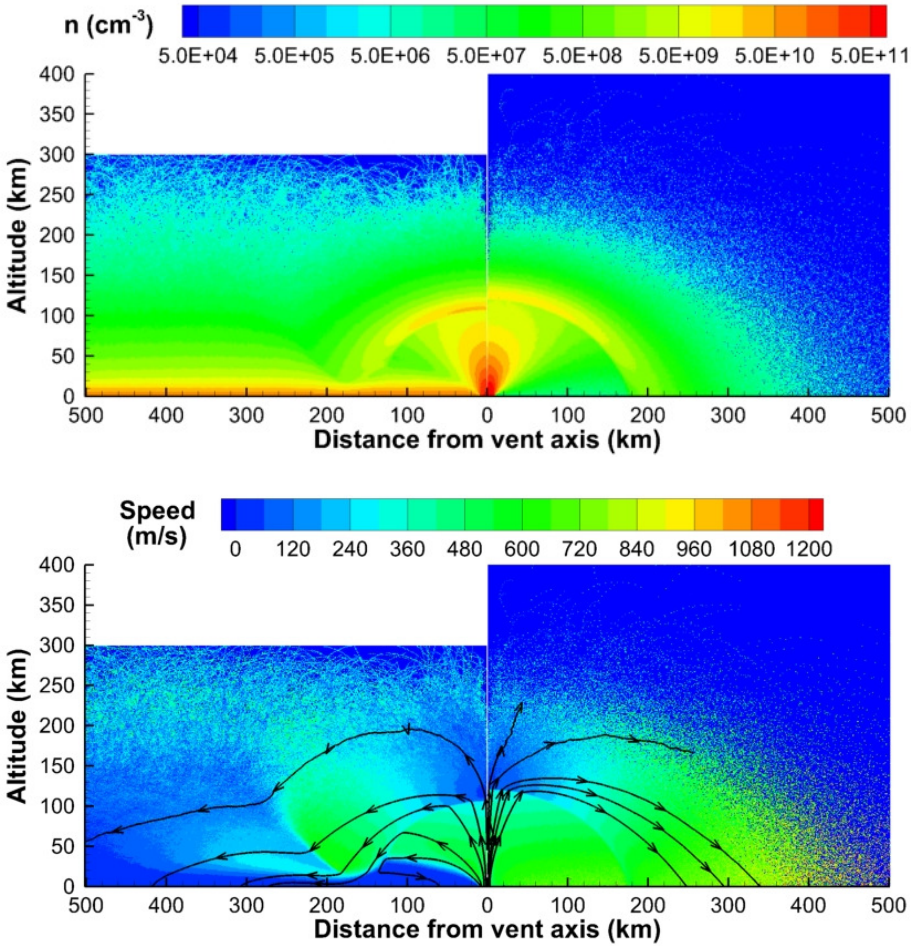

Figure 5-5: Comparison of (a) number density and (b) speed contours between the model dayside (left) and nightside (right) Prometheus-type plume.

Seen in Figure 5-4(b) and Figure 5-5(b), the downfalling plume material from the canopy region undergoes a shock as it encounters the dense dayside atmosphere and a gas flow nearly parallel to the surface develops that convects the plume material approximately an additional ring radius from the vent. In addition, the relatively large velocities in the vicinity of the plumes mean that forbidden line emission from plume materials, if not quenched, will convect ~50 km for Pele and ~25 km for Prometheus. Figure 5-4(b) also shows that the domain boundary was clearly influencing the gas flow. However, except for the relatively large velocity parallel to the surface, the effect of the plume gas on the sublimation column is minimal ~100 km beyond the ring radius. Furthermore, the model used to superimpose the plume properties onto the sublimation atmosphere (Eqn. 5-1) ensures that the flow near the outer boundary will have minimal effect. The current model's neglect of

surface temperature changes with distance from the vent and of sublimation-driven circumplanetary flow limit the model's accuracy beyond the plume's ring radius, therefore not much was to be gained by re-running the simulation with a much larger domain. However, the convection of plume material is most likely important for spreading minor gas species, such as S_2, across Io and should therefore be examined more fully with a fully coupled 3D plume-sublimation atmospheric model.

While simulations of the plumes using the new photo- and plasma-chemistry (see Chapter 3) models would certainly alter the composition (and possibly structure) of the plume, the results using the early simulated plumes suggest that this would not matter a great deal, except perhaps if the S_2 concentration was greatly affected. Zhang *et al.* (2004b) found that molecular (or atomic) species expected to be present in the plumes (e.g. S_2, Na, O) did not separate from the SO_2 gas flow in a plume. Zolotov and Fegley (1998) and Moses *et al.* (2002) computed the equilibrium gas species mole fractions at various volcanic vent temperatures, pressures, and O/S ratios. In order to approximately account for the equilibrium gas composition, the plumes' simulated SO_2 densities are uniformly scaled by the equilibrium vent mole fractions. The oxygen mole fraction in a plume vent was found to be at most ~10^{-4} (Zolotov and Fegley, 1998; Moses *et al.*, 2002); in the current plume simulations an upper limit of 0.1% is used. In Pele the S_2 mole fraction has been observed to be between 0.08 and 0.33 (Spencer *et al.*, 2000; Jessup *et al.*, 2007), whereas the upper limit for S_2 in Prometheus was 0.005 (Jessup *et al.*, 2007). For these plume simulations the Prometheus-type plumes are assumed to contain no S_2 (unless specified) and the Pele-type plumes are assumed to contain a variable amount of S_2 up to 33%.

In order to generate the hybrid plume-sublimation atmosphere used in the electron transport code, the pre-computed volcanic plumes are overlaid onto the sublimation atmosphere, neglecting the gas dynamic interactions with nearby plumes and the non-uniform sublimation atmosphere. At a given location inside a simulated plume's domain, the model density was computed by superimposing the plume simulation density and the sublimation atmosphere density. Inside the plume's ring radius, S_{Ring}, it was assumed that the non-uniform sublimation atmosphere gas flows would have a negligible effect on the gas properties and therefore the model gas densities were set to the plume gas densities. Outside of the plume's ring radius the plume simulation density, n_P, is reduced exponentially based on the distance along the surface, S, and a plume-type dependent length scale, L_P:

$$n = n_P \times exp\left(-\frac{S-S_{Ring}}{L_P}\right). \quad 5\text{-}1$$

We assumed that L_P was equal to 30 km for Prometheus-type plumes and 90 km for Pele-type plumes. This offsets the contribution of the far-field sublimation atmosphere that is accounted for in the dayside plume simulations and limits "double counting" of the sublimation atmosphere inside the plume domain and consequent density jumps across the outer plume boundary. Other properties (such as temperature) are mass-averaged such that a given property, ξ, inside a plume domain would be equal to

$$\xi = \frac{\xi_P n_P + \xi_S n_S}{n_p + n_S}, \quad 5\text{-}2$$

where the subscript "*P*" refers to the simulated plume value and "*S*" refers to the sublimation value (see below, Eqns. 5-3 and 5-4).

5.2.2 Continuum Sublimation Atmosphere Component

The sublimation atmosphere component in the current model is derived from curve-fits to the 2–D continuum gas results shown in Wong and Smyth (2000) and Smyth and Wong (2004). Wong and Smyth's (2000) model considered plasma and Joule heating (but not plasma-induced chemistry), non-local thermodynamic equilibrium cooling, and photochemical reactions. Their result, which was qualitatively consistent with results of other models, showed that SO_2 was the dominant atmospheric species and that the sub-solar/nightside SO_2 column density ratio was ~10^3. Their simulated nightside atmosphere was mainly SO and O_2 since they assumed that both SO and O_2 were non-condensable and non-reactive on the surface. Smyth and Wong's (2004) more recent simulation atmosphere which included plasma-induced chemistry was also investigated. Because the oxygen density (and that of other SO_2 dissociation products) falls off with altitude much more slowly than SO_2 in the newer model, it was hoped that this would increase the altitude and brightness of the wake spot. However, our simulations with Smyth and Wong's (2004) atmosphere found a peak [OI] 6300 Å brightness that was ~2 times higher than observed and it was found to produce an upstream auroral spot that was significantly brighter than the wake spot, counter to what is observed. Since both the Wong and Smyth (2000) and the Smyth and Wong (2004) base atmospheric models produced unsatisfactory auroral morphologies, the atmospheric densities were scaled to bring the subsolar SO_2 column density more in-line with recent observations (Feaga *et al.*, 2009) and to model the effects of eclipse.

The asymmetric continuum atmospheric model is generated from an axisymmetric SO_2/O/SO/S/O_2 sublimation atmosphere. The specific atmospheric data described below are from Wong and Smyth (2000), though the same procedure has also been performed on the Smyth and Wong (2004) atmospheric profiles. Note that S_2 is not included in the sublimation atmosphere component since Moses *et al.* (2002) found that the lifetime of S_2 was short and hence significant S_2 gas should only be found in the vicinity of the giant plumes. Representative density profiles, $n_{h,i}(h,\Gamma)$, as a function of altitude were used at two different subsolar zenith angles were used: a dayside profile, $n_{h,i}(h,\Gamma = 30°)$, for solar zenith angles up to the dayside/nightside transition angle, $\varphi_{D/N}$, and a nightside profile, $n_{h,i}(h,\Gamma = 150°)$, for solar zenith angles greater than $\varphi_{D/N}$ (Wong and Smyth, 2000; Figure 6). In order for the total column at a given SZA along the equator to match Wong and Smyth's (2000; Figure 5) value, the atmospheric density profiles are scaled by the normalized longitudinal variation in column density $N_i(\varphi)/N_i(\Gamma)$ for gas species i at SZA φ. A continuous number density, $n_i(h,\varphi)$, for gas species i at altitude z and SZA of φ is therefore obtained by

$$n_i(h,\varphi) = n_{h,i}(h,\Gamma) * \frac{N_i(\varphi)}{N_i(\Gamma)}, \qquad 5\text{-}3$$

where Γ corresponds to a SZA of either 150° or 30° depending on whether φ is greater or less than $\varphi_{D/N}$, respectively. For the simulations shown here, $\varphi_{D/N}$ was set to 90°. Additional values for $\varphi_{D/N}$ were investigated, including 120° (the approximate shock location in Wong and Smyth's (2000) simulation), and we found little difference in the simulated emission intensity as viewed from Earth. However, abruptly switching the atmospheric profiles between dayside and nightside leads to discontinuous emission in that region. To remove the discontinuity, we used linear smoothing over $\pm\varphi_{smooth}$ (set to 15°). The density at a given altitude and SZA in this region ($\varphi_{D/N} - \varphi_{smooth} \leq \varphi \leq \varphi_{D/N} + \varphi_{smooth}$) was computed by

$$\begin{gathered} n_{h,i}(h,\varphi) = f_{Day} * n_{h,i}(h,30°) + \left(1 - f_{Day}\right) * n_{h,i}(h,150°) \\ f_{Day} = \frac{(\varphi_{D/N}+\varphi_{smooth})-\varphi}{2*\varphi_{smooth}} \end{gathered} \qquad 5\text{-}4$$

The sensitivity of the [OI] 6300 Å emission intensity to the local gas density (due to quenching) requires that the SO_2 density be as accurate as possible. Recent observations by Feaga *et al.* (2009) found that the average sub-jovian column density was ~1.5×10^{16} cm^{-2}; however, the sub-solar density in Wong and Smyth's (2000) high density case (sub-solar temperature of 120 K) is ~6×10^{17} cm^{-2}. Walker *et al.* (2010a) found that a sub-solar temperature of 115 K produced column densities more in-line with Feaga's observations and

that the atmosphere remains mostly in hydrostatic equilibrium even far away from the sub-solar point. Therefore, in order to reduce the Wong and Smyth SO_2 gas density to a more appropriate level, we scale (on the dayside) the SO_2 density at a given latitude and longitude by the ratio of the analytic hydrostatic column density assuming a subsolar temperature of 115 K to the hydrostatic column density for a subsolar temperature of 120 K. In order to get the SO_2 density at a given location we multiply the density obtained from Eqn. 5-4 by

$$\frac{N_{SO_2}(T_{SS}=115K)}{N_{SO_2}(T_{SS}=120K)} = exp\left(\frac{-4510}{T(T_{SS}=115)} + \frac{4510}{T(T_{SS}=120)}\right), \quad 5\text{-}5$$

where $T(T_{SS}) = (T_{SS} - 80)cos^{0.75}(\varphi) + 80$ is the local surface temperature (see Eq. 1 in Wong and Smyth, 2000). This results in a sub-solar density of ~10^{17} cm^{-2}, which is in much better agreement with the observational value of Feaga *et al.* (2009) given that the observational density is the average value, not the sub-solar column density. Note that, by only scaling the SO_2 density, the concentration of the minor species (O, SO, S, and O_2) increases, especially near the subsolar point. However, inclusion of electron chemistry naturally leads to an increase in the minor species concentrations as shown by Wong and Smyth (2004) and therefore the minor species concentrations obtained by the scaling are probably reasonable.

Since the vapor pressure of SO_2 is extremely sensitive to temperatures near Io's day/night surface temperature, the sublimation atmosphere might be expected to collapse significantly during eclipse. Thus, during the observation period being modeled (the first ~20 minutes of eclipse), the non-volcanic component of the atmosphere is not truly steady. Therefore, the atmospheric collapse upon ingress into eclipse with and without the presence of various non-condensable species was simulated (see Chapter 4). If there is no non-condensable, it was found that the atmospheric number density 10 minutes into eclipse drops by an order of magnitude near the surface, but does not change above ~100 km (see Figure 4-5). However, the presence of a nominal amount of non-condensable was found to greatly slow the collapse due to the formation of a quasi-static diffusion layer near the surface. With a non-condensable present, the near-surface SO_2 number density decreased only by a factor of ~4 and did not change above 20 km (see Figure 4-5). Furthermore, the rate of the atmospheric column decrease was found to slow as eclipse progressed, eventually resulting in quasi-steady atmospheric density profiles. Thus Moore *et al.*'s (2009) results (see Chapter 4)

suggest that using a steady atmosphere 5-10 minutes into eclipse to simulate 5 minute observations should be reasonably accurate.

As mentioned above, the sensitivity of [OI] emission to the local neutral density means that any asymmetry in the atmosphere should affect the emission morphology. Since the plasma "wake" enters eclipse ~210 s before the "upstream" region, the 210 s difference in the extent of partial atmospheric collapse across Io could significantly alter the emission intensity and morphology. For example, the ratio of upstream emission intensity to downstream emission intensity might be expected to decrease since the atmospheric density (and correspondingly the quenching rate) drops more on the wake side than the upstream side.

To approximate this behavior, the SO_2 density computed from Eqn. 5-5 is further scaled by the fractional drop in density versus altitude (relative to steady state) at 5 and 10 minutes into eclipse as computed by our 1–D DSMC collapse simulation for a pure SO_2 atmosphere (see Figure 4-5). The pure SO_2 collapse results are used because the dominant non-condensable candidate, SO, is most likely condensable (Baklouti *et al.*, 2008) and most of the buildup of O_2 on the (former) dayside during the collapse of the sublimation SO_2 atmosphere may be expected to be partially swept away by strong circumplanetary winds that develop from the dayside to the nightside (Walker *et al.*, 2010a). Over the observational time frame (Trauger *et al.*, 1997) the wake side was in eclipse from ~5 minutes post-ingress to 13 minutes post-ingress. Therefore, the fractional drop in density 10 minutes after ingress is used to scale the SO_2 on the wake side at a longitude of ~51° (60° SZA). Since the upstream side was in eclipse from ~1 minute post-ingress until 9 minutes post-ingress, the drop in density after 5 minutes scales the upstream SO_2 density at a longitude of ~291° (60° SZA). For longitudes in-between (e.g. SZA≤60°), the scaling factor is linearly interpolated between the two. Also, during the first few minutes of eclipse there should be negligible reduction in circumplanetary flow from the sub-solar point to the nightside. Therefore only minor changes in the nightside density near the terminator should occur during the first few minutes of eclipse. To account for this, the altitude dependent partial collapse scaling factor is linearly increased from the 1–D DSMC value at a SZA of 60° to unity (i.e. no change in the density computed from Eqn. 5-5) at a SZA of 100°. Note that the results did not change dramatically even when the cutoff angle (100°) was increased to 180°.

One might expect the atomic oxygen density to decrease early in eclipse like the SO_2 density. However, unlike SO_2 whose source (sublimation from frost) is dramatically reduced as the surface cools, the source of O is primarily SO_2, SO and O_2 that are dissociated by sunlight and energetic plasma particles. During eclipse there is no solar dissociation, but early in eclipse this should have little effect on the O density except near the surface where significant loss to the surface might occur depending on the non-condensable layer. The plasma-induced dissociation, on the other hand, will continue during eclipse and primarily occurs at altitudes above several kilometers where very little change in the source species' densities takes place during the first 10 minutes of eclipse. Therefore, while the near surface oxygen density will change due to loss of solar production of O and the slight bulk flow into the surface that will develop, the O density above a kilometer should remain relatively constant early in eclipse.

Due to the variable atmospheric collapse across Io, the model's sublimation atmosphere is asymmetric longitudinally on the dayside and partially onto the nightside. However, it should be noted that the continuum model sublimation atmosphere does not include the asymmetry that results from the thermal inertia of the frost and non-frost surface (and hence a skewed surface temperature, Walker *et al.*, 2010a) or from the drag of the plasma torus on Io's atmosphere. The momentum transfer from the plasma acts to reduce the upstream atmospheric scale height relative to the wake (Saur *et al.*, 2002) which should tend to dim the emission on the upstream side relative to the wake due to increased quenching rates upstream.

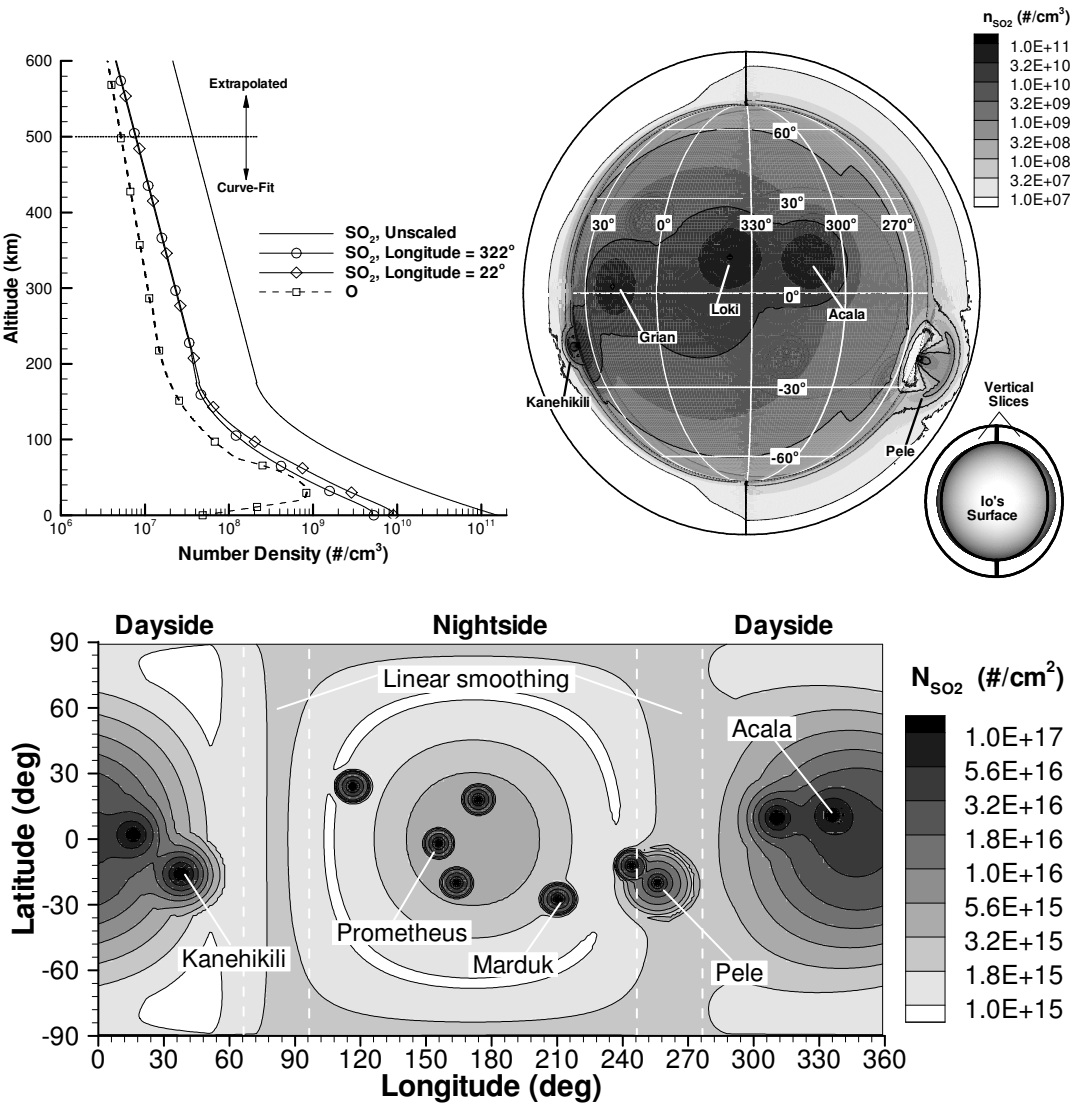

Figure 5-6: The simulation atmosphere based on curve-fits of Wong and Smyth's (2000) data with superimposed plumes. **(a)** Reproduction of the sublimation number density profiles for SO_2 and O at 30° SZA including the extension to higher altitudes as well as the result of scaling the SO_2 density which increases the near surface scale height to ~30 km on the dayside. **(b)** SO_2 number density near the surface (~100 m) and in vertical slices near each limb cutting through two plumes (Pele and Kanehikili). Contour lines are drawn every other level for clarity. The averaging of the dayside and nightside profiles is especially apparent near the poles – the Pele slice shows the nightside atmospheric profile (with a larger scale height due to increased plasma heating at lower altitudes) and the Kanehikili slice shows the dayside. **(c)** Longitude-Latitude plot of SO_2 column density for our full atmosphere model with active plumes and asymmetrical partial collapse. The subsolar SO_2 column density is 5×10^{16} cm^{-2} and the average sub-jovian SO_2 column density is 2.4×10^{16} cm^{-2}. The region over which dayside (SZA = 30°) and nightside (SZA = 150°) profiles are averaged is marked by dashed lines.

Representative plots of the final composite model atmosphere are shown in Figure 5-6. Figure 5-6(a) shows density profiles (for clarity, only SO_2 and O profiles are shown) at a SZA of 30° obtained from curve-fits to the profiles of Wong and Smyth (2000). Note that the scaled SO_2 density profiles depend on longitude (see Figure 5-6(a)) because the time since ingress varies with longitude; however, the effect on the column is relatively small and is difficult to discern in Figure 5-6(c). The upstream side is characterized by the 322° longitude (30° SZA) curve which has a higher density than the wake side curve (22° longitude). Also, note that both scaled curves have been reduced by a factor of ~10 in order to bring the sub-solar column more in-line with recent observations, as discussed above (Eqn. 5-5). Furthermore, the profiles are extended assuming an exponential drop-off for altitudes above 500 km. If we set the number density above 500 km to zero instead of extrapolating, the emission morphology remains essentially the same and the overall intensity becomes slightly weaker. The SO_2 number density at the surface and in two altitudinal slices (chosen to highlight plumes) near each limb is shown from nearly Earth view (rotated 12° to show Pele) in Figure 5-6(b). Several plumes are visible; note that near the surface underneath Pele the SO_2 density is very low. The atmospheric scale height in the Pele slice (on the nightside) is seen to be larger than in the Kanehikili slice (on the dayside) demonstrating the need for smoothing the dayside and nightside profiles (Eqn. 5-4) near the poles. Figure 5-3(c) shows the SO_2 column density as a function of longitude and latitude. Dashed lines indicate the longitudes (SZA = 90°±15°) over which the dayside and nightside density profiles are linearly averaged. Also, it is seen that the plumes contribute locally to the column of the background sublimation atmosphere.

5.3 EXCITATION MODEL

In the Excitation model, the plasma torus electrons can interact with the atmosphere of SO_2, O, SO, and O_2 described above in section 5.2. The model includes thermal (~5 eV) electrons in the plasma torus and a small component (<10%) of field-aligned, non-thermal, 30-40 eV electrons. The upper limit of 10% for the low energy non-thermal component is based on the fact that, on timescales of ~10 minutes, the total electron flux only varies several percent and yet the total energy flux fluctuates by 30-50% (Oliverson *et al.*, 2001). Previous work concluded that energetic (~10 keV) non-thermal electrons do not produce significant emission (Bhardwaj and Michael, 1999a). Since the mean time between electron-neutral

collisions is long compared to the interaction time during a collision, the Excitation routine decouples the electron motion, in which electrons move along the magnetic field lines as they sweep past Io, from the collision process, when an electron might undergo a collision. From the Excitation model, steady-state spatial distributions of the excited neutrals are obtained.

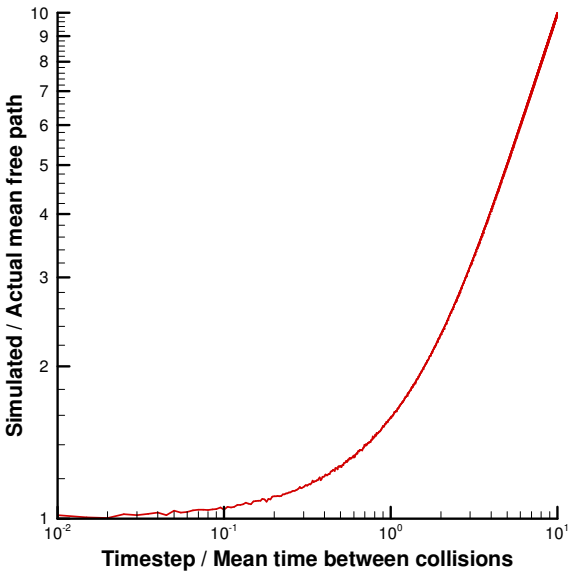

Figure 5-7: Ratio of the simulated to actual mean free path as a function of the timestep size normalized by the mean time collisions.

The time step for each electron is determined by the electron energy and the local density. The first condition is that the fastest electrons move less than one of the precomputed field cells so that magnetic mirroring is accurately simulated. The second condition is that the electrons collide on average less than once per timestep. Since the simulation model only allows at most one collision per timestep, it is necessary for the timestep to be much less than the mean collision time in order to obtain reasonable accuracy for the simulated mean free path, as shown in Figure 5-7. Therefore, our model has an overall global timestep to capture the fast electron motion across (field) cells and then, if necessary, an electron is substepped with a (smaller) timestep $\lesssim 0.1$ times the local mean time between collisions. This is generally only necessary near the subsolar point close to the surface. Figure 5-7 shows that forcing this timestep size will result in a simulated mean free path that is ~4% larger than the true mean free path. While this certainly biases the simulation results, a much larger contributor to the overall uncertainty comes from other uncertainties and errors in the

simulation (e.g. the atmospheric model itself, the cross sections used, the non-self consistent magnetic field and atmosphere).

5.3.1 Electric and Magnetic Fields

Complex interactions between Io's ionosphere and the Jovian magnetosphere (Neubauer, 1998) make it difficult to create a comprehensive simulation of Io's auroral emission. The Galileo spacecraft showed that the ionosphere around Io is strongly perturbed by the plasma flow and that the Jovian magnetic field is bent in the vicinity of Io (Frank *et al.*, 1996). There are several sophisticated MHD models for the interaction of Io with Jupiter's magnetosphere that are reasonably consistent with the observations of Pioneer 10, Voyager 1 and Galileo, e.g. Lipatov and Combi (2006), Kivelson *et al.* (2001), Combi *et al.* (1998), Neubauer *et al.* (1998), Linker *et al.* (1991, 1998), and Saur *et al*. (1999, 2002).

The plasma's bulk motion relative to Io, $\vec{v}_{Io}$ (= 57 km/s), and the Jovian magnetic field, $\vec{B}_J$, establish a corotational electric field:

$$\vec{E}_{corot} = -\vec{v}_{Io} \times \vec{B}_J. \qquad 5\text{-}6$$

For the present model, the magnetic and drift velocity fields are provided by Combi (see Fig. 1c, Combi *et al.*, 1998). Their 3D MHD model considers the ion mass loading, ion-neutral drag, no intrinsic Ionian magnetic field, and can qualitatively explain the measurements made during Galileo's flyby of Io as noted previously. Note that it was necessary to rotate their simulated magnetic field in order for the upstream magnetic field to be oriented correctly relative to Io-north at the time of the observation. This rotation introduces additional approximations, but, since they used a uniform atmosphere model, rotation of the field relative to Io's geographical coordinates should be self-consistent with the model of Combi *et al.* (1998). However, the present field model is limited because large atmospheric features (such as Pele) do not perturb the modeled magnetic and electric fields as they should.

Since the electrons move in space (not on a grid), the magnetic field must be interpolated from the pre-computed magnetic field data. In order to speed up this interpolation, the pre-computed magnetic field data (given on Combi's (1998) unstructured Cartesian grid) is initially interpolated to our Cartesian grid having a cell size $\Delta X = \Delta Y = \Delta Z$ = 60 km. Figure 5-8 shows, at Io's geodetic equator, the initial interpolated magnetic field (specifically B_z) and the bulk plasma velocity (V_x) as it diverges around Io. The magnetic field

is then linearly interpolated from the 8 surrounding Cartesian grid points to each electron's current position.

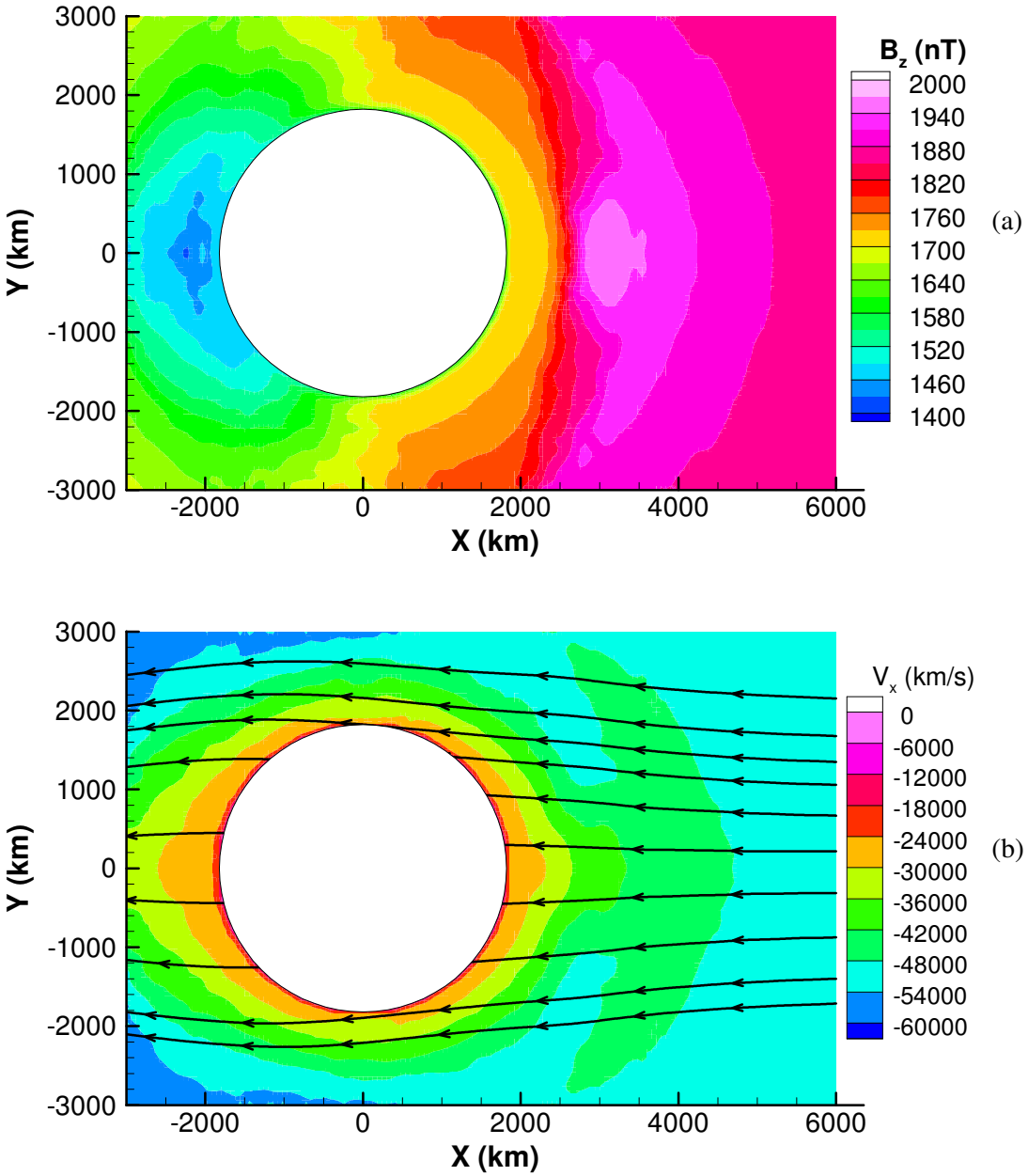

Figure 5-8: Interpolated (a) magnetic field and (b) plasma velocity data in the *xy*-plane (Figure 5-2) given by the sub-plasma spot and the upstream magnetic field using the data from Combi *et al.* (1998). Streamlines are shown in (b) by solid black lines with arrows.

5.3.2 Electron Motion

It is convenient to divide an electron's motion into two parts: a velocity component parallel to the magnetic field ($\vec{v}_{\parallel}$) and another component perpendicular to it ($\vec{v}_{\perp}$). Near Io, the perpendicular component of the drift velocity ($v_{\perp,drift} = \left(\vec{E} \times \vec{B}\right)/B^2$) becomes large relative to its value far from Io and thus there exists a bulk electron flow around the surface in addition to Io's relative motion through the plasma torus. The motion of electrons can be described by

$$\vec{v}_e = \frac{(\vec{E}_{corot} - \vec{E}_{pol}) \times \vec{B}_J}{B_J^2} + \vec{v}_{\parallel}\,, \tag{5-7}$$

where $\vec{E}_{pol}$ is the polarization electric field. Other drifts such as the gravitational drift, $\vec{v}_g = m\left(\vec{g} \times \vec{B}\right)/qB^2$, and field curvature drift, $v_{curve} = m\left(\vec{R}_c \times \vec{B}\right)\left(v_{\parallel}^2 + \frac{1}{2}v_{\perp}^2\right)/(qR_c^2B^2)$ (where m is the charged particle mass, q is the charge, $\vec{g}$ is the gravitational acceleration, and $\vec{R}_c$ is the radius of curvature of the magnetic field), are neglected since they are less than ~10 m/s near Io for typical thermal electrons and reasonable magnetic fields. Furthermore, near Io the corotational electric field is nearly canceled by the polarization field and so the velocity component perpendicular to the magnetic field is very small compared to the parallel velocity (Saur *et al.*, 2000).

We exclude the gyration motion of the electrons because in the plasma torus near Io, a typical gyration radius, $r_{gyro} = v_{\perp}m/\left(q\left|\vec{B}\right|\right)$ (where $\left|\vec{B}\right|$ is the magnitude of the perturbed Jovian magnetic field), is several meters (< 7 m for 7.5 eV electrons), which is much smaller than the atmospheric scale height and length scales present in volcanoes. Because r_{gyro} is so small, it is reasonable to neglect the gyration and move the electrons solely along the magnetic field lines. However, note that the total electron velocity (including both the velocity along the field lines and the gyration velocity), v_e, is used to compute the collision probability. Also, note that the ratio of the gyrofrequency to the electron collision frequency, i.e. the Hall parameter, β_H, is given by

$$\beta_H = \frac{\omega_c}{\upsilon_{e-n}} \approx \frac{q|\vec{B}|/m_e}{n_n\overline{\sigma_{tot}(v_r)v_r}}\,, \tag{5-8}$$

where n_n is the local neutral number density, v_r is the relative velocity between the electrons and neutrals ($v_r \approx v_e$), $\sigma_{tot}(v_r)$ is the total collision cross section between the electrons and neutrals as a function of relative velocity, and the bar represents the average value. Near the

surface at the subsolar point $\beta_H \approx 3$, and is much larger elsewhere. Therefore the electrons do not diffuse off their field lines (through collisions) and an average drift velocity for the electron's motion can be used.

To model the helical motion of the electron along the magnetic field line and account for the magnetic mirror effect, we introduce the adiabatic invariant magnetic moment, μ_{mag}

$$\mu_{mag} = \frac{\frac{1}{2}m_e v_\perp^2}{|\vec{B}|}. \tag{5-9}$$

We store μ_{mag} for each electron and update it when the electron undergoes a collision. If the magnetic field strength increases smoothly along the field line, Eqn. 5-9 can be rearranged to yield the following condition for the local pitch angle:

$$sin(\alpha) = sin(\alpha_{Initial})\sqrt{\frac{|\vec{B}|}{|\vec{B}_{Initial}|}}, \tag{5-10}$$

where the subscript '*Initial*' denotes the value at the location of the last collision (or where the electron was created if it has never undergone a collision), and α is the pitch angle of the electron defined by $tan(\alpha) = v_\perp / v_\parallel$. Note that the electron velocity parallel to the magnetic field is zero at the mirror point; therefore, α = 90°. Hence, the magnitude of the magnetic field required to reflect the electron, $|\vec{B}_{mirror}|$, can be obtained by rearranging Eqn. 5-10

$$|\vec{B}_{mirror}| = \frac{|\vec{B}_{Initial}|}{sin^2(\alpha_{Initial})}. \tag{5-11}$$

In the simulation, the electron's velocity parallel to the magnetic field is reversed when the local magnetic field is within 0.005% of $|\vec{B}_{mirror}|$. Any electron which reaches Io's surface is assumed to attach to Io and is removed from the computation. This surface sticking tends to occur predominantly in regions with very low neutral column density and for very energetic electrons (>100 eV), whose total cross sections are small.

5.3.3 Electron Collision Model

The electron-neutral collision routine is very similar to the routine described for determining electron-neutral collisions in the DSMC code (see Chapter 3.5). The two methods use the same cross sections versus incident energy, pre-computed at a finite number of incident energies, in order to determine which given interaction occurs and treat the post-collision dynamics in the same way. However, while the DSMC method first determines a number of collision pairs to select and then tests whether each selection is accepted, in the

Monte Carlo electron transport code each electron is individually tested to see if it undergoes a neutral collision each timestep, as described below.

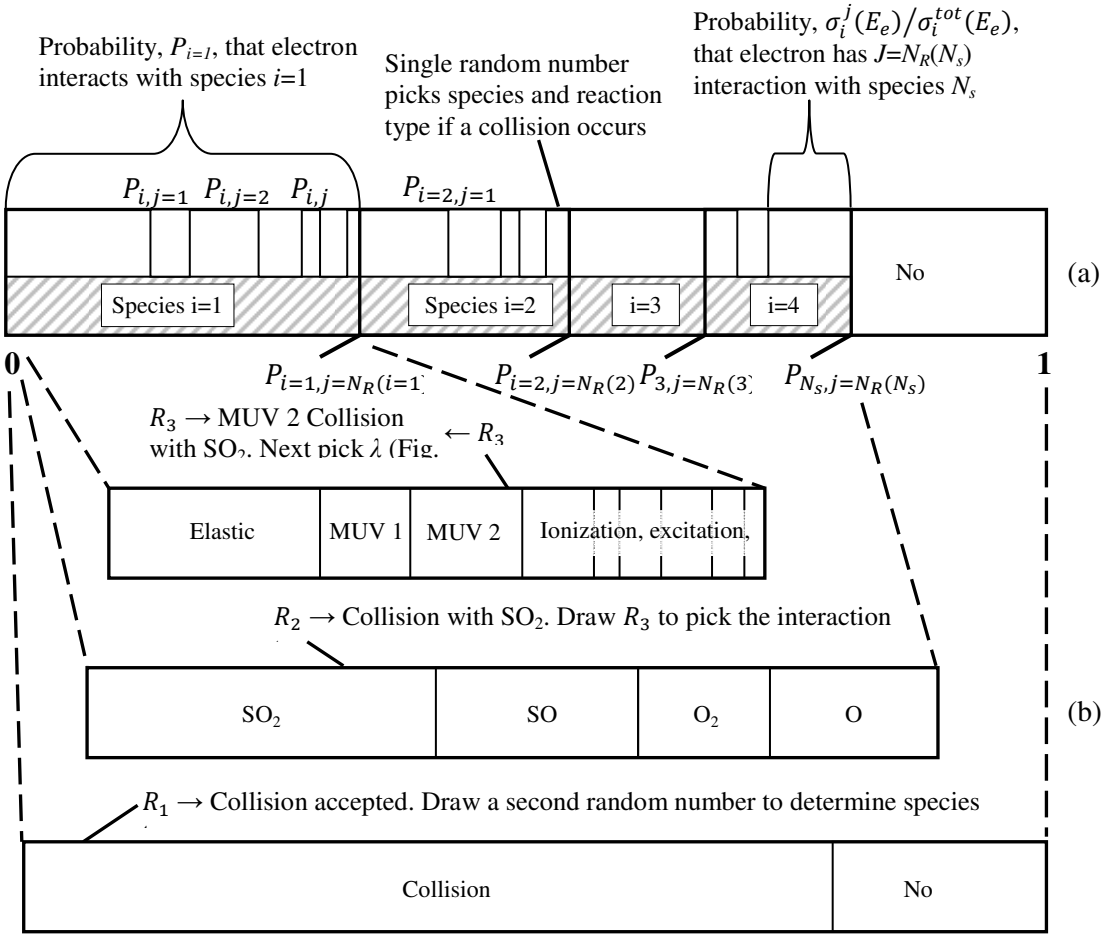

Figure 5-9: Schematic representation of (a) the normalized cumulative interaction probability (for N_s=4) which requires one random number draw to determine the species and reaction type if a collision occurs and (b) a simpler representation of the same process using three random numbers to first pick if a collision occurs, then pick the species, and finally to pick the reaction type. Note that the notation $P_{i,j=N_R(i)}$ refers to the cumulative probability of the last reaction, $N_R(i)$, of the i^{th} species and that, in general the number of reactions, $N_R(i)$, for each species is different.

The electron transport code determines whether an electron-neutral collision occurs, the neutral species with which the electron interacts, and the collision (interaction) type all in a Monte Carlo fashion by comparing probabilities to (pseudo) random numbers. In practice, only one random number is needed per electron per time step to determine what type of collision, if any, occurs. This method for selecting the collision type will be described by separating it into three conceptually simpler pieces which can then be combined to recover

the final probability for the collision type scaled from zero to unity. Figure 5-9 schematically shows (a) the simulation method using a single random number to select the collision type as well as (b) the method decomposed into three separate parts. As seen in Figure 5-9(b), first one compares a random number to an electron-neutral collision probability to determine if such a collision occurs, then a second random number is used to determine the collision partner based on the mole fractions of the neutral species present, and finally a third random number is compared to determine the type of interaction (elastic, ionization, MUV excitation, etc.) based on their relative probabilities. An electron-neutral collision occurs in a given time step, Δt, if a random number, R_1, is less than the total collision probability, $P_{col,tot}(E_e)$:

$$P_{col,tot}(E_e) = 1 - exp\left(-\Delta t \sum_i^{N_s}\left[n_i v_{rel}\sigma_i^{tot}(E_e)\right]\right), \qquad \sigma_i^{tot}(E_e) = \sum_j^{N_R(i)} \sigma_i^j(E_e)\,, \tag{5-12}$$

where the subscript i denotes the neutral species (e.g. SO_2, SO, O_2, O, and S), j denotes the interaction type, N_s is the total number of target species, $N_R(i)$ is the total number of electron-neutral reactions for species i, n_i is the number density, v_{rel} is the relative velocity between the electrons and the neutrals, and $\sigma_i^j(E_e)$ is the j^{th} interaction cross section for species i and an electron with energy E_e. The electron–neutral interaction cross sections used in these simulations are given in Chapter 3.5.

If a collision occurs, a second random number, R_2, can be generated and the species type can be determined. The probability of an electron interaction, P_i, with the i^{th} species is given by

$$P_i = \frac{n_i\sigma_i^{tot}(E_e)}{\sum_k^{N_s} n_k\sigma_k^{tot}(E_e)}, \tag{5-13}$$

where k is the dummy variable for summation over the included species. In order to determine the species type, R_2 is sequentially compared to the cumulative species probability up to the i^{th} species, $\sum_k^i P_k$, and the electron collides with the i^{th} species if R_2 is less than the corresponding cumulative species probability. Similarly, once the species type has been determined, the reaction type is determined by picking a third random number, R_3, and comparing it to the cumulative reaction probability, $P_{i,j}$, for the j^{th} reaction type involving the i^{th} species

$$P_{i,j} = \frac{\sum_l^j \sigma_i^l(E_e)}{\sigma_i^{tot}(E_e)}, \tag{5-14}$$

where l is the dummy variable for summation over the included reactions for species i. Again, if R_3 is less than $P_{i,j,}$ then the j^{th} reaction is accepted; if not then R_3 is compared to the next reaction.

As shown in Figure 5-9(a), only one random number is needed to determine what type of collision, if any, occurs since one can simply use the procedure described above, but combine Eqns. 1–3 such that the probabilities are appropriately re-scaled. The result is that the probability of species i having interaction j with an electron is computed by the total reaction probability,

$$P_{i,j}^{tot} = P_{col,tot}(E_e)\left[P_i\left(P_{i,j}\right) + \sum_k^{i-1} P_k\right]. \quad 5\text{-}15$$

The random number is still sequentially compared to the various reaction probabilities and if it is less than $P_{i,j}^{tot}$ then the i,j interaction is accepted. Note that if the random number is greater than $P_{coll,tot}(E_e)$, then no collision occurs because the probability for the last species and last reaction type (i=N_s and j=$N_R(i)$) is equal to $P_{i,j}^{tot} = P_{col,tot}(E_e)$ from Eqn. 5-15. In practice, since $P_{i,j}^{tot}$ is typically small (<0.1), it is more efficient to first check if a collision occurs (i.e. $R < P_{i,j}^{tot}$) and then, if one does, the reaction is determined (using the same random number) via sequentially comparing each reaction. This cumulative probability formulation could lead to some loss of precision for extremely rare collisions due to round-off error. However, the time step for each electron is the smaller of two possible values, one that gives a total collision probability of ~0.1 and the other a fixed maximum acceptable value for transport along the field lines. In general, the collision probability is therefore ~0.1 and with double precision variables, round-off is only significant for $\Delta P_{i,j}^{tot} < 10^{-15}$ which doesn't occur with the included reactions except very near various threshold energies. Furthermore, since we precompute the reaction probabilities at a finite number of electron energies, probabilities this small are not resolved and the reaction is considered to not occur (i.e. if $\Delta P_{i,j}^{tot} < 10^{-15}$ then the reaction is not included and its probability is set to 0).

5.3.4 Electron Input Model

Thermal and low energy non-thermal electrons from the plasma torus are modeled in the current simulations. The contribution of high energy (~1 keV) non-thermal electrons to direct excitation of atomic oxygen to the ^{1}D state (the only ^{1}D excitation mechanism

considered here) should be small relative to the thermal excitation rate (Bhardwaj and Michael 1999a). First, the excitation cross section decreases with increasing energy above ~5 eV and is an order of magnitude smaller than the peak value at 100 eV (Figure 3-7(b)). Furthermore, the non-thermal electron density (at energies below 100 eV) is significantly smaller than the density of thermal electrons (Oliverson *et al.*, 2001). However, the low energy non-thermal electrons do carry a non-negligible amount of energy and are important for several dissociation processes, such as MUV 1 excitation, and therefore this flux is included.

In order to model the input conditions along the domain boundaries properly, one must determine if the flux tube depletion across Io is significant. If the flux tube depletion is negligible, electrons can be input uniformly along the top and bottom domain boundaries; however if it is large, the electrons cannot be input uniformly across Io. To estimate the amount of depletion, we examine an electron's round trip motion to the torus "edge" and back to Io's atmosphere where the flux tube terminates. The electron must then scatter off the atmosphere if it is to remain in the flux tube as the end of the flux tube crosses Io. Moreover, electrons created from ionization processes may leave the atmosphere along the flux tube in which they were created.

This model of the flux tube depletion is similar to Retherford's (2002, 2003) analysis where he compared the time scales for a flux tube to cross Io and for a typical *thermal* electron to complete a round trip to the torus edge and back and concluded that most of the flux tube energy would be deposited as it crossed Io. For *thermal* electrons, we assume the torus scale height is $\approx\sqrt{2}R_J$ (Bagenal and Sullivan, 1981; Bagenal, 1985) and the plasma velocity across Io's poles is 7 km/s (Saur *et al.* 2002), implying a travel time across Io of $\sim 2R_{Io}/v_{plasma} \approx 520$ s. For $T_e = 5$ eV ($\bar{E}_e = 7.5$ eV) and an isotropic pitch angle distribution, the average parallel velocity[14], $\bar{v}_\parallel$, is 1035 km/s since $|\vec{v}_e\,(\bar{E}_e)| \approx 1625$ km/s. Further, it is assumed that T_e and $\vec{v}_\parallel$ remain approximately constant far from Io since the perturbation in the magnetic field strength is only significant near Io. The average electron travel time to the torus edge and back to Io (at the torus equator) is then $2\sqrt{2}R_J/\bar{v}_\parallel \approx 190\ s$. This implies that,

[14] $\bar{v}_\parallel = |\vec{v}_e| \int_0^{\pi/2} cos(\alpha) d\alpha / \int_0^{\pi/2} d\alpha$

in order to reach the wake, the typical *thermal* electron traveling across Io must either scatter off Io's atmosphere or be mirrored off the magnetic field.

One can take the analysis one step further and simulate the *partial* depletion of the flux tube by modeling the electron scattering off Io's atmosphere. Figure 5-10 shows a schematic diagram of the plasma flow past Io with Io at its maximum magnetic latitude (~10º) in the torus. The electron path angles are exaggerated for clarity. In Figure 5-10 the line with square symbols (line a) is the path of an average thermal electron heading north that just misses Io upstream, travels to the northern torus edge and back to Io, and then scatters off the atmosphere back towards the torus edge. If it scatters all these times or is lost but creates another electron via ionization, then it (or its daughter) will reach the wake. The line with circles (line b) represents the electron heading south passing upstream of Io which then proceeds to scatter off the southern "edge" of the torus and the southern atmosphere until it reaches the wake. In the figure, there is no significant depletion of the flux tube in region I because an average electron in the region must have originated further upstream than the electron on the (b) line, as illustrated by the dashed line. On the other hand, the electron number density and mean energy will be depleted in region II (though for the figure we have assumed the energy depletion is small) because some fraction of electrons, $f_j = n_{e,OUT,j} / n_{e,IN,j}$ ($j = N$ for north and S for south), will scatter off the atmosphere and the rest will either undergo attachment or impact Io. If the fraction lost can be considered roughly constant across Io, then after K scattering events, the flux tube number density will be $(f_j)^K n_p$, where n_p is the electron density in the plasma far upstream. Similarly, the average energy of the electrons will be $\left(f_{e,j}\right)^K \bar{E}_p$ where $f_{e,j}$ is the fraction of energy remaining after scattering once and $\bar{E}_p$ is the average electron energy upstream.

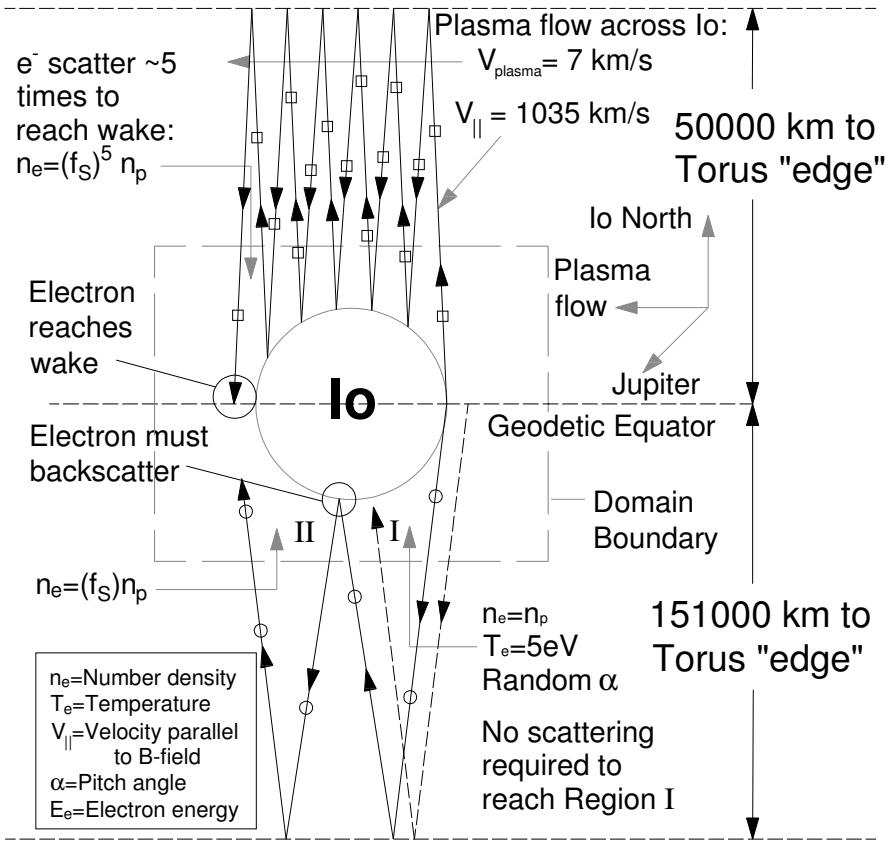

Figure 5-10: Schematic diagram of plasma flow past Io at its maximum latitude in the torus. The plasma velocity across Io is assumed to be 7 km/s and the electron temperature is assumed to be constant. Two average electron paths are shown: one just missing Io upstream and heading north, the other heading south. Note that the electron path angles are exaggerated for clarity and not inclined by the Alfvén angle. There is little depletion of the flux tube in region I because the average electron passing through there originates further upstream than the solid lower electron path, as indicated by the dashed electron path.

Figure 5-10 shows that for Io's northern-most latitude in the plasma torus (~10°), an electron reaching the wake from the north would have had to scatter ~four times (depending on its pitch angle and energy), compared to only once for electrons reaching the wake from the south. Thus if the fraction scattered per bounce were the same for the north and south, then fewer electrons would reach the wake from the north side of Io when Io is north of the torus equator (and vice versa when Io is south of the torus equator). This electron flux imbalance should tend to make the wake brighter in one hemisphere based only on Io's position in the torus. Furthermore, note that the fraction scattered per bounce would probably differ if the atmospheric number density was not roughly equal in the south and north. This

implies, for example, that the wake morphology might change substantially if Tvashtar is active or inactive.

The flux tube depletion is modeled by initializing the *thermal* electrons randomly in the plasma torus upstream of our simulation domain (out to 36,000 km) with a thermal energy distribution and an isotropic pitch angle distribution. Since the electrons are assumed to be in equilibrium, the plasma is effectively collisionless (in the Boltzmann equation the collision integral is zero) and therefore no collisions are performed upstream of our domain allowing us to efficiently move the randomly positioned electrons to their starting position along the domain boundary. Once inside the domain, the electrons are allowed to collide and convect downstream (with the local drift velocity) while moving along the magnetic field lines.

When an electron exits our domain along the top and bottom boundaries it is assumed to travel to a fixed, artificial torus "edge" set at $\pm\sqrt{2}R_J$ from the torus equator, off which the electron mirrors instantaneously, and then proceeds to travel back to the simulation domain. During the electron's transit of the torus, electron-ion collisions are computed that alter its pitch angle but not its energy. The effect of including re-thermalization of the electrons (through electron-electron collisions) was investigated and there was little change in both the [OI] emission and the overall electron energy deposition. This is most likely because there was a high energy electron which lost energy for nearly every low energy electron which gained energy through re-thermalization. It was also assumed that the electrons equilibrate (in terms of helical angle) in the plasma torus away from Io's perturbation of Jupiter's magnetic field. This should be reasonable because the mean time between collisions (electron-electron and electron-ion, ~74 s, Sittler and Strobel, 1987) is long compared to the (average) transit time spent near Io ($6R_{Io}/\vec{v}_{\parallel}$ ~10 s), but short compared to the (average) transit time to the torus edge and back (~190 s). Furthermore, while a given electron's velocity parallel to the magnetic field changes during transit of the torus, we assume that the electron drift velocity (relative to Io) remains constant upon leaving the domain. The electron continues to convect downstream until it leaves the domain downstream at the $X = -3000$ km plane. We also automatically remove any electrons with $E_e < 1.9$ eV because the activation energy of O ^{1}D (the lowest energy line we are interested in) is 1.96 eV. This allows for greater computational efficiency and simulations with a cutoff energy of 0 eV resulted in nearly identical auroral intensities. This is not surprising because the current model does not allow for the electrons to be re-energized except when they leave and subsequently re-enter the domain, though low

energy electrons will generally convect past Io in the time it takes to transit up and down the flux tube to the torus edge. Furthermore, the model does not include electron-electron collisions inside the domain because the time between collisions is long compared to the electron transport time across Io. Finally, it is not necessary to track the low energy electrons and their effect on the target atmosphere since the target atmosphere is held fixed and any effect that the electrons should have on the atmosphere is assumed to have been accounted for in the atmospheric simulations).

As described earlier, it is assumed that the electrons are thermalized away from Io's perturbation of the magnetic field. Therefore, when electrons re-enter the domain they are first given a random, isotropic pitch distribution at a magnetic field magnitude of $|B_{Initial}| = \left|\vec{B}_J\right|$ = 1835 nT (Combi et al., 1998) and Eqn. 5-10 is then used to adjust the pitch angle based on the local magnetic field at the electron's point of entry into the domain. If the local magnetic field at the domain boundary exceeds $\left|\vec{B}_{mirror}\right|$ for the electron, then the electron is assumed to have been reflected before it reached the domain boundary. These (few) reflected electrons then drift further downstream as they travel to the torus edge and possibly back to the domain boundary, where the process of obtaining a new pitch angle is repeated.

In addition to the thermal electrons described above, a small non-thermal component of electrons was input along the domain boundary. Based on the discussion in Oliversen *et al.* (2001) the electron distribution is well fit by a stable thermal population (described above) and a smaller (<5% of the thermal electron flux), fluctuating, primarily field-aligned non-thermal population at 30-40 eV that explains the significant fluctuations in the electron energy flux observed by Galileo (Frank and Patterson, 2000). As pointed out by Oliversen *et al.* (2001), this 30-40 eV non-thermal component is most likely a natural feature of the plasma torus because the short-term variability seen throughout the torus for the 685 Å S^{++} can be explained by this low energy non-thermal component. Therefore, in the current model a non-thermal component is added to the thermal component and it is input across Io without any decay in the number or energy flux. Furthremore, it is assumed that the energy distribution for the non-thermal component is a simple Gaussian centered at 35 eV with a standard deviation of 2.5 eV (simulations with a 5 eV standard deviation were nearly identical). The non-thermal component was found to be negligible for the [OI] 6300 Å emission intensity (Chapter 6), but very important for the MUV 1 SO emission band intensity

(Chapter 7) since most of the thermal electrons do not have sufficient energy to excite the MUV 1 emission.

5.4 EMISSION MODEL

After simulation of the electron transport through and collisions with Io's atmosphere in the Excitation Model, the Monte Carlo Emission model is used to compute the simulated observed spontaneous emission and it's reflection from Io's surface. Our model distinguishes between two types of emission: those from forbidden transitions and those from allowed transitions. It is necessary to treat the two transition types differently because of the large difference in lifetimes. The forbidden line transition lifetimes are long enough that the excited particle can be transported a significant distance from where it was excited whereas the non-forbidden transition lifetimes are so short that emission occurs essentially at the point of excitation. Finally, note that many excited states radiatively decay to another excited state which then also emits. These cascade emissions are accounted for in the model; the cascade of excited oxygen in the $2p^4\ ^1S$ state which radiatively decays (5577 Å) to the $2p^4\ ^1D$ state (which results in the 6300 Å forbidden line emission) is the most important cascade for the current analysis and accounts for several percent of the total 6300 Å emission.

The current model assumes that the atmosphere is optically thin over the wavelength range of interest, namely the UV-Vis spectrum from ~2000–8000 Å. This is a decent assumption since the photoabsorption cross section of Io's major atmospheric species, SO_2, oscillates between 10^{-19} to 10^{-18} cm^2 from 2500 Å to 6000 Å (Manatt *et. al*, 1993 and Ahmed *et. al*, 1992) and decreases at longer wavelengths. Since the largest line-of-sight column densities through Io's atmosphere (including Pele-type volcanos on the limb) are ~10^{17} cm^{-2}, the maximum optical depth of the SO_2 is less than ~0.1. It is possible, however, that localized large columns of the minor species might result in moderate optical depths over certain wavelengths and this should be more thoroughly investigated in the future.

5.4.1 Forbidden Line Emission

As mentioned above, forbidden line emission is treated differently than the non-forbidden line emission. The current work focuses on modeling the emission due to the forbidden transition (primarily via magnetic dipole transitions) from the ^1D state to the ^3P state which has a lifetime of ~134 s. This long lifetime means that collisions, which de-excite

(quench) the oxygen before spontaneous emission occurs, are critical to the emission intensity/morphology. Additionally, it was originally thought that transport of the excited oxygen would also significantly affect the emission morphology since an excited oxygen might travel ~100 km before emitting in the hot upper atmosphere. However, while the transport of excited oxygen did tend to diffuse the overall emission, it did not dramatically alter the morphology.

Excited oxygen atoms in the ^{1}D state obtained from the Excitation Model are assumed to start with an initial thermal velocity based on the local atmospheric temperature (Figure 3 from Wong and Smyth, 2000) and, if the atom is in a volcanic plume, a bulk velocity and temperature based on the precomputed local gas velocity and temperature in the plume. That is, it is assumed that the O atoms are in thermal equilibrium with the surrounding local atmosphere before they are excited by electron impact. The velocity of the excited oxygen is then altered via hard sphere collision dynamics with the electron to approximate the recoil due to the electron impact (this is a small effect). The subsequent O atom trajectory is then simulated with an adaptive timestep much smaller than both the local mean time between molecular collisions and the mean lifetime of [OI]. After moving the excited oxygen, the probability that the excited oxygen collides with another neutral is again given by

$$P_C \approx 1 - exp(-\Delta t \sum_i n_i \sigma_{O^*-i}\, v_{O^*-i}) \qquad 5\text{-}16$$

where σ_{O^*-i} is the hard sphere collision cross section between the excited oxygen (using the effective diameter of ground state oxygen) and the i^{th} species (Bird, 1994) and v_{O^*-i} is the relative speed between the excited oxygen and the i^{th} species (SO_2, SO, O_2, S, and O). The relative speed, v_{O^*-i}, is assumed to be the most probable relative speed given the excited oxygen's velocity and the local temperature of the gas. A collision occurs (and the excited oxygen given a new velocity) if P_C is greater than a random number.

Collisions with a neutral de-excite (quench) the excited O atom with a probability P_{Quench}. While the quenching probability is, in general, a function of (at least) the identity of the collision partner and the relative velocity between the two particles, here we assume that P_{Quench} is constant and independent of species type. Clark and Noxon (1972) generated excited O(^{1}D) via photolysis of O_2 and found that the quenching probability was unity for collisions with CO_2, 0.55 for O_2, 0.45 for N_2, and 0.2 for CO. Therefore it is reasonable to assume that the quenching probability for collisions with molecules ranges from 0.1 to 1.0 and a constant value of 0.5 is used for the base simulation case. P_{Quench} is unknown for

collisions of O(^{1}D) with O or S atoms and we have assumed that they quench with the same probability as the molecules. One might expect that the atomic quenching probability would be significantly less than the molecular quenching probability because atomic quenching of the excited state requires the formation of a transient molecule that then transfers the electronic energy into kinetic energy. To test the sensitivity of the simulated emission to the atomic quenching probability, P_{Quench} for O and S atoms was set to zero. The emission as viewed from Earth was found to change very little. This is because less than 10% (on the dayside) of the O(^{1}D) collision rate is due to collisions with O or S atoms and hence setting P_{Quench} to zero reduces the quenching rate by 10% and increases the mean-time between quenching collisions by a factor of 1.11. This small increase in the quenching lifetime does not appreciably change the region of the atmosphere containing excited O that can effectively emit O(^{1}D) before being quenched.

If the excited oxygen was not quenched on a given timestep, then we check if it emits spontaneously. The excited oxygen transition (decay) can proceed to three different states ($^1D_2 \rightarrow {}^3P_2$ for 6300 Å, $^1D_2 \rightarrow {}^3P_1$ for 6364 Å, and $^1D_2 \rightarrow {}^3P_0$ for 6392 Å), each of which has a different Einstein A coefficient, A_λ: $A_{6300} = 5.63\times10^{-3}$ s^{-1}, $A_{6364} = 1.82\times10^{-3}$ s^{-1}, and $A_{6392} = 1.1\times10^{-6}$ s^{-1} (Ralchenko *et al.*, 2008, and Sharpee and Slanger, 2006). The probability that an excited oxygen spontaneously decays in a given timestep is given by

$$P_E = 1 - exp(-\Delta t \sum A_\lambda), \qquad 5\text{-}17$$

and an [OI] emission event is simulated if the emission probability (Eq. 4-16), P_E, is greater than a randomly generated number. If an excited oxygen spontaneously decays via radiative emission, then the probability of emission at a given wavelength, λ, is equal to

$$P_{E,\lambda} = \frac{A_\lambda}{\sum A_\lambda}. \qquad 5\text{-}18$$

Notice that the emission branching ratio (Eq. 4-17) into the de-excited states (emission wavelengths) is a constant. Therefore, the simulation simply multiplies $P_{E,\lambda}$ by the total number of [OI] emission events in a given output cell in order to determine the number of photons emitted due to decay into each of the three lower states. One would expect that most excited oxygen atoms created in regions with high neutral density will de-excite through collisions before they emit because of the long lifetime of the ^{1}D state (~134 s). As expected, we find that high density regions, such as the sub-solar point and volcanic plumes, look dark at 6300 Å (and 6364 Å, 6392 Å). It should also be noted that we find no appreciable emission at 6392 Å; this is not unexpected since its lifetime is ~253 hours.

5.4.2 Non-Forbidden Line Emission

For non-forbidden transitions, the mean lifetime of the excited particle is much shorter than forbidden transitions like those that produce [OI] 6300 Å emission. Even if the mean lifetime is ~1 s, an excited particle will only travel ~1 km before it spontaneously emits. Therefore, for non-forbidden transitions with an Einstein *A* coefficient greater than unity the emission is assumed to occur at the position of the electron-neutral interaction that produced the excited particle. The probability that the m^{th} excited neutral will emit rather than be collisionally quenched is given by

$$P_{emit,m} = A/(\nu_{Q,tot} + A) \qquad 5\text{-}19$$

where *A* is the total Einstein *A* coefficient (accounting for all decay paths) and $\nu_{Q,tot}$ is the total quenching collision rate. The total quenching rate, $\nu_{Q,tot}$, is computed using the species densities and the gas temperature at the position of the excited particle with an assumed quenching probability of unity. For example, if an electron-O($2p^4$ ^1S) excitation occurs (emission primarily at 5577 Å and 2972 Å) with Einstein *A* coefficients equal to 1.26 s^{-1} and 7.54×10^{-2} s^{-1} respectively, then the distance a typical excited O($2p^4$ ^1S) would travel during the mean lifetime of the excited state (~0.7 s) is small (~1 km) compared to the atmospheric scale height (~10 km) and to the resolution of the simulation's output grid (~60 km). Therefore the motion of the excited oxygen is neglected and emission is counted as occurring at the excitation location. Since each simulated electron (and hence each electron-neutral interaction) represents a large number (~10^{10}) of real electrons, Eqn. 5-19 is used to scale the individual simulated emission event (as opposed to allowing emission if a random number was less than P_{emit}) in order to obtain better statistics.

5.4.3 Molecular Band Emission Spectra

In order to simulate the MUV spectrum, cross section and spectral data provided by Ajello (Ajello *et al.*, 2002) were used to determine if an SO_2 MUV excitation collision occurred and, if so, what wavelength photon was spontaneously emitted. Representative lab spectra at incident electron energies of 9, 11, 12, and 18 eV are shown in Figure 5-11; the model includes the measured lab spectra obtained at a resolution of 6 Å (at 9, 11, 12, 14, 16, 18, 20, 22, 26, 31, and 100 eV) similar to those shown in Ajello *et al*. (2002, Fig. 4). Like Ajello *et al.* (1992), our model distinguishes between MUV 1 ($SO_2 + e^- \rightarrow SO(\tilde{A}^3\Pi) + O(^3P) + e^-$) and MUV 2 ($SO_2 + e^- \rightarrow SO_2(\tilde{A}^1A_2, \tilde{B}^1B_1,\tilde{a}^3B_1) + e^-$) excitations and therefore the

Ajello *et al.* spectral data are divided into two regions: MUV 1 below 2670 Å and MUV 2 above (as shown in Figure 5-11). Note that the emission in the MUV 1 wavelength range includes some quasi-continuum MUV 2 emission (from excited SO_2) and that the MUV 2 wavelength range includes some band emission from excited SO. The MUV 1 and MUV 2 distinction is therefore purely based on the wavelength range as defined by Ajello *et al.* (1992).

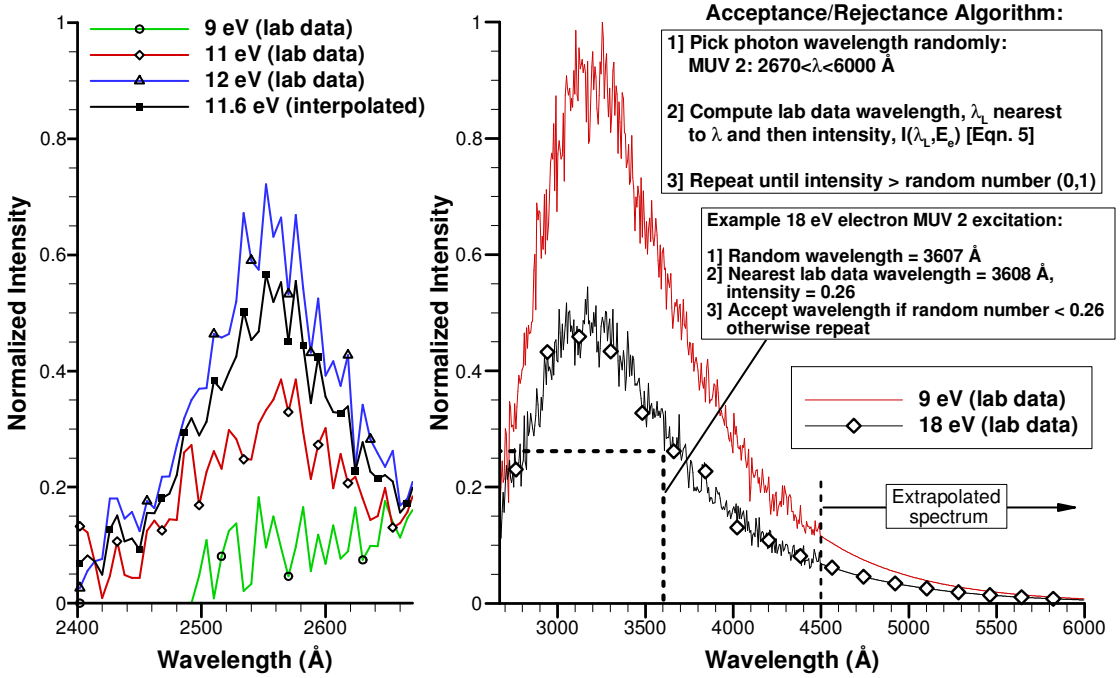

Figure 5-11: Representative measured spectra for electron-SO_2 excitation (Ajello et al., 2002) at several incident electron energies for (a) MUV 1 and (b) MUV 2 spectra. In (a) you see that even below the threshold energy for MUV 1 excitation (10.43 eV) there is emission because the SO_2 quasicontinuum extends to ~2500 Å for MUV 2 excitations. Note that the intensity of the 9 eV spectrum below a wavelength of 2492 Å is set to zero because the intensity at lower wavelengths oscillates about zero. Also shown in (a) is the interpolated spectrum (Eqn. 5-20) for an MUV 1 excitation occurring due to an 11.6 eV electron. In (b) the exponential curve fit used to extend the MUV 2 spectra to 6000 Å is shown as well as an outline of the acceptance/rejectance algorithm for an MUV 2 excitation due to an 18 eV electron. Note that, for computational efficiency, the MUV 1 and MUV 2 spectra have been scaled such that the peak intensity for all electron energies is less than or equal to unity.

In Figure 5-11 it is clear that Ajello *et al.*'s (2002) spectral data for these energies and spectral resolution only extends to 4400 Å. However, the total MUV 2 emission spectrum extends to 6000 Å. In order to make the spectral data consistent with the cross section data which are computed using the total emission intensity, it was necessary to extend the lab

spectra to 6000 Å. This was accomplished by fitting an exponential curve from 3900 Å to 4400 Å for each of the measured spectra which was then used to extend the spectrum out to 6000 Å as seen in Figure 5-11(b).

It should be noted that the area under the simulated emission spectrum is determined by the number of excitation-emission events which is in turn dependent on the MUV cross sections. The energy dependent cross sections were obtained via curve-fits to Ajello *et al.*'s (2002, Table 2) data at many incident electron energies (see Chapter 3.5 and Appendix A). This is important because we have spectral data at relatively few incident electron energies so, for a typical electron energy, we must interpolate between the available spectral data. While the shape of the spectrum may be distorted due to interpolation error, the overall emission intensity in that spectral band should not be affected. Also, as the incident electron energy increases, the shape of the MUV 1 spectra changes very little (though the area increases dramatically, Figure 5-11(a)) and the shape of MUV 2 spectra changes relatively gradually (Figure 5-11(b)). Therefore simple linear interpolation between the two laboratory spectra at energies bracketing the electron's energy is used to generate an approximate spectrum from which the emitted photon's wavelength is determined. In other words, for a simulation electron with an energy, E_e, above 9 eV undergoing an MUV interaction, the resultant spectrum is

$$I(\lambda, E_e) = WI(\lambda, E_l) + (1 - W)I(\lambda, E_u); \quad W = \frac{E_u - E_e}{E_u - E_l}, \tag{5-20}$$

where $I(\lambda,E_u)$ is the lab spectrum with the closest energy, E_u, above the energy of the electron and $I(\lambda,E_l)$ is the nearest lab spectrum with energy, E_l, lower than E_e. Since the threshold for MUV 2 emission is 5.3 eV and the lowest incident electron energy for which we have spectral data is 9 eV, we assume that the MUV 2 emission spectrum does not change significantly for incident electrons below 9 eV. Therefore, all electrons below 9 eV which cause an MUV 2 excitation use the 9 eV spectrum and any electrons above 100 eV use the 100 eV spectra (MUV 1 or MUV 2) to generate the emitted photon. All electrons with energies between 9 eV and 100 eV use Eqn. 5-20 to generate a spectrum from which the photon wavelength is drawn. For a given MUV excitation event, the wavelength of the emitted photon is chosen via acceptance/rejectance on the appropriate spectrum given the incident electron's energy (Figure 5-11(b)). Acceptance/rejectance of the photon wavelength for a given excitation event and electron energy is accomplished by picking a random wavelength (within the spectral range for that emission type) and a random number until the

intensity of the normalized spectrum at the currently picked wavelength is greater than the current random number.

In addition to the SO_2 (MUV 2) and SO (MUV 1) electronic band emission spectrum discussed above, there is intense band emission from the S_2 B $^3\Sigma_u^-$ $\leftarrow$X $^3\Sigma_g^-$ transition that emits from 2800–6400 Å (Pearse and Gaydon, 1976; Peterson and Schlie, 1980). Emission from S_2 might be expected to be important since S_2 in absorption has been detected in concentrations of up to 30% in Pele (Spencer *et al.*, 2000) and other regions of Io's atmosphere (Jessup *et al.*, 2007). Unfortunately, there is no laboratory data on the emission spectrum due to electron impact at conditions typical of Io's atmosphere, therefore the spectrum is pre-computed using the spectroscopic constants given in Radzig and Smirnov (1985) and Franck-Condon factors computed by Langhoff (2010). Peterson and Schlie (1980) determined the spectroscopic constants for the upper state; however, these were not used so that the ground state and upper state constants were derived from the same source. The Franck-Condon factors for the B $^3\Sigma_u^-$ $\leftarrow$X $^3\Sigma_g^-$ transition experimentally obtained by Anderson *et al.* (1979) are nearly identical to those computed by Langhoff (2010) except for transitions with very small Franck-Condon factors on which the experiment could only give an upper limit. The pre-computed spectrum (for radiative decay from a specific upper vibrational state) is then used in the electron transport code in the same way that the laboratory MUV 1 and MUV 2 spectra are used in order to draw a photon wavelength after excitation occurs.

The S_2 band emission spectrum is generated in the following way. First, the S_2 is assumed to be cold (<500 K) and therefore predominantly in the ground electronic and vibrational state; θ_v = 1044 K and thus only ~13% of the gas is in an excited vibrational state at 500 K. This assumption should be good since the gas temperature in a volcanic plume rapidly drops to <100 K outside the plume core as the plume expands and radiatively cools (Zhang *et al.*, 2003). Furthermore, the majority of plasma energy does not penetrate to the near-vent plume core region of the plume and therefore the assumption that the target S_2 gas is cold is acceptable. Whether an excitation event occurs is determined using the excitation cross section from Garrett *et al.* (1985) as discussed in Chapter 5.3.3. Since the excitation cross section computed by Garrett *et al.* (1985) refers to bound vibrational states, it is assumed that the cross section is for excitation to vibrational levels less than 10; above this the molecule predissociates. Predissociation for an upper state vibrational level, v', greater

than 9 has been observed and occurs via coupling to a $^1\Pi_u$ state for $v' \leq 16$ and to either a $^5\Sigma_u^-$ or a $^5\Pi_u$ state for $v' > 16$ (Wheeler *et al.*, 1998).

If one uses the Born-Oppenheimer approximation and separates the electronic, vibrational, and rotational energies of a molecule, then the frequency (expressed in wavenumbers, cm^{-1}) for a given transition from the upper state to the lower state, including the electronic energy and neglecting the rotational energies, is given by (Banwell, 1983)

$$\bar{\nu}_{(e'v',e''v'')} = T_e + \left[\bar{\omega}_e'\left(v' + \frac{1}{2}\right) - \bar{\omega}_e' x_e'\left(v' + \frac{1}{2}\right)^2\right] - \left[\bar{\omega}_e''\left(v'' + \frac{1}{2}\right) - \bar{\omega}_e'' x_e''\left(v'' + \frac{1}{2}\right)^2\right] \quad 5\text{-}21$$

where T_e is the electronic state energy separation in wavenumbers, and $\bar{\omega}_e$ and $\bar{\omega}_e x_e$ are the vibrational constants (the primes denote the upper and lower states as before) from Radzig and Smirnov (1985).

For a given electronic-vibration transition from v' to v'', there exists a rotational fine structure since the selection rules for the rotational quantum number are $\Delta J = 0$ (except $J = 0 \nleftrightarrow J = 0$) and $\Delta J = \pm 1$. The three possible values for ΔJ result in three branches: the Q-branch ($\Delta J = 0$), the P-branch ($\Delta J = -1$), and the R-branch ($\Delta J = +1$). However, note that $^3\Sigma_u^- \leftarrow {}^3\Sigma_g^-$ transitions obey Hund's case (b) and therefore, since there is no electronic orbital angular momentum there is no Q-branch in the emission spectrum. On the other hand, the triplet state does result in 3 spin-split P- and R-branches for a total of 6 main branches (Herzberg, 1989; Jevons, 1932). However, in the current analysis the spin splitting is ignored since it is expected to be much smaller[15] than the observational resolution (~10 Å, at best). Furthermore, the pre-computed spectrum is binned into 1 Å bins and the spin splitting would be mostly lost inside a given bin. The wavenumber of a given transition (in cm^{-1}) from the upper state (e',v', J') to a lower state (e'',v'', J'') is therefore (Banwell, 1983)

$$\bar{\nu} = \bar{\nu}_{(e'v',e''v'')} + [B'J'(J'+1)] - [B''J''(J''+1)], \quad 5\text{-}22$$

where J'' is equal to $J'+1$ for the P-branch, $J'-1$ for the R-branch, and J' for the Q-branch and B is the rotational constant equal to

$$B = B_e - \alpha\left(v + \frac{1}{2}\right), \quad 5\text{-}23$$

[15] S_2 is isoelectronic with O_2 which, for the same transition has a spin splitting of 1–3 cm^{-1} (< 0.01 Å for the emission band wavelength range), Jevons (1932).

where B_e is the equilibrium rotational constant and α is a constant that accounts approximately for the interaction between rotation and vibration. Note that the current model neglects the effect of centrifugal distortion on the rotational line spacing.

In order to obtain the spectrum for transitions from a given v', the frequency (cm^{-1}) is first determined by Eqn. 5-22 and then the relative intensity of the transition line must be computed. If an S_2 excitation event (to the B $^3\Sigma_u^-$ state) is determined to occur then the excitation to upper state vibrational level, v', is assumed to be proportional to the Franck-Condon factors since the excitation timescales are much shorter than the vibrational timescales.[16] Theoretical values for the Franck-Condon factors have been obtained by Langhoff (2010) and are in good agreement with the experimentally obtained values of Anderson *et al.* (1979). Note that theoretical Franck-Condon values computed by Prahan and Partridge (1996) are not used because of discrepancies in their values, most likely due to an inaccurate potential function at small inter-nuclear distances (Langhoff, 2010). As mentioned earlier, the theoretical Franck-Condon values of Langhoff (2010) are used in these calculations since they are in good agreement with the Anderson *et al.* (1979) results and are more comprehensive. Langhoff (2010) also computed the Einstein *A* coefficients for each transition and since all are greater than 10^4 s^{-1}, it is assumed that the excited states are negligibly quenched in Io's nearly rarefied atmosphere and therefore preferential quenching of the states can be neglected. The intensity of radiative decay from the various upper state vibrational levels to a given ground state vibrational level (for all J'') is proportional to the Franck-Condon factor for the given transition, $q_{v'v''}$, the Hönl-London factor ($S_{J'J''}$, the rotational line strength), and a Boltzman factor

$$I_{emission} \propto q_{v'v''} S_{J'J''} \left(\frac{(2J'+1)e^{-J'(J'+1)\theta_R/T}}{T/2\theta_R} \right), \qquad 5\text{-}24$$

where the partition function has been set equal to $T/2\theta_R$ since S_2 is homonuclear[17]. For a $^3\Sigma_u^- \leftarrow {}^3\Sigma_g^-$ transition, the Hönl-London factor for the P-branch is equal to J'+1 and for the Q-branch it is equal to J' (Herzberg, 1989).

---

[16] This means that the internuclear distance in the vibrating molecule does not change appreciably during the electronic excitation. Therefore the probability (Franck-Condon factor) of a transition from v'' to v' is based on the overlap between $\psi^*\psi$ of the ground state vibrational level (v'') and that of the excited vibrational state (v') (Herzberg, 1989).

[17] This assumes that the sulfur atoms in the S_2 are the same isotopes (i.e. $^{32}S_2$); on Earth only ~90% of the S_2 is $^{32}S_2$ and the same proportion probably holds true on Io.

For a given v' the emission spectrum can now be generated by looping over the final vibrational states and all J', obtaining for each the wavenumber (Eqn. 5-22) and then adding the intensity for the specific transition (Eqn. 5-24) to the appropriate wavelength bin. Note that in the electron transport simulation, these precomputed v' spectra are used to accept/reject the photon wavelength because for each excitation event the v' is chosen using the Franck-Condon factors. This way, the relative collision energy is decremented by the appropriate amount for each excitation and then an elastic collision between the electron and S_2 is performed to rotate the relative velocity vector.

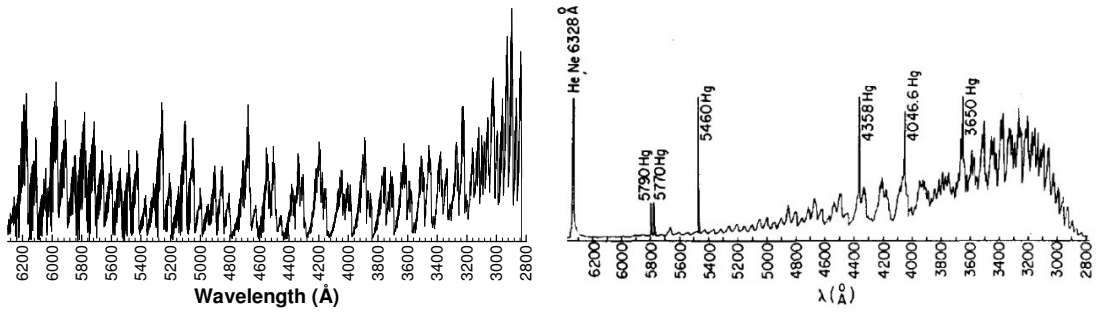

(a) (b)

Figure 5-12: Comparison between (a) Simulated S_2 spectrum from which photon wavelengths are drawn in the Monte Carlo electron transport simulations of Io's aurora and (b) observed S_2 spectrum in gas discharge (*From Peterson and Schlie (1980), courtesy of AIP*). .

To show the resultant cold-S_2 spectrum for the B $^3\Sigma_u^-$ ←X $^3\Sigma_g^-$ transition here, the sum is taken of each precomputed v' spectrum multiplied by $q_{v'v''=0}$ (the Frank-Condon factor from $v'' = 0$ to the respective v'). Figure 5-12(a) shows the resultant spectrum and it is seen that it is unfortunately not in good agreement to the spectrum measured in a gas discharge (Peterson *et al*, 1980), as seen in Figure 5-12(b). However, it is not clear how similar the two spectra should be, because they represent different excitation (and emission) conditions. The simulated spectrum increases in intensity far more rapidly at ~2800 Å than the observed spectrum which rises gradually from ~2800 to 3000 Å. Also, from ~3000 to 4000 Å the simulated spectrum is not full enough or intense enough compared to the spectrum at longer wavelengths. The shape of the simulated and observed spectra agrees much better if excited state vibrational levels higher than $v' = 9$ are included since these naturally tend to emit at shorter wavelengths because the separation energy increases. Therefore the computed intensity from ~2800 to 4000 Å increases relative to the longer wavelengths. However, it is

unclear how to include the vibrational levels which can predissociate and still be consistent with the theoretical excitation cross section to bound B $^3\Sigma_u^-$ states. Future simulations should aim to improve the model for the S_2 spectrum and the excitation cross section.

Obviously the S_2 band emission should affect Io's UV-Vis spectrum provided that there is sufficient S_2 gas, as expected inside Pele-type plumes. The current model includes the SO_2, SO, and S_2 band emission as discussed; however, there are other molecular species present with band emissions that could contribute to the UV-Vis emission spectrum. They include, but are not limited to, the analogous O_2 B $^3\Sigma_u^-$ ← X $^3\Sigma_g^-$ transition (the Schumann-Runge system; approximate wavelength range: 2440–4375 Å), the Herzberg system I in O_2 (A $^3\Sigma_u^+$ ← X $^3\Sigma_g^-$; 2563–4880 Å), Chamerlains airglow system which is a forbidden transition seen in the night sky airglow on earth (C $^3\Delta_u$ ← a $^1\Delta_g$; 3698–4378 Å), O_2^+ first negative system (b $^4\Sigma_g^-$ ← a $^3\Pi_u$; 4992–8527 Å), and the O_2^+ second negative system (A $^2\Pi_u$ ← X $^2\Pi_g$; 2060–6103 Å). These additional band emissions were not included in the current model because they are emissions from minor species and therefore it was believed that the contribution would be small (O_2 and O_2^+ are expected to be minor species, except perhaps on the nightside which is not visible for our observations).

5.4.4 Surface Reflection

While photoabsorption and scattering in Io's atmosphere can be neglected, it is important to account for the reflection of incident MUV light off Io's frost-covered surface. Much of the MUV emission is close to Io's surface and the reflectivity of SO_2 frost increases rapidly from ~0.15 to ~0.8 from ~3000–5000 Å (Hapke *et al.*, 1981 and shown in Figure 5-13), and therefore one might expect surface reflectivity to affect not only the magnitude of the spectrum, but its shape as well. Specifically it was hoped that the surface reflectivity would help the simulations of the UV-Vis spectrum match the observed intensity above ~3500 Å (see Chapter 7). However, even with increased surface reflectivity above ~3500 Å the simulated spectrum intensity falls off at larger wavelengths unlike the observations (see Figure 2-12) indicating that another species not modeled is contributing significant band emission in this wavelength range.

In order to compute the contribution of reflected light to the (spatially resolved) observed intensity, the solid angle of each surface element visible to the observer, as seen by

the emitting particle, is computed. To do so, many ($N_{photons,tot}$ ~ 10^5) tracer photons are emitted for each emission event with random orientations inside Io's solid angle as seen by the (m^{th}) emitting particle, Ω_m. The number of tracer photons, $N_{photons,jk}$, to hit the 1°×1° j,k surface element is recorded and, assuming a Lambert surface with a known reflectivity as a function the emission wavelength, $\rho_{frost}(\lambda_m)$, the contribution to the j,k surface element brightness, $I_{j,k}^m$, from the m^{th} emitter is equal to

$$I_{j,k}^m(\lambda_m) = \rho_{frost}(\lambda_m)\left(\frac{\Omega_m}{2\pi}\right)\left(\frac{N_{photons,jk}}{N_{photons,total}}\right)P_{emit,m} \qquad 5\text{-}25$$

The code then sums $I_{j,k}^m$ over all the emitting particles to get the total surface element brightness, $I_{j,k}^{tot}$ at a given wavelength. Furthermore, in order to obtain the contribution of surface reflection to the intensity of the disk-integrated spectrum, $I_{j,k}^{tot}$ is summed over all the surface elements.

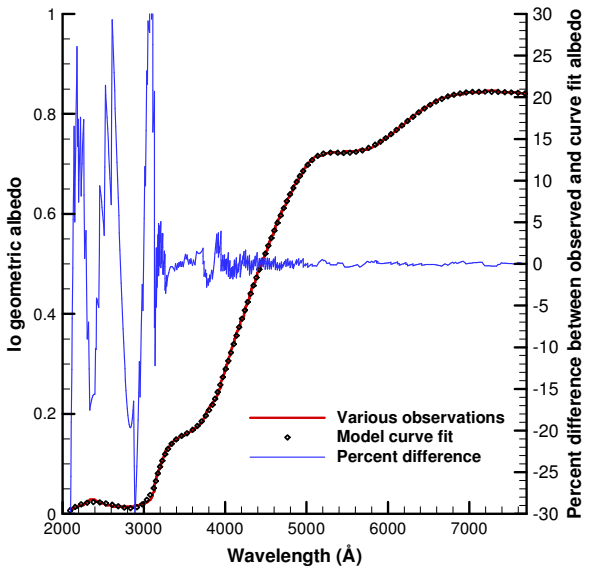

Figure 5-13: Comparison of Io's observed geometric albedo with wavelength versus the curve-fit geometric albedo used in the emission routine of the electron transport simulation. The observations used are given in Carlson *et al.* (2006).

Currently the model assumes an average geometric albedo across Io's surface that varies with wavelength and which is assumed to be equal to the reflectivity. Figure 5-13 shows the observed geometric albedo of Io as a function of wavelength and the curve fit to observations used in the model. Note that the observed geometric albedo was obtained by

pulling data points off of Figure 9.1 in Carlson *et al.*, 2006. While the curve fit is least accurate from ~2000–3000 Å, the low reflectivity means that the contribution of reflected emission to the total emission is very small. Above ~3000Å the difference in the observed albedo and the curve fit is less than 5%; almost certainly within the combined error of extracting the data from the original plot and the error in the observations themselves. Future work might be able to constrain the local SO_2 frost fraction using a global fractional frost coverage map and the reflectivities of the SO_2 frost and "non-frost" surfaces.

Chapter 6

[OI] 6300 Å Emission

6.1 Overview

Io possesses a spectacular [OI] 6300 Å aurora concentrated at low latitudes that differs from Earth's polar aurora. It is known that electrons (and, to a lesser extent, protons) traveling along the magnetic field lines result in a polar aurora near Earth. However, the precise mechanism (atmospheric variability, magnetic field orientation, torus position, etc.) that produces the Ionian 6300 Å auroral features remains uncertain. Several general features characterizing Io's aurora have been observed over the years: an equatorial band located along the extended Jovian magnetic equatorial plane, a limb glow near each pole, a bright spot in the wake, and extended diffuse emission particularly on the downstream side. In May 1997 Trauger *et al.* (1997) observed Io with the Hubble Space Telescope Wide Field and Planetary Camera 2 (HST/WFPC2) ~10 minutes after it entered Jupiter's shadow. Their observations showed several bright regions of [OI] 6300 Å emission (shown in Figure 2-10), and virtually no [SII] 6716 and 6731 Å emission. Oliverson, *et al.* (2001) showed that the disc-averaged [OI] 6300 Å intensity of Io varies with Io's system III longitude. Retherford (2002, 2003) noted that the brightness ratio between the north and south limb glows agreed with the ratio of the thermal electron column densities in the plasma torus above the respective poles. Furthermore, the latitude (on Io) of the equatorial spots seems to be correlated with Io's system III longitude based on many images of the aurora at different system III longitudes (Roesler 1999, Retherford 2000, Geissler 2001). A recent series of auroral observations during eclipse as Io crosses the torus by NASA's Cassini spacecraft definitively show that the equatorial auroral spots gradually shift in latitude (relative to Io) as Io's system III longitude changes (Porco *et. al.*, 2003, Geissler *et al.*, 2004b).

6.2 Observations

On four separate visits during the 1995 and 1997 Jovian oppositions Io was observed in eclipse using HST/WFPC2. These observations were first reported by Trauger *et al.*, 1997 (see Chapter 2.3). Here, the data from the HST archive has been re-analyzed, primarily by

Karl Stapelfeldt (Moore *et al.*, 2010) in order to compare the observations to the electron transport code simulations. For a more complete description of the observations see Moore *et al.* (2010); the most relevant details are given below.

Table 6-1: Io's position in the torus during observations.

Image Name	UT Date (start time)	λ_{III} (°)[A]	Ψ_{III} (°)[B]	Z_c [C]
u3wh0103m1	5/17/1997 (6:39)	63.069	-0.0240	-20.76
u3wh0104m1	5/17/1997 (6:45)	65.849	-0.0241	-20.16
u3wh0203m1	5/22/1997 (14:04)	121.383	-0.0241	3.61
u3wh0204m1	5/22/1997 (14:10)	124.163	-0.0241	5.15

[A] Jovian System III (magnetic) Longitude
[B] Jovian System III Latitude. The O4 offset tilted dipole magnetic field model was used, Acuña *et al.* (1983)
[C] Io's distance from torus centrifugal equator (Positive above the equator) in units of R_{Io} (see Figure 5-10).

Io was observed with the Planetary Camera PC1 at a resolution of 0.0455 arcsec per pixel, offset 6 arcsec diagonally from the WFPC2 pyramid apex. The brightness of scattered light was reduced and detector saturation effects were prevented by placing Io near the detector edge and keeping Jupiter within Wide Field Camera 3 (WF3). The position of Io during each of the F631N observations used here is listed in Table 6-1. To allow calibration of the images in Jovian coordinates, each visit began and ended with unsaturated images of Jupiter in the WF3 camera. Two narrowband filters were employed to isolate specific emission features: F673N admits the [SII] doublet at 6716 and 6731 Å; F631N only admits the [OI] 6300 Å line (and rejects the 6364 Å and 6392 Å lines). Multiple exposures were taken in order to reject cosmic rays, and to guard against possible timing errors in the start of the exposure sequence. No emission was detected near Io in the F673N filter in any of the four exposures (not listed in Table 6-1, see Moore *et al.*, 2010). The corresponding upper limit for [SII] emission (6716 Å and 6731 Å) near Io is ~5 kR.

The PC1 images had a strong background radial brightness gradient in the jovian/anti-jovian direction which was largely removed using a 2 dimensional high-pass filter. However, as seen in Figure 6-1, a residual brightness gradient of ~5 kR remained across the image field of view. Cosmic rays were removed by comparing image pairs, and rejecting large positive outliers. Flux calibration was done for all of the above exposure times following the WFPC2 Instrument Handbook (Heyer and Biretta, 2004); the conversion factor was found to be 1 kR = 1.21 DN (data number). The position of Io in the images was

established using images taken just before eclipse ingress, or just after egress, along with the assumption that HST accurately tracked Io's motion in the following/preceding 30 minutes. The orientation of Io North was derived from HST pointing information and the JPL Horizons database. The System III longitudes of Io and sub-earth coordinates were derived using JPL's Navigation Ancillary Information Facility (NAIF) subroutines.

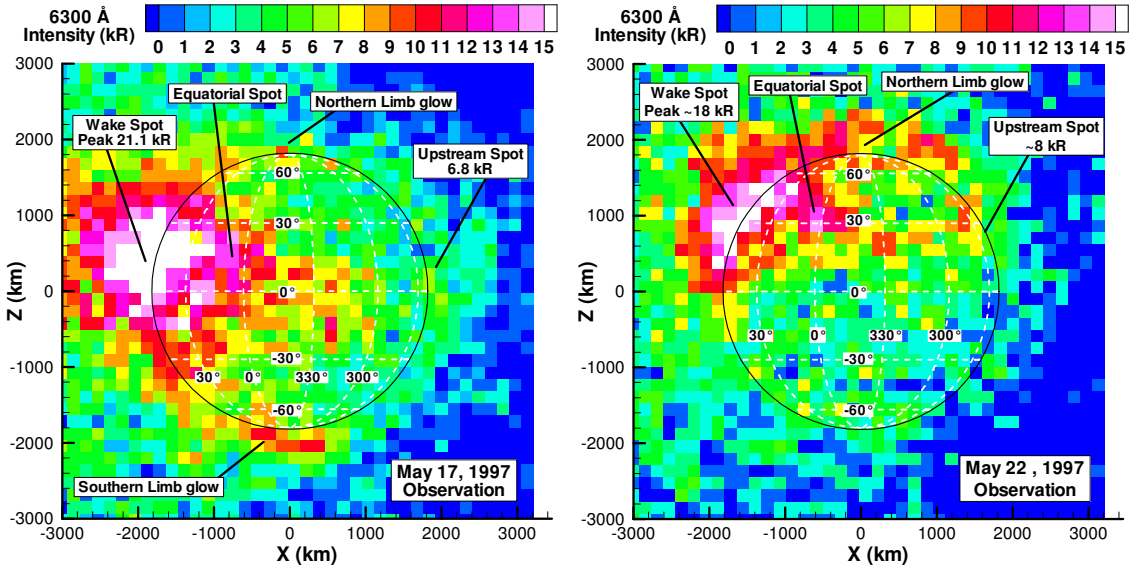

(a) (b)

Figure 6-1: Observations of [OI] 6300 Å emission from Io in eclipse. Average of two 260 second exposures taken by Trauger *et al.* (1997) with WFPC2. (Table 4). (a) Taken on May 17, 1997 starting at 06:39:14. (b) Taken on May 22, 1997 starting at 14:04. (*Data reduction done by Karl Stapelfeldt, from Moore et al.* (2010)*, courtesy of Elsevier*)

Two observations of [OI] 6300 Å emission upon ingress are shown in Figure 6-1. The May 17, 1997 observation is shown in Figure 6-1 (a). A bright wake spot is seen shifted to the north by ~5° that extends ~700 km beyond the limb and has a peak intensity (~21 kR) at an altitude of ~120 km above the limb. The upstream/wake spot brightness ratio is ~0.32 (though this is most likely too low due to the previously discussed brightness gradient) and a southern limb glow roughly twice as bright as the northern limb glow is seen. In Figure 6-1(b) (May 22, 1997 observation), the bright wake spot is seen to be shifted to the north by ~29°, extend to ~400 km, and have a peak intensity (~18 kR) ~90 km above the limb. For the May 22 observation, the upstream/wake spot brightness ratio is ~0.44 and a northern limb

glow ~2.5 times brighter than the southern limb glow is seen. Equatorial spots are seen in both observations extending across Io from the wake and fading toward the upstream.

6.3 [SII] AND [OI] 1-D CALCULATION RESULTS

A one-dimensional Excitation and Emission Model was used initially by Kenji Miki (a former graduate student in our group) to examine the emission intensity from [OI] and [SII]. His results, along with additional analysis are included here for completeness and to illustrate in a simple way some of the key concepts that affect the emission simulated in the 3D code (such as magnetic mirroring and collisional quenching). The discussion and figures originally appeared in Moore *et al.* (2010).

The 1-D code used 151 grid cells in the altitude (Z) direction with a ΔZ of 10 km. The electrons are input high in Io's SO_2 and O atmosphere at 1500 km with a temperature of 5 eV. In this region, the neutral density is several orders of magnitudes lower than at the surface and the atmosphere is nearly collisionless. For the 1-D simulation, the initial vertical velocity components of all electrons are oriented toward the surface. In this model, electrons are moved only along the Z-axis and can change their direction and energy through collisions. The vertical neutral density profile is taken from Wong and Johnson (1996; Figure 3) for a solar zenith angle (SZA or φ) of 30° and the vertical S^+ density profile simulated by Kumar (1985) is used. This model is used to examine the emission intensity ratio between [OI] and [SII] and the effect that Pele has on the [OI] emission. Such a model is comparable to the 1-D model by Bhardwaj and Michael (1999a, 2000) with the exception that we calculate the emission intensity of a specific line, as opposed to calculating yield spectra (Singhal and Haider, 1984), and include the magnetic field. Electrons from the plasma torus are input continuously and, once steady state is reached, a time-averaged emission rate for [SII] and [OI] is obtained.

We use the one-dimensional simulation to examine the intensity of [SII] emission from sulfur ions at 6716 Å and 6731 Å (A_{6716} = 4.7×10^{-4} s^{-1} and A_{6731} = 4.3×10^{-4} s^{-1}, Ralchenko *et al.*, 2008) relative to [OI] 6300 Å emission. The electron-S^+ excitation cross section for [SII] is not known. Hence, as a crude approximation for the excitation cross section, we took the [OI] excitation cross section, shifted the threshold energy from 1.96 eV to 2.1 eV, and then scaled the cross section parametrically by a constant, γ, in order to compare the resultant [SII] emission with the [OI] 6300 Å emission. In Figure 6-2, we see

that [SII] emission is significantly weaker than [OI] 6300 Å emission even if the electron excitation cross section were as much as 3 orders of magnitude larger than the [OI] excitation cross section (which is unlikely). Therefore, we know that if the cross section were small, then the [SII] emission intensity would be much lower than the [OI] intensity.

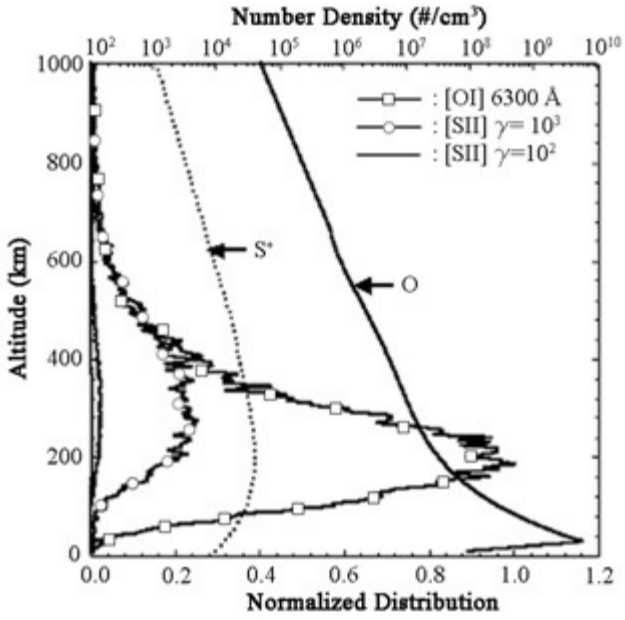

Figure 6-2: The [OI] 6300 Å and [SII] 6716 Å and 6731 Å emission. We normalize the emission intensity by the peak value of [OI] at ~200km. γ is the ratio of excitation cross section of [SII] 6716 Å and 6731 Å to that of [OI]. Even when γ is 100 (circles), the emission intensity is still small. S+ and O number densities (cm-3) are also shown. (*From Moore et al., 2010; courtesy of Elsevier; simulation by Kenji Miki*).

Even if the excitation cross section were un-physically large, the [SII] emission would be relatively dim due to two additional factors. First, the S^+ density is more than 2 orders of magnitude lower than the O density which directly influences the possible emission intensity through the number of [SII] excitation events. Also, the Einstein *A* coefficient for [SII] emission is ~10 times smaller than the Einstein-*A* coefficient for [OI] emission. A small Einstein-*A* coefficient allows for increased collisional quenching due to the state's increased lifetime and therefore reduces the fraction of excited sulfur ions that spontaneously emit. Consequently the peak emission from excited sulfur ions occurs at lower total gas densities (higher altitudes) than for [OI] emission. The [SII] emission is seen to peak at ~300 km,

roughly 100 km higher than the simulated [OI] peak emission, primarily because of the difference in the two Einstein *A* coefficients.

I also briefly examined alternate production paths for [SII] emission such as ionization-excitation of SO_2 (or S). While the ratio of SO_2 to S^+ density is ~10^4 above 200 km where collisional quenching is negligible, there are 14 times more thermal electrons with sufficient energy (2.1 eV) to excite S^+ directly than to ionize and excite SO_2 (18.6 eV). Similarly, there are significantly more S atoms than ions, but fewer thermal electrons are capable of ionization-excitation. Therefore the emission due to SO_2 and S may exceed emission due to direct excitation of S^+, though the ionization-excitation cross sections are unknown. In each case, the excitation cross section was assumed to be a constant fraction, δ, of the respective ionization cross section to S^+ with the threshold energy shifted by 2.1 eV to account for the excitation energy. Even if every ionization event above threshold produced [SII] (δ=1), the simulated emission produced from these other production paths was less than 0.2 kR, or ~2% of the [OI] 6300 Å emission intensity. Therefore, the [SII] emission intensity from ionization-excitation of SO_2 and S is roughly equivalent to the intensity due to S^+ excitation if γ=100. Therefore, even if ionization-excitation of SO_2 (or S) is the dominant excitation mechanism (e.g. $\gamma \ll 100$, $\delta \sim 1$), it would still produce negligible [SII] emission relative to [OI] emission. [SII] emission from ionization-excitation of S_2 present in the plumes was not simulated in this model, though the densities present in the plumes should quench virtually all of the resultant emission. These results suggest that Trauger *et al.'s* (1997) lack of detectable [SII] emission is consistent with reasonable excitation cross sections and densities found on Io.

Figure 6-3 shows the emission profile with inclusion of a single volcanic plume (Pele) and the magnetic field. Instead of doing a 1-D simulation along a simple radial line out of the planet center, the thermal electrons travel normal to the equatorial plane along the line tangent to Io's surface and perpendicular to the plasma flow, as shown in the inset in Figure 6-3. Also note that the atmospheric density profiles (other than Pele) used were identical upstream and in the wake in order to isolate the effects of Pele and the magnetic field. The solid line without symbols corresponds to the emission profile in the wake (X = –1900 km), and the lines with circles and squares are the profiles on the upstream side (X = 1900 km).

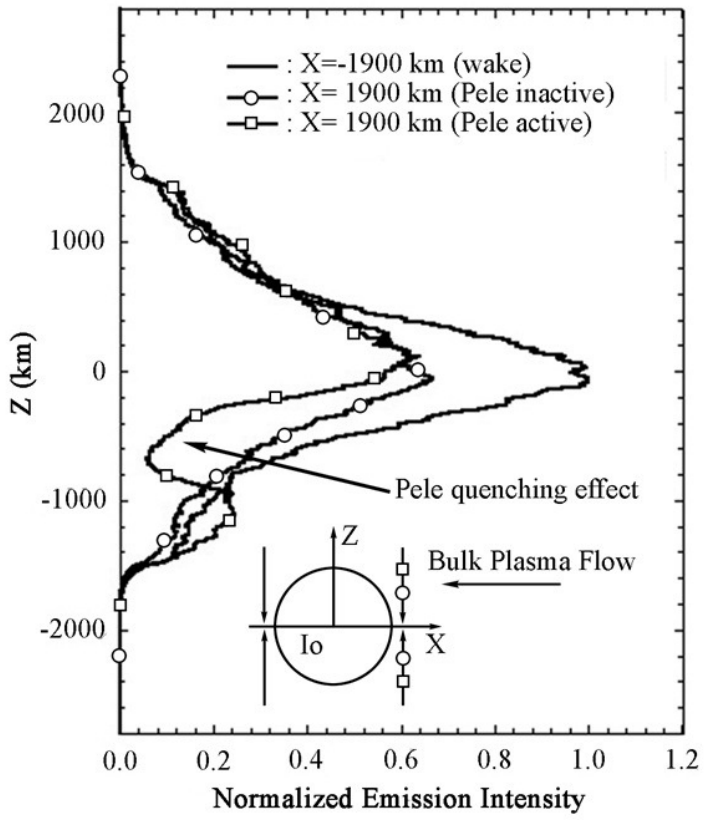

Figure 6-3: Upstream and wake [OI] 6300 Å emission profiles for a 1-D simulation what considers a single active plume (Pele) and the perturbed magnetic field. Three cases are shown: one (no symbols) represents the wake region and the others (circles and squares) are for the upstream region. As shown in the corner schematic, the Z axis is perpendicular to the plasma flow and Io's equatorial plane. We normalize the emission intensity by the value of the wake emission at the equator (Z = 0 km). In order to check the quenching effect of Pele, we calculate the intensity in two cases where Pele is active (square symbols), and where Pele is dormant (circles). Similarly, the mirror effect is examined by comparing the wake emission (no symbols) to the upstream emission without Pele (circles). (*From Moore et al., 2010; courtesy of Elsevier; simulation by Kenji Miki*).

In Figure 6-3 the simulation does not account for the flux tube depletion across Io in order to better compare the effect on emission due to mirroring. An incoming electron on the upstream side encounters an increasing magnetic field and the dense atmosphere of Pele's plume. On the other hand, in the wake, the magnetic field decreases and the atmosphere is not enhanced by Pele. To quantify the quenching effect of Pele, we calculated the intensity of upstream emission when Pele is active (squares) for comparison to the case when Pele is dormant (circles). We see that Pele quenches the emission strongly around $Z = -600$ km and

actually increases the emission around $Z = -1200$ km. Both effects occur because many electrons entering from the south are backscattered by the plume (or produce low-energy secondaries). Therefore, fewer electrons penetrate into the plume and the excitation rate of [OI] at the edge of Pele is increased. Furthermore, by comparing the peak wake emission to the peak upstream emission without Pele, one sees that the magnetic mirror effect reduces the upstream intensity by ~40%. The mirror effect and, to a much lesser extent, Pele's quenching effect are important contributors to the reduced overall upstream [OI] intensity. However, note that the magnitude of the intensity reduction due to the mirror effect is controlled by the magnitude of the upstream magnetic field perturbation and the pitch angle distribution of the electrons.

6.4 3D RESULTS – CONTINUUM ATMOSPHERE

The key features to be explained in the eclipse ingress images of [OI] 6300 Å emission are the bright spot in the plasma wake (its intensity, altitude, and longitude on Io), the much smaller and dimmer upstream emission, the limb glow, the diffuse coronal emission, and the lack of bright plumes. For the simulations, Io's latitude in the torus and the Jovian magnetic field orientation at Io's location was computed using the O_4 offset tilted dipole magnetic field model (Acuña *et al.*, 1983). Our simulated absolute emission intensity is directly proportional to the upstream electron density because the electron number flux is proportional to the upstream electron density and the model's magnetic field and atmospheric profiles are unchanged by upstream electron density changes. The lack of significant [SII] emission (and plume emission) was explained with the 1D emission simulations, and so no 3D [SII] emission simulations will be presented here. Explaining the presence of a bright wake feature shifted latitudinally off Io's equator and the lack of a corresponding upstream feature is crucial. First, a base case that best matches the observations will be shown, then several parameters will be varied to show how they affect the emission around Io. For all the results presented here, each case was simulated 10 times with different random number seeds. The sampled properties (e.g. 6300 Å intensity) were then ensemble averaged to give the plotted results. The Monte Carlo error was estimated assuming that our results were sampled from a normal distribution. For all the results shown, the error was less than 6% below 600 km altitude except in the vicinity of Pele, where it was up to ~10%.

Table 6-2: Volcano list, May 1997 (Geissler *et al.*, 2004a; Rathbun *et al.*, 2002).

Plume	Longitude, Latitude	Type
Grian (S. Karei)	16W, 2N	Day Prometheus
Kanehikili	38W, 16S	Day Prometheus
Amirani	117W, 24N	Night Prometheus
Tvashtar[1]	125W, 59N	Night Pele
Prometheus	156W, 2S	Night Prometheus
Culann	164W, 20S	Night Prometheus
Zamama	174W, 18N	Night Prometheus
Marduk	210W, 27S	Night Prometheus
Pillan	244W, 12S	Night Prometheus
Pele	256W, 20S	Night Pele
Loki	311W, 10N	Day Prometheus
Dazhbog[1]	302W, 54N	Day Pele
Acala	336W, 11N	Day Prometheus

[1]Assumed to be dormant for most simulations

The list of plumes assumed to be active during the observations (May, 1997) is given in Table 6-2. As mentioned in section 6.2.1 the activity of many of the plumes was unknown due to, among other issues, image coverage by Galileo. In general it was found that variation in the activity of the smaller Prometheus-type plumes caused little variation in the overall emission morphology. Therefore, the smaller plume activity was held fixed as indicated in Table 6-2. However, the activity of the larger Pele-type plumes did substantially affect the emission and hence their activity is varied for certain cases as indicated. For the simulations shown here, the non-thermal electron flux was assumed to be zero; for the small non-thermal fluxes expected (see Chapter 5.3.4) the [OI] 6300 Å intensity was found to increase by less than 1% (~0.1 kR peak) everywhere. In addition, the aurora simulations using the continuum atmosphere model do not include S_2 in the Pele-type plumes. One case was run which included S_2 in the plumes and confirmed that the effect of S_2 on the 6300 Å emission was negligible. The intense band emission from the S_2 B $^3\Sigma_u^- \leftarrow$ X $^3\Sigma_u^-$ transition which emits from ~2800–6400 Å (peaking around 3000 Å) and the implications on giant, S_2–rich plume activity are examined in Chapter 7.

6.4.1 Base Case

Base case simulations are presented in Figure 6-4 (and unconvolved in Figure 6-5) which provide the best match to the observations shown in Figure 6-1. In Figure 6-4 the

original simulation results (Figure 6-5) have been binned into the coarser observational grid and convolved with observation-specific point spread functions. These were generated using the publically available Tiny Tim software developed at the Space Telescope Science Institute to replicate their instrumental point spread functions. Io's position in the torus and the upstream magnetic field orientation are set to the corresponding values at the time of the two observations (Table 6-1) and the plumes (Table 6-2) are all active except Tvashtar and Dazhbog. The sublimation SO_2 density across the dayside was scaled by the ratio of the column density for T_{SS} = 115 K to the column density for T_{SS} = 120 K (Eqn. 5-5) and by the partial collapse factor as discussed above (Chapter 5.2.2). The probability of quenching was assumed to be 0.5 for collisions with all neutral species. Finally, it was assumed that the non-thermal electron flux was zero and that the upstream temperature of the thermal electrons was 5 eV. The electrons were assumed to re-thermalize with the plasma torus if they left the domain and returned, and their pitch angle was assumed to be isotropic far from Io (and then perturbed by the local magnetic field at the edge of the domain).

In this case, the emission morphology, including the wake spot and upstream brightness agrees with the observations reasonably well, though the peak [OI] 6300 Å wake spot intensity in the convolved simulation results (Figure 6-4) is off by a factor of ~3 compared to the observations in Figure 6-1. Though not shown, simulations with Io above the torus equator yield similarly intense wake spots which are a factor of ~1.5 less than Retherford's (2002) observed [OI] 6300 Å wake spot intensity when Io was above the torus equator (Z_C = 15.9).

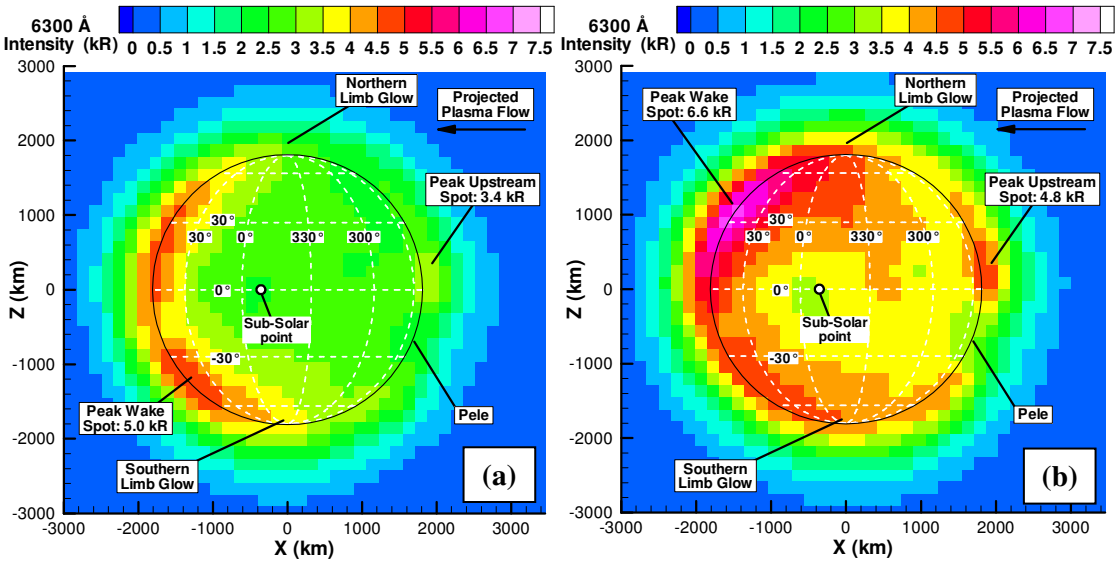

Figure 6-4: The simulated line of sight [OI] 6300 Å emission profiles (viewed from Earth, the upstream plasma comes roughly from the right). Shown are (a) the convolved May 17 simulation results, (b) the convolved May 22 simulation results. Note that the colorbar is from 0 to 7.5 kR in order to bring out details in the emission contours.

For Figure 6-4(a), the upstream/downstream brightness ratio (defined as the ratio of the peaks) is 0.68 while the observed ratio (Figure 6-1(a)) is ~0.32. For Figure 6-4(b) the upstream/downstream brightness ratio is ~0.73 compared to the observed ratio (Figure 6-1(b)) of 0.44. For comparison, Retherford's observations showed an upstream/downstream brightness ratio of ~0.36. While the simulation results have higher upstream/downstream brightness ratios than the observations, the processed observation images (in Figure 6-1) still contain a residual brightness gradient across Io that likely acts to reduce the observed upstream/downstream brightness ratio. The latitudinal location of the simulated peak wake emission (~30°N, Figure 6-4(b)) agrees well with the May 22 observation (~29°N, Figure 6-1(b)), The emission extends across Io and reproduces the morphology of the observation reasonably well given the level of approximation used in generating the sublimation atmosphere. The morphology of the simulated emission on May 17 (Figure 6-4(a)) does not agree well with the observation (Figure 6-1(a)). The observed peak wake emission occurs at ~5°N and extends over ~30° latitude whereas the simulated peak wake emission straddles the equator. Furthermore, the simulation results do not seem to have as prominent an equatorial spot (which we could approximately match only if we further reduced the atmospheric density across Io). The altitude of the simulated peak emission (~25 km, essentially on the

limb) is lower than the observed peak emission at ~100 km. Also, the simulated wake spot brightness above Io's limb falls off with altitude faster than observed. The simulated northern limb glow is slightly more intense than the southern limb glow; however, the ratio of north/south limb glow emission does not agree well with observations (Retherford *et al.*, 2003). Finally, the simulated coronal emission is much dimmer than observed, again possibly due to incomplete subtraction of scattered light from Jupiter in the observations.

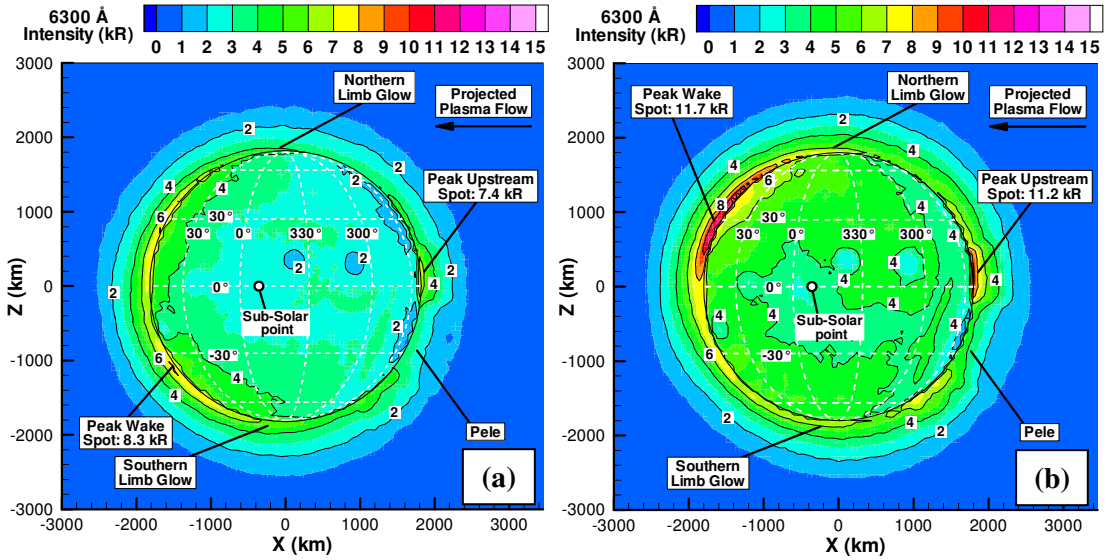

Figure 6-5: The simulated line of sight [OI] 6300 Å emission profiles (viewed from Earth, the upstream plasma comes roughly from the right). Shown are (a) the un-convolved May 17 data, and (b) the un-convolved May 22 data. Several circular regions of low intensity are due to (from left to right) the quenching effect of the plumes Kanehikili, Grian, Acala, Loki, and Pele. The thick solid black line shows Io's surface, the thinner black lines are contours every 2 kR, and the white dashed lines show lines of latitude and longitude.

Figure 6-5(a) and (b) show the simulated emission un-convolved on the original fine simulation grid. The wake emission is now only slightly brighter than the upstream emission, with an upstream/downstream ratio of ~0.89 (Figure 6-5(a)) and ~0.96 (Figure 6-5(b)). Also, in the un-convolved images several volcanic plumes on the dayside can be seen as dim circles where emission is largely quenched due to the high densities in the plumes. Upstream, Pele is seen to locally dim the limb in the southern hemisphere. The remaining simulation emission images will be shown un-convolved so that smaller changes can be seen when changing various parameters.

Average radial emission profiles (from upstream of Io and into the wake) were computed from both the simulation and the observation data following Retherford's (2002) method as illustrated in the inset schematic of Figure 6-6. The emission intensity at a given distance, R, from the center of Io (the sub-earth point in our images) is computed by averaging pixels within 90° arcs ($0.05R_{Io}$ wide) centered on Io's equator. Note that the emission is only radially averaged from $0.2R_{Io}$ to $1.7R_{Io}$. Figure 6-6 shows data from the May 22, 1997 observation, an August 27, 1999 observation (Retherford, 2002), the base case, the convolved base case, and a case showing the effect of our sublimation atmosphere scaling (Chapter 5.2.2). There is reasonably good overall agreement with the observations; the May 22 convolved base simulation's upstream emission intensity agrees very well with both observations and the simulated emission across Io's disk agrees well upstream but is somewhat too low towards the wake. The result is that the convolved simulation's wake spot intensity (radially averaged) is too dim by a factor of ~1.8. This behavior across Io's disk and into the wake could be interpreted as a modeling error due to an overestimate of the flux tube depletion across Io. However, if the flux tube depletion across Io is neglected (see Moore *et al.*, 2004), then the simulated wake spot is more intense, but the latitudinal position is not in agreement with the observations. Another possibility for the low wake emission is that we are neglecting dissociative-excitation from SO_2 as a source of excited O, and that the current simulated upstream intensity is larger than it should be for direct O excitation. This could be because the continuum atmosphere model does not account for the compression of the upstream atmosphere (which would increase quenching) due to plasma impingement (Saur *et al.*, 2002) and the field model might under-predict the compression of magnetic field upstream which would increase mirroring and reduce the electron flux to the upstream region.

In Figure 6-6, the peak simulated emission altitude above the limb of Io is seen to be lower than the peak of the observed emission altitude. In addition, above the limb the simulated emission intensity falls off with altitude faster than observed, both upstream and in the wake (assuming Retherford's data are more accurate because there is a smaller brightness gradient across Io). The falloff is insensitive to the quenching probability because above ~100 km, effectively no quenching occurs and hence all excited O atoms are already spontaneously emitting for nominal values of P_{Quench}. Also, the rate of falloff is unaffected whether or not the atmosphere is scaled due to partial collapse during eclipse because above ~100 km the atmospheric density does not collapse early in eclipse (Moore *et al.*, 2009). Furthermore,

though not shown, the falloff in intensity above the limb is not affected by the upstream electron temperature or the presence of volcanoes. In Figure 6-6, the un-convolved base case is seen to have sharper peaks on the limb of Io and decrease slightly faster away from the limb in comparison to the convolved case, as one would expect. Finally, note that the simulated radial (un-convolved) emission curve with no atmospheric scaling (both eclipse scaling and subsolar temperature scaling (Eqn. 5-5) turned off) is much dimmer than the base case in the wake and across Io.

The differences between the simulated and observed emission features (absolute intensity, upstream/wake spot intensity ratio, altitude of peak wake emission, emission intensity across Io, north/south limb glows) arise from several factors. The various model assumptions and simplifications that are the most likely cause of significant differences with the observations will be discussed below, as will the results of sensitivity analysis for some of the parameters. Note that 3D DSMC atmospheric simulations (Chapter 8) should correct many of the errors mentioned since it will accurately simulate the rarefied, reacting flow. However, it will still be limited because it still will not fully couple the atmosphereic gas dynamics with the plasma dynamics and the perturbation of the jovian fields around Io. Future work will incorporate a 3D DSMC simulation of Io's rarefied sublimation atmosphere after ingress into eclipse. The DSMC model is currently under development; the main remaining issue is extending the current model (including chemistry and sputtering, see Chapter 8) to have a two-temperature thermal model for the surface with variable frost coverage. Once finished it should include an inhomogeneous frost map distribution, a two temperature model for the surface that accounts for Io's rotation (Walker *et al.*, 2010, Gratiy *et al.*, 2010), surface sputtering and ion, electron, and photo-chemistry (see Chapter 3).

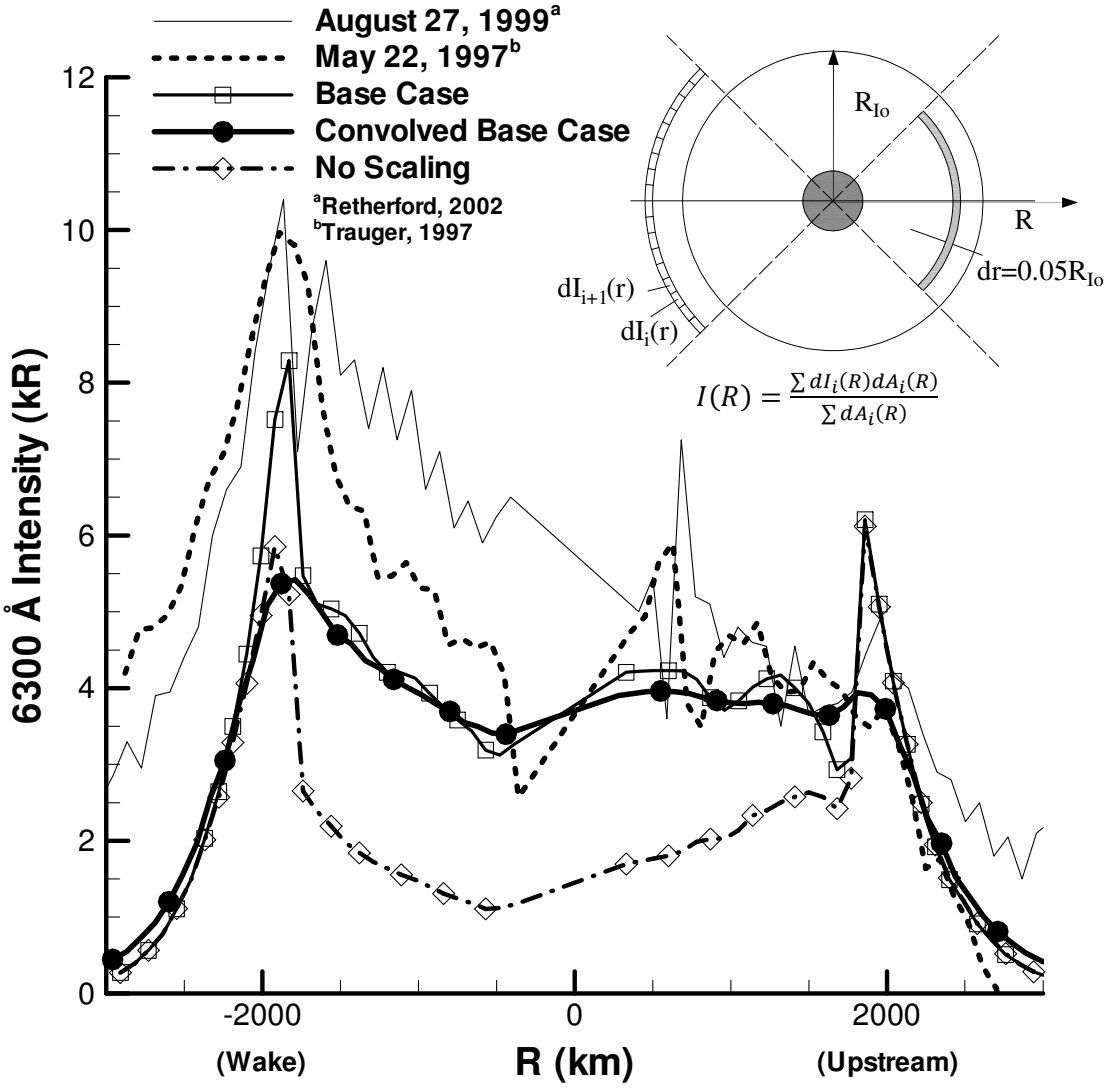

Figure 6-6: Radial brightness profiles (see schematic inset, note that the R-axis is in the direction of Fig. 9's *X*-axis) of [OI] 6300 Å emission for May 22, 1997 observations and simulations. To show that the observed radial profiles are largely independent of Io's position in the torus, Retherford's (2002) data for August 27, 1999 when Io is above the torus equator (Z_c=15.9) is shown. The wake is shown for negative values of R.

The simulated emission intensity should be sensitive to the quenching probability since ~65% of the excited oxygen atoms are quenched in the base case simulation. However, the relative speed dependence of the probability that the excited oxygen de-excites (quenches) upon collision with each of the neutral species (SO_2, SO, O_2, O, and S) is not known precisely. Therefore, a constant, nominal value of 0.5 was assumed, though values ranging from 0.1 to 1.0 seem to be reasonable for O(^{1}D) collisions with molecules (Clark and

Noxon, 1972). Figure 6-7 shows the emission intensity if the quenching probability is reduced by a factor of five (P_{Quench} = 0.1). The overall emission intensity is seen to increase, though the plumes are still seen to be dim. Notice that the wake spot broadens and brightens more than the upstream spot. Decreasing the quenching probability by a factor of five caused the simulated wake spot brightness to increase by a factor of ~1.8. Also, as expected, the altitude at which the emission peaks is sensitive to the quenching probability since lower probabilities allow emission to occur at higher neutral densities closer to the surface. A related result is that the upstream/wake spot intensity ratio decreases (to 0.79 for P_{Quench} = 0.1) for smaller quenching probabilities because the wake viewing geometry from Earth looks partially across the dense dayside atmosphere whereas the upstream viewing geometry looks partially across the nightside atmosphere. If P_{Quench} is increased to unity, then the peak wake intensity becomes roughly equal to the upstream spot and the overall emission decreases correspondingly.

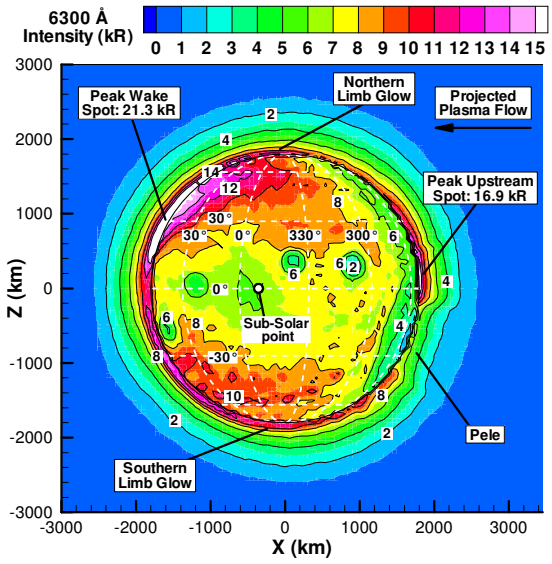

Figure 6-7: Simulated [OI] 6300 Å emission for May 22, 1997 assuming P_{Quench} = 0.1. The plumes are still relatively dim, but the intensity upstream and in the wake is seen to increase, respectively, 51% and 82% as compared to the base case (Fig. 9d).

As discussed earlier, the model lacks direct reaction paths from SO_2 and SO to $O(^1D)$ since no electron impact dissociation-excitation cross sections are available. However, there is suggestive evidence that substantial emission occurs from oxygen excited via dissociation-excitation (Oliverson *et al.*, 2001) and therefore our simulated intensity should be less than

the observed intensity. In addition to increasing the overall emission intensity, one might expect the addition of this excitation pathway to decrease the upstream/wake spot intensity ratio because the wake line of sight intersects the larger dayside SO_2 column as opposed to the upstream line of sight which intersects the much lower nightside SO_2 column. Finally, inclusion of direct dissociative excitation of SO_2 to $O(^1D)$ should preferentially increase the excitation rate in the equatorial regions where the SO_2 column density is highest (Strobel and Wolven, 2001; Jessup *et al.*, 2007; Feaga *et al.*, 2009) which may be one reason the May 17 simulated emission does not agree with the observations.

Another error source is the atmospheric model used in the simulation. A complete model would simulate an Ionian atmosphere that extends up to ~500 km in altitude, includes a longitude and latitude dependence due to both frost coverage and surface temperature distribution, multiple species accounting for chemistry, volcanic plumes, and has time variability during eclipse. The atmospheric profiles used in the present model are the best currently available that account for chemistry self-consistently; however, they are from a continuum simulation (Wong and Smyth, 2000, Smyth and Wong, 2004). Since most of the [OI] 6300 Å emission occurs at high altitudes where the atmosphere is rarefied, the accuracy of the continuum model at typical emission altitudes is questionable. The error in the altitude of the peak wake spot emission and its vertical extent is probably dominated by errors in the vertical neutral profiles, especially O and SO_2 (since the SO_2 dominates quenching). As mentioned previously, Smyth and Wong's (2004) atmosphere, which has a very different altitudinal distribution of species due to inclusion of electron chemistry, was also used. However, it was found to yield [OI] emission intensities that were higher on the upstream side of Io and the intensities were in general much higher than observed when using our curve-fit to their published data. Provided our simulation results would not change substantially given their complete simulated atmospheric profiles, we conclude that the newer Smyth and Wong (2004) atmospheric model contains too much atomic oxygen at high altitudes (or not enough other species for quenching) since our model should tend to under-predict the emission intensity.

There is further possible error in the model atmosphere because the atmospheric profiles assumed a sub-solar temperature of 120 K which more recent evidence suggests is too high (Feaga *et al.*, 2009 and Walker *et al.*, 2010a). Figure 6-8(a) shows the base case simulation for May 22 with Wong and Smyth's (2000) original atmosphere scaled for

collapse during eclipse but without scaling the atmospheric column density down to a sub-solar temperature of 115 K (Eqn. 5-5). It is seen that the overall intensity decreases and the simulated emission has a pronounced local minimum near the subsolar point (also seen in the radial emission plot, Figure 6-6) that is not observed. Also, the upstream spot is now brighter than the wake such that the upstream/downstream brightness ratio increased to 1.4. It seems that Wong and Smyth's (2000) high density case has SO_2 column densities that are too high whereas their low density case (at T_{SS} = 113K; not shown) produced much less emission than observed. In addition, the Wong and Smyth (2000) atmospheric profiles are for Io in sunlight. Therefore the partial collapse of the atmosphere due to eclipse, the severity of which varies from the wake ("dawn" terminator) to the upstream ("dusk" terminator) side, is not accounted for by the original simulated atmospheric profiles. As discussed previously, the partial atmospheric collapse is only crudely modeled and inclusion of an atmosphere which directly simulates collapse would reduce errors from the simplified model used to account for collapse. Figure 6-8(b) shows the base case simulation for May 22 without inclusion of partial atmospheric collapse. The upstream spot is seen to be more intense than the wake spot, and the overall emission intensity is slightly weaker when partial collapse is not modeled.

The current atmosphere is adopted from simulations that assume a uniform frost distribution and neglect Io's rotation resulting in an axisymmetric solution for the atmosphere as a function of altitude and SZA. The assumption of uniform frost might lead to densities near the poles that are too high and hence affect the simulated limb glow emission (by changing the quenching rate) and the flux tube depletion across Io (via increased/decreased electron backscatter). Finally, inclusion of Io's rotation and reasonable thermal inertias for the rock and frost into the simulation of the neutral atmosphere lead to a skewed frost surface temperature that lags the subsolar point by up to 30° towards the dusk terminator (Walker *et al.*, 2009). The frost temperature lag yields a corresponding lag in the peak SO_2 column density and hence the SO_2 column should peak closer to the upstream side of Io leading to increased quenching upstream relative to the wake.

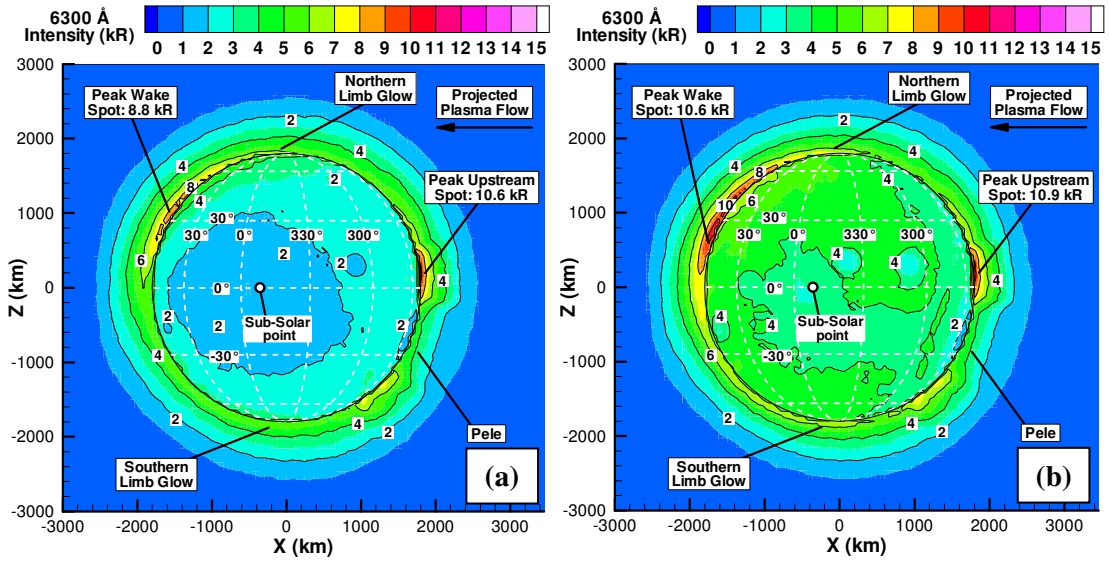

Figure 6-8: Simulated [OI] 6300 Å emission on May 22 if the SO_2 density is (a) not scaled to correct the column density for a sub-solar temperature of 115K (Eqn. 5-5) and (b) not scaled to account for varying partial collapse across Io during eclipse. In (a) the increased SO_2 density, especially near the sub-solar point, results in decreased emission. In (b) the increased SO_2 density on the wake side (relative to the upstream side) results in an increase in the upstream/downstream brightness ratio. Note that simulations with Wong and Smyth's (2000) original (no scaling) atmosphere are not shown since the emission is very similar to (a) except that the wake is ~12% dimmer.

Further possible sources of error in the simulated morphology and upstream/wake spot brightness ratio include errors in (i) the approximate model for flux tube depletion across Io, (ii) the compression of the atmosphere on the upstream side of Io due to the force of the impinging plasma (Saur *et al.*, 2002), (iii) the lack of the Hall effect in our model (Saur *et al.*, 2000), (iv) the percentage of the plasma diverted around Io, (v) the bulk plasma velocity below Io's ionosphere, and (vi) the magnitude of the magnetic field compression upstream of Io. Error in the flux tube depletion and the fraction of plasma diverted around Io primarily affects the wake spot intensity whereas the upstream intensity is affected by error in the compression of the upstream atmosphere (higher quenching) and magnetic field (reduce the upstream flux of electrons via mirroring). The lack of Hall effect is discussed below. Finally, error in the bulk plasma velocity, especially near the surface in the wake, affects the wake intensity near the equator; simulations of May 17 with an artificial reduction in the wake region's plasma velocity resulted in better agreement with the observation's emission morphology.

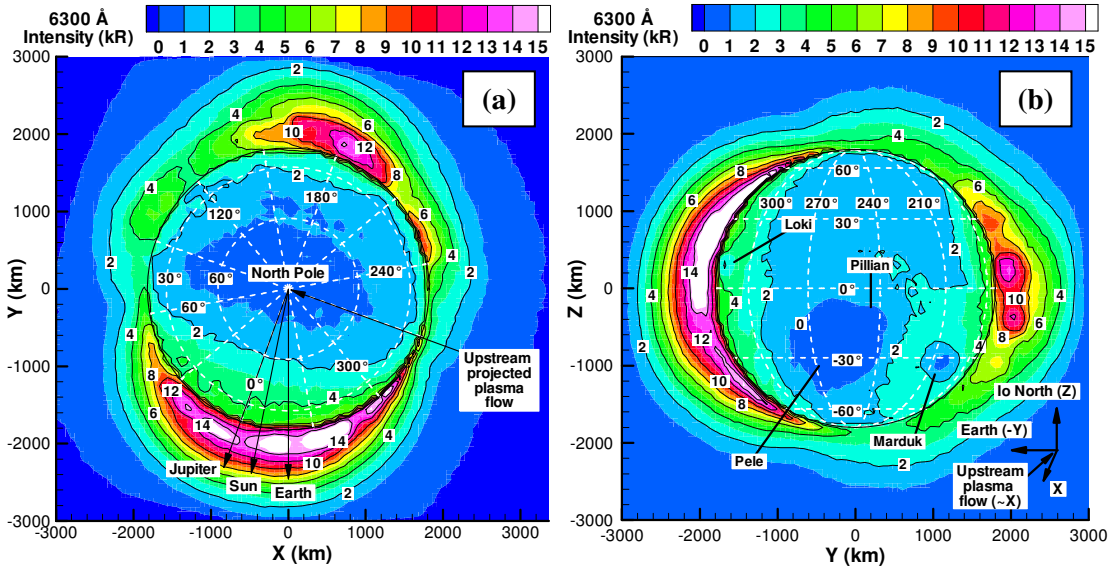

Figure 6-9: Simulated [OI] 6300 Å line of sight integrated emission on May 22 from (a) the north polar view and (b) the upstream view. The emission is seen to be dimmer on the nightside due to the relative lack of oxygen there. The anti-jovian spot is dim relative to the jovian spot; however, our model does not include the Hall effect, which should tend to increase the anti-jovian spot intensity.

Figure 6-9 (a) is the North polar view of the aurora and Figure 6-9(b) shows the emission seen from roughly upstream of Io for the base case. Figure 6-9(a) shows that the [OI] emission is brighter on the sub-jovian side than the anti-jovian side. However, the field model used in our simulations does not account for the Hall effect which has been argued to preferentially brighten the anti-jovian side (Saur *et al.*, 2000). In Figure 6-9(b) the sub-earth spot (roughly the sub-jovian spot) is once again seen to be brighter than the anti-earth spot and several plumes are again seen as dim regions with little emission.

6.4.2 Parametric Studies

To better understand the effects of various parameters on the [OI] emission, we now explore several of them parametrically. In order to examine the origin of the wake spot shift, we first artificially set Io's position at the plasma torus equator but keep the upstream jovian magnetic field orientation at the time of the observation ($\lambda_{III} = 64.5°$, $\Psi_{III} = -0.024°$, $Z_c = 0$). Then the upstream jovian magnetic field is oriented as if Io were located at the torus equator and Io's actual position in the torus is set to the correct value at the time of the observation ($\lambda_{III} = 120°$, $\Psi_{III} = 0°$, $Z_c = -20.4$). To examine the effects of the volcanic plumes on emission,

we simulate the emission with Tvashtar and Dazhbog active and also simulate the emission with all the volcanoes dormant. Finally, we examine the sensitivity of the emission to the upstream electron temperature.

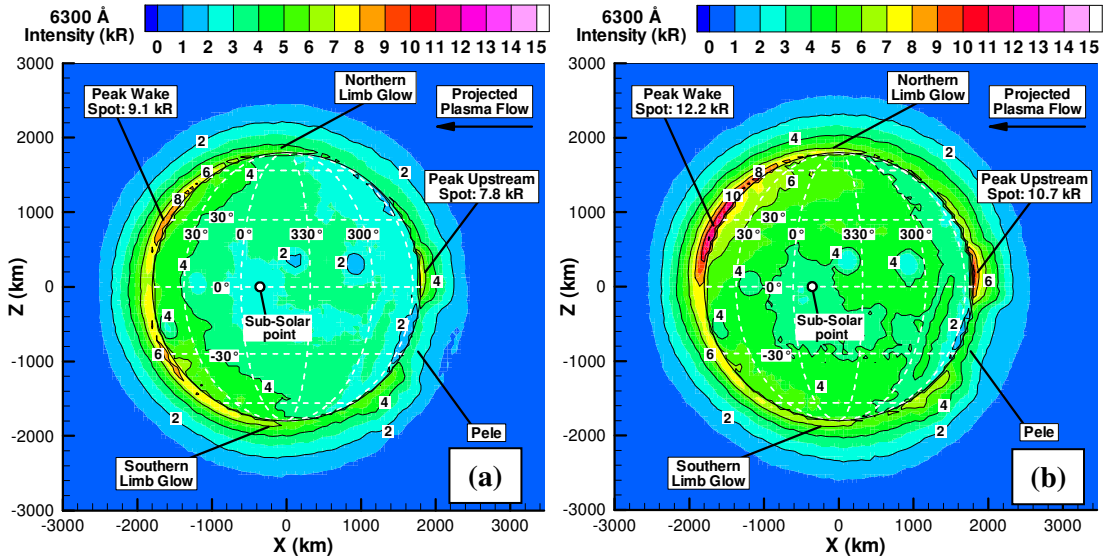

Figure 6-10: Simulated [OI] 6300 Å emission for May 22 observation (a) with the magnetic field oriented properly, but Io artificially located at the plasma torus equator and (b) with Io properly located in the plasma torus, but with the magnetic field oriented as if Io were at the torus equator. In (a) the wake emission is located roughly symmetrically about Io's equator whereas in (b) the wake emission is located ~23° above the equator.

Figure 6-10(a) shows the simulated line of sight integrated emission intensity for the far-southern magnetic latitude May 22 observation (Figure 6-5(b)), but with Io located at the torus equator (Z_c = 0). It is seen that the wake spot is no longer located at the appropriate latitude on Io and, in fact, the emission across Io looks very similar to the May 17 simulations (Figure 6-5(a)). Figure 6-10(b) shows the computed line of sight emission intensity with Io properly offset from the torus equator (Z_c = –20.4), but with the magnetic field oriented as if Io were actually at the torus equator. The wake spot is now brighter and located at the approximate latitude observed because the electron flux tube depletion across the northern hemisphere decreases due to the increase in the distance to the northern plasma torus edge (therefore decreasing the number of scattering events required to reach the wake). Based on these results, it seems reasonable to conclude that Io's latitude in the torus is an important contributor to the behavior of the wake spot through the asymmetric flux tube depletion across Io as described earlier. However, one cannot conclude from these results that the

magnetic field orientation does not affect the wake spot latitude; the field used in our model is not self-consistent because it was computed for a given location in the torus (Combi *et al.*, 1998) and we then rotated the upstream field to match the conditions at the time of our observations.

Figure 6-11(a) shows the emission with Tvashtar and Dazhbog active and all other parameters the same as for the base case (Figure 6-5(b)). Dazhbog is visible as a dim region that extends over the limb in the northern hemisphere on the upstream side of Io. Similarly, even though Tvashtar is on the nightside of Io, its canopy rises above the limb and results in a small region of decreased emission; the effect is limited because the majority of the line of sight integrated emission comes from the dayside atmosphere. Also, compared to Figure 6-5(b), the wake spot in Figure 6-11(a) is slightly brighter and the upstream spot is dimmer though both variations are within the Monte Carlo noise for the simulations. Figure 6-11(b) shows the emission with all the volcanoes dormant. The most striking change in the emission relative to the base case (Figure 6-5(b)) is that there are no longer dim regions across Io where several of the smaller plumes were located. The peak wake spot brightness is seen to decrease ~3% with no active plumes (within the noise) while the peak upstream brightness is seen to decrease ~30% with all plumes dormant (notably Pele). However, the total, or average, upstream emission remains roughly constant whether the plumes are active or dormant. When Pele is dormant the upstream emission on the limb is much more uniform between ±25° latitude. As seen in Figure 6-3 (and in comparing Figure 6-5(b) and Figure 6-11(b)), when Pele is active, the emission increases just outside of Pele. Comparison of Figure 6-5(b) and Figure 6-11(b) demonstrates that volcanoes with nominal oxygen concentrations do not produce locally bright [OI] emissions due to the low oxygen content and the increased quenching inside the plume.

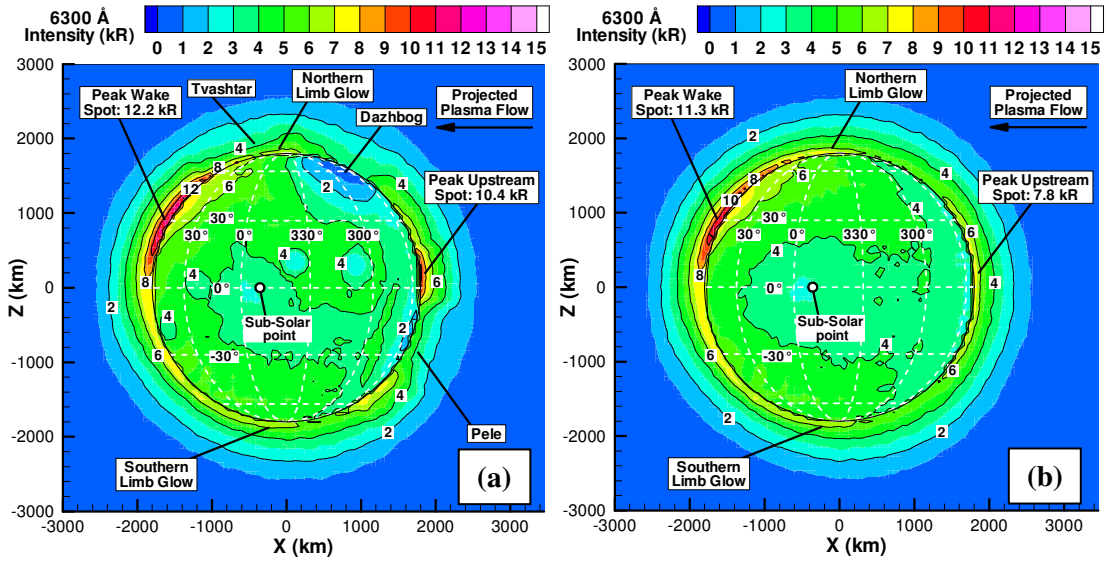

Figure 6-11: Simulated [OI] 6300 Å emission profiles on May 22 (a) with Tvashtar and Dazhbog active in addition to the standard plumes (Table 2) and (b) with all plumes dormant. In (a) Dazhbog is seen to decrease the emission on the upstream, northern limb and Tvashtar slightly alters the limb glow emission. With all the plumes inactive (b), the peak upstream spot intensity decreases, but the average upstream emission is unchanged as the emission now extends more evenly across the limb. The change in the upstream emission is mostly due to Pele being dormant.

Clear filter images show bright plumes (particularly Pele) as seen in Radebaugh *et al.* 2003, Geissler *et al.* 2004b, Retherford *et al.* 2007a,b, and Spencer *et al.* 2007. As a proxy for the clear filter emission morphology, Figure 6-12 shows the column integrated electron energy deposition (through all electron interactions included in our model, see Table 3-2 and Table 3-3) from the Earth view for the case with Tvashtar and Dazhbog active (Figure 6-11(a)). As one might expect, we find that the large volcanic plumes are very energy-absorbing; Pele, Tvashtar, and Dazhbog are easy to see in Figure 6-12. Since much of the electron energy is deposited into excitation of neutrals, this suggests that non-forbidden emission (such as FUV or MUV emission) would be bright around volcanic plumes because the lifetimes for excited states of allowed transitions are much shorter than the mean time between collisions. We also see in Figure 6-12 that Dazhbog "shields" Io in the region around 300°W, 45°N from energy deposition via electrons since the electrons are scattered by the dense plume instead of continuing south along the field lines which diverge around Io. If Dazhbog is dormant, this region has ~4 erg–s^{-1}–cm^{-2} deposited, similar to that seen downstream of Dazhbog in Figure 6-12. Tvashtar exhibits a similar effect on the electron energy deposition though it is not seen because it is on the nightside.

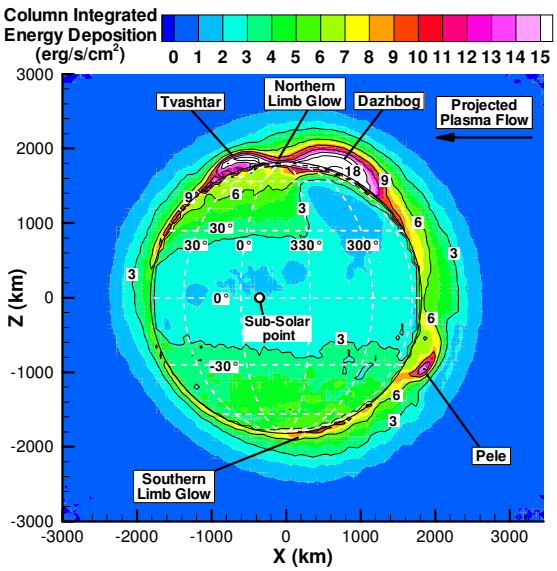

Figure 6-12: Electron energy deposition (integrated along line of sight) into the neutral gas on May 22 by electrons with energy above 1.96 eV via the interactions listed in Chapter 3.5. We normalize the profile by the peak value. Unlike for emission profiles, absorption in the larger volcanic plumes of Pele, Tvashtar, and Dazhbog is quite apparent. This suggests that for non-forbidden emission, these plumes will be bright

The upstream electron temperature was varied to investigate the [OI] 6300 Å emission sensitivity to the upstream thermal electrons' temperature. Figure 6-13(a,b) shows the simulated emission with upstream electron temperatures of (a) T_e = 4 eV and (b) T_e = 6 eV. Note that examining much lower temperatures is not helpful since at ~2 eV the emission intensity drops off sharply as the bulk of the electrons do not have enough energy to produce [OI] upon collision with an oxygen atom. Similarly, above ~15 eV the emission intensity also drops because the bulk of electrons have energies large enough that the electron excitation cross section for [OI] has begun to fall sharply (see Figure 3-8). As seen in Figure 6-13(a), the overall emission decreases as the electron temperature is reduced, especially across the disk of Io. Also, the upstream/downstream intensity ratio decreases (relative to the base case) to 0.84. Conversely, if the electron temperature increases (Figure 6-13(b)) the overall brightness increases and the upstream/downstream brightness ratio remains the same as the base case (0.96). The vertical extent of the [OI] emission above the limb seems to be independent of the electron temperature, and is most likely controlled by the oxygen density falloff with altitude.

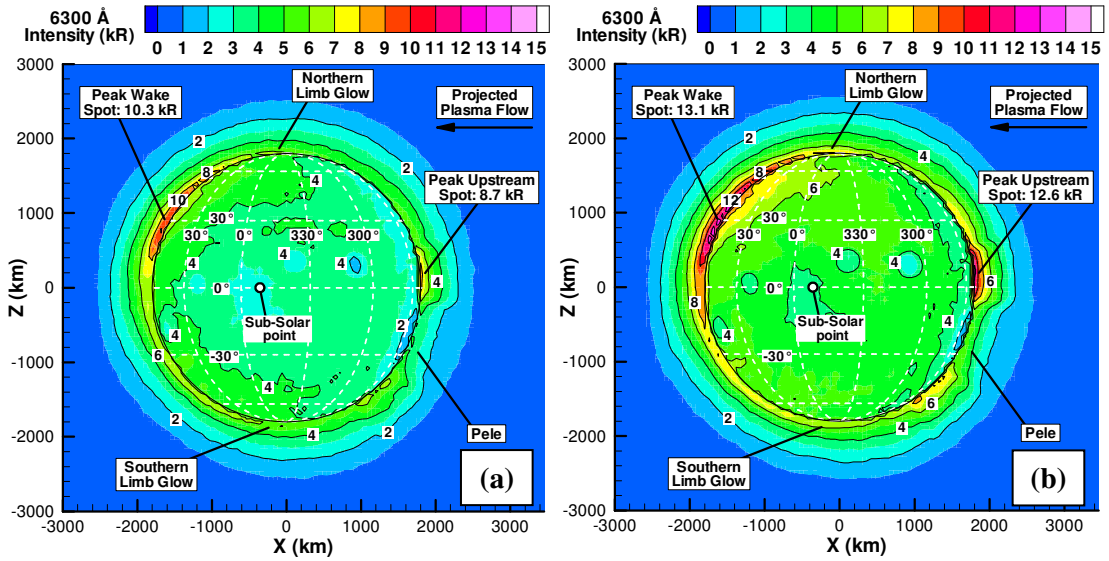

Figure 6-13: Simulated [OI] emission on May 22 for (a) upstream electron temperature of 4 eV and (b) 6 eV. In general the emission in (a) is less intense than in (b) as might be expected because the total energy flux is higher in (b) than (a).

6.6 CONCLUSIONS

A three-dimensional Monte Carlo (MC) model of [OI] 6300 Å emission from Io during ingress into Jovian shadow was presented. The simulation accounts for the 3D variation of SO_2, O, SO, and O_2 in the atmosphere, several volcanic plumes, and the perturbation of the Jovian magnetic field around Io. Maxwellian electrons from the Jovian plasma torus with a temperature of 5 eV are input along the simulation domain boundaries and move along the magnetic field lines distorted by Io, occasionally participating in collisions with neutrals. Since the travel time for an electron flux tube to pass Io is ~520 s and the time for individual electrons to stream along a flux tube to Io is ~190 s, the depletion of electrons from the flux tube as it crosses Io is accounted for approximately by computing the travel time (T_{trip}) to the torus edge and back for each electron leaving the domain, and then moving the electron downstream by $v_{\perp,drift} * T_{trip}$ (see Chapter 5.3.4).

For the base case simulation (Figure 6-4(b)), the [OI] emission intensity in the wake is ~3 times smaller than the observations (Figure 6-1(b)) and the peak intensity occurs at a somewhat lower altitude, but the wake is clearly brighter than the upstream emission. Note that the observed [OI] emission intensity varies in time by up to a factor of two for Io at a given location in the torus. The discrepancy in the upstream/downstream brightness ratio

most likely arises from the approximations used for the atmospheric model (e.g. use of atmosphere with T_{SS} = 120 K versus T_{SS} = 115 K, use of dayside versus partially collapsed atmosphere) and the strength of the magnetic field perturbation upstream of Io. The simulated north/south limb glow feature is slightly brighter in the north than the south, though not by as much as observed.

Flux tube depletion across Io is crucial to the latitude of the wake spot. The orientation of the magnetic field itself (though the magnetic field orientation is linked to Io's location in the plasma torus) did not seem to affect the latitude of the wake spot in our simulations. However, the limitations of our magnetic field model prevent us from concluding that the field orientation has *no* effect on the wake spot latitude. The north/south flux tube depletion is controlled by Io's location in the torus, the divergence of the magnetic field lines around Io, the atmosphere over the poles, and the plasma drift velocity across Io.

The neutral density profile in Io's atmosphere has a significant influence on the observed aurora morphology and intensity. Our 1-D calculation shows that the dense neutral (predominatly SO_2) atmosphere near the surface quenches ^{1}D excited oxygen and so the near-surface region should look dark in 6300 Å emission (Note that in 3D cases, the limb is not dim because we see the total integrated column intensity). The competition between this quenching effect and the larger O density near the surface causes the emission peak to be at ~25 km for the dayside atmosphere. In order to get the simulated peak emission to the observed altitude of ~100 km, the vertical O profile and/or the SO_2 profile must change. Furthermore, weaker diffuse emission than observed was found in the simulations at high altitude (> 400 km). In this region, the neutral density is low enough for any ^{1}D excited oxygen to emit photons without collisional de-excitation; therefore, such diffuse or coronal emission intensity is solely a function of the vertical number density profile for oxygen at high altitudes. These results highlight the need for the use of the chemically reactive, 3D DSMC atmospheric model currently under development (Walker *et al.*, 2009); Wong and Smyth's (2000) continuum model for the atmosphere is probably not valid beyond several scale heights above the surface.

The atmospheric "dayside" column is important for matching the upstream/downstream brightness ratio since the wake spot's line of sight is partially across the dayside atmosphere. The simulation results suggest a subsolar temperature in the vicinity of 115 K as opposed to higher temperatures (120 K). Furthermore, the partial atmospheric

collapse during eclipse, and the fact that the level of collapse varies across Io, is also important for matching the upstream/downstream brightness ratio. This is because virtually all the ^{1}D excited oxygen at low altitudes is collisionally quenched. Therefore, reducing the atmospheric number density increases the emission in nearly the inverse proportion. Hence, even small reductions in the atmospheric density near the surface due to partial collapse can dramatically increase the overall emission.

Volcanic plumes, especially large plumes (Pele, Tvashtar, and Dazhbog) are found to reduce the intensity of 6300 Å emission appreciably within their respective canopies. This is because of the increased probability of collisional de-excitation due to the increased neutral density. If Tvashtar (and/or Dazhbog) is active, the depletion of the electron flux tubes as they cross the northern hemisphere of Io is reduced due to increased scattering off the dense plume canopies. This impacts the overall upstream/downstream brightness ratio. Furthermore, large energy deposition into the plumes (especially Pele-sized plumes) explains why the plumes are visible in emission for optically allowed transitions. Finally, Pele and Dazhbog (if active) decrease the upstream intensity locally and in the process increase the intensity just outside of the dense canopy, noticeably altering the upstream emission morphology.

The perturbed magnetic field in the vicinity of Io affects the emission morphology since the magnetic field is weaker in the wake and stronger upstream. Because of the magnetic mirror effect, the weaker magnetic field can trap electrons after a collision and may result in enhanced wake emission as trapped electrons have more chances to excite oxygen atoms. On the other hand, electrons with a large pitch angle (~68^o) are reflected by the stronger magnetic field upstream. This results in reduced upstream emission because many electrons never reach the atmosphere on the upstream side of Io.

[SII] 6716 Å emission was examined through parametric study of the excitation cross section. We found that [SII] emission is much weaker than [OI] 6300 Å emission even if the cross section is unrealistically high. The reason for the lack of [SII] emission was two-fold: (i) the Einstein *A* coefficient for [SII] emission is ~10 times smaller than the coefficient for [OI] emission allowing for more-frequent quenching, and (ii) the density of S^+ is relatively low.

Chapter 7

UV–Vis Eclipse Spectrum

Io's atmospheric interaction with the Jovian plasma torus produces an intense UV–Vis aurora. Galileo images (Figure 1-1), and more recently, Cassini images (Geissler *et al.*, 2004a; Spencer *et al.*, 2007) of Io in eclipse showed red, green, and blue glows from electron impact of both atomic and molecular species in Io's atmosphere. In eclipse, the auroral glows are generated primarily via electron impact excitation of Io's atmosphere; the UV-Vis spectrum shows emission features from SO_2 and S_2 molecular band emission (e.g. 2670–6000 Å), atomic oxygen lines (e.g. 2958 Å, 2972 Å, 5577 Å, 6300 Å), atomic sulfur lines (e.g. 1479 Å), and several other lines from trace atomic species in Io's atmosphere (e.g. Na, K, Cl). The following analysis will compare observed and simulated eclipse spectra from 2400–3500 Å in order to constrain the upstream thermal electron temperature, the upstream non-thermal (low energy) electron density, the volcanic plume activity, and S_2 concentrations.

7.1 OBSERVATIONS

Two ~12-minute exposures of Io's auroral spectrum from 1700–6000Å were taken with HST/STIS on August 7 and August 18, 1999 during Io's eclipse (Trafton *et al.*, 2011b). The observations attempted to minimize contamination by Jupiter's disk and the solar spectrum which is scattered through Jupiter's atmosphere. The August 18, 1999 observations were made with the MAMA detector and the G230L grating for wavelengths from 1800–3100 Å (Figure 7-1(a)). The first MAMA exposure began 1 minute after ingress and the second exposure ended 28 minutes after ingress. The August 7, 1999 observations were made with the CCD detector and the G430L grating for wavelengths from 2900–5700 Å (Figure 7-1(b)). The first CCD exposure began 13 minutes after ingress and the second exposure ended 39 minutes after ingress. The CCD exposures were begun further into eclipse which had the benefit of mitigating refracted and scattered sunlight through Jupiter's atmosphere. Solar contamination was negligible for the MAMA observations despite being taken earlier in eclipse because the solar spectrum decreases rapidly as the wavelength decreases. On each date, two 2×2 arcsecond sequential exposures were taken upon ingress into eclipse.

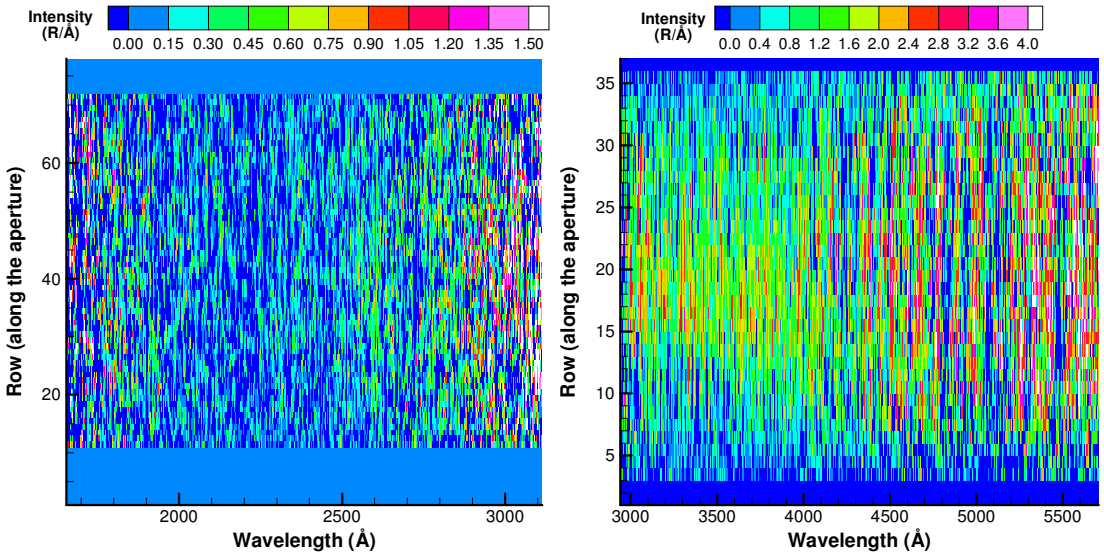

(a) (b)

Figure 7-1: HST/STIS spectra from each observation (a) MAMA detector; each pixel is 0."0245 × 0."0248 (spectral × spatial) and Io is ~45.2 pixels across. (b) CCD detector; each pixel is 0."051 square and Io is ~21.2 pixels across. Note that the two spectra overlap from 2940–3113 Å.

The data shown in Figure 7-1 have been median smoothed[18] with a 3×3 pixel element; therefore the apparent spatial extent of the emission has been increased slightly and the spectrum itself smoothed too. In addition, the background sky intensity has been subtracted out in the following way. First, the average emission versus wavelength (over several rows) at the top and bottom of the detector is obtained. Then, to subtract out the background sky emission, the average intensities from the top and bottom are linearly interpolated to the specific detector row and then subtracted from the row's emission intensity. Note that, due to noise, this procedure results in some pixels with unphysical negative intensities; however, integration spatially and/or over a range of wavelengths yields useful signals. For example, it is clear that the disk integrated intensity (the intensity summed across all spatial rows) increases substantially around ~2900 Å. Also, in Figure 7-1(b), note that the signal is roughly Io's diameter (~21 rows across); however, above ~4000 Å the signal becomes spatially wider than Io. This emission is probably not due to refracted and scattered

[18] Median smoothing discards the highest and lowest data values in succession until only one value remains from the original group of pixels. The entire group of pixels is given the remaining value.

sunlight through Jupiter's atmosphere; instead it is thought to be extended band emission from an unidentified species (Trafton *et al.*, 2011a).

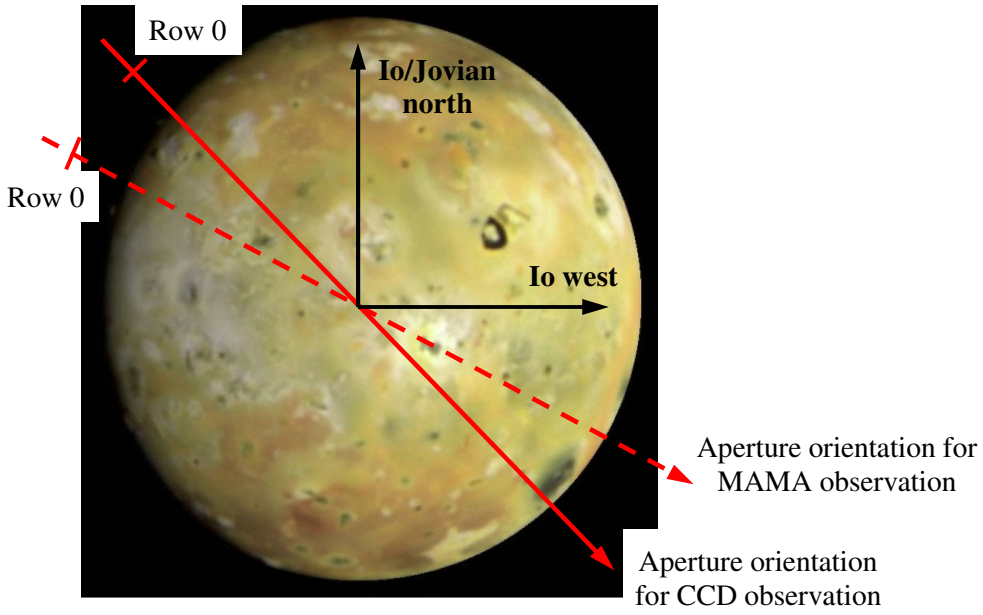

Figure 7-2: Schematic of the aperture spatial dimension orientation, shown by red arrows, for the two observations superimposed on a true color image of Io taken by Galileo in June, 1996 (NASA image PIA00715). The arrow tails correspond to the first rows of the detector; with row number increasing towards the arrow head. Note that the image orientation of Io is close to, but not exactly, the same as the orientation of Io in the HST/STIS observations shown in Figure 7-1.

While the observations do not spatially resolve Io's disk in two dimensions, they do spatially resolve the emission along the spatial axis of the aperture. The 2×2 arcsecond observation area encompassed the entire disk of Io (~1.1 arcseconds) and the spectrum was obtained along the aperture (red arrows, shown in Figure 7-2). Therefore, the observed emission intensity at a given location along the aperture is the sum of emission in a ~±1 arcsecond line perpendicular to the aperture orientation. For the MAMA observations, the aperture was oriented -118° relative to Jovian north and for the CCD observations it was oriented at -136°, as shown in Figure 7-2. In Section 8.3 simulations will be shown that constrain plume activity based solely on Io's observed spatial axis intensity distribution.

7.2 UV-VIS SPECTRUM

The possible active plumes during the observations (August, 1999) are listed in Table 7-1. With the exception of Grian, Ra, and Loki, the Prometheus-type plumes listed were most likely active based on the observed surface changes (see Figure 2-6) and therefore their activity was held fixed. However it should be noted that, due to the episodic nature of the gas plumes, observations of surface changes (or other evidence of plume activity) at two times does not guarantee that the plumes were active during the entire intervening time period. Similarly, plumes in steady state might not leave detectable changes on the surface during two observations close together. Therefore, an initial analysis of the UV-Vis spectrum is performed with "nominal" plume activity (Kanehikili, Masubi, Amirani, Arianna Fluctus, Prometheus, Culann, Zamama, Marduk, Pele, Acala, and Surt all active) based on Geissler *et al.* (2004a) and Rathbun *et al.* (2002) and then a more detailed analysis will use the UV-Vis spectrum to infer the activity of the visible (dayside) plumes listed in Table 7-1.

Table 7-1: Volcano list, August 1999 (Geissler *et al.*, 2004a; Rathbun *et al.*, 2002).

Plume	Longitude, Latitude	Type
Grian (S. Karei)	16W, 2N	Day Prometheus
Kanehikili	38W, 16S	Day Prometheus
Masubi	55W, 44S	Day Prometheus
Amirani	117W, 24N	Night Prometheus
Tvashtar	125W, 59N	Night Pele
Arianna Fl.	150W, 32N	Night Prometheus
Prometheus	156W, 2S	Night Prometheus
Culann	164W, 20S	Night Prometheus
Zamama	174W, 18N	Night Prometheus
Marduk	210W, 27S	Night Prometheus
Pele	256W, 20S	Night Pele
Dazhbog	302W, 54N	Day Pele
Loki	311W, 10N	Day Prometheus
Ra	325W, 9S	Day Prometheus
Acala	336W, 11N	Day Prometheus
Surt	338W, 46N	Day Pele

In each simulation, a fixed upstream electron temperature (from 3 to 8 eV) and density (3600 cm^{-3}, Frank *et al.*, 1996) for the thermal component of the plasma torus were assumed. In addition, a low density, low energy non-thermal component of torus electrons could be very important to the UV-Vis emission as opposed to the ~keV component which is not expected to contribute much to the UV-Vis emission intensity (Bhardwaj and Michael,

1999). Oliverson *et al.* (2001) discussed this low energy non-thermal component and its importance for [OI] 6300 Å emission; here we simulate cases with several different densities ($n_{non\text{-}thermal}/n_{thermal}$ from 0–5%) for the non-thermal component. Furthermore, the energy distribution of the non-thermal component was assumed to be a Gaussian centered at a mean energy of 35 eV and with a standard deviation of 2.5 eV.

In order to reduce the simulation noise, each case presented here was run multiple times with different random number seeds and the resultant UV-Vis spectra were then ensemble averaged to give the displayed results. In order to compare to the observed spectrum, the simulated spatially resolved spectral data viewable to HST are summed across, and averaged by, the area of Io's disk. Furthermore, Io's simulated spectrum (computed with a resolution of 6 Å) was boxcar smoothed using a resolution element of 108 Å in order to approximately compare to the observed disk-averaged spectrum which was also boxcar smoothed over 108 Å (Trafton *et al.*, 2011b). Note that the fine resolution features seen in the lab spectra (see Figure 5-11 and Figure 5-12) are therefore smoothed out and the resultant simulated emission spectrum is a gradually changing, smooth curve without large-scale features. In the future, the simulated spatially resolved emission spectrum should be convolved with the instrument function and then the median smoothing and boxcar smoothing should be applied for more exact comparison to the observational data. For the smoothed simulated spectrum, the Monte Carlo noise was small except near 2220 Å where there is virtually no emission.

The simulated and observed (Trafton *et al.*, 2011b) disk-averaged UV-Vis emission spectra from 2400–3500 Å are shown in Figure 7-3 for several upstream thermal electron temperatures and assuming Pele and Surt are active and Tvashtar and Dazhbog are inactive. The wavelength is only shown up to 3500 Å because an unknown band emission (or scatter and refracted light through Jupiter's atmosphere, though this seems unlikely) dominates above ~4000 Å (Trafton *et al.* 2011a) and therefore the current model intensity falls off above ~3500 Å instead of showing the structure (seen in Figure 2-12). Note that the following simulations assume that the S_2 concentration in all of the plumes is negligible. The addition of S_2 to the plumes and its effect on the emission is examined later. Furthermore, MUV 1 refers to emission in the wavelength range from 2460–2670 Å and MUV 2 refers to the wavelengths from 2670–6000 Å (as discussed in Chapter 5.3.3). The large-scale spectral emission features seen in the observation lay within the ±2σ error bars and it is not clear

whether they represent real emission features. However, these features are not seen in the simulated spectrum (which is smooth) and this, if these features are real, indicates that the current model is lacking an emission source in this wavelength range. In Figure 7-3(a) the thermal spectra and a 1% non-thermal emission spectrum are shown separately. While the non-thermal MUV 2 emission (~3100 Å) is small compared to the thermal MUV 2 emission, the MUV 1 non-thermal emission (~2500 Å) is significant, essentially equal to the MUV 1 intensity for an upstream temperature of 3 eV. Figure 7-3 (a) implies that if there is no non-thermal component of torus electrons, then the emission spectrum is best fit by an upstream temperature of >8 eV, greater than the otherwise observed ~5 eV (Sittler and Strobel, 1987). In Figure 7-3 (b) the spectra are simulated assuming a 5% non-thermal component. In this case an upstream electron temperature of 5–6 eV for the thermal component has remarkably good agreement with the observed spectrum.

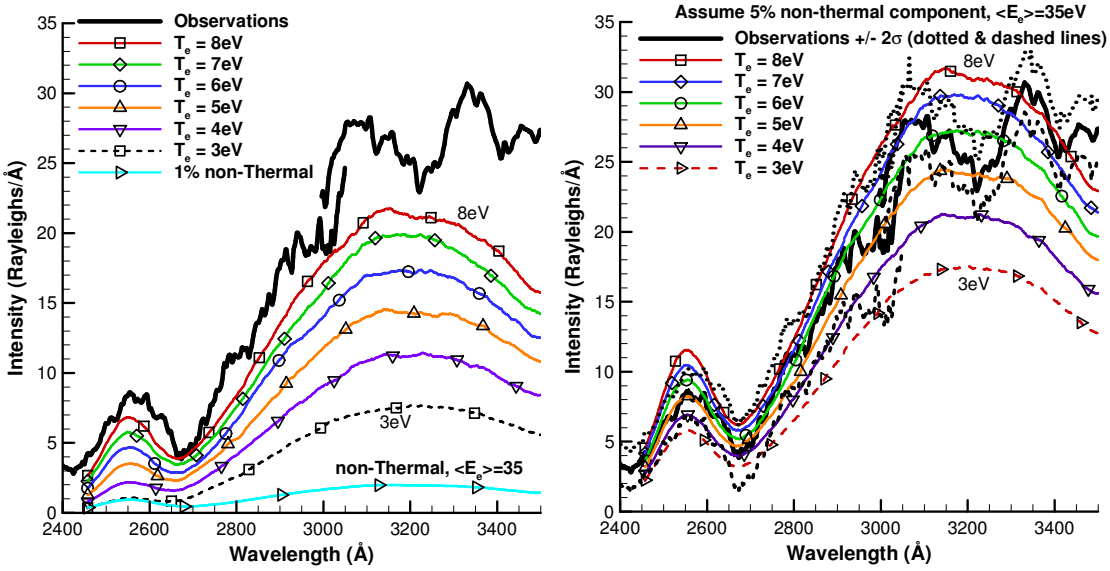

(a) (b)

Figure 7-3: Simulated UV-Vis emission spectrum with Pele and Surt active. (a) The simulated spectrum is shown for various upstream thermal electron temperatures (3-8 eV) and for a 1% non-thermal component with a mean energy of 35 eV. (b) The simulated spectrum is shown for a combination of upstream thermal electrons and a 5% non-thermal component.

To examine the sensitivity of the simulated spectrum to Pele-type plume activity, cases were run for each of the various combinations of active Pele-type plumes. Figure 7-4 shows the cases with all the Pele-type plumes active, only Pele and Surt active, only Tvashtar and Dazhbog active, and none of the Pele-type plumes active. While the MUV 2 emission

intensity is moderately sensitive to the number of Pele-type plumes that are active, it does not depend strongly on which of the Pele-type plumes are active. This is because, for this viewing geometry, the canopies of the Pele-type plumes are all still visible and most of the added emission due to the Pele-type plumes originates from the canopy region (see Figure 7-6). Furthermore, the MUV 1 emission intensity was not even sensitive to the number of Pele-type plumes, presumably because the electron energy rapidly degrades below the threshold energy required for the MUV 1 excitation. Finally, variation of the smaller, Prometheus-type plumes causes similar, but smaller changes in the emission spectrum. Unfortunately, this means that the specific plume activity cannot be well constrained through examination of the disk-averaged MUV emission spectrum.

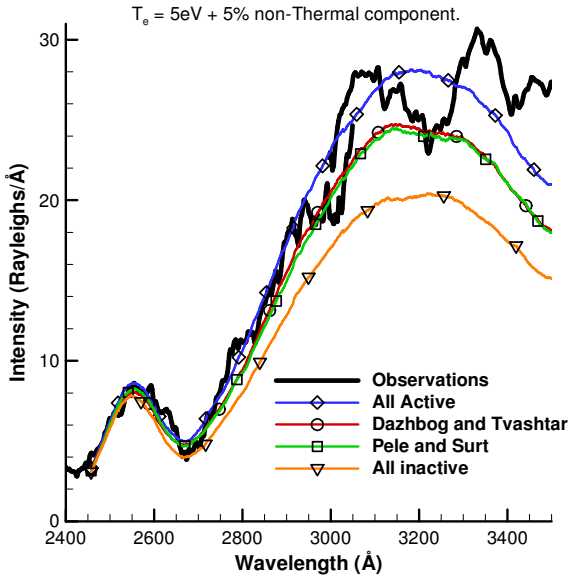

Figure 7-4: Sensitivity of the simulated spectrum on Pele-type plume activity (Prometheus-type plume activity held constant) for an upstream electron temperature of 5 eV and a 5% non-thermal component. Plume activity varied for several cases: Case 1 (All Active: Dazhbog, Pele, Surt, and Tvashtar), Case 2 (Pele and Surt), Case 3 (Dazhbog and Tvashtar), and Case 4 (All inactive).

Figure 7-5 shows the ratio of the peak MUV 2 to peak MUV 1 emission intensity versus upstream thermal electron temperatures and a range of possible (constant) non-thermal fractions. The peak MUV 1 wavelength is taken to be 2550 Å and the peak MUV 2 wavelength is taken to be 3150 Å. The observed ratio is 3.2 ± 0.4 with most of the uncertainty arising from the peak intensity of MUV 2. Given the amount of non-thermal electrons, one can constrain the electron temperature from Figure 7-5. Unfortunately the large uncertainty in

the observed ratio and the fraction of non-thermal electrons limits the constraint on the upstream electron temperature. In order to reproduce the peak intensity ratio between the two bands without any non-thermal electrons, the upstream electron temperature needs to be ~8 eV (± ~1 eV). At lower thermal temperatures there is insufficient flux of the high energy electrons in the tail of the thermal energy distribution necessary for MUV 1 emission relative to the flux of the lower energy electrons that excite MUV 2 emission. For this reason the ratio of peak intensities generally decreases with increasing upstream electron temperature. However, at low upstream temperatures (low energy flux at energies required for MUV 1 and MUV 2 excitation) and high non-thermal fractions, the intensity becomes dominated by the non-thermal component of the emission which has an MUV 2 / MUV 1 emission ratio of ~2.1 for a 35 eV non-thermal component (see Figure 7-3). Therefore, at low upstream electron temperatures, the non-thermal component tends to reduce the sensitivity of the peak intensity ratio to the upstream temperature. In Figure 7-5 this effect is most obvious for the 5% non-thermal component where the peak intensity ratio is relatively constant from 3–8 eV and there is no upstream electron temperature that yields the exact observed ratio, though it does fall within the uncertainty limits. This is because at the 5% level the non-thermal emission is comparable to the low temperature thermal emission (due to lower energy flux at the energies required for MUV 1 and MUV 2 excitation) and the MUV 2/MUV 1 emission ratio for a 35 eV non-thermal component is ~2.1 (see Figure 7-3). The best fit upstream electron temperature accounting for the peak intensity ratios and the absolute intensities (Figure 7-3(b)) is a thermal temperature of 5 eV and a non-thermal density that is ~5% of the thermal density with the nominal plumes active.

The electron transport simulations are also capable of generating the emission intensity in a given wavelength band. Figure 7-6 shows the line of sight emission intensity, including surface reflection, in the wavelength ranges 2460–2670 Å (MUV 1) and 2670–6000 Å (MUV 2). Nominal plume activity is assumed (Table 7-1) and an upstream electron temperature of 5 eV and a 2% 35 eV non-thermal component is used. The emission in both spectral ranges is enhanced in the plumes which create the dominant morphological features of the emission. The plumes are bright because the SO_2 MUV 1 and MUV 2 band emission is not quenched and increased density inside the plumes allows for increased absorption of the electron energy flux which then leads predominantly to emission. Also, Surt is seen to partially shield Acala by absorbing much of the electron energy flux along the nearly north-

south magnetic field lines and reducing the local electron temperature. Without Surt (or a similar northern volcano) absorbing much of the electron energy flux, Acala's overall brightness increases by ~10% (in the current atmosphere model a large amount of electron energy is still absorbed north of Acala even without Surt). Finally, note that the equatorial bright spot marking the sub-jovian point is absent, as discussed in Chapter 6.4.1, because our magnetic and electric field model does not include the Hall effect which Saur *et al.* (2000) found to cause the equatorial spot.

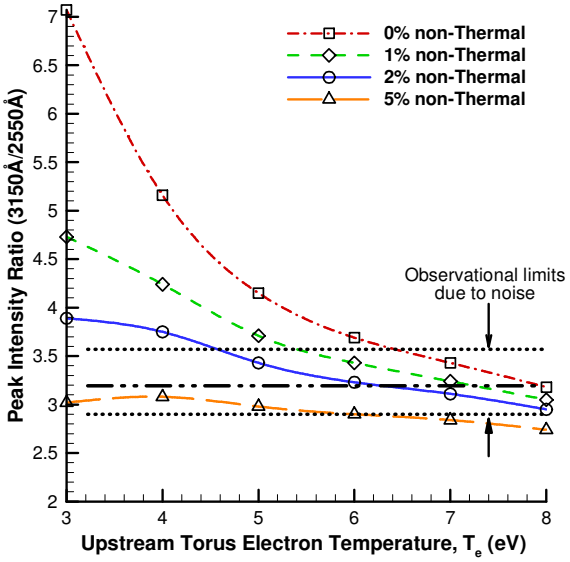

Figure 7-5: Ratio of the peak MUV 2 (3150 Å) to peak MUV 1 (2550 Å) emission intensity for various upstream thermal electron temperatures. Symbols are the simulated ratios (assuming a constant non-thermal component with mean energy of 35 eV) and the observation and the noise constraints are given by dashed and dotted horizontal lines.

The results shown in Figure 7-6 assumed that there was no S_2 in the giant plumes (or that the electron excitation of the S_2 was negligible). However, the theoretical electron-S_2 excitation (B $^3\Sigma_u^-$ ← X $^3\Sigma_u^-$) cross section (Garett *et al.*, 1985) is much larger than the electron-SO_2 MUV 2 excitation cross section and therefore even a modest amount of S_2 in the plumes is expected to increase the UV-Vis emission intensity above ~2800 Å. In the current model, S_2 was included in the plumes in the same way that oxygen was included (Section 6.2.1). The simulated SO_2 density was assumed to be the total gas density; the S_2 density was equal to the simulated SO_2 density times the concentration fraction and the SO_2 density was reduced by a factor of one minus the concentration fraction of S_2. This assumes that the S_2

gas follows the SO_2 (a good assumption given their identical mass and similar cross sections). However, our simulated S_2 concentration is not necessarily the same as the S_2 concentration at the vent since the current plume model does not include creation and destruction mechanisms from plasma impact after the gas leaves the vent. While the current model only includes band emission from SO_2, SO, and S_2, there are other band emission sources which are not included such as O_2 and O_2^+ as discussed in Chapter 5.4.3. As shown in Figure 2-12, there is substantial emission above ~3500 Å whereas the current simulated intensity falls off to zero relatively smoothly above ~3500 Å. In the future, the O_2 and O_2^+ band emission transitions discussed in Chapter 5.4.3 should be included as a first guess at matching the unknown band emission.

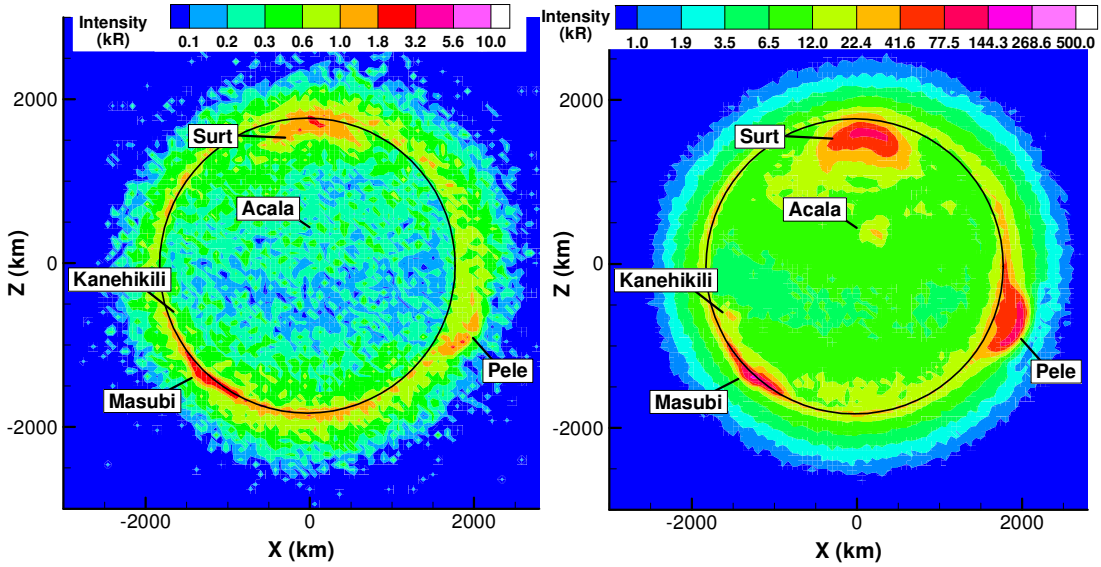

(a) (b)

Figure 7-6: Line of sight integrated emission intensity for (a) MUV 1 (2400–2670 Å) and (b) MUV 2 (2670–6000 Å) given an upstream electron temperature of 5 eV and a 2% 35 eV non-thermal component. Note the intensity is shown on an exponential colorbar.

As shown in Figure 7-7, the line of sight emission intensity from 2670–6000 Å is ~4 times higher in Pele and Surt when they contain 15% S_2 compared to the 0% S_2 case of Figure 7-6(b). Provided that the structure (ring radius, canopy height) and density of the plumes are similar enough to the simulated "ideal" Pele (or Prometheus) upon which they are all based, the S_2 concentration should be well constrained by the observed emission due to the sensitivity of the emission intensity. Figure 7-7 also shows the orientation of the aperture

during the CCD observation and it is clear that plume activity, especially giant S_2-rich plumes, should be visible in the spatially resolved (along the aperture) emission morphology. This will be investigated in the following section, though care must be taken since our simulation lacks the ability to reproduce the equatorial spot.

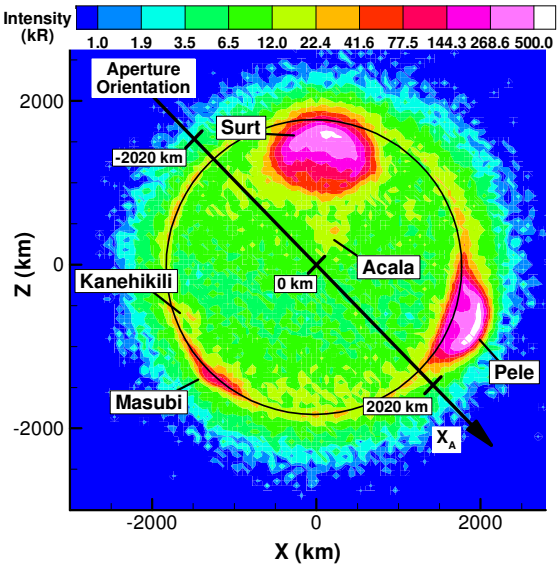

Figure 7-7: Simulated line of sight integrated MUV 2 (2670–6000 Å) emission intensity (on an exponential colorbar) if both Pele and Surt have a 15% S_2 concentration and the upstream electron temperature is 5 eV with a 2% 35 eV non-thermal component. Note the orientation of the CCD aperture's spatial dimension is shown along with the location of the ±2000 km and zero point on the aperture axis, X_A.

7.3 Plume Activity

While the UV-Vis spectrum is relatively insensitive to the plume activity if there is little to no S_2 in the plumes (Figure 7-4), the spatially resolved emission (Figure 7-6) should indicate the activity of the visible plumes (especially those with S_2), including those on the nightside with canopies that extend past Io's limb. Resolved images of Io's aurora have been used previously to determine plume activity (labeled with an "E" in Figure 2-6); however, our spectral data are noisy and, when integrated over a wavelength range to reduce the noise, are only resolved along the spatial dimension of the aperture. Therefore, one cannot correlate plume activity to the observed intensity along the aperture by simply looking at the location of the bright spots on Io. However, as mentioned previously it should be possible to constrain plume activity by comparison to the simulated intensity along the aperture's spatial axis.

Figure 7-8 (a) shows the observed CCD spectrum below 3500 Å; as discussed earlier, above this wavelength there is extended emission from an unidentified molecule (Trafton *et al.*, 2011a). Io is ~21 pixels across in the CCD observation; however, emission is seen to occur over ~26 pixels (rows 7–33). This suggests that the emission due to the atmosphere above each limb extends to an altitude of ~400 km, assuming the emission is relatively symmetrical and extends to the same altitude off each limb. The spatial rows within the aperture have been transformed into an Io-centric coordinate system assuming that the emission is symmetrical and that each row is ~173 km wide. This coordinate system is shown along on the top axis in Figure 7-8(a). The aperture is oriented such that negative values of X_A correspond to Io's north-west hemisphere, positive values with the south-east (see Figure 7-7). If the assumption of nearly symmetric emission from each limb does not hold, then the zero location of Io (the sub-Earth spot) will shift rows on the CCD.

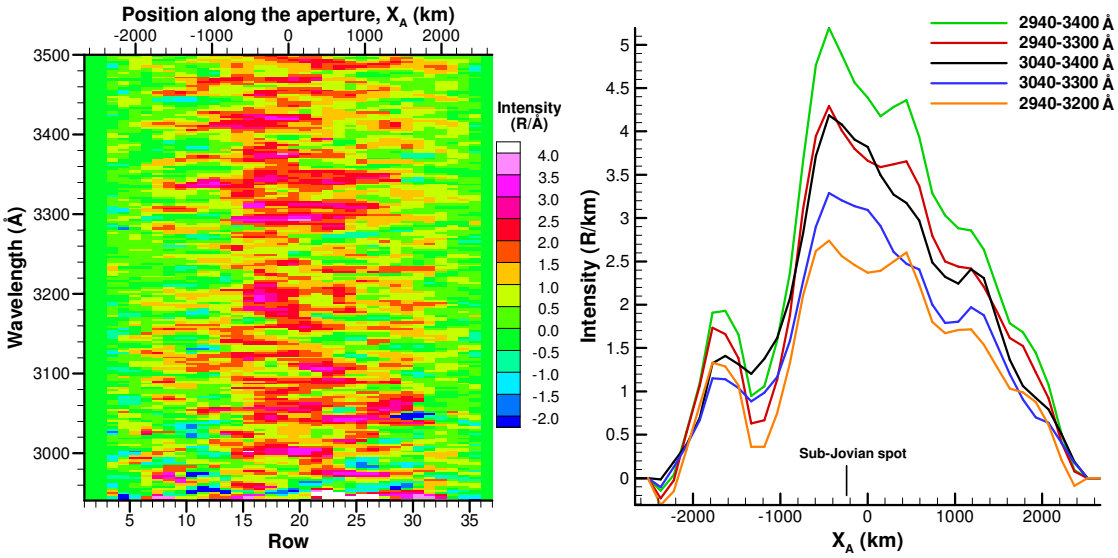

(a) (b)

Figure 7-8: (a) Close-up of the CCD spectrum. The spectrum has been rotated (from Figure 7-1(a)) so that the spatial direction is horizontal to match (b). The approximate position along the aperture is indicated on the upper horizontal axis; Io's is centered at X_A = 0. (b) The intensity obtained by integrating the spectrum in (a) over the various wavelength ranges indicated. The intensity distribution is relatively invariant to the wavelength range used except for a "feature" at X_A ~500 km and the relative depth of the intensity decrease at ~−1200 km.

In Figure 7-8(b) the observed CCD spectrum has been integrated over several different wavelength bands while keeping the spatial information along the aperture. As seen in Figure 7-8(b), larger wavelength bands are more intense since they sum over more of the

emission. The overall emission morphology and intensity is consistent for each wavelength band indicating that the emission morphology across Io is real, not noise. However, the amount that the emission decreases at $X_A \approx -1200$ km and the increase in emission at $X_A \approx 500$ km is uncertain as these features vary depending on the wavelength range used. Furthermore, there is a substantial emission feature on Io's north-eastern limb which might mean that the emission does not extend to the same altitude above the limb on each side of Io. This will be examined by comparison to the simulated spatially resolved line of sight emission. Finally, the increase in emission near $X_A \approx -400$ km may be at least partially due to the equatorial bright spot that has been observed in many spatially resolved images (Geissler *et al.*, 2004b; Retherford *et al.*, 2007b) at the sub-jovian point (located at $X_A = -240$ km) and for various wavelengths.

In order to compare the observed emission intensity versus aperture position, the simulated spatially resolved spectral data were summed over the equivalent wavelength range and across Io's disk in the dispersion direction normal to the aperture spatial orientation. Note that, because the electron transport (and excitation) is a non-linear process across Io that depends on the upstream flux depletion and ionization, the simulations cannot simply turn a single plume on at a time and then superimpose multiple single-plume results to obtain the observed intensity. Therefore the plume activity and S_2 concentration were varied parametrically and the most relevant combinations of plume activity are shown below. The following simulations assume an upstream thermal electron temperature of 5 eV and a 2% (Gaussian) non-thermal component with a mean energy of 35 eV and a standard deviation of 2.5 eV. The upstream thermal temperature and non-thermal component will be varied parametrically a second time once the plume activity and S_2 concentration have been better constrained.

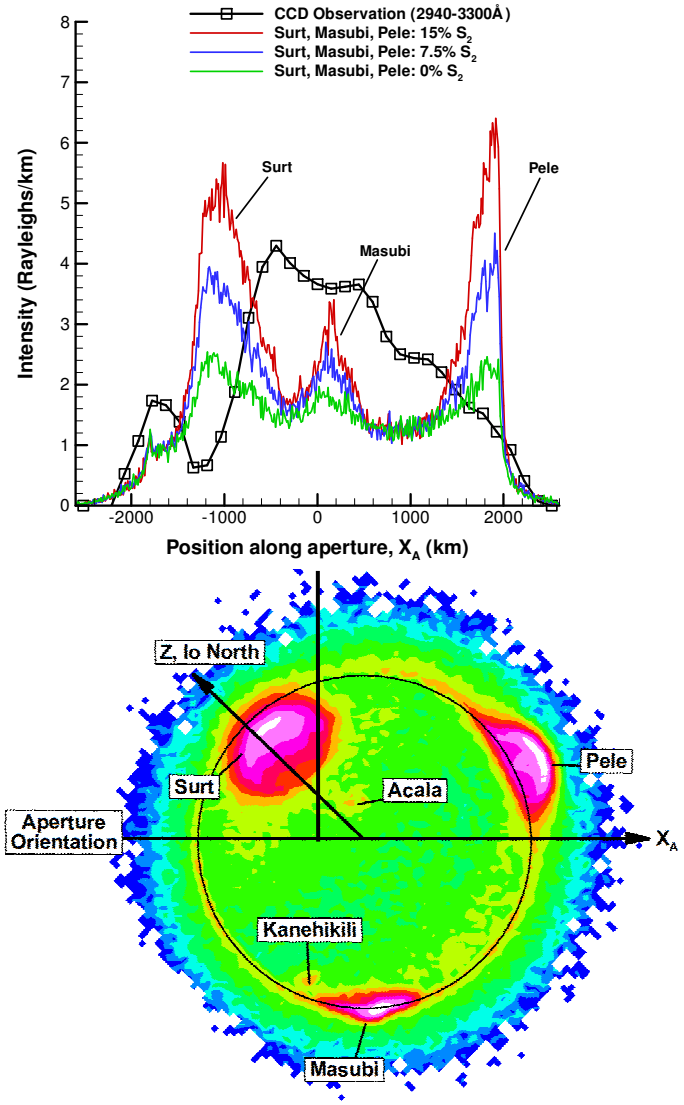

Figure 7-9: (Top) Integrated intensity along the aperture for nominal plume activity, 5 eV thermal electrons and 2% 35eV non-thermal electrons. (Bottom) The spatially resolved emission rotated such that X_A is horizontal. Io north is therefore up and to the left, as indicated.

Figure 7-9 shows the integrated intensity along the aperture beneath which the spatially resolved simulated emission (Figure 7-7) is shown rotated such that the aperture axis is now horizontal. This is done to allow easy visualization of how the plume bright spots correlate with the peaks in integrated emission along the aperture. It is obvious that both Pele and Surt generate emission features that do not agree with the observed intensity, either with or without S_2 gas. Similarly, the brightening due to Masubi's canopy rising above the limb does not align well with the observed peak intensity feature at $X_A \approx -400$ km. In addition,

Masubi (simulated as a Prometheus type plume) is not the source of the feature unless it has a significant S_2 concentration which is unlikely since Masubi is not thought to have a red ring and thus probably outgases little S_2 gas. It is seen that a 15% concentration of S_2 results in an increase by a factor of ~2.5 in the intensity inside the plumes. Finally, a slight brightening is seen to occur above the limb at −1800 km. The increase in intensity is not enough to account for the large emission feature seen on that limb and therefore the source of this feature is most likely a plume.

The emission intensity with Dazhbog, Loki (modeled as a dayside Prometheus plume), and the nominal plumes (excluding Pele and Surt) all active is shown in Figure 7-10(a). Figure 7-10(b) shows the intensity with Dazhbog, Grian, Ra, and Tvashtar active. While Dazhbog does not match the peak emission feature at −450 km perfectly, the best fit to the intensity of the feature is obtained if Dazhbog has a 7.5–15% concentration of S_2. The position of Loki is seen to match the local bright feature at ~400 km. However, a Prometheus sized Loki would require ~40% S_2 to match the observed intensity and the intensity would fall off much too quickly if Loki were the only source of brightening over the background sublimation atmosphere.

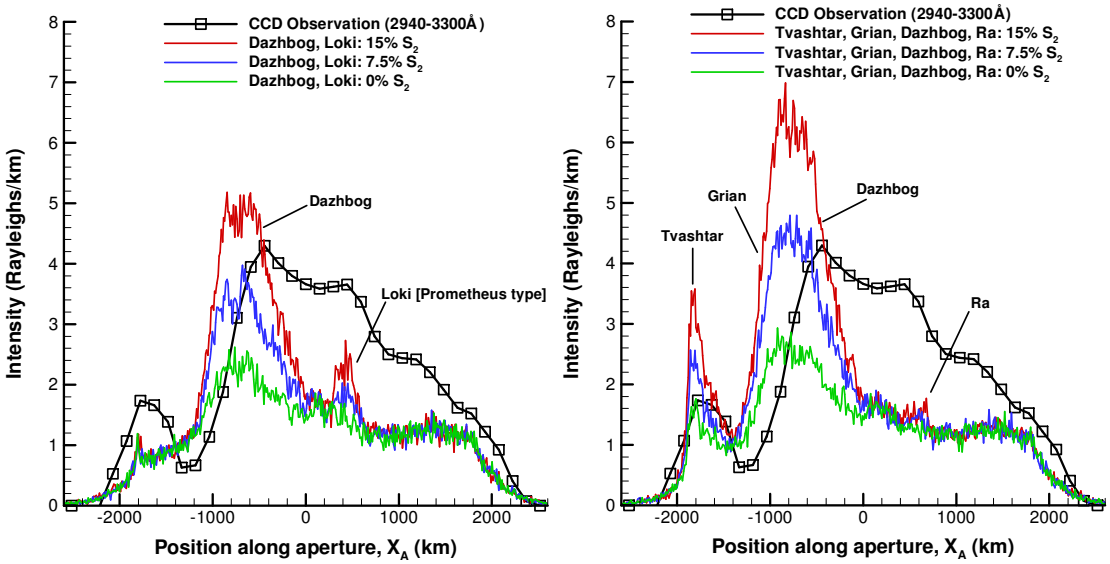

(a) (b)

Figure 7-10: Integrated intensity along the aperture for (a) Dazhbog and Loki (modeled as a dayside Prometheus-type plume) active and (b) Dazhbog, Grian, Ra, and Tvashtar active. Note that the "nominal" plumes Pele and Surt are inactive.

In Figure 7-10(b) it appears that Tvashtar matches the north-west limb feature extremely well with an S_2 concentration less than 7.5%. The slight difference in the simulated Tvashtar emission feature compared to the observed might be due to the real Tvashtar plume having a more diffuse canopy than in our simulations (possibly due to higher plasma heating than used when pre-computing the plume). The local brightening due to Grian is seen to lie between brightening caused by Surt and Dazhbog. Overall, Grian's emission feature is a poorer match than Dazhbog for the observed feature peaking at −400 km; however, if it has no S_2 gas then it merely tends to increase the emission near the local minimum around −1200 km. Since the observed depth of emission decrease changes significantly based on the wavelength range used for integration, it is not possible to conclude whether Grian is active with a low fraction of S_2 or just inactive. Finally, Ra does not seem to match the gradual decrease in emission observed in the south-eastern hemisphere (X_A greater than ~0).

Figure 7-11 shows the simulated emission intensity with Dazhbog, Tvashtar, Loki and all the nominal plumes active except Pele and Surt which are inactive. Here Loki has been modeled as a Pele type plume as compared to a Prometheus type plume (as in Figure 7-10(a)) in order to determine if a large Loki plume could explain the observed emission intensity. The north-east intensity feature is seen to still be well fit by Tvashtar if it contains less than 7.5% S_2; changing the activity of the upstream (relative to the plasma flow past Io) plumes seems to have little effect on Tvashtar's brightness. This makes sense because the activity changes were on the sunlit (if not in eclipse) side whereas Tvashtar is on the nightside and the current model uses fixed precomputed fields so the plumes cannot significantly change the electron flux to other plumes that are not downstream. While the emission due to Dazhbog extends too far to the north-east (negative X_A), it seems to be the most likely candidate for the increased emission and there are several possible explanations for why our simulated emission does not agree. The simplest is that the Dazhbog plume has a smaller ring radius and/or the canopy is at a lower altitude than the Pele type plume model used in our simulation. Figure 7-11(bottom) shows the line of sight emission from the MUV 2 wavelength band (rotated so that the horizontal axis is X_A), and it is clear that a smaller plume for Dazhbog would tend to reduce the extent of the Dazhbog emission feature and bring it into better agreement with observations. This is actually supported by observations of Dazhbog's surface ring (Geissler *et al.*, 2004a) which varied from ~270 km to ~480 km during the Galileo mission.

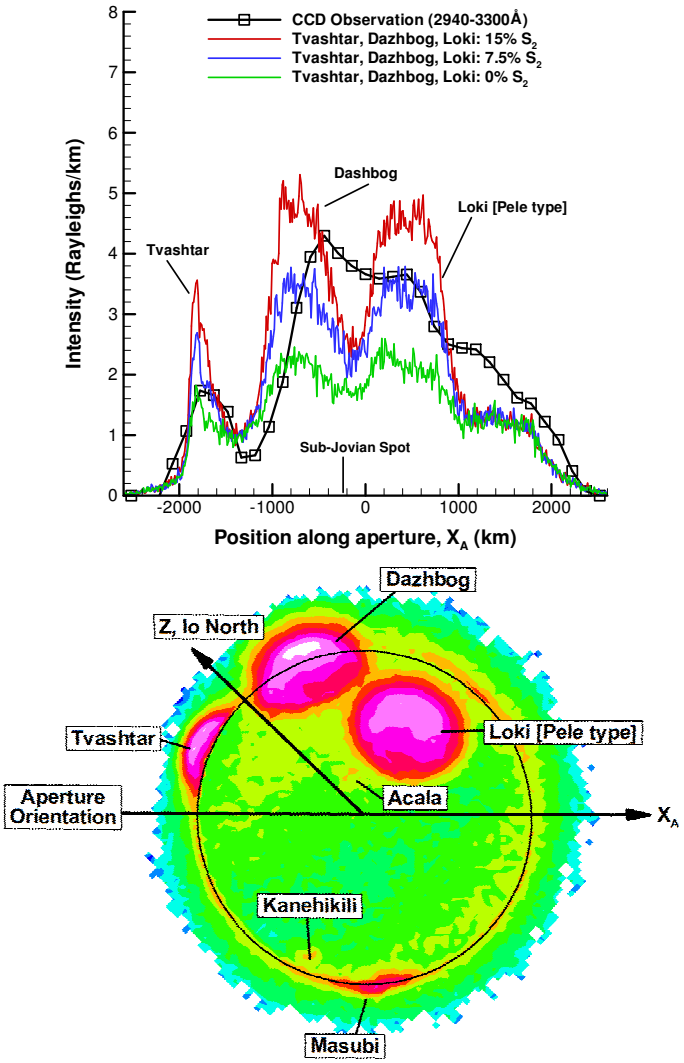

Figure 7-11: (Top) Integrated intensity along the aperture for Dazhbog, Tvashtar, and Loki (Pele type plume model) active. The "nominal" plumes Pele and Surt are inactive. (Bottom) The spatially resolved emission rotated such that X_A is horizontal.

In addition, note that the current plume models are axisymmetric 2D simulations rotated onto the 3D planet. The emission from Dazhbog might also fit the emission feature much better if Dazhbog were modeled in 3D. Observations of the surface ring during Galileo (Geissler *et al.*, 2004a) found an elongated orange ring with an east-west ring radius that was ~100 km less than the north-south radius. As mentioned previously, the actual vent geometry has been shown (McDoniel *et al.*, 2011) to produce striking 3D geometry to the overall plume (Figure 2-7) and the deposited surface ring. Furthermore, Zhang *et al.* (2003, 2004) found that the radial spreading of the plume beyond the ring was very sensitive to the surface

temperature (e.g. the difference in day and night plume extent in Figure 5-4 and in Figure 5-5) and hence the extent of the plume in the north-east direction might be less than the extent in the south-west direction. Therefore, more realistic plume/atmospheric interaction models should be investigated in the future.

The local intensity peak around X_a~400 km is matched if Loki (a Pele type plume in these simulations) has a 7.5% S_2 concentration. The observed gradual intensity fall-off away from Loki in the south-western hemisphere is only decently matched by Loki; however, this mismatch might be primarily because the simulation spectrum has not been properly convolved with the instrument function as well as median smoothed, both of which will serve to smear the intensity. Also, as discussed previously for Dazhbog, any asymmetry in Loki's plume might contribute to the differences between simulation and the observation. The current simulations suggest that Loki erupts with a Pele-type plume radius (the emission observed here is insensitive to the canopy shock altitude for Loki) rather than a Prometheus-type plume radius (compare Figure 7-11(top) and Figure 7-10(a)). This is not unexpected since Loki is an overturning lava lake (Rathbun *et al.*, 2002) and the broader Pele-type plume results from high vent temperatures. In late August, 1999 (after these observations) Loki's thermal output brightened by an order of magnitude. The gradual fall-off in intensity away from Loki might indicate that prior to the dramatic brightening in late August, Loki was outgassing significant S_2 (and SO_2) gas which was then spreading throughout the dayside atmosphere, gradually falling off away from Loki as the S_2 stuck to the surface or was broken into sulfur atoms via photo- and electron-chemistry. Moses *et al.* (2002) found that the lifetime of S_2 in Io's atmosphere was ~2 hours and Zhang *et al.* (2003) showed that when erupting onto a collisional dayside atmosphere, down-falling plume material can "bounce" several plume radii away from the vent. The two hour lifetime coupled with some loss of S_2 to the surface with each "bounce" could lead to the observed intensity fall-off over several plume radii from the vent. Instead of Loki (or Ra) outgassing S_2, it is also possible that the gradual intensity fall-off is caused by the S_2 streaming out and away from Dazhbog. In that case the asymmetric drop in intensity around Dazhbog might be explained by two factors. The predominately east to west atmospheric winds (Moullet *et al.*, 2008) which would convect the S_2 preferentially in the $+X_A$ direction. Also the expected larger sublimation gas columns (due to the temperature lag, Walker *et al.*, 2010) west of the sub-solar point would allow multiple "bounces" of the plume material to develop in the $+X_A$ direction.

Finally, it is seen in Figure 7-11(top) that the simulated emission intensity decreases sharply between Dazhbog and Loki whereas the observed emission intensity gradually decreases monotonically from Dazhbog to Loki. The minimum simulated intensity occurs at X_A~160 km, very close to the sub-jovian spot at which our model is expected to under-predict the emission intensity since the Hall effect is not included in the model. It is not known whether this would account for the entire difference between the simulations and observations. However, it would bring the two into better agreement and, coupled with the uncertainties in the 3D plume shapes, the observed and simulated intensities along the aperture agree remarkably well.

7.4 UV-VIS SPECTRUM WITH S_2 AND SO BAND EMISSION

Since inclusion of S_2 into the plumes resulted in significantly more intense emission, the sensitivity study on the upstream thermal electron temperature (Figure 7-3 and Figure 7-5) was performed again using the results from the previous section. The following simulations assume nominal plume activity except that Pele and Surt are *inactive* and that Tvashtar, Dashbog, and Loki are all Pele-type giant plumes and *active* with 0%, 10%, and 7.5% S_2 concentrations respectively.

Figure 7-12(a) shows the simulated spectrum for upstream thermal electron temperatures from 3–8 eV and a 35 eV non-thermal component from 0–5% of the thermal density. The MUV 2 (~2800–6000 Å) emission intensity is seen to increase with the addition of S_2 into Dazhbog and Loki however the emission intensity still drops off at longer wavelengths unlike the observations. Again, a 5 eV upstream thermal electron temperature and a 2% 35 eV non-thermal component match the MUV 2 (~3100 Å) emission intensity reasonably well. However, the MUV 1 (~2550 Å) emission peak is not well matched unless the upstream thermal electron temperature is 7 eV.

It can be seen in Figure 7-12(b) that the peak intensity ratio does not match observations unless either the upstream electron temperature increases to unexpectedly large values (> 8 eV) or the non-thermal electron density increases to more than 5% relative to the thermal density. In general this is because the addition of S_2 generates more intense emission than SO_2 over the MUV 2 (3150 Å) wavelength range and thus, for the same upstream electron temperature and non-thermal fraction, the MUV 2 to MUV 1 peak intensity ratio increases. In addition, the effect is even more pronounced at lower thermal energies because

the intense S_2 excitation band threshold energy (3.7 eV) is much lower than the SO_2 dissociative-excitation threshold energy (10.43 eV) for the MUV 1 (~2550 Å) emission. Unfortunately, a tight constraint on the upstream thermal electron temperature cannot be obtained for the modeled plumes and S_2 concentrations since if the non-thermal component is large enough, the peak intensity ratio becomes insensitive to the upstream thermal temerature. The lack of sensitivity to the upstream electron temperature for higher non-thermal fractions is once again due to the competition between the two emission sources. At low upstream temperatures the non-thermal emission begins to dominate the total emission and the peak intensity ratio drops towards the non-thermal limit of ~2.7 (note the addition of S_2 band emission increases the non-thermal intensity ratio). For higher upstream temperatures the intensity ratio also decreases, this time due to the increase of higher energy electrons in the tail of the thermal energy distribution and the corresponding decrease in the MUV 2 to MUV 1 excitation cross sections.

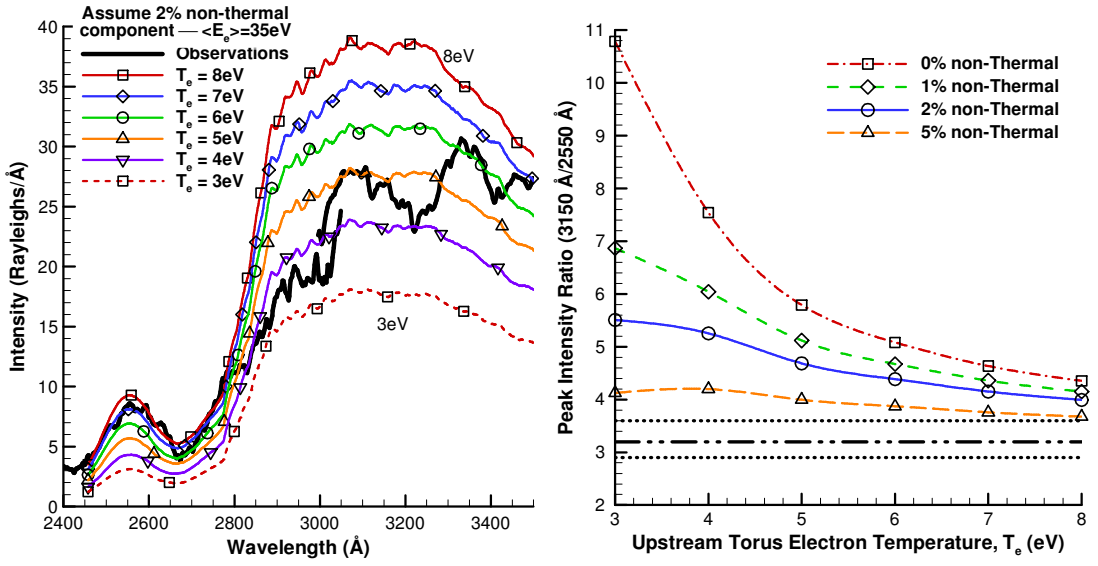

(a) (b)

Figure 7-12: (a) Simulated UV-Vis emission spectrum for upstream thermal electron temperature range of 3 to 8 eV and a 2% 35 eV non-thermal electron component. Tvashtar, Dazhbog, and Loki are active and they contain an S_2 concentration of 0%, 10%, and 7.5% respectively. (b) Peak intensity ratio versus upstream electron temperature for several non-thermal fractions. The observed ratio is given by the black dash-dot-dot line with the uncertainty indicated by the black dotted lines.

The inclusion of S_2 and the resultant intense B $^3\Sigma_u^- \leftarrow$ X $^3\Sigma_u^-$ band emission significantly altered both spectrum shape and the peak intensity ratio versus upstream

electron temperature. Another excitation pathway which might significantly alter the spectrum is the direct electron impact excitation of SO into the $\tilde{A}\ ^3\Pi$ or $B\ ^3\Sigma$ excited states which then emit in the MUV 1 band. The inclusion of the direct excitation may increase the MUV 1 emission sufficiently to resolve the issues matching the observed peak intensity ratio (Figure 7-12(b)) and thereby allow the constraint of the upstream electron temperature. To my knowledge, the direct excitation cross section to these states is unknown. The excitation cross sections obtained by crossing electron and SO_2 beams (Ajello *et al.*, 2002) should, at least partially, account for direct excitation of SO produced by electron dissociation because SO produced by electron dissociation can then itself be directly excited by the electron beam in the experiment. However, these experimental cross sections do not account for the direct excitation of SO which is produced via other sources like photo- and ion-dissociation and plume outgassing. Unfortunately, these production mechanisms are not negligible for Io's atmosphere (Summers and Strobel, 1996; Smyth and Wong, 2004) and therefore if the direct excitation cross section is large then the effect on the spectrum could be significant, even if there were only a ~10% SO concentration in Io's global atmosphere.

In order to qualitatively examine the potential effect of the direct SO excitation mechanism on the emission spectrum, the emission was simulated assuming that the direct SO excitation cross section (to the $\tilde{A}\ ^3\Pi$ or $B\ ^3\Sigma$ excited states), σ_{SO^*}, was equal to the SO_2 dissociation-excitation MUV 1 cross section, $\sigma_{SO_2,MUV1}$, shifted by 5.65 eV (the energy required to dissociate the SO_2 into SO and O) and multiplied by a scaling factor, γ_{SO*}. Specifically, for a given incident electron energy, E_e (eV), $\sigma_{SO^*}(E_e) = \gamma_{SO^*} \times \sigma_{SO_2,MUV1}(E_e + 5.65)$, and therefore the direct SO excitation occurs at lower energies than SO_2 dissociation-excitation. While this cross section for the direct SO excitation is not quantitatively accurate, the qualitative shape of the electron excitation curve versus relative energy is similar across various species and for excitation to many different states (see Figure 3-7) and therefore should be adequate for this analysis which is solely attempting to determine if direct SO excitation might be important.

Additionally, it was assumed that the emission spectrum from directly excited SO was identical to the MUV 1 spectrum (generated by dissociation of SO_2 to excited SO) when the relative energy was shifted to account for the dissociation energy (as for the cross section). Again, this is not quantitatively accurate since the SO excited state ($\tilde{A}\ ^3\Pi$ or $B\ ^3\Sigma$) distribution of vibrational and rotational states for direct SO excitation are probably slightly

different from the distribution of states given dissocitive-excitation of SO_2. Therefore, the emission spectrum from the excited state to the SO ground state will be slightly different; however, the overall qualitative shape of the spectrum should remain the same allowing for a qualitative comparision to determine the relative significance of direct SO excitation. A potentially more accurate estimate of the resultant spectrum would use the Frank-Condon factors for the excited states to the ground state as done for S_2 (see Chapter 5.4.3); however, these were not available.

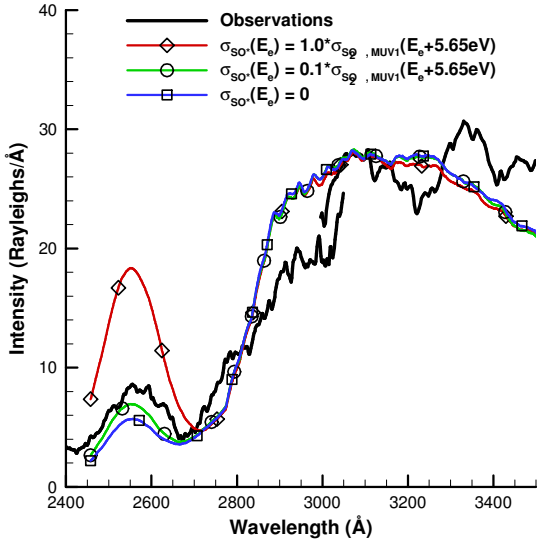

Figure 7-13: Comparison of the simulated UV-Vis spectrum with and without an approximate direct SO excitation mechanism (σ_{SO^*}) to the MUV 1 excited states proportional to the SO_2 dissociation-excitation MUV 1 cross section ($\sigma_{SO_2,MUV1}$). Simulations used a 5 eV upstream electron temperature, 2% non-thermal component, and nominal plume activity (Table 7-1) with Tvashtar, Dazhbog, and Loki active (0%, 10%, and 7.5% S_2 concentrations respectively).

Figure 7-13 compares the emission spectra with and without the approximate direct SO excitation. If γ_{SO*} is equal to one, then even with only ~7% SO in the dayside atmosphere, the MUV 1 emission feature becomes significantly brighter (by a factor of ~3) and, in fact, is the dominant production mechanism for the MUV 1 band emission. If the direct SO excitation cross section is an order of magnitude smaller than the SO_2 dissociation-excitation MUV 1 cross section ($\gamma_{SO*} = 0.1$), then the peak MUV 1 intensity is still increased by ~25%. Of course γ_{SO*} might be much smaller than unity; however, the cross section used has a peak value and shape that is typical for many molecular excitations and it would be surprising if the direct SO excitation cross section is much smaller than the SO_2 dissociation-excitation

cross section. Therefore, it is probable that direct excitation of SO is, at the least, a moderately significant source of the MUV 1 emission intensity. Finally, note that the MUV 2 emission intensity does not change, because the electron energy flux was not being completely absorbed by the atmospheric column. Therefore the (relatively minor) additional energy put into direct SO excitation did not significantly reduce the energy put into the other processes by much, if at all. This result is also unsurprising since excitations resulting in MUV 2 emission are a relatively small fraction of the total number of reactions.

Unfortunately the results above mean that we cannot tightly constrain the upstream electron temperature based on the MUV 2 to MUV 1 peak intensity ratio. However, the upstream electron temperature, in conjunction with the non-thermal fraction and the S_2 concentration, can still be constrained based on the absolute peak intensity in the MUV 2 wavelength range. A much better constraint on the upstream thermal electron temperature could be obtained if the direct SO excitation cross section versus incident electron energy was known. Also, better knowledge of the non-thermal component would, to a lesser extent, help the simulation constrain the upstream thermal electron temperature.

7.5 CONCLUSIONS

UV-Vis emission spectra of Io in eclipse were taken on August 7 and August 18, 1999 by HST/STIS. Simulations of the electron impact excitation of the atmosphere were performed to constrain the upstream thermal electron temperature based on the ratio of MUV 2 to MUV 1 emission. While this ratio was sensitive to the upstream thermal electron temperature, the uncertainty in the 35 eV non-thermal electron density and the direct SO excitation cross section meant that the upstream thermal electron temperature could not be constrained well. Given the plume activity and S_2 concentrations in the giant plumes, the upstream electron temperature and non-thermal fraction are constrained based on the absolute peak intensity in the MUV 2 wavelength range.

Simulations of the emission intensity along the aperture indicate that, during the August 7, 1999 observation Tvashtar was active with less than a 7.5% concentration of S_2 whereas Pele and Surt were inactive. Dazhbog was also most likely active (with <15% S_2) and it is also possible, but unlikely, that Grian was active. Additionally, there was most likely a source of S_2 (and SO_2) from Loki in order to explain the local increase in emission intensity and the gradual fall off in intensity away from Loki's location (in X_A). Also, the disagreement

between our model and the observations near the sub-jovian spot is not unexpected. With Dazhbog and Loki active and increasing the local emission, our simulations show a distinct depression in the emission intensity at the sub-jovian spot where the observations show none.

Chapter 8

Atmospheric Structure and Composition with Plasma Interaction

In order to better simulate the electron excitation of Io's neutral atmosphere during eclipse, the planetary DSMC code (Chapter 3) was used to simulate an improved target (multi-species) atmosphere for the Monte Carlo electron transport code (Chapter 5) to better simulate Io's aurora. 1-D simulations of Io's atmospheric dynamics upon entry into eclipse (Chapter 4) found that the eclipse dynamics are very sensitive to the initial non-condensable mole fraction and the ability of the non-condensable diffusion layer to react with or stick onto the surface (presumably the dynamics would be similiary sensitive to the loss of non-condensable due to 3D gas flow). Additionally, initial aurora simulations using the Wong and Smyth (2000) continuum 2D atmosphere (Chapter 6) indicated a need for a better target atmosphere model which also accounted for the rarefied nature of Io's atmosphere and included plasma momentum transfer, the (expected) sputtered polar atmosphere component, and self-consistent simulation of the gas dynamics into eclipse. The present 3D DSMC simulations of Io's sublimation and sputtered atmosphere will provide this more accurate target atmosphere for more accurate auroral simulations in future. Finally, the effects of sputtering and realistic plasma interaction on the dynamics of Io's global atmosphere are presented.

8.1 Simulation Overview

For computational simplicity, the present simulations assume that Io's surface is covered uniformly by SO_2 frost and that the surface temperature is in instantaneous radiative equilibrium. These surface boundary conditions were used in the past by Austin and Goldstein (2000) and Wong and Smyth (2000). Furthermore, while this surface model does not represent the actual Ionian conditions, in order to understand the more complicated atmosphere that will result from non-uniform frost and more accurate surface temperature distributions, it is useful to first examine the more simple atmosphere simulated here. Both of these approximations have been supplanted in Walker *et al.* (2010a) which used a surface frost map and a two temperature rock/frost surface model that accounted for Io's rotation in

order to simulate a pure SO_2 sublimation atmosphere (see Figure 2-5). The Walker *et al.* (2010a) and Austin and Goldstein (2000) simulations used a radial plasma heating model with no plasma-neutral momentum transfer or chemistry. Walker *et al.* (2010a) found that the non-uniformity of the frost had little effect on the overall atmosphere, except in the formation of a dawn atmospheric enhancement in the column density which depended upon the SO_2 residence time on the non-frost surface. While the frost was not in instantaneous radiative equilibrium due to Io's rotation, the principal effect was to shift the frost temperature distribution longitudinally relative to the instantaneous radiative equilibrium distribution. More recent simulations (Walker *et al.*, 2010b) have found that, for the predicted frost thermal inertias, the frost temperature distribution forms a latitudinal warm "band" shape centered at the equator; this is unlike the "bulls-eye" shape that results from instantaneous radiative equilibrium. The atmospheric dynamics will certainly change depending on the surface temperature distribution; but for the current work it was computationally necessary to assume Io's frost surface was in radiative equilibrium.

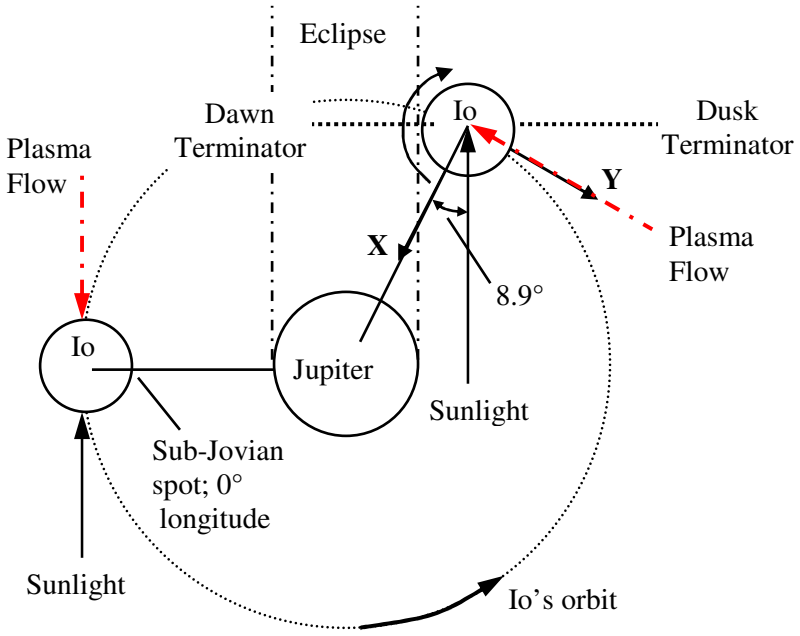

Figure 8-1: Schematic of Io's location in the Jovian system for the current simulations (not to scale). The DSMC simulation's X (sub-jovian) and Y (sub-plasma) axis (see axis insets in the 3D plots) as well as the direction of increasing longitude are shown to orient the simulation results.

The following simulation examines the steady state atmosphere developed on Io due to sublimation, sputtering, plasma flow past Io, and photo- and plasma-chemistry just before

eclipse. For the present simulations, the Galileo J0 flyby upstream plasma conditions (plasma density of 3600 cm^{-3}, electron temperature of 5 eV, and ion temperature of 100 eV) are used as well as Combi *et al.*'s (1998) simulated MHD magnetic field data which used parameters so that their results best-fit the J0 magnetic field data. The plasma model (including chemistry) is described in detail in Chapters 3.4 through 3.6, the photo-chemistry in Chapter 3.3, and the surface sputtering model in Chapter 3.7. The present simulation models the O^+ and S^+ plasma flow past Io and the resultant atmospheric dynamics, modeling the SO_2, SO, O_2, O, S, SO_2^+, SO+, O_2^+, O^+, S^+, and electrons. Note that in the current model it has been assumed that the condensable species are lost when incident onto the surface. However, in reality the particles should reside on the surface for some time and eventually gain enough energy to leave the surface, possibly after undergoing surface chemistry with another surface-bound particle (and in the case of ions, neutralizing). While this production mechanism is not modeled, it is expected that the O and S atoms on the surface predominately undergo surface chemistry and then leave the surface as SO_2, O_2, or possibly SO (allotropes of sulfur, S_2, S_4, S_8, etc. are expected to remain on the surface). If more SO_2 is formed in this way it would merely add to the frost layer and sublimate (or sputter) from the surface in the same way as current frost model. However, since the current simulation assumes an infinite, uniform resovoir of SO_2 frost adding SO_2 to the frost layer will have no effect on the sublimation rate. The O_2 or SO created on the surface which then sublimates away could very well matter for the near surface gas density, especially on the nightside, and should be examined in future work.

Figure 8-1 shows a schematic of Io's position in the Jovian system for the current simulations just prior to ingress into eclipse. Io and the bulk plasma rotate counter-clockwise about Jupiter, however, the plasma velocity is ~57 km/s greater than Io's orbital speed and it overtakes Io's trailing[19] hemisphere with the subplasma point at 270° longitude. Note that the subsolar longitude is 351.1° just prior to eclipse, the effect of which is seen in the surface temperature contours shown in Figure 8-2. The surface temperature model is given by Eqn. 4-1; future work will simulate the atmospheric response upon entry into eclipse and incorporate our sophisticated dual-surface temperature model (Walker *et al.*, 2010b).

[19] The leading hemisphere refers to the hemisphere which faces the direction of Io's orbit.

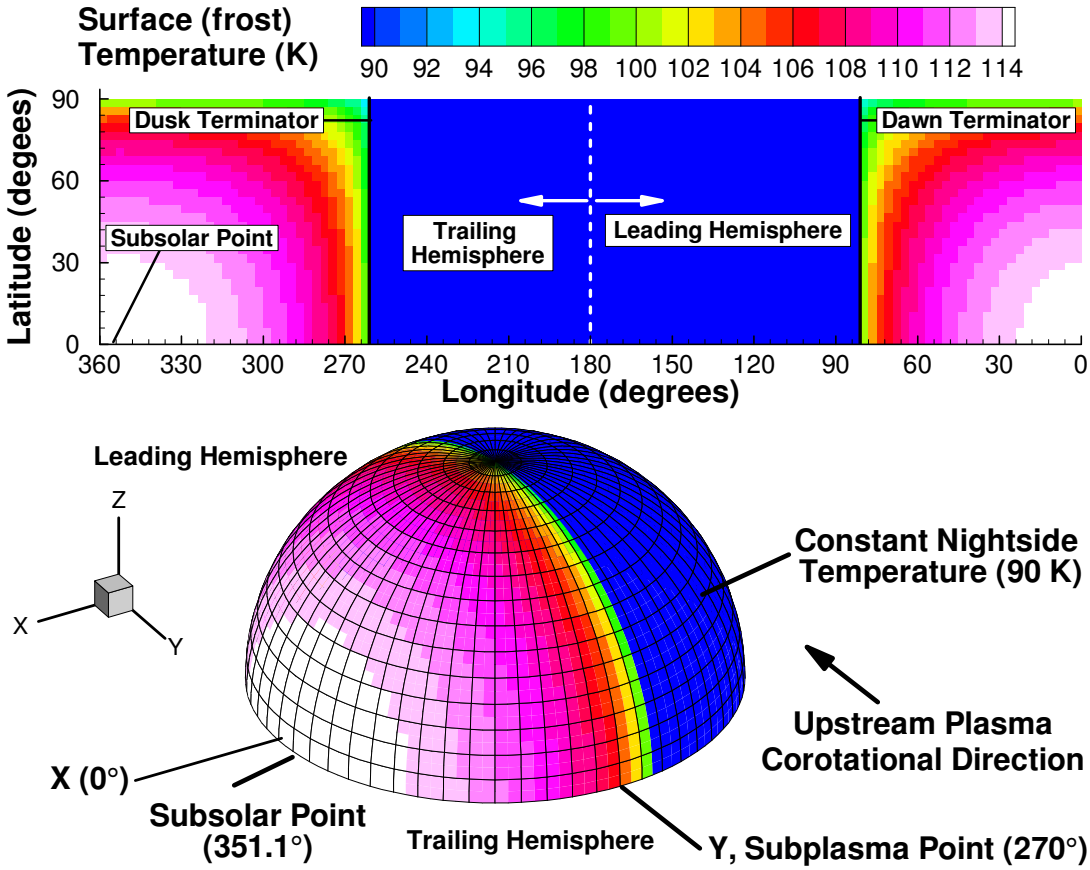

Figure 8-2: Contours of the initial dayside surface (frost) temperature before ingress into eclipse as a function of latitude and longitude. The subsolar point is at a longitude of 351.1°. The 3D perspective view shows the processor decomposition (900 cpu's, black mesh) and the temperature variation on the trailing hemisphere; the upstream bulk plasma velocity is along the Y-axis.

The current simulation solves for the atmosphere in the northern hemisphere of Io with collision cells that extend to 800 km altitude and a free molecular buffer cell that extends the domain to one Io-radius above the surface (1820 km). It is assumed that the plasma flow is symmetric about Io's equator. Four hundred radial collision cells with five linearly adapting segments (Chapter 3.2) are used. The resulting grid is mean free path resolved in the radial dimension over most of the surface; regions of the surface above ~113 K have large enough near surface densities that the radial cells are not quite mean free path resolved. However, the radial density gradients are easily resolved. On the other hand, the latitudinal and longitudinal grid is currently not well resolved, using 3°×3° cells. This was done for efficiency and so that an adequate number of plasma particles would be simulated in each column given that the gas is weakly ionized over much of the domain. However,

appreciable differences were not observed between the current simulations and a separate 6°×6° latitude/longitude cell size simulation (not presented). The computation was load balanced by adaptively weighting simulation particles such that each column contains the same number (currently 4×10^4) of simulation particles averaged over many timesteps.

The ambipolar electric field discussed in Chapter 3.4 is not used in the current simulation. The original intent was to run with and without it in order to clearly identify its effect; however, time limits (computational, etc.) have prevented running and analyzing the resultant atmosphere with the ambipolar field included. Additionally, electron-ion attachement is not included in the current DSMC simulation of Io's atmosphere and therefore charged particles are not lost in Io's atmosphere unless they reach the surface. However, the cross section for attachement is relatively small ($<10^{-17}$ cm^2, see Figure 3-7) and while this loss mechanism might dominate if the plasma is cooled far from the surface, it is not expected that this mechanism has much effect on the overall plasma density (though future simulations should include this mechanism for completeness). Finally, note that the simulations presented here do not include electron-neutral interactions so that the effects of plasma momentum transfer and heavy chemistry on the atmospheric dynamics can be separated from the effects due to electron chemistry. Simulations including electron-neutral reactions and the ambipolar field will be presented in Moore *et al.* (2012).

8.2 STEADY STATE ATMOSPHERE: OVERALL FLOW FEATURES

As in prior models (Austin and Goldstein, 2000; Wong and Smyth 2000; Walker *et al.*, 2010a), circumplanetary flow develops from the high vapor pressure region near the subsolar point to the low vapor pressure nightside. However, now the flow is complicated by momentum flux from the plasma flowing past Io. To examine the overall flow features, near surface (4 km altitude, for comparison to Walker *et al.*, 2010a) contours of several representative species (SO_2, O_2, O, and O^+) densities and their respective streamlines are shown in the following figures. The current simulations are truly steady because the surface temperature and sub-plasma point are not changing. Therefore, the following plots (Figure 8-4 through Figure 8-7) show 20 minute time averages of the simulation after 8 hours of simulation time to improve the statistics. The top panel shows the trailing hemisphere (the same viewpoint as in Figure 8-2) and the bottom panel shows the leading hemisphere (the

viewpoint rotated 180° from the top panel). The properties over the last few simulation hours changed very little so the following results are at least in quasi-steady state.

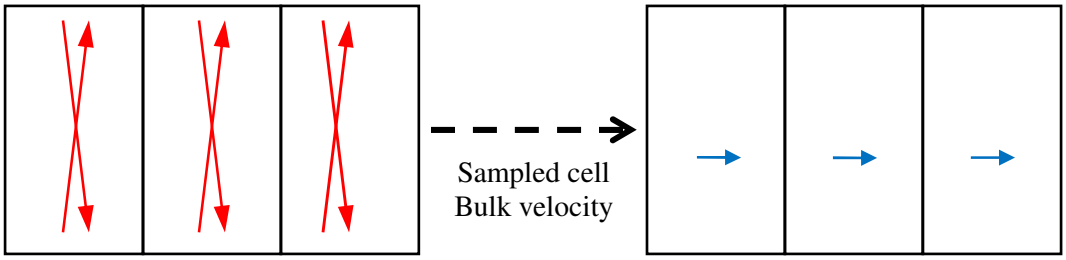

Figure 8-3: Schematic of two collisionless particle streams (red velocity vectors) passing through one another and the resultant sampled bulk velocity (blue) in the DSMC cells.

Note that streamlines in a collisionless flow[20], like those above the exobase (~100 km on the dayside), can be deceptive. For example, if two collisionless particle streams with nearly opposite velocities cross in a cell, as shown in Figure 8-3, the resultant bulk sampled velocity in the DSMC cells is nearly horizontal. A streamline drawn using the bulk velocity would show the flow going from left to right, and, while not incorrect, the actual pathlines (particle trajectories) would not follow the streamline. Streamlines are still useful to interpret the flow where the gas is collisional (near the surface on the dayside), and may be useful even when the gas is rarefied (such as the O^+ streamlines which follow field lines) as they still show the net gas flux.

The near-surface SO_2 number density on both the trailing (top) and leading (bottom) hemispheres is shown in Figure 8-4. The SO_2 number density is seen to peak (as expected) in the subsolar region where the sublimation rate is greatest and falls off sharply at the terminator due to the steep surface temperature gradient in the current surface model. Similar to prior models, the near surface SO_2 streamlines (black) show a flow predominantly from the dense dayside region towards the cold nightside. The streamlines do not appear to originate from the subsolar point region (Figure 8-4, top), probably because the SO_2 pressure (not shown) at 4 km altitude peaks several degrees from the subsolar point in the direction of the subplasma point; this is likely due to plasma heating. Unlike the near surface flow towards the dusk terminator, the near surface flow from the leading hemisphere in the equatorial region travels far onto the nightside across the dawn terminator. For Io's orbital location in

[20] Really just a collection of ballistic particle trajectories.

this simulation, the field lines are sweeping past Io from the dusk to dawn terminators and the ions which travel on the field lines transfer momentum (roughly) in the negative Y-axis direction (see Figure 8-2) because of this. Additionally, the ion motion along the field lines transfers momentum in the Z-axis direction towards the equator because ions that reach Io's surface are assumed lost (see O^+ streamlines in Figure 8-7). The result is that the atmospheric winds on the leading hemisphere extend much further onto the nightside than the trailing hemisphere winds do. The resultant retrograde winds disagree with the observations of prograde winds by Moullet *et al.* (2008); however, their observations were of Io at eastern and western elongation when the subplasma point is at the antisolar and subsolar point respectively. Also, the current simulation surface temperature distribution does not include a surface thermal inertia and it assumes the subsolar point is at a constant longitude. Walker *et al*. (2010a,b) found that these effects change the overall wind dynamics a great deal.

The SO_2 density on the nightside trailing hemisphere increases slightly towards the poles (see Figure 8-4, top); this is due to increased sputtering near the poles (Figure 8-11). Due to the increased sputtering (and, to a lesser extent, plasma heating), the SO_2 pressure in the nightside polar region is roughly twice that of the nightside equatorial region[21]. The increased gas pressure at high latitudes on the nightside along with momentum transfer from the plasma (discussed earlier) explains why the day-to-night flow on the leading hemisphere curves gradually *towards* the equator over hundreds of kilometers, instead of spreading radially out from the subsolar point across the terminator. The diversion of the day-to-night flow towards the equator leads to a region of much higher SO_2 density than predicted from vapor pressure equilibrium (or sputtering) near the equator on the leading hemisphere's nightside. The combination of neutral winds towards the equatorial region (and sputtering) may explain why Io's high latitude regions remain relatively SO_2 frost poor compared to the equatorial regions despite the sublimation of the surface frost during the day. The SO_2 density reaches its minimum on the nightside between the dusk terminator and the equatorial region of high density near the dawn terminator. This minimum occurs because the plasma particles traveling south along the field lines are partially shielded by the (thin) atmosphere and the sputtering rate is reduced (see Figure 8-11). A corresponding high density region far into the

[21] The nightside is in strong thermal non-equilibrium and therefore the precise effect of "pressure" gradients on the gas flow is difficult to determine with the sampled DSMC data.

nightside on the trailing hemisphere does not occur due to the difference in momentum transfer from the plasma at the dusk terminator which tends to push the gas towards the surface, upon which it sticks. The dramatic difference between the equatorial nightside SO_2 densities near the dusk and dawn terminators indicates the importance of the directionality of the plasma flow on Io's global atmospheric dynamics.

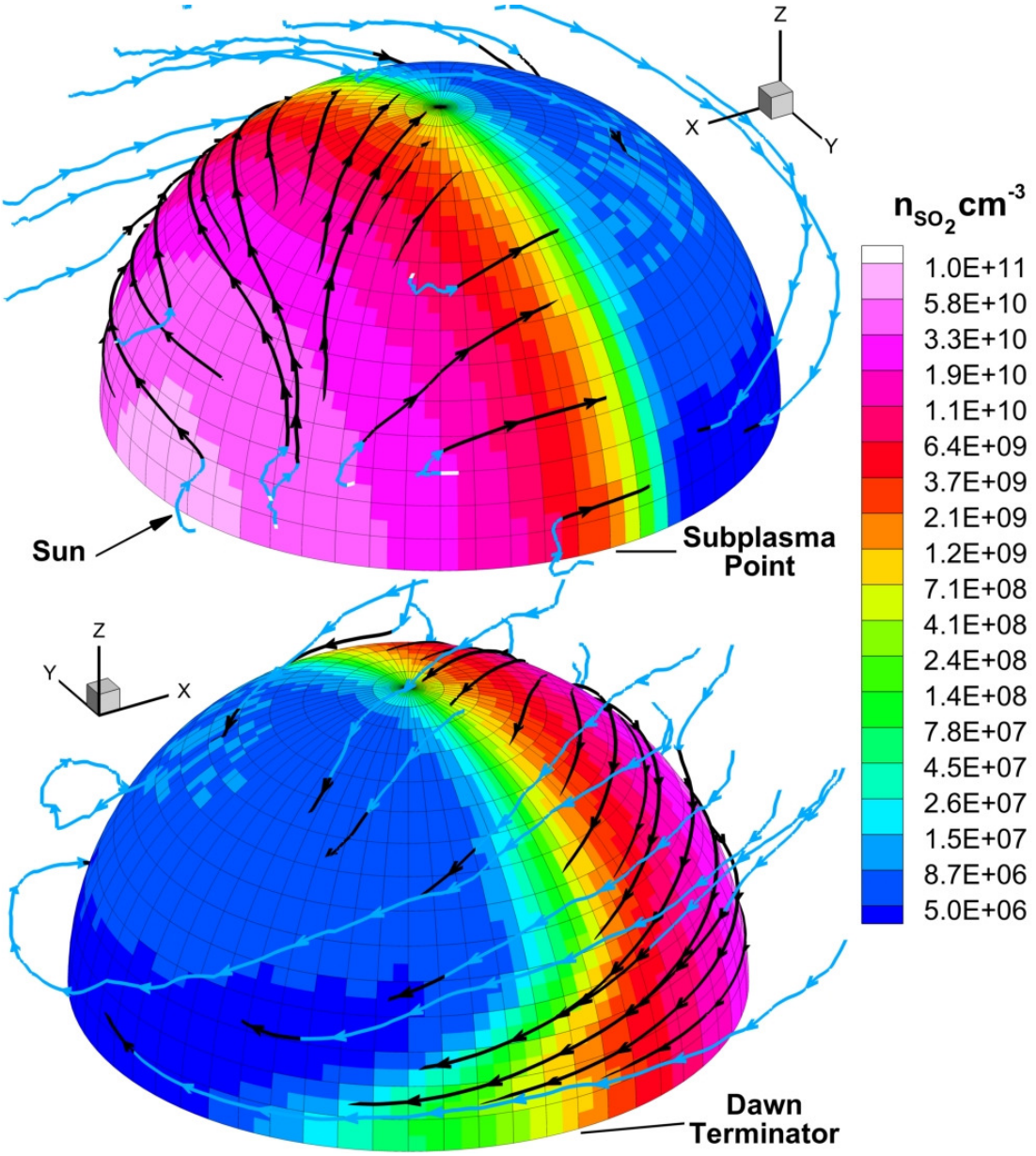

Figure 8-4: Color contours of the SO_2 density 4 km above the surface on the trailing (top) and leading (bottom) hemispheres. Solid lines with arrows are streamlines; above 100 km altitude they are light blue, below they are black. The upstream plasma flows inward along the Y-axis.

High altitude streamlines, which might be deceptive, show SO_2 flows around Io from the leading hemisphere dayside (Figure 8-4, top image) to the trailing hemisphere's nightside (bottom image) where it then abruptly turns towards the surface as it encounters the plasma flow (however this might not correspond to particle paths). It is possible that this is exactly the situation described in Figure 8-3, with two streams of particles passing through one another resulting in a deceptive streamline. However, since these are SO_2 streamlines the counter-flowing stream would have to be SO_2 also, and there is no evidence of such a flow. Instead it seems more likely that the nearly orbital SO_2 flow encounters the plasma flowing in the opposite direction and then "slowly" collides with it over several hundred kilometers until the SO_2 falls to the surface. Finally, note that the blue streamlines on the upper left of the top image in Figure 8-4 are ending at the edge of the output grid (though the free molecular buffer cell extends another 1020 km).

Figure 8-5 shows the near surface atomic oxygen density along with the O velocity streamlines. The oxygen density is highest on the dayside since the parent species densities (SO_2, SO, O_2) are highest on the dayside and O is condensable on the nightside. However, this might also indicate that photo-dissociation dominates plasma impact as a production mechanism, as Smyth and Wong (2004) claim. Again, the day-to-night flow of oxygen on the trailing hemisphere is found to stop near the dusk terminator and high altitude "flows" originate from streamlines starting ~20° from the subsolar point. These high altitude streamlines are seen to flow most of the way around Io until meeting the plasma flow on the trailing hemisphere. Finally, similar to SO_2, there is a clear buildup of oxygen on the leading hemisphere's nightside as the circumplanetary flow streams away from the northern latitudes due to momentum transfer from the plasma and increased nightside pressures at latitudes due to sputtering. The nightside is collisionless over atmospheric scale height length scales; however, the length scales for the streamline curvature are significantly larger indicating that the nightside pressure distribution affects the curvature of the streamlines.

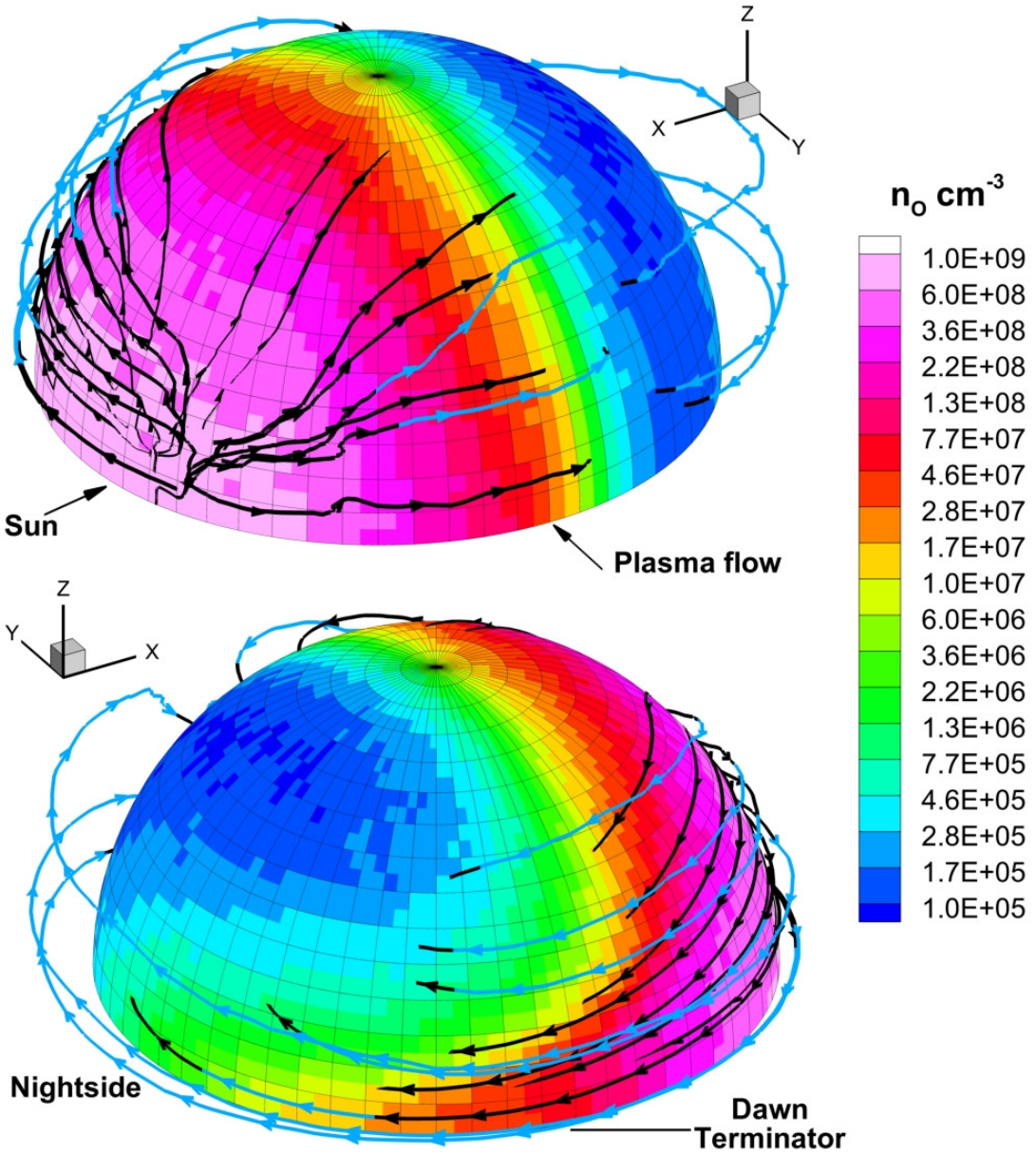

Figure 8-5: Color contours of the O density 4 km above the surface on the trailing (top) and leading (bottom) hemispheres. Solid lines with arrows are streamlines; above 100 km altitude they are light blue, below they are black. The upstream plasma flows inward along the Y-axis.

The O_2 near-surface density and streamlines are shown in Figure 8-6. There are striking differences from the previous two species because, in the current model, O_2 is non-condensable. It is seen that the O_2 density is highest on the dayside where is formed via photo-dissociation of SO_2 (the plasma-dissociation cross section is negligible). However, the density variation from dayside to nightside is much less (only ~100×) than for the

condensable species, as expected. Thus the logarithmic color scale on this figure only extends over roughly two orders of magnitude instead of four or five orders of magnitude in the two previous figures. This leads to the nightside high density region near the equator extending from the dawn terminator nearly all the way to the dusk terminator. The day-to-night O_2 near-surface flow begins from the same region as the SO_2 and O flows; at ~20° towards the dusk terminator. However, at the dusk terminator on the trailing hemisphere the flow now encounters the flow traveling in the opposite direction originating from the leading hemisphere's dayside. The O_2 may be driven into the ground by the condensing SO_2 flow and the plasma flux; since O_2 does not condense, it forms a buffer layer which then migrates very slowly northward in a series of nearly ballistic hops biased towards the pole at which point momentum transfer from the plasma pushes the O_2 back down onto the nightside and/or strips away and dissociates the O_2. It can be seen that the O_2 density locally increases at the dusk terminator due to this flow, an indication that the flow is real and not due to oddities with the streamlines.

Another interesting feature seen in Figure 8-6 (bottom panel) is the presence of a relatively low O_2 density region on the nightside of the leading hemisphere. Streamlines that enter the region travelling latitudinally swirl upon encountering the longitudinal flow from the leading hemisphere's dayside to the dusk terminator. However, because the gas is relatively collisionless on the nightside, it is unclear if the swirl streamlines are real. It is entirely possible that instead of swirling, the O_2 molecules present in the low density region are actually just bouncing repeatedly off the cold night surface until they are either stripped away or dissociated by the plasma. These features have remained persistent over several hours Io time; more detailed study with tracer particles is required to fully understand the complex rarefied flow dynamics and its interaction with the plasma.

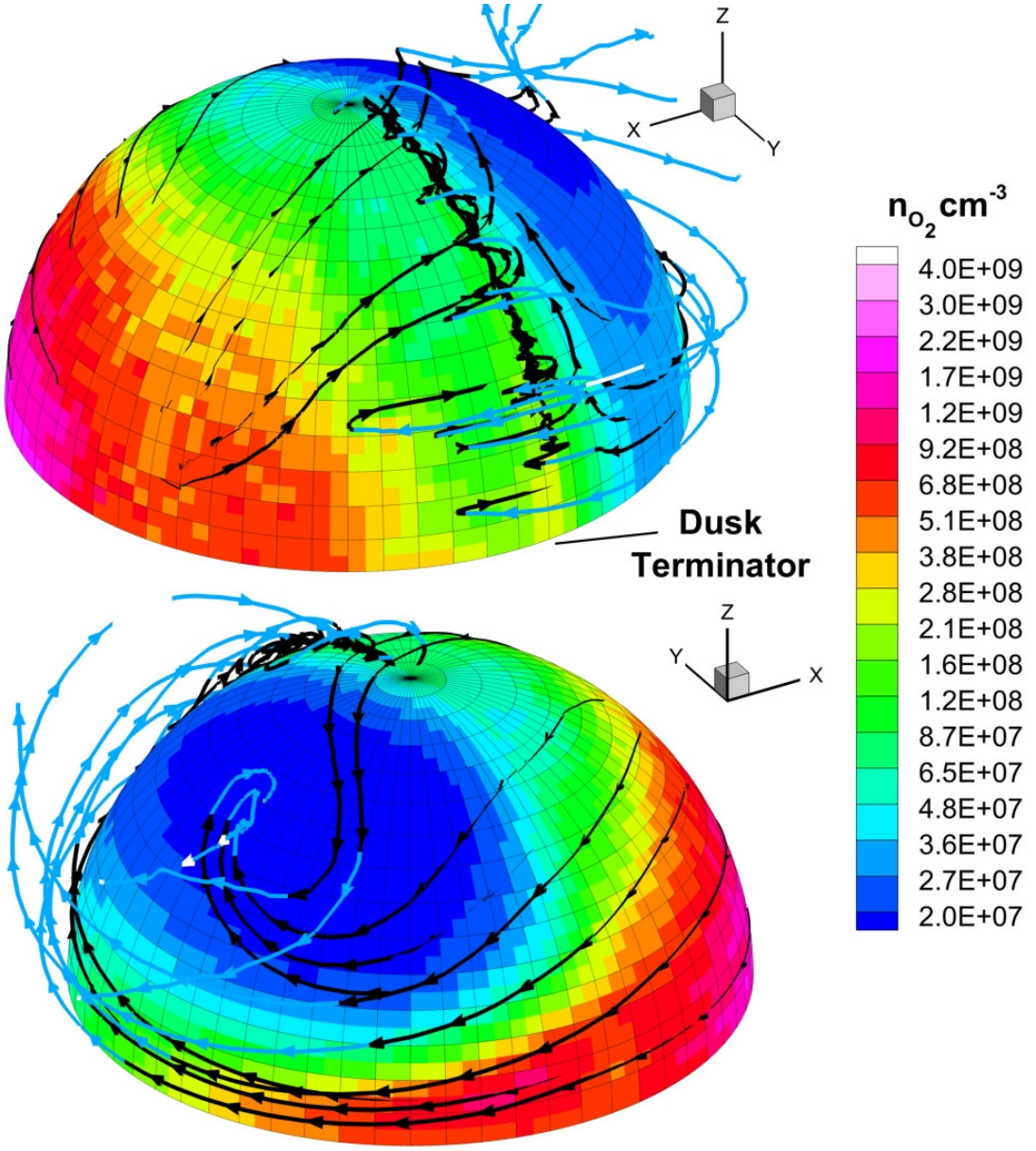

Figure 8-6: Color contours of the O_2 density 4 km above the surface on the trailing (top) and leading (bottom) hemispheres. Solid lines with arrows are streamlines; above 100 km altitude they are light blue, below they are black. The upstream plasma flows inward along the Y-axis.

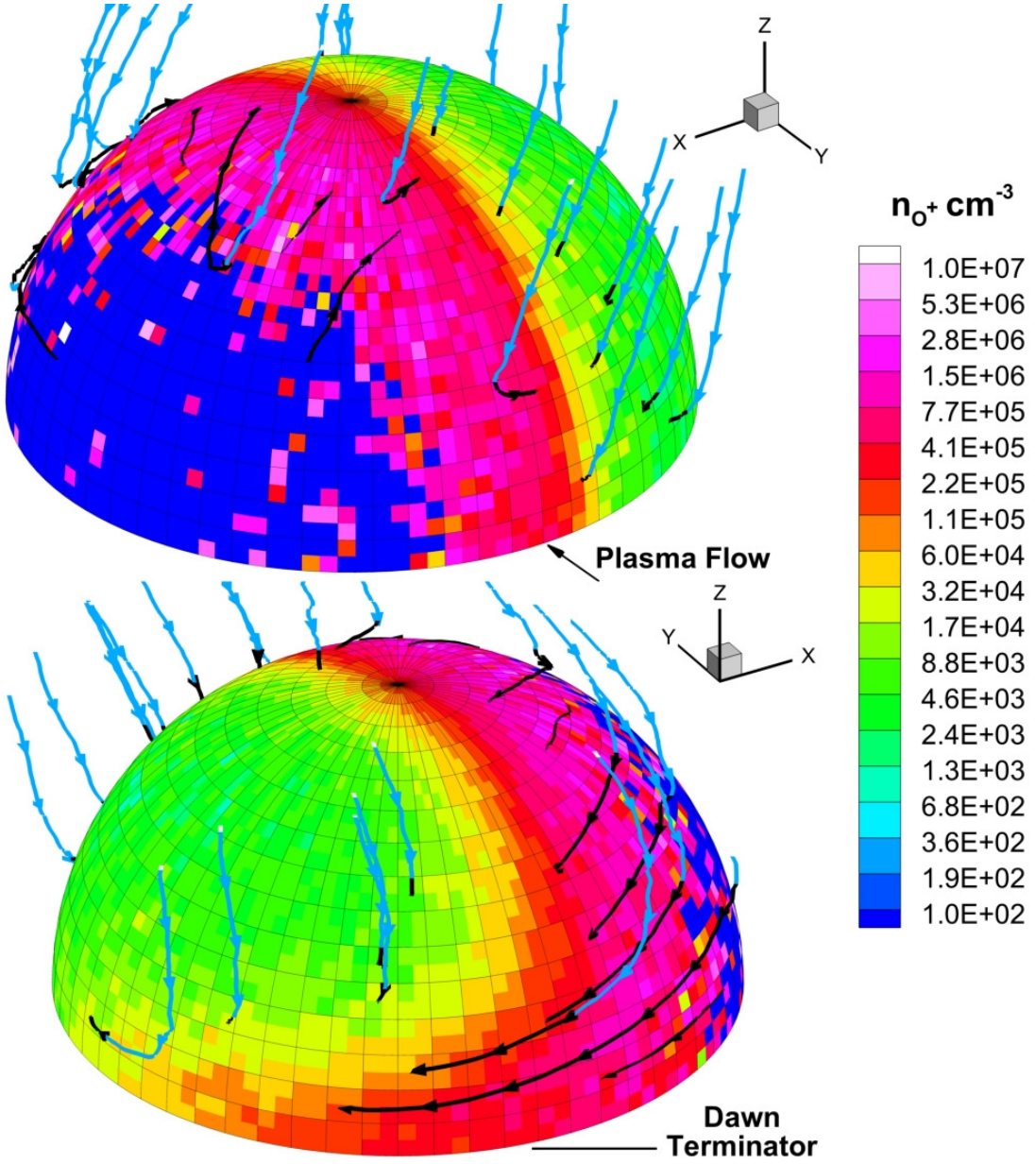

Figure 8-7: Color contours of the O^+ density 4 km above the surface on the trailing (top) and leading (bottom) hemispheres. Solid lines with arrows are streamlines; above 100 km altitude they are light blue, below they are black. The upstream plasma flows inward along the Y-axis and has an O^+ density of 2400 cm^{-3}. Note that the abrupt change on the dayside (from pink to blue in one cell) is partly due to insufficient ion particle statistics on the dayside and grid resolution.

Figure 8-7 shows the near surface O^+ ion density and streamlines. Recall that the upstream O^+ density in the plasma is 2400 cm^{-3} (total plasma density, including S^+ is 3600 cm^{-3}). The dense, primarily SO_2, dayside atmosphere above the subsolar region is found to

prevent penetration of the plasma to low altitude. Around the edge of the dense region the plasma density is enhanced, both because of conservation of mass (the plasma velocity normal to the surface decreases as the plasma collides with the atmospheric column) and due to ionization. In this high density O^+ ion region the plasma is actually fairly cold and slow due to collisions with the (still relatively dense) neutral gas. This can be seen especially in how the streamlines turn near the equator on the leading hemisphere. On the nightside the gas density is low enough that the O^+ streamlines tend to follow the field lines into the surface of Io. Note that the current model assumes that the O^+ (or S^+) incident on the surface is lost whereas in reality the ions would (eventually) be neutralized and possibly leave the surface. One the cold nightside surface, the gas species (except O_2 and possibly SO) are all expected to stick to the surface essentially indefinitely and so the assumption that a particle (not O_2 or SO) incident on the nightside is "lost" is acceptable. On the dayside, it is assumed that the particles incident on the surface (whether O^+ or O) recombine into SO_2 frost which is then sublimated based on the vapor pressure of SO_2, since the model currently assumes an infinite SO_2 reservoir. Future work should improve the surface chemistry model.

8.3 STEADY STATE ATMOSPHERE: DENSITY

The distribution of the atmospheric component species is of great interest when attempting to model auroral emission; therefore, the species column densities and density profiles at several places on Io are examined in detail. Figure 8-8 shows the radial column density for the neutral molecular species. The dayside SO_2 gas column is dominated by the surface temperature dependence as implied by the column's clear "bulls-eye" shape about the subsolar point. Note however that the SO_2 column density is reduced below the hydrostatic column density at a given surface frost temperature because of photo and plasma dissocitation. For example the simulated subsolar point column density (T_s = 115 K) is ~3.6×10^{16} cm^{-2} whereas the analytic hydrostatic column density is ~7.4×10^{16} cm^{-2}. The magnitude of this difference is surprising (the dissociation rate does not seem fast enough to result in such a low column) and further analysis will be provided in Moore *et al.* (2012). On the nightside the analytic hydrostatic SO_2 sublimation column is 1.4×10^{12} cm^{-2} (T_s = 90 K; Eqn. 4-3) which assumes no circumplanetary winds from the dense dayside or dissociation of SO_2. Clearly, Figure 8-8 shows that the nightside SO_2 column is enhanced by at least a factor of 10 even with plasma dissociation, (equivalent to a surface temperature of 96.5 K in vapor

pressure equilibrium), mostly due to sputtering of SO_2 off the nightside surface (Figure 8-11). However, the global day-to-night winds on the leading hemisphere create a separate enhancement of the SO_2 column on the nightside extending to ~150° longitude independent of sputtering. Wong and Johnson (1996) and Austin and Goldstein (2000) found that the buildup of non-condensable on the nightside reduced the day-to-night windspeed and pushed the condensable gases into the surface as they cross the terminator. In the current simulations, the buildup of O_2 on the nightside[22] influences the near surface winds in a similar way, turning the condensable gas stream into the surface. As discussed earlier, because the O_2 does not recondense onto the surface in the current simulations, the O_2 must be either dissociate via photo-reactions (only when in sunlight) and plasma reactions or be stripped away into the plasma torus by momentum transfer or ionization. These loss rates will be examined in more detail with future simulations. Additionally, SO_2 gas molecules with large ballistic arcs rain down onto the nightside and the formation of a relatively dense O_2 nightside atmosphere (5-10 times larger column than SO_2) also helps to support the enhanced SO_2 columns. Without sputtering, Wong and Smyth (2000) found a similar enhancement of SO_2 on the nightside assuming both SO and O_2 are perfectly non-condensable.

[22] O_2 is almost entirely produced by photo-dissociation of SO_2, therefore the O_2 present on the nightside originated on the dayside and was then convected to the nightside where it then is slowly dissociated or stripped away by the plasma. The buildup of O_2 on the nightside is slow, and it is possible that the current simulations are not yet fully at steady state; though the O_2 densities changed very little over 2 hours.

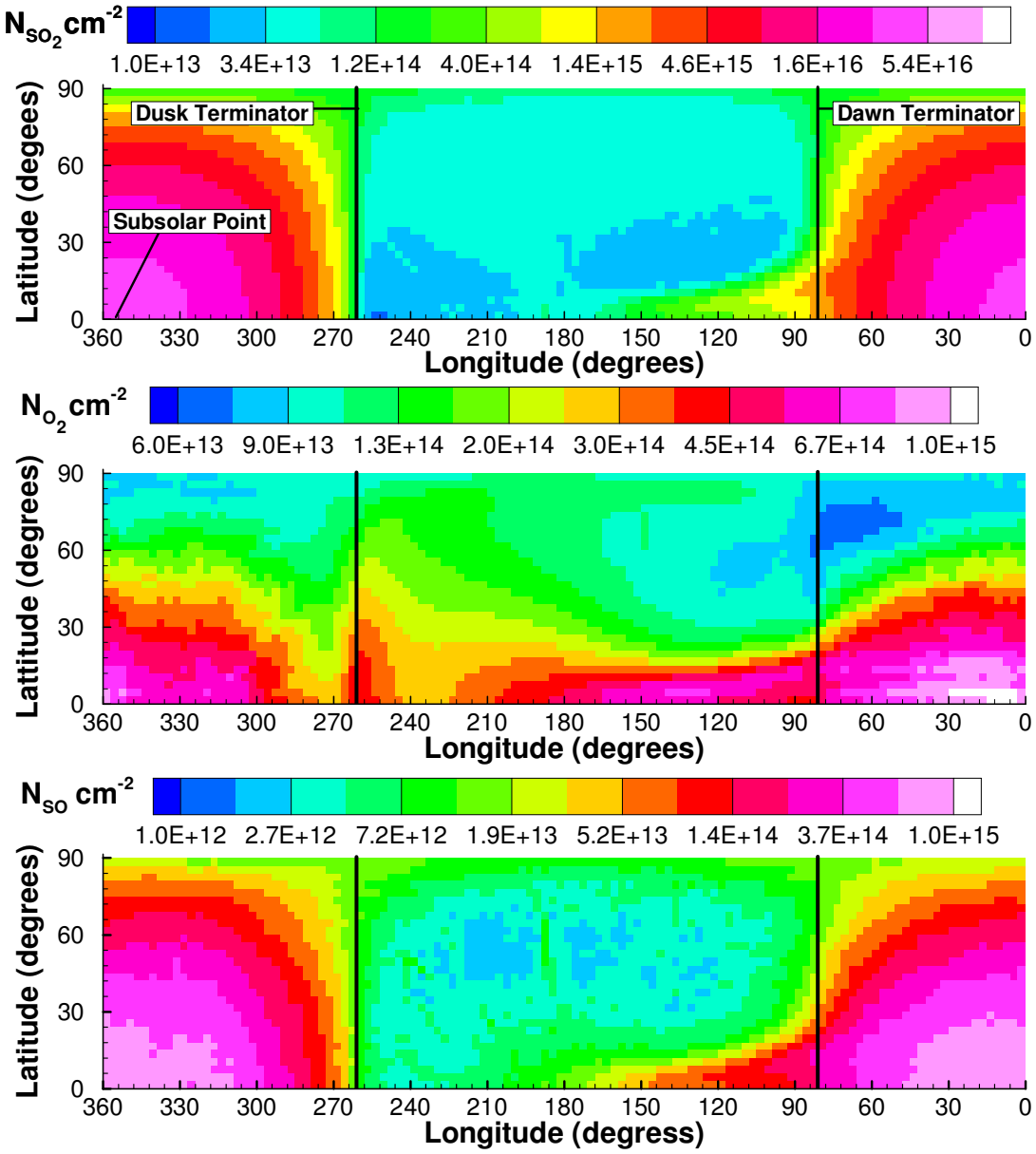

Figure 8-8: Color contours of the SO_2 (top), O_2 (middle), and SO (bottom) column density versus longitude and latitude. Unique contour levels for each species are used to bring out spatial details.

The O_2 (middle) and SO (bottom) columns are shown in Figure 8-8 as well. The morphology differences in the respective columns are primarily due to the condensability of the SO (sticking probability of 0.5) in the current model. Additionally, the photo- and plasma-dissociation rates for the two species are different. The SO column essentially follows the SO_2 column on the dayside since SO_2 is the parent species; though the SO column is slightly

more extended latitudinally due to the partial non-condensability of SO and the global winds. Towards the poles the SO column falls off much like SO_2 suggesting that SO production is dominated by the uniform photo-dissociation[23] and not the pole-biased plasma-dissociation. On the other hand the O_2 column is slightly more confined to low latitudes on the dayside than the SO column; presumably the fall-off towards the pole on the dayside is due to increased plasma-dissociation of the O_2 at higher latitudes (O_2 production via SO_2 plasma-dissociation is negligible). On the nightside the O_2 is very confined to low latitudes because the day-to-night winds flow towards the equator and O_2 is mainly produced on the dayside. Currently the model does not include plasma-SO dissociation (Table 3-4) and therefore the SO does not exhibit the same falloff. However, the magnitude of the O_2 drop-off is exaggerated because the O_2 column contour scale does not span as large a range as the SO or SO_2 contour scales. As discussed earlier, the enhanced O_2 column near the equator is seen to extend across nearly the entire nightside and there is a buildup of O_2 at the dusk terminator where the two flows from the dayside meet and are then forced to the ground by the plasma and the condensing SO_2 flow. The O_2 column also exhibits the same low density region on the leading hemisphere seen in Figure 8-6, though less defined.

The atomic species column densities are shown in Figure 8-9. Again, on the dayside, the columns mostly follow the SO_2 column distribution, shifted latitudinally slightly due to the global winds towards the dawn terminator as seen in Figure 8-5. Again, the columns are enhanced near the equator on the nightside due to the day-to-night flow across the dawn terminator. The enhanced near-equator oxygen column is seen to extend further than the enhanced sulfur column (the sulfur column density colorbar extends over a 10 times larger range than the oxygen colorbar and hence the two enhancements appear to extend nearly equally onto the nightside). The difference between the oxygen extent and the sulfur extent is due to production of oxygen via plasma dissociation of the non-condensable O_2 which dominates the nightside column. Finally, while the morphology of the oxygen and sulfur columns is relatively similar, the peak oxygen column is roughly twice the sulfur column. This is likely because, ultimately, in SO_2 there are two O atoms for each S and the photo- and

[23] The solar flux is assumed to be uniform across the dayside of Io and the gas is assumed to be optically thin (Chapter 3.3).

plasma-dissociation rates are dominated by $SO_2 \rightarrow SO+O$ and then followed by photo-dissociation of SO (see Table 3-1 and Figure 3-10).

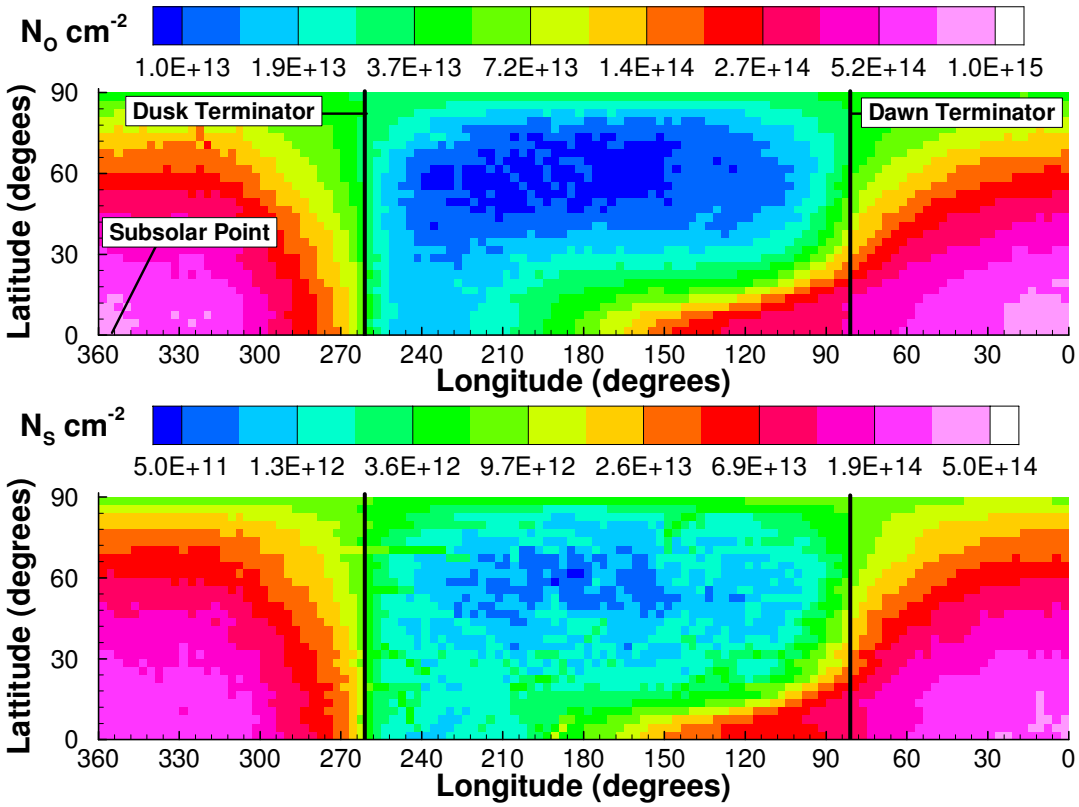

Figure 8-9: Color contours of the O (top) and S (bottom) column densities versus longitude and latitude. Note that the contour levels are unique for each species in order to emphasize spatial detail in each column; the S column density range is an order of magnitude wider than the O column density range.

While the 2D column density plots versus longitude and latitude are useful for examining the spatial features of the various species, it is desirable to compare each species' column directly. Therefore, Figure 8-10 shows the column density of each neutral species versus longitude extracted from the 2D data along the equator. The SO_2 dayside column's extreme dependence on the surface temperature is obvious, as is the asymmetry between the columns on the leading (0°–180° longitude) and trailing (180°–360°) hemispheres. This asymmetry is a product of the directional plasma flow past Io which forces the day-to-night winds to flow predominately past the dawn terminator. While the O_2 column density varies very little along the equator, the O_2 column does decrease from the dayside towards the terminators and there is a local increase in the O_2 at the dusk terminator as previously

discussed. However, similar local increases in the SO_2 and S columns are most likely noise since the columns are much smaller and there is noise in the sputtering yield.Finally note that, not only does the O_2 column exceed the SO_2 column on the nightside, but the atomic oxygen column is essentially equal to the SO_2 column over the nightside even though it is condensable. This is because the primary mechanism of oxygen production on the nightside is plasma dissociation of O_2 which dominates convection from the dayside except in the equatorial enhancement region near the dawn terminator.

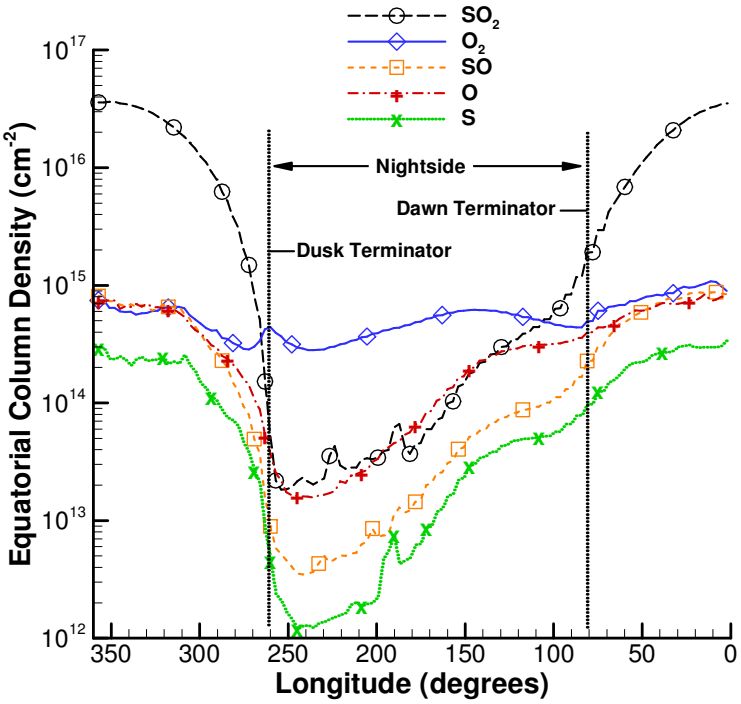

Figure 8-10: Extracted equatorial column densities versus longitude. The subsolar point is at 351.1° longitude; the subplasma point at 270°.

Figure 8-11 shows the SO_2 sputtering rate across Io's surface normalized by the peak sputtering rate. Despite the sensitivity of the sputtering yield to the surface (frost) temperature (Figure 3-14), the sputtering rate is largest across the cold nightside, with a slight bias towards the trailing hemisphere which faces the oncoming plasma. The high column density over the dayside hemisphere shields the surface from the plasma (Figure 8-7), preventing significant sputtering from occurring. Additionally, the plasma is shielded from reaching the surface on the nightside near the equator from the dusk terminator until ~150° longitude because the day-to-night circumplanetary winds have locally increased the column density in

the intervening longitudes. In this case though, sputtering is reduced because the ion energies are reduced to near threshold via collisions with the dense neutral gas; the local ion density is actually enhanced at 4 km altitude (Figure 8-7). Geissler *et al.* (1999) reported green auroral glows, presumably due to [OI] 5577 Å and Na I 5890 Å and 5896 Å emission, which extended across the nightside but stopped at the terminator (see Figure 1-1). They suggested this was possibly due to shielding of the plasma torus electrons by the remains of a dense subsolar atmosphere on the dayside even 50 minutes into eclipse. However, if the emission is due to sputtered Na, then Figure 8-11 suggests that it is the suppression of sputtering by the dense dayside atmosphere due to shielding which causes the glow to stop abruptly at the terminator. Note that Na sputtered on the nightside would be unable to reach the dayside since the prevailing winds go from the high pressure dayside to the low pressure nightside.

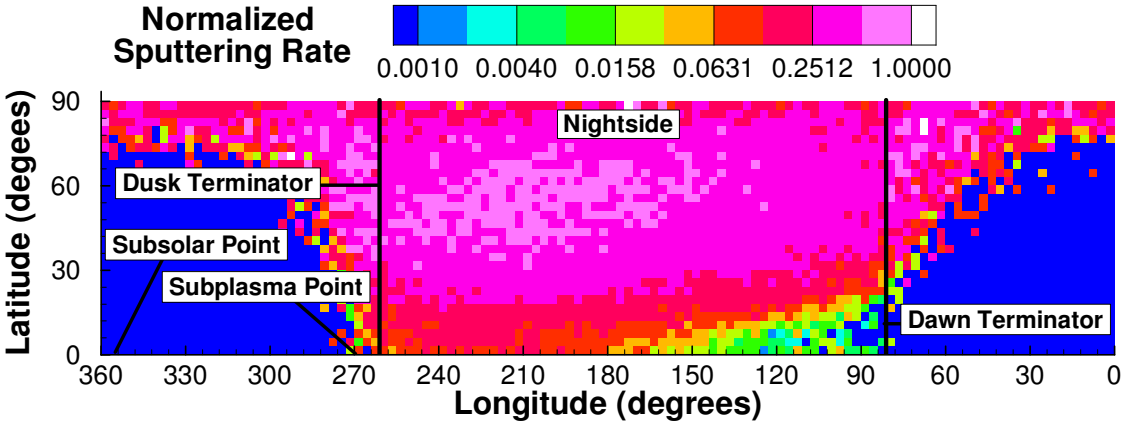

Figure 8-11: Color contours of the normalized SO_2 sputtering rate versus latitude and longitude.

In addition to the column density at the equator, 1D density profiles have been extracted at several points of interest. Figure 8-12 shows the density profiles for the neutral gas species at a subsolar zenith angle of 60° and compares the SO_2 and O profiles at different longitude/latitude combinations at 60° SZA. Neutral gas density profiles on the leading hemisphere at (51° longitude, 0° latitude) are shown in Figure 8-12(a). The SO_2 density is nearly constant up to 10 km altitude because, as seen in previous simulations (Chapter 4; Moore *et al.*, 2009), the collisional gas cools via rotational and vibrational radiation away from the surface until the energy deposition from the plasma begins to dominate and warms the gas back up. Therefore, the pressure profile remains nearly hydrostatic while the gas density remains constant and the temperature drops. Near the surface (<5 km) the O, and S

densities are seen to drop significantly (~20×) whereas the SO density drops slightly less (~10×) due to its partial condensability and the O_2 density remains nearly constant since it is assumed perfectly non-condensable in this simulation and the density of SO_2, the source of O_2, is nearly constant.

At higher altitudes, when the gas is nearly collisionless the species decouple and each has its own scale height (related to the density slope) based on its molecular mass and temperature (determined by collisions with the plasma). As expected, the atomic oxygen and sulfur are seen to have larger scale heights than the heavier SO and SO_2 molecules; though above ~200 km the SO_2 density levels off as the SO_2 gas heats up due to plasma heating. Additionally, the atomic oxygen density is seen to exceed the SO_2 at ~100 km; the local increase in O density is likely due to charge exchange which creates fast neutrals which then puff out the oxygen atmosphere since the local plasma velocity is away from Io's surface on the leading hemisphere.

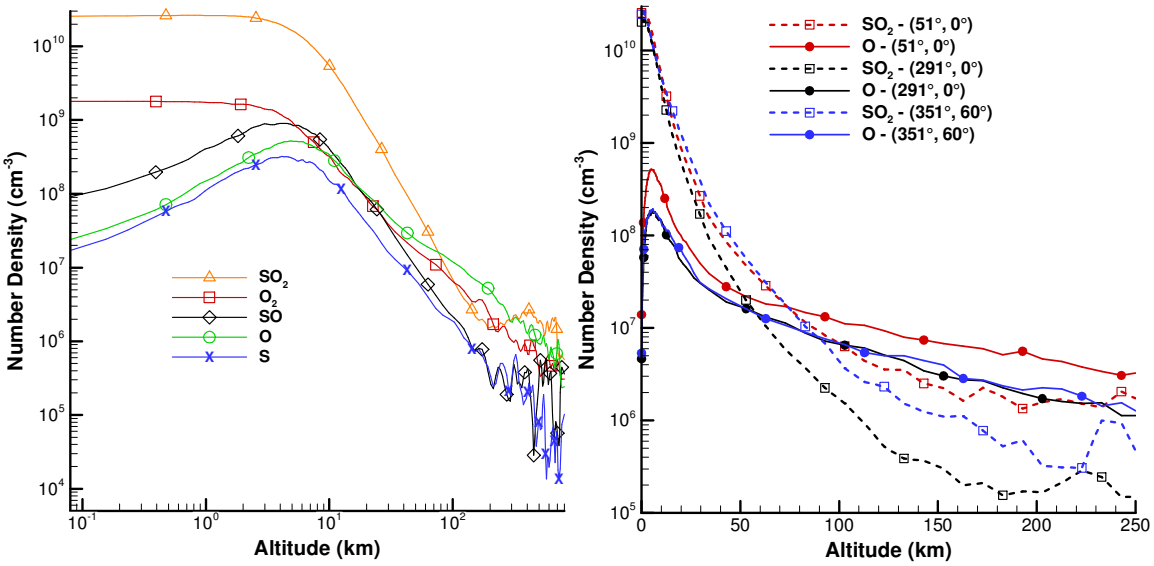

(a) (b)

Figure 8-12: Extracted species density profiles at a 60° subsolar zenith angle. (a) Neutral gas density profiles on the leading hemisphere at 51° longitude at the equator and (b) Comparison between the SO_2 and atomic oxygen density profiles at several (longitude, latitude) coordinates corresponding to a 60° SZA.

Figure 8-12(b) compares the SO_2 and O density profiles at three different locations on Io corresponding to a SZA of 60°. The plasma impacts the trailing hemisphere and it is

seen that the trailing hemisphere SO_2 density profile (longitude of 291°) is compressed relative to the leading hemisphere profile (51° longitude) and even compared to the polar density profile (351° longitude, 60° latitude). The polar density SO_2 profile is seen to be slightly compressed. However, the effect is about half that of the compression on the trailing hemisphere. The compression of the atmosphere on the trailing hemisphere (reducing the scale height) was predicted analytically by Saur et al. (2000) by comparing the plasma pressure and the gravitational force. This effect is not seen if radial plasma heating is used. However, the magnitude of the simulated compression is less than predicted analytically and this is attributed to plasma heating which tends to inflate the atmosphere, offsetting some of the compression due to momentum transfer from the plasma. Moore *et al.* (2011) found that the plasma heating dominated and the neutral gas scale heights increased; however, that was for a 1D simulation where the gas had nowhere to go when compressed by the plasma. In the 3D simulation, the gas pressed toward the surface can flow laterally away from the region of compression and towards the lower density nightside and therefore the scale heights are reduced by momentum transfer from the plasma. The atomic oxygen density on the leading hemisphere (51° longitude) is greater than the density on either the trailing hemisphere (291° longitude) or the polar profile (351° longitude, 60° latitude). This is does not seem to be because of increased oxygen production (the SO_2 densities are essentially the same at low altitudes) on the leading hemisphere; instead it is likely due to the retrograde gas flow from the dense subsolar region towards the dawn terminator convecting significant quantities of atomic oxygen towards the nightside.

The simulation presented here has shown, among other things, the importance of the direction of the plasma flow past Io relative to the subsolar point. Figure 8-13 shows the changing plasma flow direction relative to the subsolar point at various points in Io's orbit. Io is just prior to ingress in the current simulation and the plasma flow is nearly directly onto the dusk terminator and perpendicular to the subsolar point. As Io orbits, the subplasma point does not change, but the subsolar point does. At eastern elongation the momentum transfer from the plasma flow would directly oppose the circumplanetary day-to-night winds. Similarly, when Io is in transit across Jupiter, the plasma flows onto the dawn terminator. This is almost the opposite of the current simulation and therefore it is expected that, instead of a retrograde wind, a prograde wind would develop due to the plasma pressure. The importance of the plasma flow direction relative to the subsolar point is very intriguing and

should be studied further in the future with more accurate surface models allowing for comparison to observations of Io. Finally, note that the surface from 270°–360° longitude should be preferentially scoured by plasma sputtering relative to the rest of Io's surface because the eclipse by Jupiter reduces the local surface temperature (and thus the sublimated column) and the sub-plasma point is at 270° longitude. The increased sputtering might explain why the surface of Io has been observed to remain relatively frost poor at these longitudes.[24]

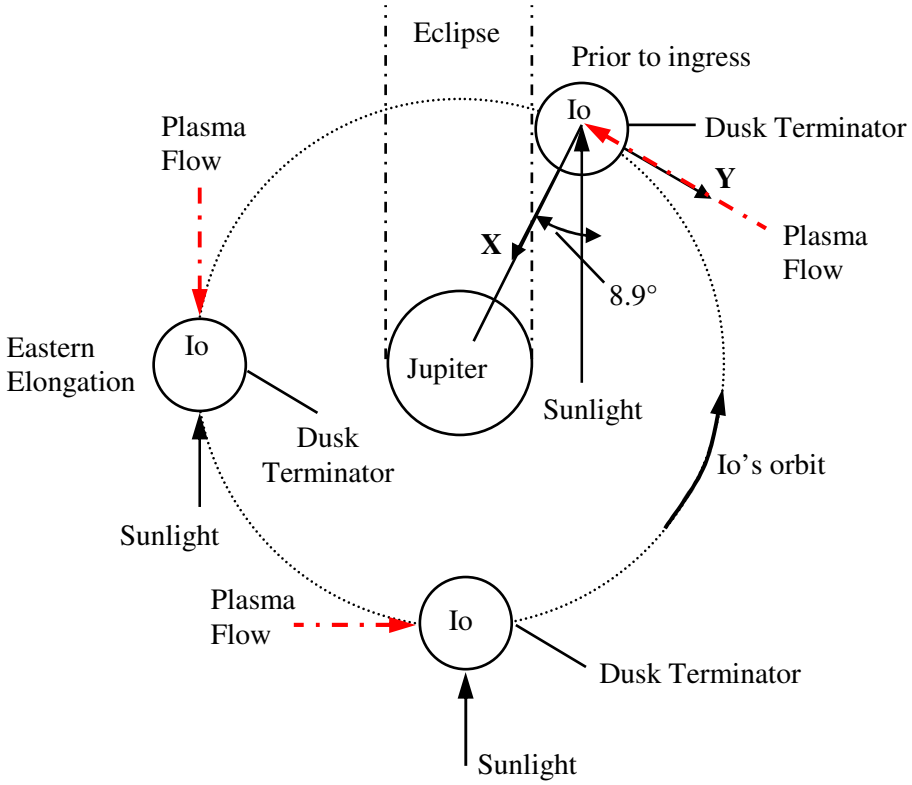

Figure 8-13: Schematic of Io's location in the Jovian system at various times (not to scale) and the corresponding plasma flow versus the subsolar point.

8.4 CONCLUSIONS

In order to provide a more accurate target atmosphere for future aurora simulations, a three dimensional DSMC simulation of Io's atmosphere just prior to ingress into eclipse has been performed including photo and plasma chemistry and ion surface sputtering. Sputtering

[24] McEwen *et al.* (1988) observed reduced surface frost from 270°–360° with Voyager data and Douté *et al.* (2001) observed a similar reduction using Galileo NIMS data.

was found to be blocked over the dayside by the dense sublimation atmosphere; however, sputtering supplied most of the nightside atmosphere and peaked at higher latitudes where the ion flux was more normal to the surface. The influence of the dynamic plasma pressure on the day-to-night flow of the sublimation atmosphere was found to be quite substantial. An overall retrograde wind was formed for Io just prior to entry into eclipse. Based on these results a prograde wind would be expected for Io in transit across Jupiter. In addition, the day-to-night wind across the dawn terminator flows towards the equator due to the plasma pressure from ions streaming down the field lines and the increased nightside pressure at high latitudes. Due to the diversion of the day-to-night wind across the dawn terminator, a region of high density extends far onto the nightside near the equator (~2000 km for the condensable species), and highly asymmetric equatorial column densities result relative to the subsolar point even without thermal lag due to rotation. The apparent flow of material from high latitudes to the equator due to sputtering and the effects of the plasma on the global day-to-night winds possibly explains why the poles remain frost poor relative to the equatorial regions. The non-condensable O_2, which is a trace species on the dayside, is the dominant species on the nightside, despite increased sputtering; this is because the loss rate of O_2 due to plasma dissociation and atmospheric escape is slow. Finally, a very intriguing O_2 flow feature was observed near the dusk terminator as the flow from the leading hemisphere met the flow from the dayside trailing hemisphere. Since the O_2 does not condense on the surface, it slowly convects towards the poles where it is then free to convect back onto the nightside and eventually be dissociated or stripped away by the plasma.

Chapter 9

Conclusions

9.1 SUMMARY

Io's atmospheric interaction with the Jovian plasma torus and the resultant aurora produced (in the UV-Vis) via electron-neutral excitation has been simulated via Monte Carlo simulation methods. Comparisons between observations and the present simulations of the many unique auroral features present at different wavelengths at Io provide insight into the relative importance of the various mechanisms behind Io's auroral features (such as Io's location in the torus, collisional quenching, interaction of the Jovian fields with Io, etc.) and help to constrain the physical parameters (such as upstream electron temperature, atmospheric structure, column abundances and densities, etc.) involved in the interaction.

The Monte Carlo electron transport simulation models the collisions of electrons with the neutral atmosphere and electron transport along field lines as they sweep past Io, using a pre-computed steady atmosphere and magnetic field. As input to the Monte Carlo simulation, the neutral atmosphere was first modeled using prior 2D sunlit (dayside) continuum simulations of Io's atmosphere. The use of a dayside atmosphere for early eclipse observations was justified based on 1D two-species (SO_2 and a non-condensable) DSMC simulations of Io's atmospheric dynamics during and immediately after eclipse. It was found that the inclusion of a non-condensable species (SO or O_2) leads to the formation of a diffusion layer which prevents rapid collapse. The degree to which the diffusion layer slowed the atmospheric collapse was found to be highly sensitive to both the initial non-condensable mole fraction and the reaction (or sticking) probability on the surface of the "non-condensable". Furthermore, vertical stratification of the atmosphere occurred upon egress with the non-condensable species being lifted to higher altitudes by the rapid sublimation of SO_2 as the surface warms. This vertical stratification upon egress could potentially be observable with resolved spectra across Io's limb as it emerges from eclipse since the stratification occurs in <30 minutes; however, care must be taken since the spectra would be line of sight integrated.

The simulated aurorae (specifically the [OI] 6300 Å and the S_2, SO, and SO_2 molecular band emission in the middle ultraviolet) are in reasonably good agreement with observations of Io in eclipse given the observed temporal variability of Io's atmosphere and the jovian plasma torus. Initially it was thought that convection of O ^{1}D would result in significant diffuse [OI] 6300 Å emission. However, even though the lifetime is long (~134 s), it was found that most emission occurred within 100 km ($0.05R_{Io}$) of the excitation event and there was little difference in the emission morphology if the emission was just assumed to occur where excitation occurred. While convection of the excited oxygen was relatively unimportant, collisional quenching before spontaneous emission for the forbidden [OI] emission was found to be important. Unsurprisingly, collisional quenching caused the dense plumes to be dark in 6300 Å emission and also decreased the 6300 Å emission intensity very near the surface. Furthermore, the varying amount of atmospheric collapse due to eclipse across Io was found to affect the emission intensity through increased quenching on the upstream hemisphere (relative to the plasma) since it enters eclipse later than the downstream hemisphere. Finally, it was found that the position of the bright [OI] 6300 Å wake spot relative to Io's equator depends on the position of Io relative to the plasma torus equator and the asymmetric electron number flux that results.

Comparison of the HST/STIS and simulated UV-Vis spectrum showed good agreement up to ~3400 Å. Above this wavelength a presently unknown molecular band emission dominated the observed spectrum. Using the MUV 1 (2550 Å) and MUV 2 (3150 Å) local intensity peaks the upstream electron temperature is weakly constrained to lie between 3 eV and 8 eV depending on the flux of a low energy (35 eV), non-thermal component of the plasma (more non-thermal flux requires lower thermal plasma temperatures to fit the spectrum). Furthermore, an upper limit of 5% of the thermal torus density (or 180 cm^{-3} based on the Galileo J0 plasma density at Io) is obtained for the low energy non-thermal component of the plasma. These limits are consistent with Galileo observations of the upstream torus temperature and estimates for the non-thermal component. Finally, plume activity and S_2 content during eclipse observations with HST/STIS were constrained by examining the emission intensity along the spatial axis of the aperture. During the August 1999 UV-Vis observations, the auroral simulation indicate that the large volcanoes Pele and Surt were inactive whereas Tvashtar was active and that Dazhbog and possibly Loki were also actively venting gas. The S_2 content inferred for the large Pele-type plumes ranged from

trace (<7.5%; Tvashtar) to substantial (15%; Loki, if active) concentrations of S_2, consistent with prior observations (Spencer *et al.*, 2000; Jessup *et al.*, 2007).

The continuum atmosphere in the auroral model must be replaced with an unsteady 3D DSMC atmospheric simulation in eclipse that includes sublimation, surface sputtering, and photo- and plasma-chemistry. This is needed in order to obtain a better match to the observed high altitude emission. Therefore, as a first step the 3D planetary DSMC code was improved to include charged particles that follow field lines and sweep past Io, surface sputtering, and photo- and plasma-chemistry and then a steady 3D DSMC simulation just prior to eclipse was performed to aid in our understanding of the new atmospheric dynamics given the new simulation physics. The plasma in the planetary DSMC code was modeled using a two time-step method in which the neutrals move and then are stationary while the ions move with a much smaller time-step assuming that the plasma is quasi-neutral and that the electrons move with "parent" ions. Ions undergo non-reactive and charge exchange collisions with the neutral species. Those that impact the surface cause sputtering of the SO_2 frost. Fast neutrals produced via charge exchange can dissociate the neutral molecular species; these interaction cross sections have been computed using MD/QCT simulations. The electron interactions with the neutral species are functions of the collision energy and are based on measured reaction cross sections (elastic, excitation, ionization, and dissociation).

A 3D DSMC simulation of Io's atmosphere assuming a simple thermal model for the surface just prior to ingress into eclipse and uniform frost coverage has been performed in order to understand how Io's general atmospheric dynamics are affected by the new plasma model with chemistry and sputtering. The dense dayside sublimation atmosphere was found to block sputtering of the surface; however, sputtering supplied most of the nightside atmosphere (producing an SO_2 column of ~5×10^{13} cm^{-2}) and peaked at higher latitudes where the ion flux was more normal to the surface. The influence of the dynamic plasma pressure on the day-to-night circumplanetary flow was found to be quite substantial. An overall retrograde wind was formed for Io just prior to entry into eclipse and therefore a prograde wind is expected for Io in transit across Jupiter. In addition, the day-to-night wind across the dawn terminator flows slightly towards the equator due to the plasma pressure from ions streaming down the field lines and the increased nightside pressure at high latitudes due to sputtering. This results in a region of high density near the equator that extends far (~2000 km for the condensable species) onto the nightside across the dawn terminator which is not

present at the dusk terminator. It was found therefore, that even without thermal lag due to rotation or variable surface frost, highly asymmetric equatorial column densities relative to the subsolar point occur. Additionally, the apparent flow of material from high latitudes to the equator due to sputtering and the effects of the plasma momentum on the global day-to-night winds possibly explains why the poles remain frost poor relative to the equatorial regions. The non-condensable O_2, which is a trace species on the dayside, is the dominant species on the nightside despite increased SO_2 sputtering because the loss rate of O_2 is slow. Finally, a very intriguing O_2 flow feature was observed near the dusk terminator where the flow from the leading hemisphere (pushed by the plasma) meets the flow from the dayside trailing hemisphere. Since the O_2 does not condense on the surface, it slowly convects towards the poles and then back onto the nightside, eventually to be dissociated or stripped away by the plasma.

9.2 FUTURE WORK

There are many avenues for possible future improvements and extensions to the present work. Below is a brief summary of several possible ideas.

Now that the effects of the new model physics on the neutral atmosphere are better understood (Chapter 8), the logical first step is to run the 3D DSMC neutral atmosphere simulation into eclipse with the ambipolar field due to gradients in plasma density and the much more sophisticated surface temperature and frost models developed by Walker *et al.* (2010a,b). Another improvement to the 3D DSMC model would be to include the magnetic field tilt and approximate the flux tube depletion across Io when applying the plasma boundary conditions. It is possible that these mechanisms will tend to build up atomic oxygen in the north or south wake regions and thereby dramatically changing the emission morphology. This neutral atmosphere could then be used as the target atmosphere (with superimposed volcanoes) for the electron transport code. Hopefully this will yield improved agreement with [OI] 6300 Å observations (especially at higher, more rarefied altitudes) and allow one to determine the importance of the early eclipse (and its variation across Io) on the auroral emission intensity and morphology. Another possibility is to output and compare the OI 1304 Å emission to the emission from the spin forbidden doublet OI] 1359/1359 Å since multiple observations of these lines have been performed (Retherford, 2002).

The Monte Carlo electron transport model can be improved in several ways. First, the constraint on the upstream electron temperature would be greatly improved if e-SO excitation cross sections to the $\tilde{A}\ ^3\Pi$ or $B\ ^3\Sigma$ states could be obtained and incorporated into the model. Inclusion of molecular band emission spectra from other sources (O_2, O_2^+) is necessary to identify the band emission source that dominates the spectrum from ~4000–6000 Å. In addition, these other sources may potentially improve the constraint on the upstream electron temperature. Additionally, the model for the S_2 spectrum and the corresponding excitation cross section should be improved by including emission from high-lying excited vibrational states that can predissociate. Finally, an ambitious goal would be to fully incorporate the Monte Carlo electron transport model into the planetary DSMC code (which already includes the electron-neutral reactions), allowing for a more self-consistent simulation.

The planetary DSMC model can also be improved in the following ways. Probably the most important improvement is to include additional MD/QCT reaction cross sections along with *differential* momentum transfer cross sections. This is important for accurately modeling both the escape rate and the plasma penetration depth and therefore the plasma flux to the surface (causing sputtering). A related improvement of secondary importance would be to sample from the MD/QCT post reaction internal energy distribution for the product molecule (i.e.: SO or O_2) since the product molecule internal energies are likely not in equilibrium as currently assumed. Similarly, the MD/QCT simulations could be used to get vibrational collision numbers (Z_v) for the various neutral collision possibilities (e.g. $O + SO_2$, $S + SO_2$, $O_2 + SO_2$, $O + O_2$, etc.) at high speeds. Getting the internal energy state is important because reaction cross sections are sensitive to the internal energy of the parent molecule. Another improvement important for the escape rate is to determine the excess energy imparted by a photo-reaction by drawing specific photon energies for each reaction (using the cross section as a function of the photon energy).

Currently in the DSMC simulation if a particle is excited (via electron impact or photo-dissociation) the excited state of the neutral is not kept since most excited states radiate away the energy much faster than the mean time between collisions. However, this is not true for forbidden transitions and in very dense regions near the surface at the subsolar point or in a plume vent; therefore, tracking the neutral particle excited states should be considered in the future since they will heat up the neutral atmosphere slightly and can preferentially dissociate molecules when the excited state is collisionally quenched. Similiarly, the electron velocities

are not changed by the fields as the electron moves through the domain; to do so would require sub-stepping the electron acceleration on a smaller timestep or improving the time integration scheme for charged particle motion. Another possible improvement would be to include a model for Io's surface chemistry and the production of O_2 or SO on the surface which would then sublimate. Finally, an ambitious improvement would couple the magnetic and electric field computation with the DSMC atmosphere simulation in order to obtain a more accurate field and atmospheric model.

References

Acuña, M.H., Neubauer, F.M., and Ness, N.F., 1981. Standing Alfvén wave current system at Io: Voyager 1 Observations. *J. Geophys. Res.* **86**, 8,513.

Acuña, M.H, Behannon, K.W., and Connerney, J.E.P, 1983. Jupiter's magnetic field and magnetosphere. In *Physics of the Jovian Magnetosphere, Cambridge Univ. Press, New York,*1–50.

Alexander, F.J., Garcia, A.L., Adler, B.J., 1997. The consistent bolztmann algorithm for the van der Waals equation of state. *Physica A* **240**, 196–201.

Ajello, J.M., James, G.K., Kanik, I., 1992. The complete UV spectrum of SO_2 by electron impact 2. The middle ultraviolet spectrum. *JGR* **97**, No. A7, 10,501–10512.

Ajello, J.M., Hansen, D.L., Beegle, L.W., Terrell, C.A., Kanik, I., James, G.K., and Makarov, O.P., 2002. Middle ultraviolet and visible spectrum of SO_2 by electron impact. *J. Geophys. Res.* **107**, A7, 2-1.

Austin, J.V. and Goldstein, D.B. (2000). Rarefied Gas Model of Io's Sublimaion Driven Atmosphere. *Icarus* **148**, 370-383.

Aoki K., Takata, S., and Taguchi, S. (2003). Vapor flows with evaporation and condensation in the continuum limit: effect of a trace non-condensable gas. *Eur. J. Mech. B/Fluids* **22**, 51-71.

Bagenal, F. and Sullivan, J.D., 1981. Direct plasma measurements in the Io torus and inner magnetosphere of Jupiter. *J. Geophys. Res.* **86**, 8,447-8,466.

Bagenal, F., 1985. Plasma conditions inside Io's orbit – Voyager measurements. *J. Geophys. Res.* **90**, 311-324.

Baklouti, D., Schmitt, B., and Brissaud, O., 2008. S_2O, polysulfuroxide and sulfur polymer on Io's surface? *Icarus* **194**, 647-659.

Ballester, G.E., Moos, H.W., Feldman, P.D., Strobel, F., Summers, M.E., Bertaux J.L., Skinner, T.E., Festou, M.C., and Lieske, J.H., 1987. Detection of neutral oxygen and sulfur emissions near Io using IUE. *Astrophys. J.* **319**, L33–L38.

Ballester, G.E., Strobel, D.F., Moos, H.W., and Feldman, P., 1990. The atmosphere abundance of SO_2 on Io. *Icarus* **88**, 1-23.

Ballester, G.E., McGrath, M.A., Strobel, D.F., Zhu, X., Feldman, P.D., and Moos, H.W., 1994. Detection of the SO_2 atmosphere on Io with the Hubble Space Telescope. *Icarus* **11**, 2-17.

Banwell, C.N., 1983. *Fundamentals of Molecular Spectroscopy*. McGraw-Hill, London.

Bellucci, G., D'Aversa, E., Formisano, V., Cruikshank, D., Nelson, R.M., Clark, R.N., Baines, K.H., Matson, D., Brown, R.H., McCord, T.B., Buratti, B.J., Nicholson, P.D., and the Cassini VIMS Team, 2004. Cassini/VIMS Observation of an Io post-Eclipse Brightening Event. *Icarus* **172**, 141-148.

Bhardwaj, A. and M. Michael, 1999a. On the excitation of Io's atmosphere by the photoelectrons: Application of the analytical yield spectral model of SO_2. *Geophys. Res. Let.* **26**, 393-396.

Bhardwaj, A., and M. Michael, 1999b. Monte Carlo model for electron degradation in SO_2 gas: Cross sections, yield spectra, and efficiencies. *J. Geophys. Res*. **104**, 24,713-24,728.

Bird, G.A., 1979. Simulation of multi-dimensional and chemically reacting flows. *Rarefied gas dynamics; Proceedings of the Eleventh International Symposium, Cannes, France,* 365–388.

Bird, G.A., 1981. Monte Carlo simulation in an engineering context. *Rarefied Gas Dynamics* **74**, Pt. 1, Progress in Astronautics and Aeronautics, AIAA, New York, 239–255.

Bird, G.A., 1985. Low density aerothermodynamics, AIAA paper 85–0994.

Bird, G.A., 1986. Direct simulation of typical AOTV entry flows. AIAA Paper 86–1310.

Bird, G.A., 1994. *Molecular Gas Dynamics and the Direct Simulation of Gas Flows*. Oxford Univ. Press, Oxford.

Birsall, C.K. and Langdon, A.B., 2005. *Plasma Physics via Computer Simulation*. Taylor & Francis Group, New York.

Boring, J.W., Johnson, R.E., Reimann, C.T., Garrett, J.W., Brown, W.L., and Marcantonio, J.W., 1983. Ion induced chemistry in condensed gas solids. *Nucl. Instrum. Methods*, **218**, 707–711.

Boring, J.W., Garrett, J.W., Cummings T.A., Johnson, R.E., and Brown, W.L., 1984. Sputtering of solid SO_2. *Nucl. Instrum. Methods, B1*, 321–326.

Boyd, I.D., Bose, D., and Candler, G.V., 1997. Monte Carlo modeling of nitric oxide formation based on quasi-classical trajectory calculations. *Physics of Fluids* **9** (4), 1162–1170.

Brown, R.A., 1973. "Optical line emission from Io", in *Exploration of the Planetary System*: eds. Woszczyk and Iwaniszewska, Reidel, Boston.

Brown, R.A. and Chaffee, F.H., 1974. High-resolution spectra of sodium emission from Io. *Astrophys. J.* **187**, L125–L126.

Brown, W.L., Lanzerotti, L.J., and Johnson, R.E., 1982. , *Science* **218**, 525.

Carlson, A.B. and Hassan, H.A., 1992. Direct simulation of re-entry flows with ionization. *J. Thermophys. Heat Transfer* **6**, No.3, 400–404.

Carlson, R.W., Kargel, J.S., Douté, S., Soderblom, L.A., and Dalton, J.B., 2006. Io's surface composition. In: *Io after Galileo* (R. Lopes and J. Spencer, Eds.). Spinger, Chichester, UK, pp. 231–264.

Chen, F.F., 1984. *Introduction to plasma physics and controlled fusion Volume 1: Plasma physics.* Springer–Verlag, New York.

Cheng, A.F., 1984. Escape of Sulfur and Oxygen from Io. *JGR* **89**, No. A6, 3939–3944.

Cheng, A.F. and Johnson, R.E., 1989. Effects of magnetospheric interactions on origin and evolution of atmospheres. In: Atreya, S.K., Pollack, J.B., and Matthews, M.S. (eds.), *Origin and Evolution of Planetary and Satellites Atmospheres*. University of Arizona Press, Tuscon, AZ, 683–722.

Chrisey, D.B., Johnson, R.E., Phipps, J.A., McGrath, M.A., and Boring, J.A., 1987. Sputtering of sulfur by kiloelectronvolt ions: Application to the magnetospheric plasma interaction with Io. *Icarus* **70**, 111–123.

Clark, I.D. and Noxon, J.F., 1972. Optical emission from $O(^1D)$ and $O_2(b^1\Sigma_g)$ in ultraviolet photolysis of O_2 and CO_2. *J. Chem. Phys.* **57**, 1,033–1038.

Clarke, J., T.J. Ajello, J. Luhmann, N. Schneider, and I. Kanik, 1994. HST UV spectral observations of Io passing into eclipse. *J. Geophys. Res*. **99**, No. E4, 8,387-8402.

Collins, S.A., 1981. Spatial color variations in the volcanic plume at Loki, on Io. *J. Geophys. Res*. **86**, 8621–8626.

Combi, M.R., K. Kabin, T.I. Gombosi, and D.L. De Zeeuw, 1998. Io's plasma environment during the Galileo flyby: Global three-dimensional MHD modeling with adaptive mesh refinement. *J. Geophys. Res*. **103**, 9,071-9,081.

Cook, A.F., Shoemaker, E.M., and Smith, B.A., 1979. Dynamics of volcanic plumes on Io. *Nature* **280**, 743–746.

Deng, H., Moore, C.H., Levin, D.A., Goldstein, D.B., and Varghese, P.L., 2011. Analysis of SO_2+O chemistry models for simulations of the atmosphere of Io. *Proceedings of the 27th International Rarefied Gas Dynamics Symposium*. **1033**, 1139–1144.

dePater, I., Laver, C., Marchis, F., Roe, H.G., Macintosh, B.A., 2007. Spatially resolved observations of the forbidden SO $a^{\Delta}X^{\Sigma}$ rovibronic transition on Io during an eclipse and a volcanic eruption at Ra Patera. *Icarus* **191**, 172–182.

Dimpfl, W.L., Wysong, I.J., Gimelshein, S.F., Braunstein, M., and Bernstein, L.W., 2008. Application of the Born-Mayer potential with a hard sphere scattering kernel to rarefied hyperthermal gas flow modeling. *Proceedings of the 26th International Rarefied Gas Dynamics Symposium*, **1084**, 323–328.

Douté, S., Schmitt B., Lopes-Gautier R., Carlson, R., Soderblom, L., Shirley, J., and the Galileo NIMS Team. Mapping SO_2 frost on Io by the modeling of NIMS hyperspectral images. *Icarus* **149**, 107–132.

Fanale, F.P., R.H. Brown, D.P. Cruikshank, and R.N. Clark, 1979. Significance of absorption features in Io's IR reflection spectrum. *Nature* **280**, 761–763.

Feaga, L.M., McGrath, M.A, Feldman, P.D., 2002. The abundance of atomic sulfur in the atmosphere of Io. *Astrophys. J.* **570**, 439–446

Feaga, L.M., McGrath, M.A, Feldman, P.D., Strobel, D.F., 2004. Detection of atomic chlorine in Io's atmosphere with the Hubble Space Telescope GHRS. *Astrophys. J.* **610**, 1191–1198.

Feaga, L.M., McGrath, M.A, and Feldman, P.D., 2009. Io's dayside SO_2 atmosphere. *Icarus* **201**, 570-584.

Frank, L.A., Paterson, W.R., Ackerson, K.L, Vasyliunas, V.M., Coroniti, F.V., and Bolton, S.J., 1996. Plasma observations at Io with the Galileo spacecraft. *Science* **274**, 394.

Frank, L.A. and Paterson W.R., 2000. Observations of plasmas in the Io torus with the Galileo spacecraft, *JGR* **105**, 16,107–16034.

Garcia, A.L. and Wagner, W., 2006. Generation of the Maxwellian inflow distribution. *JCP* **217**, 693–708.

Garrett, B.C., Redmon, L.T., McCurdy, C.W., and Redmon, M.J., 1985. Electronic excitation and dissociation of O_2 and S_2 by electron impact. *Phys. Rev. A* **32**, 3366–3375.

Geissler, P., McEwen, A., Ip, W., Belton, M., Johnson, T., Smyth, W., and Ingersoll, A., 1999. Galileo Imaging of Atmospheric Emissions from Io. *Science* **285**, 870-874.

Geissler, P., Smyth, W., McEwen, A., Ip, W., Belton, M., Johnson, Ingersoll, A., Rages, K., Hubbard, W., and Dessler, A., 2001. Morphology and Time Variability of Io's Visible Aurora. *JGR* **106**, 26137-26146.

Geissler, P., McEwen, A., Phillips, C., Keszthelyi, L., and Spencer, J., 2004a. Surface changes on Io during the Galileo mission. *Icarus* **169**, 29–64.

Geissler, P., McEwen, A., Porco, C., Strobel, D., Saur, J., Ajello, J., and West, R., 2004b. Cassini Observations of Io's Visible Aurorae. *Icarus* **172**, 127-140.

Gratiy,S.L., Walker, A.C., Levin, D.A., Goldstein, D.B., Varghese, P.L., Trafton, L.M., Moore, C.H., 2009. Multi-wavelength simulations of atmospheric radiation from Io with a 3D spherical-shell backward Monte Carlo radiative transfer model. *Icarus* **206**, 366–379.

Gulley, R.J. and Buckman, J., 1994. Elastic scattering of low energy electrons from sulphur dioxide. *J. Phys. B.* **27**, 1,833–1,843.

Haff, P.K., Watson, C.C., and Yung, Y.L., 1981. Sputter Ejection of Matter from Io. *JGR* **86**, No. A8, 6933–6938.

Herzberg, G., 1989. *Molecular Spectra and Molecular Structure: Volume 1 – Spectra of Diatomic Molecules*. Krieger Publishing Company. Malabar, Florida.

Heyer, I. and Biretta, J.A., 2004. Wide Field and Planetary Camera 2 Instrument Handbook ver. 9.0. Space Telescope Science Institute.

Huebner, W.F., Keady, J.J., and Lyon, S.P., 1992. Solar photo rates for planetary atmospheres and atmospheric pollutants. *Astrophysics and Space Science*, **195**, 1–294.

Ingersoll, A.P., Summers, M.E., and Schlipf, S.G., 1985. Supersonic meteorology of Io: Sublimation–driven flow of SO_2. *Icarus* **64**, 375–390.

Ingersoll, A. P., 1989. Io Meteorology: How Atmospheric Pressure is Controlled Locally by Volcanos and Surface Frosts. *Icarus* **81**, 298-313.

Itikawa, Y., and A. Ichimura, 1990. Cross sections for collisions of electrons and photons with atomic oxygen. *J. Phys. Chem. Ref. Data* **19**, No.3 , 637–651.

Jessup, K.L., Spencer, J.R., Ballester, G.E., Howell, R.R., Roesler, F., Vigel, M., Yelle, R., 2004. The atmospheric signature of Io's Prometheus plume and anti-jovian hemisphere: evidence for a sublimation atmosphere. *Icarus* **169**, 197–215.

Jessup, K.L., Spencer, J., Yelle, R., 2007. Sulfur volcanism on Io. *Icarus* **192**, 24–40.

Jevons, W., 1932. *Report on band-spectra of diatomic molecules by W. Jevons.* Physical Society, London.

Johnson, R.E., Garrett, J.W., Boring, J.W., Barton, L.A., and Brown, W.L., 1984. Erosion and modification of SO_2 ice by ion bombardment of the surface of Io. *JGR* **89**, B711–B715.

Johnson, R.E., 1989. Plasma ion heating of an SO_2 atmosphere on Io. *Geophys. Res. Lett.* **16**, No. 10, 1117–1120.

Johnson, R.E., 1990. *Energetic charged particle interactions with atmospheres and surfaces*. Springer–Verlag, Berlin.

Johnson, R.E, 1994. Plasma-induced sputtering of an atmosphere. *Space Science Rev.* **69**, 215–253.

Johnson, R.E., 2011. *Private communications.*

Joshipura, K.N. and Gangopadhyay, S., 2008. Electron collisions with sulfur compounds SO, SO_2, and SO_2AB (A, B = Cl, F): various total cross sections. *J. Phys. B.: At. Mol. Opt. Phys.* **41**, 215205 (7pp)

Kivelson, M.G., Khurana, K.K., Russell, C.T., Joy, S.P., Volwerk, M., Walker, R.J., Zimmer, Ch., Linker, J.A., 2001. Magnetized or unmagnetized: Ambiguity persists following Galileo's encounters with Io in 1999 and 2000. *J. Geophys. Res*. **106**, 26,121–26,136.

Kumar, S., 1985. The SO_2 atmosphere and ionosphere of Io: Ion chemistry, atmospheric escape, and models corresponding to the pioneer 10 Radio Occultation measurements. *Icarus* **61**, 101–123.

Lanzerotti, L.J., Brown, W.L., Augustyniak, W.M., Johnson, R.E., and Armstrong, T.P., 1982. Laboratory studies of charged particle erosion of SO_2 ice and applications to the frosts of Io. *Astrophys. J.* **259**, 920–929.

Lellouch, E., Belton, M., de Pater, I., Paubert, G., Gulkis, S., and Encrenaz, T., 1992. The Structure, Stability, and Global Distribution of Io's Atmosphere. *Icarus* **98**, 271-295.

Lellouch, E., 1996. Urey prize lecture. Io's atmosphere: Not yet understood. *Icarus* **124**, 1–21.

Lellouch, E., Paubert, G., Moses, J.I., Schneider, N.M., and Strobel, D.F., 2003. Volcanically emitted sodium chloride as a source for Io's neutral clouds and plasma torus. *Nature* **421**, 45–47.

Lellouch, E., McGrath, M.A., Jessup, K.L., 2006. Io's atmosphere. In: *Io after Galileo* (R. Lopes and J. Spencer, Eds.). Spinger, Chichester, UK, pp. 231–264.

Levin D.A., Candler, G.V., Collins, R.J., Erdman, P.W., Zipf, E.C., Epsy, P., and Howlett, L.C., 1993. Comparison of theory and experiment for the bow shock ultraviolet rocket flight. *J. Thermophys. Heat Transfer* **7**, 30.

Linker J.A., Kivelson, M.G., and Walker, R.J., 1988. An MHD simulation of plasma flow past Io: Alfvén and slow mode perturbations. *Geophys. Res. Lett.* **15**, No. 11, 1311–1314.

Linker, J.A., M.G. Kivelson, and R.J. Walker, 1991. A three-dimensional MHD simulation of plasma flow past Io. *J. Geophys.Res*. **96**, 21,037–21,053.

Linker, J. A., K.K. Khurana, M.G. Kivelson, and R.J. Walker, 1998. MHD simulation of Io's interaction with the plasma torus. *J. Geophys. Res.* **103**, 19,867–19,877.

Lopes, R.M.C., Kamp, L.W., Smythe, W.D., Mouginis-Mark, P., Kargel, J., Radebaugh, J., Turtle, E.P., Perry, J., Williams, D.A., Carlson, R.W., Douté S., and the Galileo NIMS and SSI Teams, 2004. Lava lakes on Io: observations of Io's volcanic activity from Galileo NIMS during the 2001 fly-bys. *Icarus* **169**, 140–174.

McDoniel, W.J., Goldstein, D.B., Varhese, P.L., Trafton, L.M., Buchta, D.A., Freund, J., and Kieffer, S.W., 2011. Simulating Irregular Source Geometries for Ionian Plumes. *Proceedings of the 27th International Rarefied Gas Dynamics Symposium*, **1033**, 1157–1162.

McEwen, A.S., Johnson, T.V., Matson, D.L., and Soderblom, L.A., 1998. The global distribution, abundance, and stability of SO_2 on Io. *Icarus* **75**, 450–478.

McEwen, A.S., Keszthelyim L., Geissler, P., Simonelli, D.P., Carr, M.H., Johnson, T.V., Klaasen, K.P., Breneman, H.H., Jones, T.J., Kaufman, J.M., Magee, K.P., Senske, D.A., Belton, M.J.S., and Schubert, G., 1998. Active volcanism on Io as seen by Galileo SSI. *Icarus* **135**, 181–219.

McGrath, M.A. and Johnson, R.E., 1987. Magnetospheric plasma sputtering of Io's atmosphere. *Icarus* **69**, 519–531.

McGrath, M.A., Belton, M.J.S., Spencer, J.R., and Sartoretti, P., 2000. Spatially Resolved Spectroscopy of Io's Pele Plume and SO_2 Atmosphere. *Icarus* **146**, 476–493.

McGrath, M.A., Lellouch, E., Strobel, D.F., Feldman, P.D., and Johnson, R.E., 2004. Satellites atmospheres. In: *Jupiter. The Planet, Satellites, and Magnetosphere* (F. Bagenal, T. Dowling, and W. McKinnon, Eds.). Cambridge University Press, Cambridge, UK, pp. 457–483.

Melcher, C.L., LePoire, D.J., Cooper, B.H., and Tombrello, T.A., 1982. Erosion of frozen sulfur dioxide by ion bombardment: Applications to Io. *Geophys. Res. Lett*. **9**, No. 10, 1151–1154.

Michael, M. and A. Bhardwaj, 2000a. Precipitation of energetic electrons in Io's atmpsphere: Production of UV emissions. *Adv. Space Res* **26**, 1,519–1,524.

Michael, M. and A. Bhardwaj, 2000b. FUV emissions on Io: Role of Galileo-observed field-aligned energetic electrons. *Geophys. Res. Lett.* **27**, 3,137–3,140.

Mitcher, M. and Kruger, Jr., C.H., 1973. Partially Ionized Gases. John Wiley & Sons. http://www-htgl.stanford.edu/PIG/PIGdefault.html

Moore, C.H., Miki, K., Goldstein, D.B., Varghese, P.L., Trafton, L., and Zhang, J., 2004. Monte Carlo modeling of [OI] 630 nm auroral emission on Io. *Lunar and Planetary Science XXXV*, #1983.

Moore, C.H., Goldstein, D.B., Varghese, P.L., Trafton, L.M., Larignon, B.D., and Walker, A.C., 2006. "1-D Monte Carlo Modeling of Io's Atmospheric Collapse in Eclipse." *LPSC XXXVII*, Abstract **2266**.

Moore, C.H., Goldstein, D.B., Varghese, P.L., Trafton, L.M., Stewart, B.D., and Walker, A.C., 2008. "Io's Atmospheric Freeze-out Dynamics in the Presence of a Non-condensable Species." *Proceedings of the 26th International Rarefied Gas Dynamics Symposium*, **1084**, 1079–1084.

Moore, C.H., Goldstein, D.B., Varghese, P.L., Trafton, L.M., and Stewart, B., 2009. 1-D DSMC simulation of Io's atmospheric collapse and reformation during and after eclipse. *Icarus* **201**, 585–597.

Moore, C.H., Goldstein, D.B., Trafton, L.M., and Varghese, P.L., 2010a. Io's UV-V Eclipse Emission: Implications for Pele-type Plumes. *Lunar and Planetary Science XXXXI*, #2353.

Moore, C.H., Miki, K., Goldstein, D.B., Varghese, P.L., Trafton, L.M., Stapelfeldt, K., Evans, R.W., 2010b. Modeling of Io's [OI] 6300 Å and [SII] 6716 Å Auroral Emission in Eclipse. *Icarus* **207**, 810-833.

Moore, C.H., Deng, H., Goldstein, D.B., Levin, D., Varghese, P.L., Trafton, L.M., Walker, A.C., and Stewart, B.D., 2010c. Impact of Plasma Chemistry on Io's Atmosphere. *DPS 42*, #32.04.

Moore, C.H., Deng, H., Goldstein, D.B., Levin, D., Varghese, P.L., Trafton, L.M., Stewart, B.D., and Walker, A.C., 2011. Simulation of plasma interaction with Io's atmosphere. *Proceedings of the 27th International Rarefied Gas Dynamics Symposium,* **1033**, 1163–1168.

Moore, C.H., Walker, A.C., Goldstein, D.B., Varghese, P.L., Trafton, L.M., Parsons, N., and Levin, D.A., 2012. DSMC simulations of the plasma bmbardment on Io's sublimated and sputtered atmosphere. 50th AIAA Aerospace Sciences Meeting, Nashville.

Moreno, M.A, Schubert, G., Baumgardner, J., Kivelson, M.G., Paige, D.A., 1991. Io's volcanic and sublimation atmospheres. *Icarus* **93**, 63–81.

Morris, A.B., Goldstein, D.B., Varghese, P.L., and Trafton, L.M., 2011. Plume impingement on a dusty lunar surface. *Proceedings of the 27th International Rarefied Gas Dynamics Symposium,* **1033**, 1187–1192.

Moses, J.I., Zolotov M.Y., and Fegely, B.F., 2002. Photochemistry of a volcanically driven atmosphere on Io: Sulfur and Oxygen species from a Pele-type eruption. *Icarus* **156**, 76–106.

Moullet, A., Lellouch, E., Moreno, R., Gurwell, M.A., and Moore, C.H., 2008. First disk-resolved millimeter observations of Io's surface and SO_2 atmosphere. *A&A* **482**, 279–292.

Moullet, A., Gurwell, M.A., Lellouch, E., Moreno, R., 2010. Simultaneous mapping of SO_2, SO, NaCl in Io's atmosphere with the Submillimeter Array. *Icarus* **208**, 353–365.

Neubauer, F.M., 1998. The sub-Alfvénic interaction of the Galilean satellites with the Jovian magnetosphere. *J. Geophys.Res*. **103**, 19,843–19,866.

Oliversen, R.J., Scherb, F., Smyth, W.H., Freed, M.E., Woodward Jr., R.C., Marconi, M.L., Retherford, K.D., Lupie, O.L., and Morgenthaler, J.P., 2001. Sunlit Io atmospheric [OI] 6300 Å emission and the plasma torus. *JGR* **106**, 26,183–26,193.

Ozawa, T., Levin, D.A., and Wysong, I.J., 2007. Chemical reaction modeling for hypervelocity collisions between O and HCl. *Phys. of Fluids* **19**, 056102.

Pearl, J., R. Hanel, V. Kunde, W. Maguire, K. Fox, S. Gupta, C. Ponnamperuma, and F. Raulin, 1979. Identification of gaseous SO_2 and new upper limits for other gases on Io. *Nature* **280**, 755–758.

Porco, C.C. and R.A. West, A. McEwen, A.D. Del Genio, A.P. Ingersoll, P. Thomas, S. Squyres, L. Dones, C.D. Murray, T.V. Johnson, J.A. Burns, A. Brahic, G. Neukum, J. Veverka, J.M. Barbara, T. Denk, M. Evans, J.J. Ferrier, P. Geissler, P. Helfenstein, T. Roatsch, H. Throop, M. Tiscareno, A.R. Vasavada, 2003. Cassini imaging of Jupiter's atmosphere, satellites, and rings. *Science* **299**, 1,541–1547.

Pospieszalska, M.K. and Johnson, R.E., 1996. Monte Carlo calculations of plasma ion-induced sputtering of an atmosphere: SO_2 ejected from Io. *JGR* **101**, No. E3, 7565-7573.

Prahan, D. and Partridge, H., 1996. Theoretical study of the B $^3\Sigma_u^-$ – X $^3\Sigma_g^-$ and B″ $^3\Pi_u$ – X $^3\Sigma_g^-$ band systems of S_2. *Chem. Phys. Lett.* **255**, 163–170.

Radebaugh, J., C. Phillips, A.S. McEwen, M. Milazzo, and L.P. Keszthelyi, 2003. Locations of hotspots on Io from Galileo SSI eclipse images. *Lunar and Planetary Science XXXIV*, #2087.

Radzig A.A. and Smirnov, B.M., 1985. *Reference Data on Atoms, Molecules, and Ions (Springer series in chemical physics)*. Springer-Verlag, Berlin.

Ralchenko, Yu., Kramida, A.E., Reader, J., and NIST ASD Team (2008). *NIST Atomic Spectra Database* (version 3.1.5), [Online]. Available: http://physics.nist.gov/asd3 [2009, March 19]. National Institute of Standards and Technology, Gaithersburg, MD.

Rathbun, J.A., Spencer, J.R., Davies, A.G., Howell, R.R., and Wilson, L., 2002. Loki, Io: A periodic volcano. *Geophys. Res. Let.* **29**, 10, 84–1.

Rathbun, J.A., Spencer, J.R., Tamppari, L.K., Martin, T.Z., Barnard, L., Travis, L.D., 2004. Mapping of Io's thermal radiation by the Galileo photopolarimeter–radiometer (PPR) instrument. *Icarus* **169**, 127–139.

Retherford, K.D., Moos, H.W., Strobel, D.F., Wolven, B.C., and Roesler F.L., 2000. Io's equatorial spots: Morphology of neutral UV emissions. *J. Geophys. Res.* **105**, 27,157–27,166.

Retherford, K.D. (2002) PhD dissertation, Johns Hopkins University. Io's aurora: HST/STIS observations.

Retherford, K.D., H.W. Moos, and D.F. Strobel, 2003. Io's auroral limb glow: Hubble Space Telescope FUV observations. *J. Geophys. Res*. **108**, A8, 7–1.

Retherford, K.D., Cheng, A., Weaver, H.A, Spencer, J.R., and Strobel, D.F., 2007a. New Horizons LORRI observations of Io's visible aurora in eclipse. *Magnetospheres of the Outer Planets 2007*.

Retherford, K.D., Spencer, J.R., Stern, S.A., Saur, J., Strobel, D.F., Steffl, A.J., Gladstone, G.R., Weaver, H.A., Cheng, A.F., Parker, J.Wm., Slater, D.C., Versteeg, M.H., Davis, M.W., Bagenal, F., Throop, H.B., Lopes, R.M.C., Reuter, D.C., Lunsford, A., Conard, S.J., Young, L.A., Moore, J.M., 2007b. Io's atmospheric response to eclipse: UV aurorae observations. *Science* **318**, 237-240.

Roesler, F.L., Moos, H.W., Oliverson, R.J., Woodward Jr., R.C., Retherford, K.D., Scherb, F., McGrath, M.A., Smyth, W.H., Feldman, P.D., Strobel, D.F., 1999. Far-ultraviolet imaging spectroscopy of Io's atmosphere with HST/STIS. *Science* **283**, 353–357.

Saur, J., F. M. Neubauer, D. F. Strobel, and M. E. Summers, 1999. Three-dimensional plasma simulation of Io's interaction with the Io plasma torus: Asymmetric plasma flow. *J. Geophys. Res.* **104**, 25,105–25,126.

Saur, J., Neubauer, F.M., Strobel, D.F., Summers, M.E., 2000. Io's ultraviolet aurora: Remote sensing of Io's interaction. *GRL* **27**, 2893-2896.

Saur, J., F.M. Neubauer, D.F. Strobel, and M.E. Summers, 2002. Interpretation of Galileo's Io plasma and field observations: The J10, I24, I27 flybys, and close polar passes. *J. Geophys. Res*. **107**, A12, 5-1.

Saur, J., Neubauer, F.M., Connerney, J.E.P., Zarka, P., and Kivelson, M.G., 2004. Plasma interaction of Io with its plasma torus. In: *Jupiter: The planet, Satellites and Magnetosphere* (F. Bagenal, T. Dowling, and W. McKinnon, Eds.). Cambridge University Press, Cambridge, UK, pp. 537–560.

Saur, J. and Strobel, D.F., 2004. Relative Contributions of Sublimation and Volcanoes to Io's Atmosphere Inferred from its Plasma Interaction During Solar Eclipse. *Icarus* **171**, 411-420.

Schneider, N.M., Hunten, D.M., Wells, W.K., Schultz, A.B., and Fink, U., 1991. The structure of Io's corona. *Astrophys. J.* **368**, 298–315.

Schneider, N.M. and Bagenal, F., 2006. Io's neutral clouds, plasma torus, and magnetospheric interaction. In: *Io after Galileo* (R. Lopes and J. Spencer, Eds.). Spinger, Chichester, UK, pp. 265–286.

Sharpee, B.D. and Slanger, T.G., 2006. O($^1D_2$–$^3P_{2,1,0}$) 630.0, 636.4, and 639.2 nm forbidden emission line intensity ratios measured in the terrestrial nightglow. *J. Phys. Chem. A* **110**, 6,707–6710

Sieveka, E.M. and Johnson, R.E., 1985. Nonisotropic coronal atmosphere on Io. *JGR* **90**, No. A6, 5327–5331.

Sigmund, P., 1969. Theory of sputtering. I: Sputtering yield of amorphous and polycrystalline targets. *Phys. Rev.*, **184**, No. 2, 383–416.

Singhal, R.P., and S.A. Haider, 1984. Analytical yield spectrum approach to photoelectron fluxes in the earth's atmosphere. *J. Geophys. Res*. **89**, 6,847–6,852.

Sinton, W. and Kaminski, C. (1988). Infrared Observations of Eclipses of Io, its Thermophysical Parameters, and the Thermal Radiation of the Loki Volcano and Environs. *Icarus* **75**, 207-232.

Sittler, E.C., and D.F. Strobel 1987. Io plasma torus electrons – Voyager 1. *J. Geophys. Res*. **92**, 5,741–5762.

Smith, B.A., Soderblom, L.A., Johnson, T.V., Ingersoll, A.P., Collins, S.A., Shoemaker, E.M., Hunt, G.E., Masursky, H., Carr, M.H., Davies, M.E., Cook II, A.F., Boyce, J., Danielson, G.E., Owen, T., Sagan, C., Beebe, R.F., Veverka, J., Strom, R.G., McCauley, J.F., Morrison, D., Briggs, G.A., and Suomi, V.E., 1979a. The Jupiter system through the eyes of Voyager 1. *Science* **204**, 951–972.

Smith, B.A., Shoemaker, E.M., Kieffer, S.W., and Cook II, A.F., 1979b. The role of SO_2 volcanism on Io. *Nature* **280**, 738–743.

Smirnov, B.M., 2000. Tables for cross sections of the resonant charge exchange process. *Phys. Scripta* **61**, 595–602.

Smyth, W.H. and Marconi, M.L., 1998. An explanation for the east–west asymmetry of the Io plasma torus. *JGR* **103**, No. A5, 9091–9100.

Smyth, W.H. and M.C. Wong, 2004. Impact of electron chemistry on the structure and composition of Io's atmosphere. *Icarus* **171**, 171–182.

Smythe, W.D., R.M. Nelson, and D.B. Nash, 1979. Spectral evidence for SO_2 frost or adsorbate on Io's surface. *Nature* **280**, 766.

Sone, Y., Aoki, K., and Doi, T., 1992. Kinetic theory analysis of gas flows condensing on a plane condensed phase: Case of a mixture of a vapor and a noncondensable gas. *Transp. Theory Stat. Phys.* **21**, 297-328

Spencer, J.R., Sartoretti, P., Ballester, G.E., McEwen, A.S., Clarke, J.T., McGrath, M.A., 1997. Pele plume (Io): Observations with the Hubble Space Telescope. *Geophys. Res. Lett.* **24**, 2471–2474.

Spencer, J.R., Jessup, K.L., McGrath, M.A., Ballester, G.E., Yelle, R.V., 2000. Discovery of gaseous S_2 in Io's Pele plume. *Science* **288**, 1208−1210.

Spencer, J.R., Lellouch, E., Richter, M.J., Lopéz-Valverde, M.A., Jessup, K.L., Greathouse, T.K., and Flaud, J., 2005. Mid-infrared detection of large longitudinal asymmetries in Io's SO_2 atmosphere. *Icarus* **176**, 283–304.

Spencer, J.R., Stern, S.A., Cheng, A.F., Weaver, H.A., Reuter, D.C., Retherfor, K., Lunsford, A., Moore, J.M., Abramov, O., Lopes, R.M.C., Perry, J.E., Kamp, L., Showalter, M., Jessup, K.L., Marchis, F., Schenk, P.M., Dumas, C., 2007. Io volcanism seen by New Horizons: A major eruption of the Tvashtar volcano. *Science* **318**, 240.

Stephani, K.A., Goldstein, D.B., and Varghese, P.L., 2011. Development of a Hybrid DSMC/Navier-Stokes Solver with Application to the STS-119 Boundary Layer Transition Flight Experiments. AIAA paper 2011-534 at the *49th AIAA Aerospace Sciences Conference*, Orlando, FL.

Stewart, B. D., Pierazzo, E., Goldstein, D. B., Varghese, P. L., Trafton, L. M., and Moore, C. H. (2009). Parallel 3D Hybrid Continuum/DSMC Method for Unsteady Expansions into a Vacuum. AIAA paper 2009-266 at the *47th AIAA Aerospace Sciences Conference*, Orlando, FL.

Stewart, B.D., 2010. PhD dissertation, The University of Texas at Austin. Numerical simulations of the flow produced by a comet impact on the Moon and its effects on ice deposition in cold traps.

Stewart, B.D., Pierazzo, E., Goldstein, D.B., Varghese, P.L., and Trafton, L.M., 2011. Simulations of a comet impact on the moon and associated ice depositions in polar cold traps. *Icarus* doi:10.1016/j.icarus.2011.03.014.

Strobel, D.F. and Wolven, B.C., 2001. The atmosphere of Io: Abundances and sources of Sulfur dioxide and atomic hydrogen. *Astrophys. Space Sci.*, **277**, 271–281.

Strom, R.G. and Schneider, N.M., 1982. Volcanic eruption plumes on Io. In *Satellites of Jupiter* (D.Morrison, Ed.). University of Arizona Press, Tuscon, pp. 598–633.

Summers, M.E. and Strobel, D.F., 1996. Photochemistry and Vertical Transport in Io's Atmosphere and Ionosphere. *Icarus* **120**, 290–316.

Szmythkowski, C., Maciag, K., and Karwasz, G. (1996). Absolute electron-scattering total cross section measurements for noble gas atoms and diatomic molecules. *Phys. Scr.* **54**, 271-280.

Taguchi, S., Aoki, K., and Takata, S., Vapor flows condensing at incidence onto a plane condensed phase in the presence of a noncondensable gas. 1. Subsonic condensation. *Physics of Fluids* **15**, 689-705 (2003).

Tashiro, M., 2008. Electron impact excitations of S_2 molecules. *Chem. Phys. Lett.* **453**, 145–149.

Trauger, J.T., K.R. Stapelfeldt, G.E. Ballester, and J.I. Clarke, 1997. HST observations of [OI] emissions from Io in eclipse. AAS-DPS abstract, 1997DPS29.1802T.

Trafton, L.M., Parkinson, T., and Macy, W., 1974. The spatial extent of sodium emission around Io. *ApJ* **190**, L85-L89.

Trafton, L.M, 1975. Detection of a potassium cloud near Io. *Nature* **258**, 690–692.

Trafton, L.M., Caldwell, J.J., Barnet, C., and Cunningham, C.C., 1996. The Gaseous Sulfur Dioxide Abundance Over Io's Leading and Trailing Hemispheres: HST Spectra of Io's C^1B_2-X^1A_1 Band of SO_2 Near 2100 Å. *Astrophys. J.* **456**, 384-392.

Trafton, L.M., 2000. Search for Proton Aurora and Ambient Hydrogen on Io. *Astron. J.* **120**, 488–495.

Trafton, L.M., Moore, C.H., Goldstein, D.B., and Varghese, P.L., 2011a. Discovery of unidentified emission band in Io's eclipse spectrum. *Magnetospheres of Outer Planets.*

Trafton, L.M., Moore, C.H., Goldstein, D.B., Varghese, P.L., and McGrath M.A., 2011b. HST/STIS observations of Io's emission spectrum in Jupiter shadow: Probing Io's Jupiter-facing eclipse atmosphere. *Submitted to Icarus.*

Tsang, C.C., Spencer, J.R., Lellouch, E., Richter, M.J., Lopez-Valverde, M.A., and Greathouse, T.K., 2010. Density and Temperature of Io's Atmosphere from Mid-Infrared Observations, 2001 to 2010: Continued Evidence for Inflation as Perihelion Approaches. *DPS 42*, #26.01.

Wagner, W., 1992. A Convergence Proof for Bird's Direct Simulation Monte Carlo Method for the Boltzmann Equation, *J. Stat. Phys.* **66**, 1011–1044.

Wagman, D.D., 1979. Sublimation Pressure and Enthalpy of SO_2, Chem. Thermodyn. Data Cent., Natl. Bur. Of Stand., Washington, D.C.

Walker, A. C., Gratiy, S. L., Goldstein, D. B., Moore, C. H., Varghese, P. L., Trafton, L. M., Levin, D. A., and Stewart, B. D., 2010a. A Comprehensive Numerical Simulation of Io's Sublimation-Driven Atmosphere. *Icarus* **207**, 409–432.

Walker, A.C., Goldstein, D.B., Varghese, P.L., Trafton, L.M., and Moore, C.H., 2010b. Simulated Ionian Column Densities. *DPS 42*, #26.11.

Walker, A.C., Goldstein, D.B., Varghese, P.L., Trafton, L.M., and Moore, C.H., 2011. Loki – A Lava Lake in Rarefied Circumplanetary Cross Flow. *Proceedings of the 27th International Rarefied Gas Dynamics Symposium,* **1033**, 1175–1180.

Wheeler, M.D., Newman, S.M., and Orr-Ewing, A.J., 1998. Predissociation of the B $^3\Sigma_u^-$ state of S_2. *J. Chem. Phys.*, **108**, 6594–6605.

Wong, M.C. and Johnson, R.E., 1996. A Three-Dimensional Azimuthally Symmetric Model Atmosphere for Io 1. Photochemistry and the Accumulation of a Nightside Atmosphere. *JGR* **101**, 23,243-23,254.

Wong, M.C. and W.H. Smyth, 2000. Model calculations for Io's atmosphere at Eastern and Western elongation. *Icarus* **146**, 60-74.

Zhang, J., Goldstein, D.B., Varghese, P.L., Gimelshein, N.E., Gimelshein, S.F., and Levin, D.A. (2003). Simulation of Gas Dynamics and Radiation in Volcanic Plumes on Io. *Icarus* **163**, 182-197.

Zhang, J., Goldstein, D.B., Varghese, P.L., Trafton, L., Moore, C., Miki, K., 2004a. Numerical Modeling of Ionian Volcanic Plumes with Entrained Particulates. *Icarus* **172**, 479-502.

Zhang, J. 2004b. PhD dissertation, The University of Texas at Austin. Simulation of Gas Dynamics, Radiation and Particulates in Volcanic Plumes on Io.

Zolotov, M.Y. and B. Fegley, Jr., 1998. Volcanic production of Sulfur Monoxide (SO) on Io. *Icarus* **132**, 431–434.

Vita

Christopher Moore was born in Oklahoma City, Oklahoma in 1980 to John and Lorie Moore. He received Bachelor of Science degrees in Physics and Aerospace Engineering at the University of Texas at Austin in 2003. In 2003 he joined the graduate program in Aerospace Engineering at the University of Texas at Austin to begin his Ph.D. studies. His research at the University of Texas at Austin in relation with this dissertation has been supported by the NASA Planetary Atmospheres program, the HST Archive program, and the Outer Planetary Research program.

Permanent Address: chmoore.314@gmail.com

This manuscript was typed by the author.